Nanostructured Non-precious Metal Electrocatalysts

for Oxygen Reduction Reaction

in Alkaline Solutions

JANGSOO LEE

Department of Energy Engineering

(Battery Science and Technology)

Graduate School of UNIST

2014

Nanostructured Non-precious Metal Electrocatalysts for Oxygen Reduction Reaction in Alkaline Solutions

A dissertation

submitted to the Graduate School of UNIST

in partial fulfillment of the

requirements for the degree of

Doctor of Philosophy

JANGSOO LEE

2. 10. 2014

Approved by

_____

Advisor

Jaephil Cho

Nanostructured Non-precious Metal Electrocatalysts for Oxygen Reduction Reaction in Alkaline Solutions

JANGSOO LEE

This certifies that the dissertation of JANGSOO LEE is approved.

2. 10. 2014

Signature

———————————————————

Advisor: Jaephil Cho

Signature

———————————————————

Soojin Park

Signature

———————————————————

Nam-Soon Choi

Signature

———————————————————

Kyu Tae Lee

Signature

———————————————————

Youngil Lee

Abstract

Advanced electrical energy storage systems play a vital role in efficient use of electricity in micro-grids or smart-grids to bridge the gaps between demand and supply, especially for renewable energy sources of intermittent and cyclic nature (e.g., solar, wind, and geothermal energy). In the transportation sector, the transition from the current hybrid electric vehicles to all-electric vehicles hinges critically on the development of electrical energy storage systems with dramatically improved energy and power density, durability, and reduced cost. Therefore, new electrochemical systems with higher energy density are being sought, and metal-air batteries with conversion chemistry have the greatest potential to offer the highest energy density and to meet the ever-increasing demands for clean and secure energy. However, the commercialization of metal-air batteries depends critically on the creation of novel air-breathing electrodes with much higher levels of functionality and performance. For example, efficient catalysts for oxygen reduction reaction (ORR) at the air-electrode are yet to be developed to significantly reduce the polarization loss in metal-air batteries. In this thesis, I started with a brief overview of the critical issues relevant to overall zinc-air batteries in chapter 1 and then discussed fundamental aspects of ORR and highlight some recent advancement in the development of non-precious catalysts for ORR in zinc-air batteries, including transition metal oxides, low-dimensional carbon-based structures, and other catalysts in chapter 2. Finally, I introduced my research papers studying electrocatalysts for ORR in alkaline solutions in the rest chapters.

Contents

List of figures

Figure 1-1. Theoretical and practical energy densities of various types of rechargeable battery. Note that the theoretical specific energy density ($\varepsilon M = -nFE/\Sigma M$, where F is the Faraday constant, E is the reaction potential and M is the molar mass of reactants) is calculated excluding O_2 for metal–air batteries.[1]

Figure 1-2. Working principle and each electrode reaction of zinc-air battery. Note the red circle where three phase reaction (oxygen (gas), catalysts (solid) and electrolyte (liquid)) occur in air cathode.[1]

Figure 1-3. a) Schematic representation indicating that the potential of an electrode is independent of its composition, and thus of the state of charge, if the residual value of the degree of freedom is zero.) b) Schematic representation of the variation of the electrical potential as a function of the overall composition when the residual value of F is not zero.[2]

Figure 1-4. Pourbaix diagram for zinc at 25°C and $[Zn(aq)]_{tot} = 10^{-6}$ molal.[3]

Figure 1-5. Strategy for designing more efficient electrocatalysts of unique architecture to facilitate higher cativity for oxygen reduction reaction (ORR) and rapid transport of electroactive species through the porous electro-catalysts in an alkaline solution. In addition to high catalytic activity and sufficient electronic conductivity, an efficient electrode architecture must allow fast transfer of other reactants (such as oxygen molecules) to and the reaction products (such as hydroxide ions) away from the catalytically active sites for ORR to minimize electrode polarization.[4]

Figure 2-1. General reaction scheme for O_2 reduction in alkaline solutions. k_i is the overall rate constant for the ith step. The subscripts sa, a, b, and * denote strongly adsorbed, weakly adsorbed, bulk, and vicinity of the electrode, respectively.[5]

Figure 2-2. (a) Different configurations of O_2 adsorption on catalyst surfaces: on top end-on, bridge end-on, bridge side-on one site, and bridge side-on two sites, from left to right. Simplified electrochemical catalysis process of the ORR on metal surfaces in the case of (b) end-on O_2 adsorption, and (c) bidentate O_2 adsorption, corresponding to the 2e reduction (with generated peroxide species) and the direct 4e reduction, respectively. (d) One of the proposed catalytic ORR pathways at a metal oxide/alkaline electrolyte interface.[6]

Figure 3-4. (a) SEM and (b) TEM images of rGO–IL/Mn_3O_4 composites with size distribution of Mn_3O_4 nanoparticles. (c) HR-TEM image of Mn_3O_4 nanoparticles with the inset of the corresponding SAED pattern and (d, e, f) STEM and the EDX elemental mapping images of hybrid rGO–IL/Mn_3O_4 (10 : 1) composites.

Figure 3-5. (a,b) High-magnification SEM images and (c) TEM image of rGO-IL/Mn_3O_4 (2:1) composites with size-distribution of Mn_3O_4 nanoparticles. (d) HRTEM image of Mn_3O_4 nanoparticles and the inset is the corresponding SAED pattern and (e) Elemental mapping image of hybrid rGO-IL/ Mn_3O_4 (2:1).

Figure 3-6. X-ray diffraction pattern of prepared hybrid rGO-IL/Mn_3O_4 (2:1) with the reference Mn_3O_4 diffraction pattern.

Figure 3-7. X-ray diffraction pattern of all samples used in this study.

Figure 3-8. Rotating disk electrode (RDE) experiments of various samples prepared in this study. (a) Half-cell data and (b) comparison of the onset potential and limiting current of each sample of GO, GO–IL, rGO–IL, rGO–IL/Mn_3O_4 (2 : 1), and rGO–IL/Mn_3O_4 (10 : 1). The rotation rate is 3200 rpm and the scan rate is 10 mV s^{-1}; 0.10 M KOH is used as an electrolyte. Pt wire and Hg/HgO are used as counter and reference electrodes with a 3 mm diameter working electrode, respectively. Onset potential was measured at -0.002 mA and limiting current was measured at -0.45 V.

Figure 3-9. TGA thermograms of all samples used in this study. rGO-IL/Mn_3O_4 (2:1) and rGO-IL/ Mn_3O_4 (10:1) show the relative percentage of Mn_3O_4 within the composite is 52.5% and 19.2%, respectively. The thermograms were obtained at a scan rate of 10 ^{o}C/min under air.

Figure 3-10. Half-cell data of rGO-IL/Mn_3O_4 samples with different Mn contents expressed by the normalization with the Mn content. Rotating disk electrode (RDE) experiments were conducted with the rotation rate 3200 rpm and the scan rate 10 mV/sec; 0.10 M KOH is used as an electrolyte. Pt wire and Hg/HgO is used as a counter and reference electrode with a 3-mm diameter working electrode, respectively.

Figure 3-11. RDE experiments and the corresponding Koutecky–Levich plots of (a, b) rGO– IL/Mn_3O_4 (2 : 1) and (c, d) rGO–IL/Mn_3O_4 (10 : 1). The experiments were conducted at a scan rate of 10 mV s^{-1} in an O_2-saturated 0.10M KOH solution. Theoretical slopes for n = 2 and 4 are also

constructed for comparison.

Figure 3-12. Schematic representation of the potential pathway of electrons during oxygen reduction reaction on the surface of rGO–IL/Mn_3O_4 electrocatalysts.

Figure 3-13. Single cell performance of the Zn–air battery assembled with hybrid rGO–IL/Mn3O4 electrocatalysts compared with 20% Pt/C and commercial cathode materials. (a) Polarization curve of zinc-air cell and (b) corresponding power density plot of (black) rGO–IL/Mn_3O_4 (2 : 1), (red) rGO–IL/Mn_3O_4 (10 : 1), (blue) 20% Pt/C, and (green) commercial cathode (MEET) under the current density from 0 to 200 mA cm^{-2}.

Figure 4-1. Schematic rates in general metal-air battery (also applied to Zinc-air battery).

Figure 4-2. (a) Schematic description of amorphous MnOx particles (a-MnOx) and nanowires on ketjenblack composite (a-MnOx NWs on KB) (b) X-ray diffraction patterns of amorphous MnOx particle, ketjenblack (KB), and amorphous MnOx nanowires on Ketjenblack composites. TEM images of (c) pristine ketjenblack and (d) amorphous MnOx nanowires on Ketjenblack composites, and (e) magnified TEM image of (d).

Figure 4-3. TEM images of amorphous MnOx nanowires on Ketjenblack and the corresponding EDAX spectra.

Figure 4-4. SEM image of as-prepared amorphous manganese oxides particles (A) and the corresponding EDS spectrum (B).

Figure 4-5. Rotating disk electrode (RDE) experiments of Mn_3O_4, amorphous MnOx particle (a-MnOx), ketjenblack (KB), amorphous MnOx nanowires on ketjenblack composites (a-MnOx NWs on KB), and 20% Pt on Vulcan XC-72 (E-tek) under oxygen saturation condition at 3200 rpm; scan rate was 10mV/sec; 0.10 M KOH was used as an electrolyte. Pt wire and Hg/HgO was used as a counter and reference electrode with a 3-mm diameter working electrode, respectively. Onset potential (red color) was measured at -0.002 mA and limiting current (blue color) was measured at -0.45 V.

Figure 4-6. X-ray diffraction patterns of amorphous MnOx particles synthesized at 80°C and asprepared Mn_3O_4 at 160°C with the reference Mn_3O_4 diffraction pattern (JCPDS #: 80-0382).

Figure 4-7. Possible configuration of oxygen molecule interaction with a metal: 1) Griffith, 2)

Pauling, and 3) Yeager's model.

Figure 4-8. (a) A schematic of a zinc-air battery, (b) polarization and (c, d) discharge curve at 200 and 250 mA/cm^2, respectively, of zinc-air full cells with different air electrodes: amorphous MnOx nanowires on ketjenblack composites and 20% Pt on Vulcan XC-72 (E-tek). A commercial air electrode (Meet) was used for comparison.

Figure 5-1. (a) Architectural features of tetrapod structures to minimize damage caused by a tsunami at a coast, commercially available melamine foam (inset), and an cross-sectional view (SEM image) of a fractured melamine foam after pyrolysis at 800°C in Ar for 2hr. It is noted that the interconnected large pores may facilitate fast mass transport. (b) Schematic scheme for the synthesis of Fe/Fe$_3$C functionalized melamine foam infiltrated with N-doped ketjenblack (KB). (1) Melamine foam was soaked with FeCl$_2$·4H$_2$O solution. (2) Adding Ketjenblack EC-600JD and dry. (3) Heat treatment in Ar atmosphere for 2 hours at 800, 900, and 1000°C. (4) Acid leaching with 2M H$_2$SO$_4$.

Figure 5-2. SEM images of (A) commercial ketjenblack carbon and (B) melamine foam pyrolyzed at 800°C under Argon.

Figure 5-3. (a) Steady-state RRDE experiments of (1) ketjenblack EC-600JD, (2) carbonized melamine foam, (3) Fe/Fe$_3$C-melamine+ KB mixture, (4) Fe/Fe$_3$C-melamine/N-KB composite catalyst, (5) 9.55μg$_{Pt}$/cm^2, and (6) 28.6μg$_{Pt}$/cm^2, respectively, in O$_2$ saturated 0.1M KOH at 2000rpm. Non-precious metal catalysts loading are 0.286mg$_{cat}$/cm^2 and the Fe/Fe$_3$C-melamine was prepared at 800°C under Ar (denoted as Ar-800). Ring current (top) and disk (bottom) current density were separated for convenience. (b) Peroxide yields (%) (top) and the number of transferred electrons (n) (bottom) of as-prepared samples.

Figure 5-4. A) XPS high resolution N 1s and (B) Steady-state LSV curve of Ketjenblack EC-600JD (KB) and N-doped KB, in O$_2$ saturated 0.1M KOH at 2000rpm. The catalyst loading was 0.286mg$_{cat}$/cm^2.

Figure 5-5. (a) chronoamperometric response with 10% (W/W) methanol (b) chronoamperometric response of Fe/Fe$_3$C-melamine/N-KB (Ar-800) and 20% Pt/C in O$_2$-saturated 0.1M KOH solution at -0.2V (vs Hg/HgO) and 1600 rpm. 10% (W/W). Methanol was injected into electrolyte at 150 sec and both catalysts loading density were 85μg/cm^2. Before both tests, linear sweep voltammetry was performed in the voltage range from 0.15V to -0.7V (vs Hg/HgO) for 4 times under the same above

conditions. Data of (A) was constructed by adding each cycle data. 1 cycle was maintained for 300 sec and 4 cycles were tested under the same conditions.

Figure 5-6. (a) Current-voltage and (b) power-voltage curves of Zn-air cells with as-prepared composite Fe/Fe$_3$C-melamine/N-KB (Ar-800) and 20% Pt/C catalysts. Gad diffusion layer without any catalysts was used as the baseline air-electrode for comparison. Catalysts loading density of Fe/Fe$_3$C-melamine/N-KB (Ar-800) and 20% Pt/C were 0.212mg$_{cat}$/cm^2 and 28.2µg$_{Pt}$/cm^2 (0.141mg$_{cat}$/cm^2), respectively.

Figure 5-7. (a) X-ray diffraction patterns of a Fe/Fe$_3$C-melamine/N-KB (Ar-800) sample. (b) an SEM image of ground melamine foam structures after carbonization, (c) an SEM image of Fe/Fe$_3$C-melamine/N-KB (Ar-800) sample, and (d) a higher magnification of the image of (c).

Figure 5-8. A) X-ray diffraction patterns and (B) Raman spectra of the composite Fe/Fe$_3$C-melamine/N-KB samples paralyzed at different temperatures (Ar-800, 900, and 1000°C).

Figure 5-9. (A) A typical SEM image of a composite Fe/Fe$_3$C-melamine/N-KB (Ar-800) and (B) the corresponding Energy-dispersive X-ray spectrum (EDS) (Fe peaks at about 0.71 and 6.39 KeV). Further, in energy-dispersive X-ray spectroscopy (EDS), the Ar-800 sample was composed of 75.1 wt. % carbon, 14.2 wt. % nitrogen, 4.99 wt. % oxygen, 3.30 wt. % iron, and 2.30 wt. % sulfur, respectively. The sulfur was originated from bisulfite group of the commercial melamine foam, formaldehyde-melamine-sodium bisulfite copolymer.

Figure 5-10. A) A magnified SEM image of a composite Fe/Fe$_3$C-melamine/N-KB (Ar-800), (B) Typical TEM image of Ar-800, (C) a magnified TEM image of (B), and (D) corresponding HR-TEM image of Ar-800.

Figure 5-11. Dependence of ORR activity on pyrolysis temperature and chemical composition of the composite Fe/Fe$_3$C-melamine/N-KB ORR catalyst. (a) Steady-state LSV curves of composite Fe/Fe$_3$C-melamine/N-KB samples pyrolyzed at different temperatures: 800°C (Ar-800), 900°C (Ar-900), and 1000°C (Ar-1000), as compared to that for19.1µg$_{Pt}$/cm^2 catalyst, tested in O$_2$ saturated 0.1M KOH at 2000 rpm. Non-precious metal catalysts loading are 0.286mg$_{cat}$/cm^2. (b) XPS survey and high resolution (c) N 1s, (d) S 2p, (e) C 1s, and (f) O 1s spectra, respectively, of as-prepared samples.

Figure 5-12. Cyclic voltammograms of the composite Fe/Fe$_3$C-melamine/N-KB (Ar-800) coated on a glassy carbon electrode tested in Ar saturated 0.1M KOH solution at different potential scan rates.

This result is consistent with the physical characterization of our catalysts: they are composed of iron metal and iron carbide, not iron oxides.

Figure 6-1. Schematic representation of a randomly stacked 3D hybrid structure of polyelectrolyte functionalized multiwalled carbon nanotubes (pMWNTs) with reduced graphene oxide (rGO) nanosheets.

Figure 6-2. High-resolution C 1s XPS spectra of all samples used in the study. (a) GO, (b) pMWNT, (c) rGO/pMWNT(0.5:1), and (d) rGO.

Figure 6-3. FT-IR spectra of rGO, pMWNT, rGO/pMWNT(0.5:1), and pure PDAC. All peaks are assigned with the data of previous literature.

Figure 6-4. High-resolution N 1s XPS spectra of all samples used in the study. Negative shift of N 1s peak from 402 eV (pure PDAC) to 401.5 eV (pMWNT) can be attributed to intermolecular charge-transfer of quaternary ammonium nitrogen.

Figure 6-5. (a) Raman spectra of all samples used in the study, (b) ratio of I_D/I_G, (c) D-band shift, and (d) G-band shift of all samples. The I_D/I_G ratio increased from 1.14 in pMWNT to 1.35 in rGO/pMWNT(0.5:1) and even to 1.49 in rGO/pMWNT(10:1), indicating the disordered graphitic structures of hybrid electrocatalysts upon introduction of rGO into pMWNT. The I_D/I_G ratio was measured at least 5 different points of each sample. Up-shift of G bands from 1594.2 cm-1 in pMWNT to 1588.6 cm^{-1} in rGO/pMWNT(10:1) illustrated the charge transfer between rGO and pMWNT.

Figure 6-6. Photograph of each suspension prepared in this study at a concentration of 0.50 mg/mL. The stability of the suspension remained over 8 months.

Figure 6-7. Representative (a) SEM and (b) TEM images of rGO/pMWNT(0.5:1). (c–e) Contact angle images of a water droplet on (c) pMWNT, (d) rGO/pMWNT(0.5:1), and (e) rGO films.

Figure 6-8. (a) Average number of electrons (n_{avg}) transferred per O_2 molecule at different rGO/pMWNT ratios, measured at -0.4, -0.5, and -0.6 V using the Koutecky–Levich plot. A comparison with control sets of pMWNTs and rGO is also presented. (b–e) Steady-state RRDE experiments of pMWNTs, rGO, hybrid rGO/pMWNT(0.5:1) and Pt/C, respectively, in O_2-saturated 0.1 M KOH at 2000 rpm. (b) Disk current density and (c) ring current were separated for convenience.

(d) Peroxide yields (%) and (e) the number of electrons (n) transferred from as-prepared samples. (f) CV curves of pMWNTs, rGO, and hybrid rGO/pMWNT(0.5:1) in N_2- and O_2-saturated 0.1Maqueous KOH electrolyte solution at a scan rate of 50 mV s^{-1}.

Figure 6-9. Linear sweep voltammetry (LSV) curves of (a) pMWNT, (b) rGO/pMWNT(0.5:1), (c) rGO/pMWNT(1:1), (d) rGO/pMWNT(2:1), (e) rGO/pMWNT(5:1), (f) rGO/pMWNT(10:1), and (g) rGO measured in O_2-saturated 0.1 M KOH solution.

Figure 6-10. Current-time (i-t) chronoamperometric response of rGO/pMWNT(0.5:1) in O_2-saturated 0.1 M KOH at -0.4 V (vs. SCE). 3 M of methanol was added at about 300 s to show crossover effect does not occur.

Figure 6-11. The chronoamperometric durability response for 20000 s verified that the rGO/pMWNT(0.5:1) composite exhibited a very slow attenuation with high current retention of 61%, a value which is higher than that of Pt/C in the O_2-saturated 0.1 M KOH solution at -0.25 V (vs. SCE). Electrode rotation rate: 1600 rpm.

Figure 7-1. Schematic view of the synthesis of Ketjenblack incorporated nitrogen doped irregular stacked carbon sheets. (a) Mixing Ketjenblack with gelatin solution via simple aqueous solution, and (b) Pyrolysis at high temperature above 800°C under inert atmosphere. Note that as-prepared catalysts yields are above 50 wt % and large scale synthesis is possible.

Figure 7-2. Pictures for synthetic process of GK-series. (a) Gelatin solution, (b) Gelatine-Ketjenblack jelly, (c) After pyrolysis process at 900℃, GK-900 catalyst on weighing machine.

Figure 7-3. Physical morphology of nitrogen-doped gelatin with Ketjenblack carbon composites (GK). TEM images of GK composites (a), Ketjenblack nanoparticles (b), carbonized gelatin (c) and respective magnified images of a, b, and c (d, e, and f), respectively. Inset is FFT of (d). Scale bars for (a-c) and (d-f) are 100 nm and 5 nm, respectively.

Figure 7-4. XRD data of GKs samples.

Figure 7-5. Chemical state of nitrogen species in GKs catalysts using XPS analysis. (a) N1s XPS analysis of GK-900. Labeled pyridinic nitrogen as (N-6), pyrrolic as (N-5), quarternary as (N-Q), and oxidized nitrogen as (N-X), (b) Overall nitrogen contents and (c) the ratio of Quarternary N to

Pyridinic N depends on pyrolysis temperature.

List of tables

Chapter 1. Electrochemical energy storage and conversion devices

Note: This chapter is partially and totally adapted with permission from "Metal–Air Batteries with High Energy Density: Li–Air versus Zn–Air", Advanced Energy Materials, 2011, 1(1), pp 34-50. Copyright © 2011 John Wiley & Sons, Inc.

1.1 Background

Fluctuation of oil prices and the effects of global warming have forced us to look for alternative energy storage and conversion systems, such as the smart grid. In addition, portable electronic equipment and devices have been developing at a rapid pace, and this progress demands ever-increasing energy and power density in power sources. Due to their energy density, which is higher than that of previous power sources such as Ni-MH batteries, lithium-ion batteries are being considered in the hope of being able to meet these demands. However, the maximum energy density of current lithium-ion batteries is limited owing to electrode materials having intercalation chemistry, and thus such batteries are not satisfactory for the practical application of electric vehicles. Therefore, metal-air batteries have attracted much attention as possible alternatives, because their energy density is extremely high compared to that of other rechargeable batteries, as shown in **Figure 1-1**.
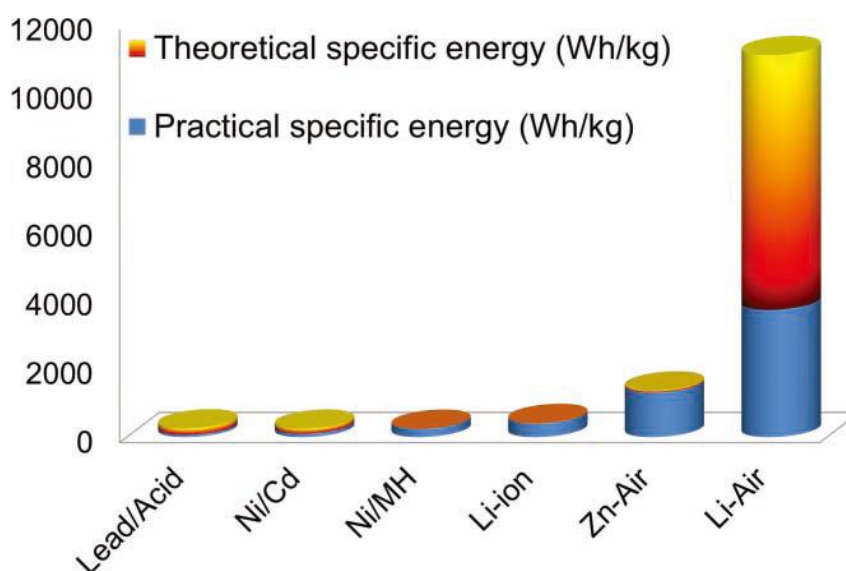
Figure 1-1. Theoretical and practical energy densities of various types of rechargeable battery. Note that the theoretical specific energy density (εM= -nFE/ΣM, where F is the Faraday constant, E is the reaction potential and M is the molar mass of reactants) is calculated excluding O_2 for metal–air batteries.[1, 16]

For example, theoretical specific energy can be calculated with the following equation, where the denominator is the summation of the molecular weights of the reactants.[17]

$$\text{Theoretical specific energy } (\frac{\text{Wh}}{\text{Kg}}) = -\Delta G(= nFE)/\sum Mw$$

Therefore, it is possible to maximize the theoretical specific energy by having a large negative value for ΔG and a small value for $\sum Mw$. The value of ΔG can be made large by selecting for the negative electrode located on the left-hand side of the periodic chart of the elements and for the cathode on the right-hand side. In this regard, using weightless oxygen gas is absolutely favorable in increasing energy density of batteries.

Therefore, to use oxygen in atmosphere, not be stored in the battery, a notable characteristic of metal-air batteries is their open cell structure where oxygen gas can be accessed to cathode and act as unlimited active materials, otherwise, conventional rechargeable batteries such as Li-ion battery is a closed system where energy storage and conversion occur in the same compartment.[7] This is big difference between Li-ion and metal-air battery. There are several kinds of metal-air batteries based on different metal species; their reaction mechanisms are variable, resulting in requests for different types of cell components. Typically, metal-air batteries are divided into two types according to their electrolytes. One is a cell system using an aqueous electrolyte; such a system is not sensitive to moisture. The other is a water-sensitive system using an electrolyte with aprotic solvents. This system is degraded by moisture. Among metal-air batteries, metals such as Ca, Al, Fe, Cd, and Zn are appropriate for the aqueous system. Zinc-air batteries in particular have powerful potential for use as alternative energy storage devices. Al can be more easily corroded than zinc in alkaline solution, although an aluminum-air cell has much more energy density than a zinc-air cell.[18] Also, zinc metal has various advantages such as low cost, abundance, low equilibrium potential, environmental benignity, a flat discharge voltage and long shelf life.[19]

1.2. Overview of Zinc-air battery

1.2.1 Working principle and energy density of Zinc-air battery

Zinc-air cells are composed of three parts; zinc metal as an anode, an air electrode as the cathode, which is divided into a gas diffusion layer and a catalytic active layer, and a separator, as shown in **Figure 1-2**.[1]
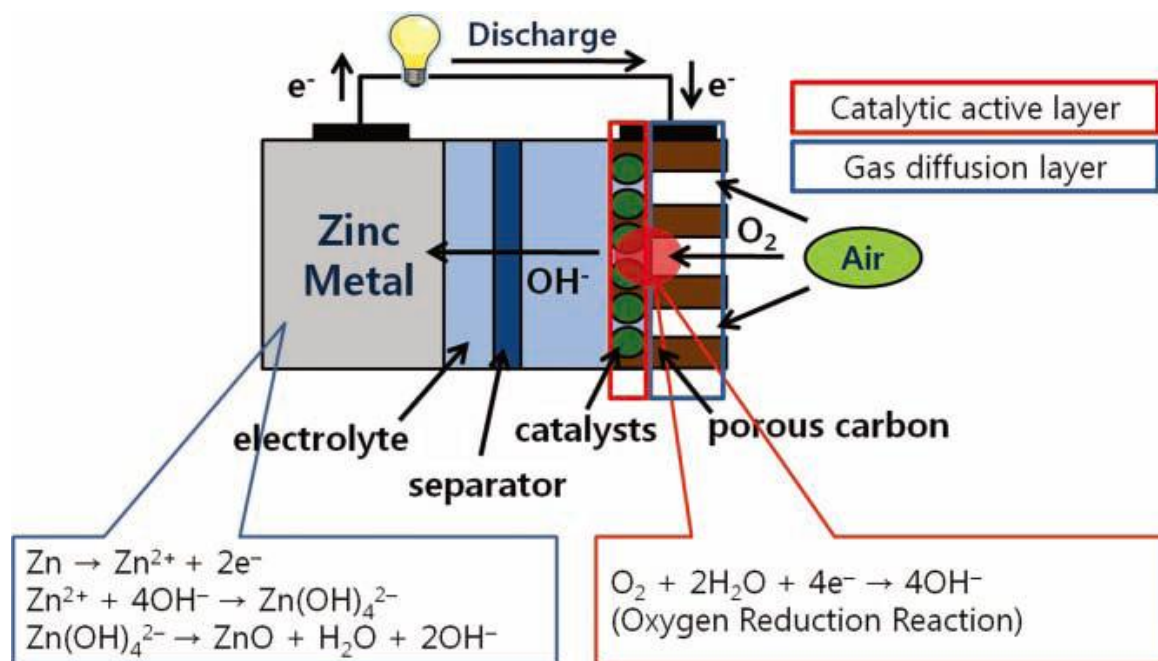
Figure 1-2. Working principle and each electrode reaction of zinc-air battery. Note the red circle where three phase reaction (oxygen (gas), catalysts (solid) and electrolyte (liquid)) occur in air cathode.[1]

Because the solubility of oxygen is very low at atmospheric pressure, it is necessary to use oxygen in the gas phase, not liquid.[20] Oxygen from the atmosphere diffuses into the porous carbon electrode by difference in pressure of oxygen between the outside and inside of the cell, and then the catalyst facilitates the reduction of oxygen to hydroxyl ions in the alkaline electrolyte with electrons generated from the oxidation of zinc metal as the anode reaction. This is why we call this process a three-phase reaction: catalyst (solid), electrolyte (liquid), and oxygen (gas).[21] Note in **Figure 1-2** the red circle where this three phase reaction occurs. This structure favors the gain of oxygen in zinc-air batteries. Generated hydroxyl ions migrate from the air cathode to the zinc anode to complete the cell reaction; this overall procedure during discharge can be described as the following electrochemical reactions of anode and cathode in alkaline solution, respectively.

Anode: $\quad\quad\quad\quad\quad\quad\quad Zn \rightarrow Zn^{2+} + 2e^-$

$\quad\quad\quad\quad\quad\quad\quad\quad\quad\quad Zn^{2+} + 4OH^- \rightarrow Zn(OH)_4^{2-} \ (E^o = -1.25V \ vs. \ NHE)$

$\quad\quad\quad\quad\quad\quad\quad\quad\quad\quad Zn(OH)_4^{2-} \rightarrow ZnO + H_2O + 2OH^-$

$\quad\quad\quad\quad\quad\quad\quad\quad\quad\quad Zn + 2H_2O \rightarrow Zn(OH)_2 + H_2\uparrow (also \ possible)$

Cathode: $\quad\quad\quad\quad\quad\quad O_2 + 2H_2O + 4e^- \rightarrow 4OH^- \ (E^o = 0.4V \ vs. \ NHE)$

Overall reaction: $\quad\quad\quad 2Zn + O_2 \rightarrow 2ZnO \ (E^o = +1.65V)$
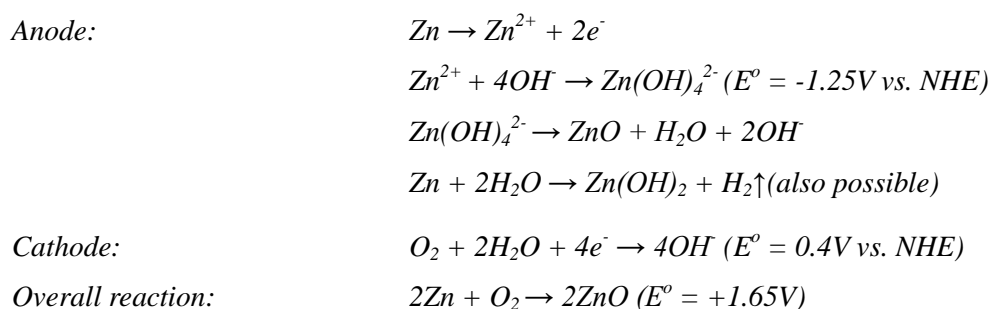
The theoretical capacity of an electrochemical cell, based only on the active materials participating in the electrochemical reaction, is calculated from the equivalent weight of the reactants. Hence, the theoretical specific energy density of Zn-air batteries is 1095 Wh·kg^{-1} (including oxygen) and 1361 Wh·kg^{-1} (excluding oxygen), respectively, that is,[2, 22]

Anode: $2Zn \rightarrow 2Zn^{2+} + 4e^-$ (Theoretical capacity of Zn: 0.82Ah/g$_{Zn}$)

$$\frac{4\,mol\ e^-}{2\,mol\ Zn} \times \frac{1\,mol\ Zn}{65.38g} \times \frac{9.64*10^4 C(A \cdot s)}{1\,mol\ e^-} \times \frac{mAh}{3.6C} = \frac{820mAh}{g_{Zn}} = \frac{0.82Ah}{g_{Zn}} \rightarrow \frac{1.21g}{Ah}$$

Cathode: $O_2 + 2H_2O + 4e^- \rightarrow 4OH^-$ (Theoretical capacity of O$_2$: 3.3Ah/g$_{O_2}$)

$$\frac{4\,mol\ e^-}{1\,mol\ O_2} \times \frac{1\,mol\ O_2}{32g} \times \frac{9.64*10^4 C(A \cdot s)}{1\,mol\ e^-} \times \frac{mAh}{3.6C} = \frac{3347mAh}{g_{O_2}} = \frac{3.3Ah}{g_{O_2}} \rightarrow \frac{0.303g}{Ah}$$

Overall: $2Zn$ (1.21g/Ah) + O_2 (0.303g/Ah) $\rightarrow 2ZnO$ (1.51g/Ah $\rightarrow$ 0.66Ah/g)

Therefore, theoretical specific energy density of Zn-air battery can be calculated, this is,

$$\frac{0.66Ah}{g} \times \frac{1000g}{1Kg} \times 1.66V = \frac{1095Wh}{Kg} (including\ oxygen)\ or$$

$$\frac{0.82Ah}{g} \times \frac{1000g}{1Kg} \times 1.66V = \frac{1361Wh}{Kg} (Excluding\ oxygen\,)$$

1.2.2 Thermodynamic discussion on Zinc-air battery

Thermodynamic potential of Zn-air battery based on the Nernst equation[2]

If no interaction with species in the electrolytes can be assumed, the virtual reaction that will determine the potential is

$$2Zn + O_2 = 2ZnO$$
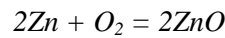
Therefore, it is possible to determine the voltage of Zn-O$_2$ cell by the difference in the chemical potential of oxygen in the two electrodes in following relations

$$\Delta\mu(O_2) = -zFE \text{ (where z is -2, the charge number of oxygen ions)}$$

If oxygen pressure can be assumed to be one atmosphere, the chemical potential of oxygen is the same as that at standard condition, $\mu(O_2) = \mu^o(O_2)$, whereas the chemical potential of oxygen at zinc electrode can be determined by the value of just Zn because ZnO is in equilibrium with Zn. Therefore, the difference in chemical potential of oxygen between Zn and pure oxygen is the totally same to the formation of ZnO. Thus,

$$\Delta\mu(O_2) = \Delta G_f^o(ZnO) = -zFE$$

The Gibbs free energy of formation of ZnO at 298K is 320.5kJ/mol. Therefore, if there is no loss in

the system, the electrical work done is equal to the Gibbs free energy change and the theoretical open circuit voltage of the Zn-air battery can be calculated by the following formula:

$$E_{O_2} = \frac{\Delta G_f}{nF}$$

Where:

E_{O_2} = Theoretical voltage of zinc-O_2 fuel cell, V.

ΔG_f = The Gibbs free energy of formation of ZnO, KJmol^{-1}.

n = Number of electrons transferred in the external circuit.

F = Faraday's constant, 96485C.

In the case of zinc-air battery operated in pure oxygen, n =2 thus the equation becomes:

$$E_{O_2} = \frac{\Delta G_r}{2F}$$

$$E_{O_2} = \frac{-(-320.5 \times 10^3)}{2 \times 96485} KJmol^{-1}C^{-1} = 1.66V \; at \; 1 \; atm \; of \; oxygen$$

The activity of oxygen, however, would be 0.21 in air, not pure oxygen. Thus, we can calculate the cell voltage using the Nernst equation.

$$\Delta E = -\frac{RT}{2F} ln \frac{P_{air}}{P_{oxygen}} = -(\frac{RT}{2F})ln \, [\frac{0.21}{1.0}]$$

$$\Delta E = -(0.012845) \times -1.56 = 0.02$$

$$E_{air} = 1.66V - 0.02V = 1.64V \; at \; ambient \; air \; condition$$

Where R is 8.315J/mol deg, T is 298K, z is -2, and F is 96500C Couloms/mol. Thus, the voltage at air condition would be reduced by about 0.02V, making an open circuit voltage 1.64V in a Zn-air cell operated in atmosphere, not pure oxygen. This theoretical voltage, however, is typically not found in actual Zn-air cells, but open circuit voltage is about 1.3V. It indicates that a formation of potassium zinc oxide phase reduce the chemical potential of oxygen, making the difference in the chemical potential of oxygen is not as large as we assumed.

Gibbs phase rule of a zinc/oxygen cell[2]

The application of Gibbs Phase rule can be used to understand the voltage across in Zn-air cells and how it will vary with the state of charge. The Gibbs Phase rule is often written as

$$F= C - P + 2$$

Where C is the number of components present and P is the number of phases present. F is the number of degrees of freedom. In Zinc-oxygen cell, both anode and cathode have no degrees of freedom left if two intensive thermodynamic parameters, such as temperature and pressure, are specified.[2] It means

that the electric potential will have a constant value as a function of the composition of these electrodes, as seen in **Figure 1-3**. In other words, its voltage will be independent of the state of charge if the oxygen pressure keeps at a constant value, resulting in its voltage profile have characteristics of a plateau, otherwise, if a degree of freedom is left, the cell voltage can vary and changes during discharge in common battery systems.[7]
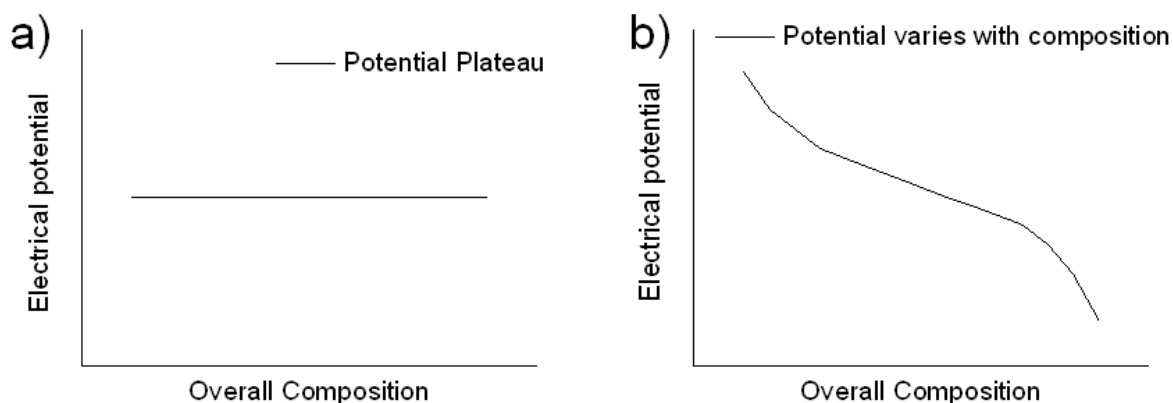
Figure 1-3. a) Schematic representation indicating that the potential of an electrode is independent of its composition, and thus of the state of charge, if the residual value of the degree of freedom is zero.) b) Schematic representation of the variation of the electrical potential as a function of the overall composition when the residual value of F is not zero.[2]

For the alkaline Zn/MnO_2 battery, the only different battery chemistry is the cathode reaction compared to Zn/air battery. In the former, MnO_2 participate in cathode reaction and its phase is changed via one and two electron discharge.[23]

First electron discharge of cell could be expressed as following equations:

$$\text{Cathode: } \gamma\text{-}MnO_2 + H_2O + e^- \rightarrow MnOOH + OH^-$$
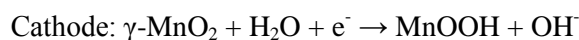
If the electrode continues to discharge, cathode and anode are further irreversibly reduced at the second step:

$$\text{Cathode: } MnOOH + H_2O + e^- \rightarrow Mn(OH)_2 + OH^-$$
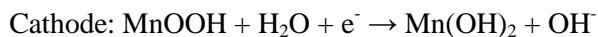
Therefore, these phase change based on the Gibbs phase rules can explain the big difference in voltage profile between them.[7]

1.3. Components of Zinc-air battery

1.3.1 Electrochemical behavior of zinc electrode based on a pourbaix diagram

Zinc-air batteries use pure zinc metal itself as an anode active material; oxidation of the zinc

occurs during discharge. This is why most studies have focused on improving the air electrode, not the zinc anode. Before discussion on electrochemical behavior of zinc in aqueous electrolyte, construction of pourbaix diagram is appropriated in **Figure 1-4 and Appendix Figure 3-1**.[24]

Revised Pourbaix diagrams for Zn
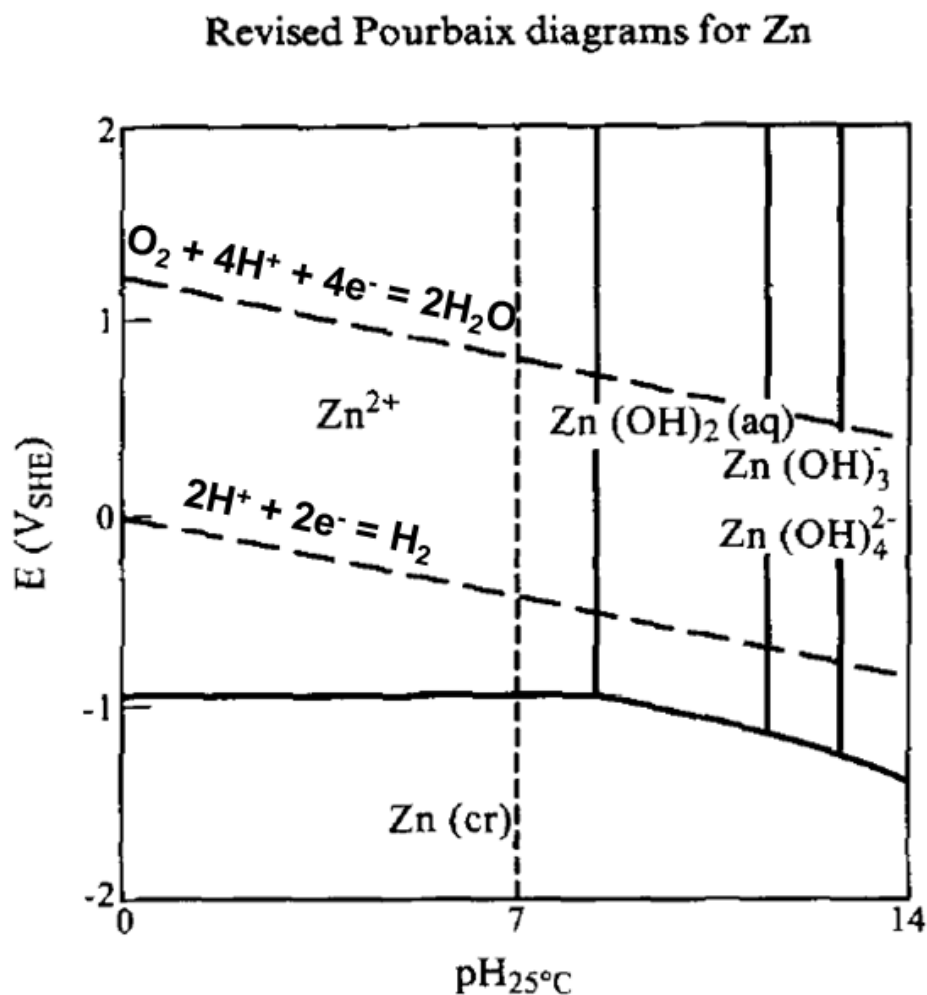
Figure 1-4. Pourbaix diagram for zinc at 25°C and $[Zn(aq)]_{tot} = 10^{-6}$ molal.[3] *Adapted with permission from "Revised pourbaix diagrams for zinc at 25-300 °C", CORROSION SCIENCE SOCIETY, 2011, 39(1), pp 107-114. Copyright © 1997 PERGAMON.*

Zn is thermodynamically stable below ca. -0.98 V with a large pH range in revised pourbaix diagrams for Zn.[3, 24] Unfortunately, the area is below the region of water stability. Therefore, this corrosion process generates hydrogen gas with the following three parts:

$$Zn \rightarrow Zn^{2+} + 2e^- \text{ (anodic reaction)}$$

$$2H_2O + 2e^- \rightarrow H_2 + 2OH^- \text{ (cathodic reaction)}$$

$$Zn^{2+} + 2OH^- \rightarrow Zn(OH)_2 \text{ (product formation)}$$
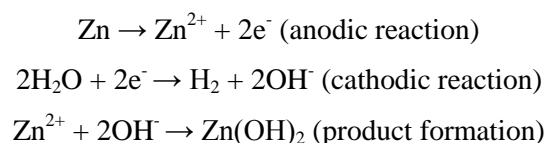
The overall corrosion reaction can be written as:
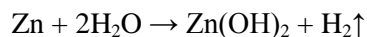
$$Zn + 2H_2O \rightarrow Zn(OH)_2 + H_2\uparrow$$

Clearly, hydrogen evolution reaction (HER), according to $Zn + 2H_2O \rightarrow Zn(OH)_2 + H_2\uparrow$, spontaneously occurs in natural and acidic solution although the zinc corrosion rate is slower than that of aluminum in an alkaline solution. Furthermore, in an electrolyte with high pH, Zn^{2+} ions are reacted with hydroxide ions to form $Zn(OH)_2$. The zinc hydroxide has low K_{sp}, and it is precipitated in aqueous medium. Hence, the formation of zinc hydroxide rather than zincate ion causes to capacity fading of the cell because the precipitate, $Zn(OH)_2$ as a passive layer, could not participate in the reversible electrochemical reactions, making reversible zinc electrode very difficult. In a mild pH electrolyte with Zn^{2+} ions, the electrochemical behavior of zinc can be described as the simple and fast reversible dissolution/deposition process and following equation:[23b]

$$Zn^{2+} + 2e^- \leftrightarrow Zn \text{ (below pH 8)}$$
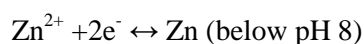
Because this HER is not supposed to occur during discharge, methods to retard the hydrogen evolution reaction have been regarded as the most important research area: it is hoped that it will be possible to consume zinc metal completely during discharge, which will eventually increase the capacity of the zinc-air battery.

As mentioned above, because zinc metal participates in the anode reaction during discharge, the most practical method of improving the performance of the zinc anode is to increase the surface area of the zinc particles so that the zinc can react with the alkaline electrolyte more efficiently. Accordingly, zinc particles with large surface area, such as Zn/MnO_2 and $Zn/NiOOH$[19a] are the best choices, and morphology control of zinc metal, such as Zinc flakes[25] and ribbons[26] in alkaline zinc-MnO_2 cells and zinc dendrites [27] and zinc fibers[28] in zinc-air cells have been reported. Although it is not exactly a case of a zinc-air cell, Minakshi et al. also showed that in the alkaline electrolyte LiOH, a porous anode electrode composed of zinc powder improves the rate capability and has a higher capacity in alkaline $Zn-MnO_2$ cells than that of a zinc planer electrode.[29] Recently, a study of porous electrodes with various shaped zinc particles, not just planner zinc electrodes, has also received attention.[30]

Generally, when preparing a zinc anode with powder, mercury has been added to the zinc anode to give better electrical conductivity between the zinc particles and the current collectors. However, removing the mercury in the zinc anode, due to environmental problems, has negative effects on discharge performance, and results in leakage problems associated with hydrogen gas and shock resistance.[25] These problems are fairly well alleviated by introducing gelling agents such as cross linked carboxymethyl cellulose (CMC), starch graft copolymers, cross linked polyacrylic acid polymer[31] or organic binders.[32] Muller et al used cellulose as a gelling agent to optimize and stabilize the porosity of the zinc electrode,[33] and Othman et al. introduced hydroponics gels such as agar to increase the capability of the storing electrolyte.[34]

When a porous zinc anode reacts with an alkaline electrolyte, the corrosion effect of the zinc

metal can be another criterion for stabilizing a zinc anode with large surface area. Hydrogen evolution on the surface of the zinc anode deteriorates the utilization efficiency of the zinc, resulting both in increased internal pressure in the cell and water electrolysis. These side reactions eventually decrease the cycle life of a zinc-air battery.[35] Two methods to overcome hydrogen evolution have been studied in zinc-air batteries. One is to alloy the zinc with other metals (Hg, Pb, and Cd) with high hydrogen evolution overvoltage.[36] However, these toxic heavy metals cause another environmental problem. As an alternative, Lee et al. reported that alloying zinc metal with nickel and indium with different weight percentages is effective in shifting to more negative potential for hydrogen evolution.[36b] Zhang et al. suggested that introducing metallic bismuth to a pasted zinc electrode improved the discharge performance because of the formation of an electronic conductive material.[37]

Another method of suppressing hydrogen evolution is to coat the zinc metal with other materials; Cho et al. suggested that the zinc surface coated with $Li_2O-2B_2O_3$ (lithium boron oxide, LBO) could increase discharge capacity and decrease hydrogen evolution. It is believed that the coating layer prevents the zinc surface from facing the alkaline electrolyte directly, which enables the zinc to avoid side reactions in the cell.[38] Zhu et al. reported that neodymium conversion films have also been applied to coat pristine zinc metal depending on the ultrasonic impregnation method. Their work demonstrated a positive effect on increasing corrosion resistance, in turn stablizing the cycle behavior of the zinc electrode.[39] The other method is to put additives into the electrolytes to stabilize the zinc anode. Ein-Eli et al. introduced polyethylene glycol (PEG) and phosphate ester acid form (GAFAC RA600) as an organic corrosion inhibiter. Their results showed that PEG had better inhibiter properties than GAFAC RA600.[40] Using anions of organic acids,[35] and phosphoric acid, tartaric acid, succinic acid and citric acid [41] exhibited positive effects on suppressing gas evolution and dendrite formation to some extents.

Making electrically a rechargeable zinc-air battery is still challenging. However, it is a very promising task to develop a secondary cell for practical use in the market if we consider the many advantages of a hypothetical zinc-air battery. Although a proper bifunctional catalyst is required to charge the zinc-air battery with lower electrical potential, it is also critical to make reversible zinc anode. It is well known that zinc metal undergoes shape changes such as the formation of dendrites in the charge-discharge cycling process.[19a] Zinc metal is oxidized to release electrons and then changed to zinc(II) ion. Oxidation process of zinc proceeds until the solubility of the zincate ion, $Zn(OH)_4^{2-}$ (aq), reaches a saturation point in the hydroxide electrolyte. After exceeding this point, zincate ions are decomposed to ZnO, a white solid powder that acts as an insulater. Because supersaturation of the zincate ion in alkaline solution is time-dependent, it is very difficult to make a rechargeable zinc-air battery.[42] Therefore, understanding the chemistry of the zincate ion, $Zn(OH)_4^{2-}$(aq) in alkaline solution is necessary to develop a secondary zinc electrode. There have been several fundamental efforts to understand the behavior of the zincate ion in an alkaline electrolyte[19a, 43] and also to understand the

electrodeposition of the zincate ion.[44] Dirkse suggested that $Zn(OH)_4^{2-}$, $Zn(OH)_3(H_2O)^-$, $Zn(OH)_2(H_2O)_2$ or polynuclear species may exist in supersaturated zincate solutions and that the existence of these species depends on the availability of OH^- and free H_2O molecules in the electrolyte.[43c] Peng studied the mechanism of zinc electroplating and suggested that $Zn(OH)_2$ became $Zn(OH)_{ad}$ by gaining one electron and then $Zn(OH)_{ad}$ was reduced to Zn by gaining a second electron.[44c] Einerhand et al. used a rotating ring disk electrode (RRDE) to determine the amount of hydrogen produced from the electrodeposition of zinc in alkaline solution and showed that hydrogen evolution increased with decreasing concentration of KOH and zincate.[44f]

1.3.2 Separator for Zn-air batteries

The function of the separator used in a zinc-air battery is to transport the hydroxyl ion, OH^-, from the air electrode to the zinc electrode.[19b] Considering the basic requirements of a proper separator, stability in the alkaline solution, proper pore sizes and porosity, highly ionic conductivity and electrical non conductivity should be fulfilled. Since a zinc-air cell uses the migration of the hydroxyl ion, not the proton, H^+,[45] separators are made of polyethylene, polyvinyl alcohol, polyolefin and polypropylene.[46] Porosity in the separator, however, makes it possible for the zinc cations to migrate from the anode to the cathode, which results in decreased capacity in the cell. Kiros developed a novel method to control the permeability of the zincate ion by introducing an inorganic material, $Mn(OH)_2$, to the microporous membrane.[47] Dewi et al. showed that cationic polysulfonium, poly(methylsulfonio-1,4-phenylenethio-1,4-phenylene trifluoromethanesulfonate) could be effectively applied to prevent the permeation of Zn^{2+} from the anode to the cathode as compared to commercial separators such as polypropylene.[46e] Wu et al. suggested that sulfonation treatment of the microporous membrane could increase the high anionic transport number to 0.89 in a 1M KOH alkaline solution. This separator demonstrated better performance than the unsulfonated samples.[48] Besides the basic requirements mentioned above, others are needed for the secondary zinc-air battery; the separator should be inert to oxidation, and should remain stable during charge and discharge. Further, it has high absorption for electrolytes and   has a fine porous structure to sustain electrolytes in the pores and retard zinc dendrite growth.[49]

1.3.3 Electrolyte for Zn-air batteries

The alkaline electrolytes used in zinc-air batteries are potassium hydroxide, sodium hydroxide and lithium hydroxide,[18] all basic except for neutral NH_4Cl[50]. Among these, KOH has been widely used in zinc-air cells because of thebetter ionic conductivity of K^+($73.50\ \Omega^{-1}cm^2$ /equiv) compared to Na^+($50.11\ \Omega^{-1}cm^2$ /equiv)[45] In addition, ~30% KOH is usually used because it shows maximum ionic conductivity at this concentration.[19a] To reduce the resistance of the electrolyte,

increasing the concentration of KOH can be a solution, but too high a concentration of KOH could lead to increased viscosity in the electrolyte. Besides this, high concentration of the electrolyte leads to the formation of ZnO, according to the reaction ($Zn(OH)_4^{2-} \rightarrow ZnO + H_2O + 2OH^-$), in turn increasing the viscosity.[45]

Because a zinc-air battery is operated in an alkaline solution and is exposed to air, the electrolyte is very sensitive to CO_2, which can react with hydroxyl ions to form carbonates ($CO_2 + 2OH^- \rightarrow CO_3^{2-} + H_2O$);[51] also, concentration of the hydroxyl ion decreases naturally during this process. Furthermore, the poor solubility of carbonates in alkaline media may cause clogging of electrode pores and thereby blocking of electrolyte channels, causing decreased cell capacity. To circumvent this drawback of CO_2 sensitivity, it is helpful to feed purified air or employ a selective membrane that is permeable to O_2. Moreover, the use of a circulating electrolyte is beneficial as the saturation of carbonate is attained much more slowly than that in immobilized electrolyte. Therefore, the carbonation of the alkaline electrolyte causes decreased cell capacity. Kim et al. reported that the concentration of potassium carbonate in the electrolyte deteriorated cell capacity linearly and that pore size of the hydrophobic membrane mainly affected the rate of carbon dioxide absorption.[52] Drillet et al. investigated the effect of CO_2 concentration in the air on the lifetime of the bifunctional electrode in alkaline solution by using solid adsorbents, including soda lime. In this study, an LiOH and LiOH-Ca(OH)_2 mixture was used to remove CO_2. Further, they showed that increasing the concentration of carbon dioxide in synthetic air up to 10000 ppm made oxygen reducing electrode rather than an oxygen evolving electrode. They suggested that the reduced lifetime of the air electrode was due to carbonate precipitation inside the pores of the air electrode.[53]

Chen et al. used the technique of combining chemical absorption with Higee (high gravity) as a CO_2-scrubber. They showed that under the same experimental conditions, piperazine (PZ) was more effective than 2-(2-aminoethylamino) ethanol (AEEA) and monoethanolamine (MEA) in reducing the concentration of CO_2 to a level below 20 ppm.[54]

1.3.4 Air electrode for Zn-air batteries

The performance of metal-air batteries depends on many factors, including a package of problems from anode, electrolyte, air cathode with current collector.[1] Unlike non-aqueous Li-air battery, no solid product is formed in aqueous electrolyte in zinc-air battery. Especially, a suitable pore structure favoring oxygen diffusion and electrolyte is needed. Thereby, it is highly desirable to optimize the conditions of every part in a metal-air battery pack to achieve higher energy storage. Among all the issues, air cathode may face the greatest challenge owing to its complicated reaction mechanism and open-air structure. The structure design, to a great extent, determines the catalytic activity of catalyst in air electrode. To making an efficient air cathode, three phase reaction sites should be maximized by proper optimization of porosity and wettability within electrodes. Especially,

careful construction of the catalysts layer is required because oxygen reduction occurs at a three phase boundary in the air electrode. Therefore, it is highly recommend that the catalysts layer have hydrophilicity on the aqueous electrolyte, but hydrophobicity on the gas side in **Figure 1-5**.[55] Thus, the optimized balance between hydrophobic and hydrophilic can be a significant issue in developing advanced air electrodes for zinc-air batteries.[56] Furthermore, air electrode should be prepared to be as thin and light as possible because air cathode mainly acts as electrocatalysts and a good catalyst dispersion and interfacial contact between catalyst and conductive materials in air electrode could improve the catalytic performance of catalysts.
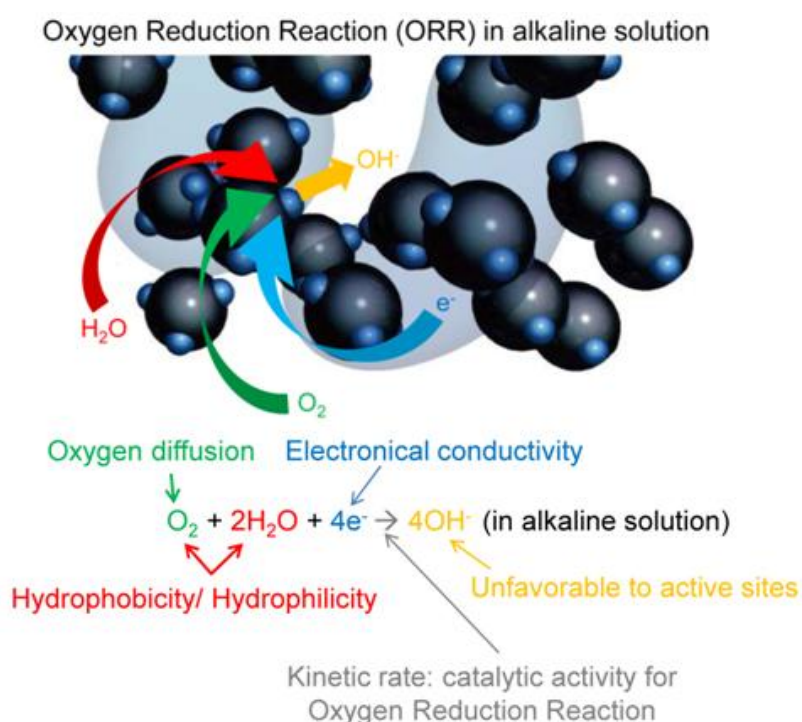
Oxygen Reduction Reaction (ORR) in alkaline solution

OH⁻

H₂O

e⁻

O₂

Oxygen diffusion   Electronical conductivity

$O_2 + 2H_2O + 4e^- \rightarrow 4OH^-$ (in alkaline solution)

Hydrophobicity/ Hydrophilicity

Unfavorable to active sites

Kinetic rate: catalytic activity for Oxygen Reduction Reaction

Figure 1-5. Strategy for designing more efficient electrocatalysts of unique architecture to facilitate higher cativity for oxygen reduction reaction (ORR) and rapid transport of electroactive species through the porous electro-catalysts in an alkaline solution. In addition to high catalytic activity and sufficient electronic conductivity, an efficient electrode architecture must allow fast transfer of other reactants (such as oxygen molecules) to and the reaction products (such as hydroxide ions) away from the catalytically active sites for ORR to minimize electrode polarization.[4]

Chapter 2. Electrocatalytic oxygen reduction reaction (ORR)

Note: This chapter is partially and totally adapted with permission from "Non-Precious Catalysts: Recent Progress in Non-Precious Catalysts for Metal-Air Batteries", Advanced Energy Materials, 2012, 2(7), pp 701. Copyright © 2012 John Wiley & Sons, Inc.

2.1 Electrochemcial O_2 reduction reactions

The most important reaction of metal-air batteries is electrochemical oxygen reduction reaction (ORR), generating electricity through a redox reaction between metal and oxygen.[57] In even well-developed air electrode architectures, however, ORR is intrinsically sluggish, causing major polarization loss in overall performance of metal-air battery. Briefly, the overall ORR process in the air electrode can be described with consecutive several steps: 1) oxygen diffusion from atmosphere to catalysts, 2) oxygen adsorption on the catalysts, 3) migration of electrons from metal to adsorbed oxygen molecules, 4) weakening and breaking of oxygen bond, and 5) the removal of hydroxyl ion product from the catalyst surface to the electrolyte. The factors that affect the performance of the air electrode in a metal-air battery include the activity of catalyst, the morphology of catalyst particles, and the architecture of the air cathode. Therefore, how to facilitate ORR with proper catalysts has been a key issue to date. In spite of the lack of understanding of details mechanisms for ORR, a formation of superoxide though a one electron transfer, ($O_2 + e^- \leftrightarrow [O_{2(ad)}]^-$), is considered as the first step for ORR. While significant efforts have been devoted to the development of ORR catalysts with high activity for metal-air batteries in the past few decades, many practical problems and fundamental questions still remain. Pt-based electrocatalysts have been widely used in fuel cell operated in acid electrolyte to address these problems, but various non-precious metal or metal-free catalysts can speed up ORR in alkaline media due to its better stability of materials and facilitated kinetics for ORR in alkaline solution because of better kinetics and lower overpotentials. For example, the exchange current density in alkaline is much higher than that in acid electrolyte, making feasible the utilization of non-precious metal catalysts. In addition, the electrode potential will shift by -0.83 V (-59 mV multiplied by 14) if the pH value changes from 0 to 14, affecting the local double layer structure and the electric field at electrode-electrolyte interface. Therefore, it can lead to changes in adsorption strengths for, especially, charged and even for neutral species. Accordingly, adsorption of spectator ions in alkaline electrolyte can be decreased, making electrocatalytic processes more facile than that in acid media. Another advantage of using non-Pt based catalysts in alkaline media can avoid unnecessary zinc corrosion caused by hydrogen evolution reaction (HER) catalysed with Pt metal-based catalysts deposited at Zn anode coming from air electrodes due to its instability under ORR

potential range during discharge. In this regard, to be economically competitive, non-precious catalysts must be developed for practical metal-air batteries. To date, several kinds of non-precious catalysts have been explored for use in metal-air batteries, including metal oxides, macrocycles, and carbon-based catalysts.

The ORR can be considered as a series of complex electrochemical reactions involving multi electron transfer process and complicated oxygen oxygen-containing species such as O, OH, O_2^- and HO_2^- in **Figure 2-1**.
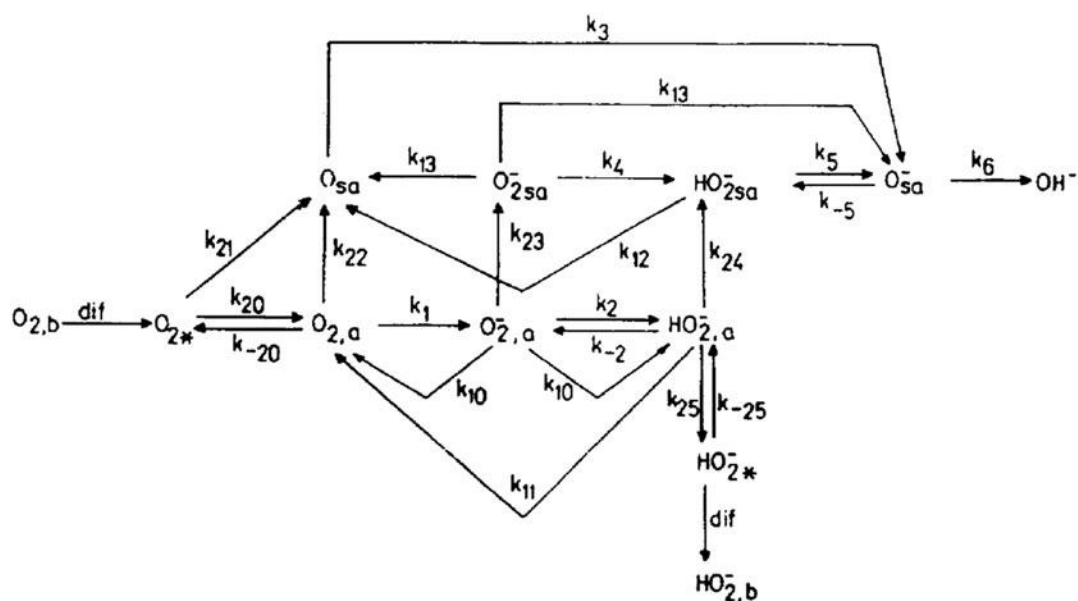
Figure 2-1. General reaction scheme for O_2 reduction in alkaline solutions. k_i is the overall rate constant for the ith step. The subscripts sa, a, b, and * denote strongly adsorbed, weakly adsorbed, bulk, and vicinity of the electrode, respectively.[5] *Reprinted from ref. 5 with permission from Elsevier.*

Although **Fig. 2-1** is quite complicated, briefly, oxygen can be reduced by either a direct four-electron pathway with a product of hydroxyl ions or an indirect two-electron pathway with a product of peroxide as intermediate in **Table 2-1**.

Table 2-1. Thermodynamic electrode potentials of oxygen reduction reaction.

Electrolyte	ORR reactions	Thermodynamic electrode potential at standard conditions, V
Acidic aqueous solution	$O_2 + 4H^+ + 4e^- \rightarrow 2H_2O$	1.229
	$O_2 + 2H^+ + 2e^- \rightarrow H_2O_2$	0.70
	$H_2O_2 + 2H^+ + 2e^- \rightarrow 2H_2O$	1.76
Alkaline aqueous solution	$O_2 + 2H_2O + 4e^- \rightarrow 4OH^-$	0.401
	$O_2 + H_2O + 2e^- \rightarrow HO_2^- + OH^-$	-0.065
	$HO_2^- + H_2O + 2e^- \rightarrow 3OH^-$	0.867
	$2HO_2^- \rightarrow 2OH^- + O_2$	chemical disproportionation

The direct 4e oxygen reduction pathway is highly desirable due to its high efficiency, while the indirect 2e pathway is not supposed to occur because the partially reduced intermediates, peroxide species, are corrosive and cause significant degradation of the metal-air batteries. In general, direct 4e reduction is dominant on precious metal catalysts, otherwise, indirect 2e reduction primarily occur on carbonaceous catalysts.

The ORR pathways and mechanisms could vary with the applied electrocatalysts and depend on its O_2 adsorption configurations and the O_2-surface interactions. Different oxygen adsorption models exist according to its crystallographic structures and the binding energy between oxygen and catalysts surface in **Figure 2-2a-b**.[6]

For example, only one oxygen atom can be adsorbed to the catalysts surface, making a perpendicular coordination. In this case, peroxide generation from 2e pathway could be dominant via one electron transfer (**Fig. 2-2a**). After the formation of peroxide, further oxygen reduction could be followed by either another 2e reduction, yielding hydroxyl ion, or a chemical disproportionation of peroxide. Therefore, a consecutive 2 by 2 e pathway is possible via above mentioned further oxygen reduction. In contrast, two oxygen atoms is coordinated parallel to the surface, direct O_2 dissociation process is favor, leading direct 4e pathway without peroxide (**Fig. 2-2b**).
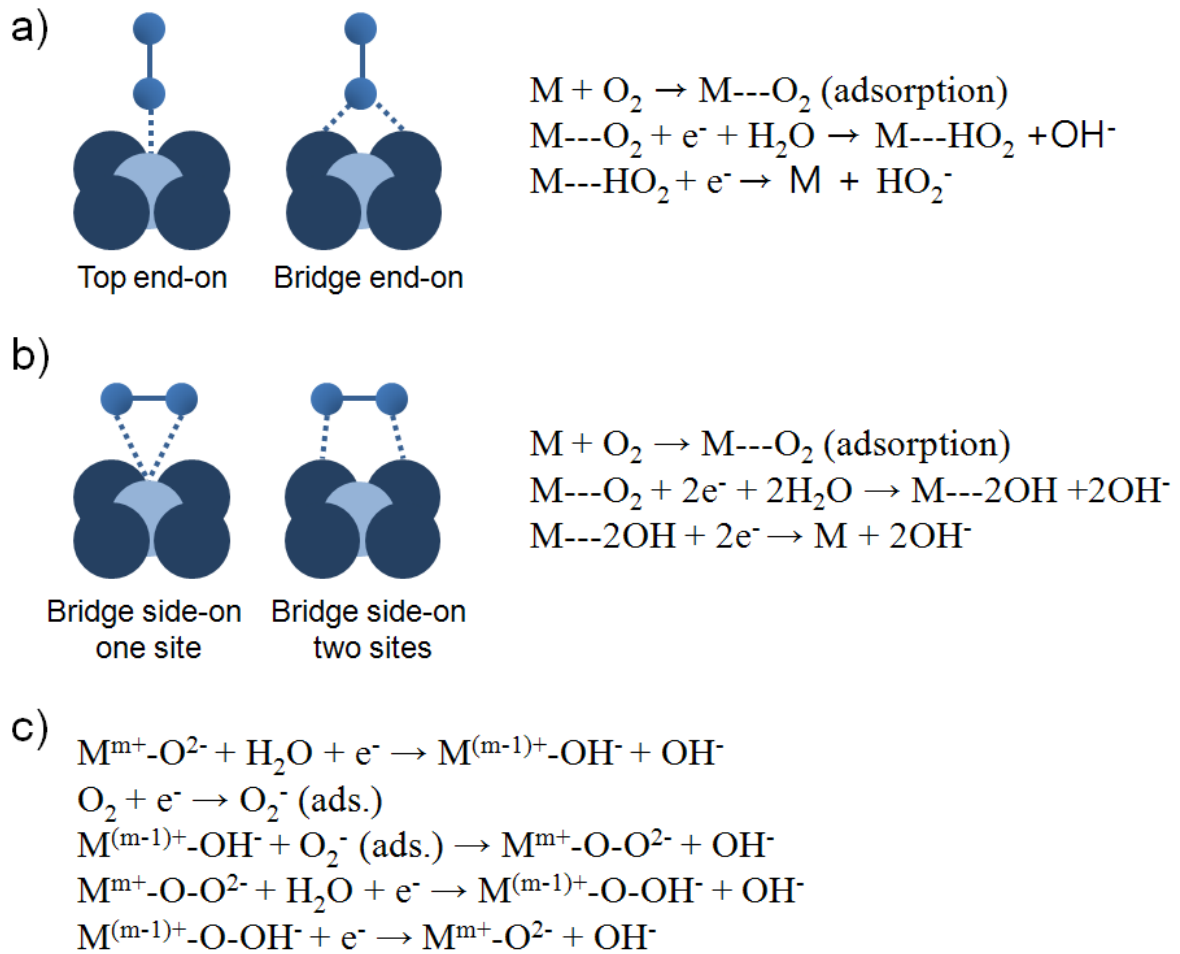
a)

Top end-on   Bridge end-on

$$M + O_2 \rightarrow M\text{---}O_2 \text{ (adsorption)}$$
$$M\text{---}O_2 + e^- + H_2O \rightarrow M\text{---}HO_2 + OH^-$$
$$M\text{---}HO_2 + e^- \rightarrow M + HO_2^-$$

b)

Bridge side-on   Bridge side-on
one site   two sites

$$M + O_2 \rightarrow M\text{---}O_2 \text{ (adsorption)}$$
$$M\text{---}O_2 + 2e^- + 2H_2O \rightarrow M\text{---}2OH + 2OH^-$$
$$M\text{---}2OH + 2e^- \rightarrow M + 2OH^-$$

c)
$$M^{m+}\text{-}O^{2-} + H_2O + e^- \rightarrow M^{(m-1)+}\text{-}OH^- + OH^-$$
$$O_2 + e^- \rightarrow O_2^- \text{ (ads.)}$$
$$M^{(m-1)+}\text{-}OH^- + O_2^- \text{ (ads.)} \rightarrow M^{m+}\text{-}O\text{-}O^{2-} + OH^-$$
$$M^{m+}\text{-}O\text{-}O^{2-} + H_2O + e^- \rightarrow M^{(m-1)+}\text{-}O\text{-}OH^- + OH^-$$
$$M^{(m-1)+}\text{-}O\text{-}OH^- + e^- \rightarrow M^{m+}\text{-}O^{2-} + OH^-$$

Figure 2-2. (a) Different configurations of O_2 adsorption on catalyst surfaces: on top end-on, bridge end-on, bridge side-on one site, and bridge side-on two sites, from left to right. Simplified electrochemical catalysis process of the ORR on metal surfaces in the case of (b) end-on O_2 adsorption, and (c) bidentate O_2 adsorption, corresponding to the 2e reduction (with generated peroxide species) and the direct 4e reduction, respectively. (d) One of the proposed catalytic ORR pathways at a metal oxide/alkaline electrolyte interface.[6] *Adapted from ref. 6 with permission from RSC.*

For the metal oxides, the surface cations in metal oxides are not coordinated with oxygen, making different surface charge distribution compared to a pure metal. Therefore, these deficient anion coordinations can be compensated by oxygen of H_2O. Following protonation of a surface oxygen ligand afford a charge to reduced surface cation for charge compensation. Accordingly, overall 4e oxygen reduction has been proposed for transition metal oxides (**Fig. 2-2c**). Although this proposed mechanism include consecutive several steps: 1) surface hydroxide displacement, 2) surface peroxide formation, 3) surface oxide formation, and 4) surface hydroxide regeneration, the competition between the O_2^{2-}/OH^- displacement and OH^- regeneration has been considered as a rate determining step (r.d.s) for ORR in alkaline solution.

Unfortunately, above mentioned 4e and 2e reaction schemes may occur simultaneously and vary with various factors such as applied potentials, desorption and re-adsorption of intermediates, and non-covalent interactions between hydrated alkalimetal cations and adsorbed species. Furthermore, limitation of state-of-art analysis techniques for real surface reactions is not sufficient to detect more underlying pathways. Therefore, the exact determination of ORR mechanism could be a challenging issue to date.

2.1.1 Evaluation of catalysts for ORR

Voltage and power profile during operation of metal-air battery[7]

Although various experimental techniques can be used to study electrochemical reactions in battery, the current-voltage profile characteristics during discharge or charge are the most common (**Figure 2-3**). In practical batteries and fuel cells, all three types of polarization affect the shape of the fuel cell discharge curve determining the cell capacity, the discharge charge rate effect, and information on the state of battery.
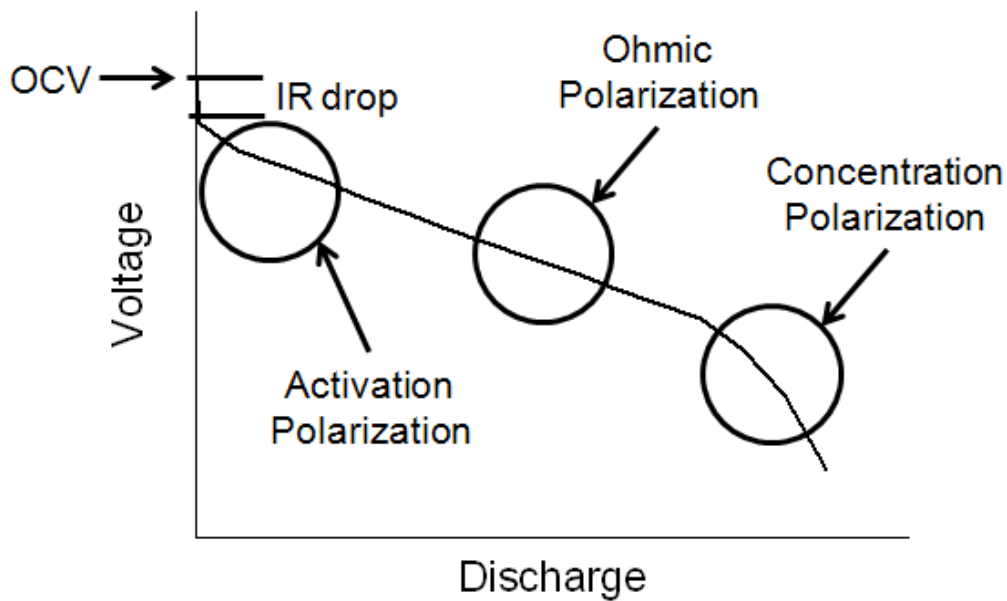
Figure 2-3. Typical discharge curve of a battery, showing the influence of the various types of polarization.[7]

The activation, ohmic, and concentration polarization determine this polarization curve.

      1) The activation polarization is governed by the Tafel equation from Butler-Volmer equation.

$$\eta = a - b \log(I/I_o)$$

where a and b are constants. The formation and decay of this polarization are fast, a time frame of 10^{-2}-10^{-4} s, and can be determined using current interruption methods.

      2) Ohmic polarization is generated from the resistance of the electrolyte, current collectors, contact between particles, and a passive film of the electrode surface. This ohmic resistance, R, make a linear voltage-current profile according to an Ohm's Law relationship between I and η.

$$\eta = IR$$

Especially, a time scale for this polarization ($\leq 10^{-6}$ s) is relatively faster than activation polarization. Therefore, if current flows and ceases, it appears and disappears instantaneously.

      3) Concentration polarization arises from limited mass transport capabilities resulting from a change in the utilization of the active species at electrode/electrolyte interface and can be described as

$$\eta = (RT/n) \ln(C/C_o)$$

where C is the concentration at the electrode surface and C_o is the concentration in the bulk of the solution.

2.1.2 Determination of the selectivity and kinetics of ORR

Rotating Disk Electrode (RDE) and Rotating Ring Disk Electrode (RRDE)[8, 57a]

Generally, ORR pathway can be determined by means of rotating disk electrode (RDE) or rotating ring-disk electrode (RRDE) voltammetry in **Figure 2-4**.
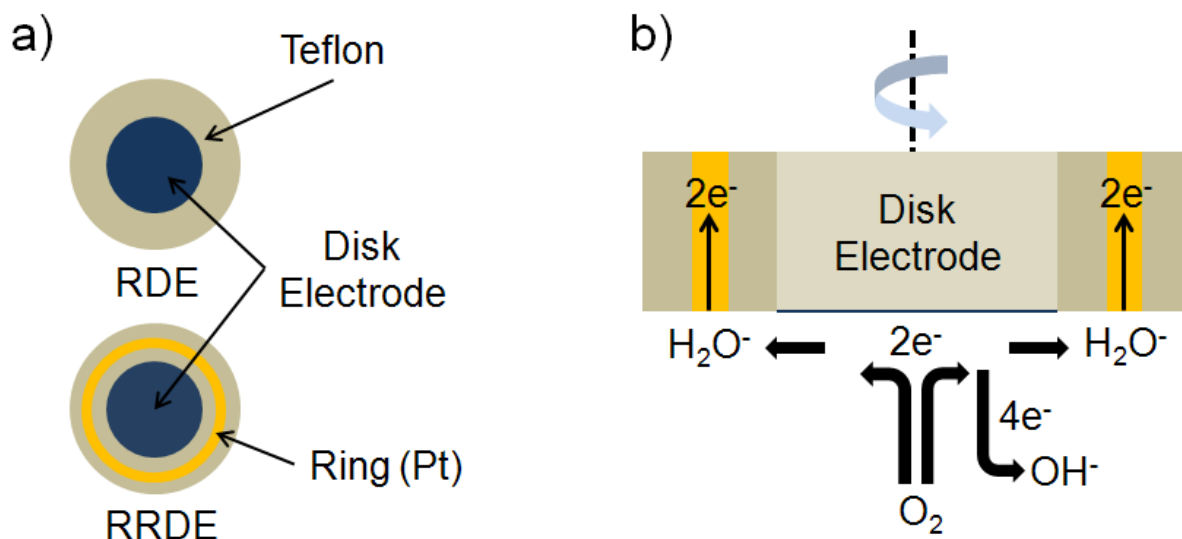
Figure 2-4. (a) Schematic description of RDE and RRDE (b) possible reaction at RRDE during ORR in alkaline electrolyte.

In RDE methods, during rotation of electrode, the electrolyte is tangentially drawn to the disk electrode to boost the diffusion of an electrolyte in condition where diffusion of the electroanalyate to the electrode surface limits an overall electrochemical reaction. Levich showed that the diffusion limited current under hydrodynamic condition is related to the angular velocity of the electrode according to Levich equation;

$$I_d = 0.62nFAC_{O_2}D_{O_2}^{\frac{2}{3}}v^{-\frac{1}{6}}\omega^{\frac{1}{2}}$$

Where n is the number of electrons exchanged per molecule, F is the Faraday constant, A is the surface area of the electrode, D_o is the diffusion coefficient of the electroanalyte, ω is the angular velocity of the electrode, v is the kinematic viscosity of the electrolyte and C_{O_2} is the bulk concentration of the electroanalyte. For the well controlled experiments under diffusion controlled region, well-defined limiting current can means all the catalysts are sufficiently active to reduce all the oxygen that has been supplied by the rotation, and that the catalysts are coated on every part of the disk. Under diffusion controlled region, a plot of I_d against $\omega^{1/2}$ yields a straight with a slope $= 0.62nFAC_{O_2}D_{O_2}^{\frac{2}{3}}v^{-\frac{1}{6}}$ from which n (number of transferred electrons) may be determined. Note that the coefficient 0.62 is used when ω is expressed in angular velocity, rad s^{-1}, while 0.21 can be

expressed in r.p.m (i.e., $0.62 \times \left(\frac{2\pi}{60}\right)^{\frac{1}{2}} = 0.21$).

A more common approach use a Koutecky- Levich (K-L) analysis for reactions under mixed kinetic and diffusion control.

$$\frac{1}{I} = \frac{1}{I_k} + \frac{1}{I_{diff}} \; or \; \frac{1}{I} = \frac{1}{I_k} + \frac{1}{B\sqrt{\omega}}$$

$$I_k = nFAK_{O_2}C_{O_2}\Gamma_{catalyst}$$

where I is the measured current, i_k is the kinetic current, $\Gamma_{catalysts}$ is the loading of the catalysts, and i_d is diffusion limited current derived from Levich equation. By using K-L equation, a plot of i^{-1} against $\omega^{-1/2}$ gives a straight line with a slope of B^{-1} where n also can be determined from B and i_k can be gained from the intercept on i^{-1} axis. Especially, i_k also can be calculated using equations used for RDE as following

$$\frac{1}{I} = \frac{1}{I_k} + \frac{1}{I_{diff}}$$

$$\frac{1}{I_k} = \frac{1}{I} - \frac{1}{I_{diff}} = \frac{I_{diff} - I}{I \times I_{diff}}$$

$$I_k = \frac{I \times I_{diff}}{I_{diff} - I} \; (kinetic \; current)$$

For RDE analysis, three non-electrochemical kinetic parameters must be known accurately. For example, there are 1) the diffusion coefficient of O_2, 2) the kinematic viscosity of the electrolyte solution, and 3) the solubility of O_2. Especially, all these three parameters are the electrolyte used and temperature dependent.

In RRDE, a ring (often platinum) surrounds the disk electrode (often glassy carbon) with an insulating material (usually Teflon) between them (**Figure 2-5**).

$$I_D = I_{H_2O} + I_{H_2O_2}$$

$$I_R = N I_{H_2O_2}$$

Ref materials: $K_3[Fe(CN)_6]$ for Collection Efficiency (N)

$$\because H_2O_2\ \% = \frac{2I_{H_2O_2}}{I_{H_2O_2} + I_{H_2O_2} + I_{H_2O}} = \frac{2I_{H_2O_2}}{I_{H_2O_2} + I_D} = \frac{2\frac{I_R}{N}}{\frac{I_R}{N} + I_D} \times 100$$
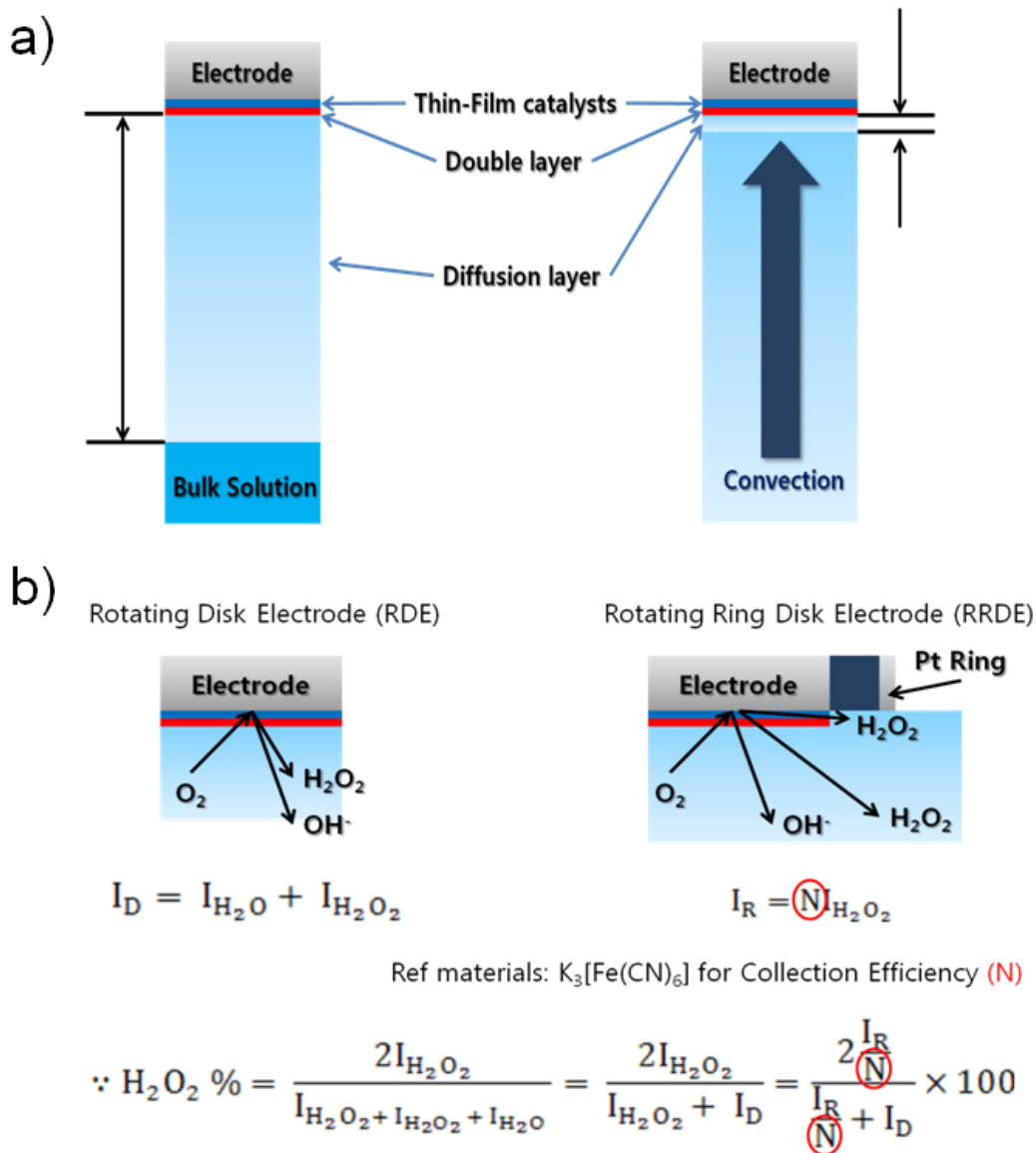
Figure 2-5. (a) Significantly reduced diffusion layer resulting from artificial convection under rotating condition and (b) Schematic representation of the RDE and RRDE, and of the possible reactions that takes place at the RRDE during ORR. Large N indicates collection efficiency of RRDE electrode.

In RRDE method compared to RDE, the big difference between them is that RRDE technique can detect intermediates directly by means of around ring electrode. These intermediate (often hydrogen peroxide in acid and peroxide in alkaline electrolyte) are produced resulting from partial reduction of oxygen on the disk electrode. Therefore, it is used to deduce the ORR pathway. On the disk, both 2e and 4e oxygen reduction can occur and intermediate is further oxidized at ring electrode. The 2e oxygen reduction current (I_{2e^-}) is expressed by

$$I_{2e^-} = I_R / N$$

where I_{2e^-} is the 2-electron ORR on the disk electrode and N is the collection efficiency which is normally supplied by the manufacturer and can be determined using a suitable redox probe. Therefore, the ORR current (I_D) on disk electrode can be expressed by

$$I_D = I_{2e^-} + I_{4e^-}$$

where I_{4e^-} is the 4-electron ORR current.

With above mention equations, the average electron number (n_{e^-}) can be calculated by following equation

$$\frac{I_D}{n_{e^-}} = \frac{I_{4e^-}}{4} + \frac{I_{2e^-}}{2}$$

$$n_{e^-} = \frac{4I_D}{I_D + I_R/N}$$

Simply, as the numbers of electrons are close to 4, direct 4e oxygen reduction pathway is favorable, otherwise, as that are close to 2, indirect 2e oxygen reduction is dominant.

Furthermore, the fraction of H_2O_2 generated during ORR is calculated by

$$X_{H_2O_2} = \frac{2I_R/N}{I_D + I_R/N}$$

Where N is the collection efficiency of the ring electrode, I_R is the ring current and I_D is the disk current.

The RDE and RRDE are very popular methods which can study the kinetics and pathway of ORR. It is worthy to note that underlying mathematical equations in these methods are strictly applied for smooth and thin electrode surface under laminar flow hydrodynamics.[58]

2.1.3 Kinetics and mechanism of ORR

The O_2 reduction reaction occurs at potential as close as possible to the thermodynamic equilibrium potential with a satisfactory reaction rate. The most general equation for studying electrode kinetics is the Butler-Volmer equation which is valid for the reactions controlled by only charge transfer.

$$i_{applied} = i_o \left(e^{\left[\frac{(1-\alpha)nF}{RT}(E-E_{eq})\right]} - e^{\left[\frac{-\alpha nF}{RT}(E-E_{eq})\right]}\right)$$

where i_o is the exchange current density, n is the number of electrons transferred in the rate determining step, α is the transfer coefficient, F is the Faraday constant, R is the gas constant, and T is the temperature in Kelvin. At equilibrium, applied current density, $i_{applied}$, becomes to exchange current density, i_o, which can imply the intrinsic kinetic properties of electrode reactions.[59] As the magnitude of the exchange current increasing, the electrochemical reactions occur more rapidly. Especially, this phenomenon depends on the reaction and the surface where electrochemical reaction occurs. For example, exchange current density of hydrogen oxidation is several orders larger than that of ORR on a Pt electrode.[57b] For the ORR, a higher exchange current on a Pt than Au electrode is observed,

indicating that surface electrode materials of catalysts affects strongly ORR kinetics. This Butler-Volmer equation can be more useful to study the electrode kinetics. If the Overpotential is large, the B-V equation simplifies to the Tafel equation for the anodic or cathodic reaction.

$$i = i_o \, e^{\frac{(1-\alpha)nF}{RT}(E-E_{eq})} \text{ (for anodic reaction)}$$

$$i = -i_o \, e^{\frac{-\alpha nF}{RT}(E-E_{eq})} \text{ (for cathodic reaction)}$$

The plot of $\log(i_c) \sim \eta_c$ gives a linear relationship and this slope (b) is called the Tafel slope in **Figure 2-6**. The significant parameters affecting the Tafel slop are actually n and α because other parameters are known. For example, the higher the Tafel slope, the faster the overpotential increases with the current density. Therefore, low Tafel slope or large $n\alpha$ should be favored for obtaining better electrochemical reactions. Thus, the electron transfer coefficient is a key factor determining the mechanism of oxygen reduction.[60] Furthermore, it depends on temperature and Relative humidity (RH).[57b, 61]
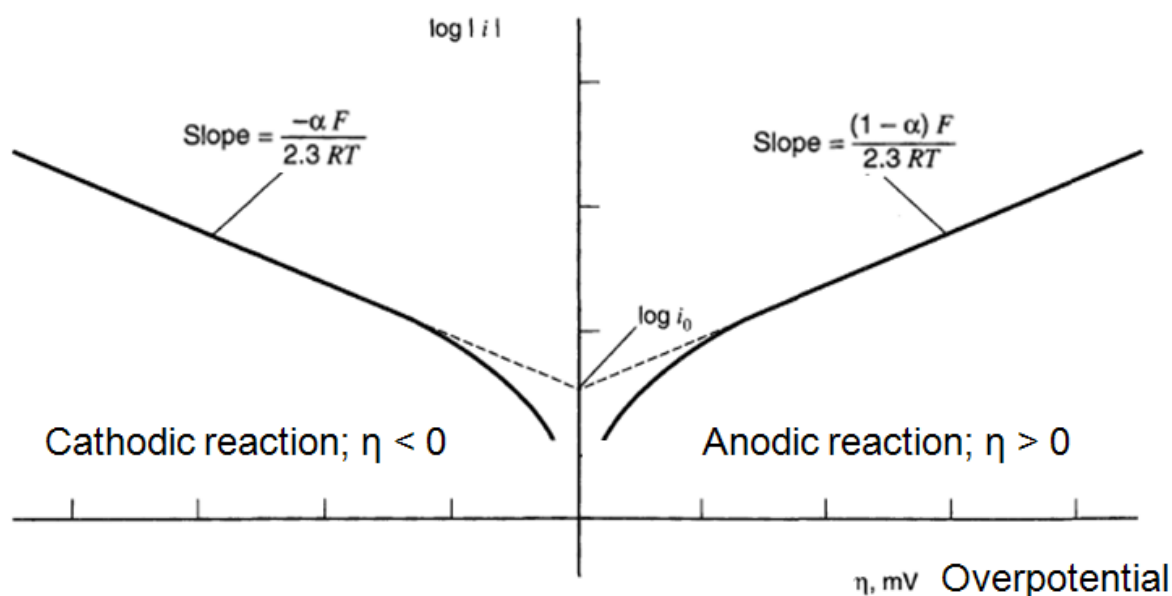
Figure 2-6. Schematic illustration of the Tafel plot of log| i | vs. overpotential (η) for the anodic and cathodic reactions of an electrode.[8]

For ORR, the Tafel plot has usually two linear regions depending on the electrode materials and the potential range.[62] In the region of low current density, a theoretical value is -2.303RT/nF or about 60mV/decade for a single electron transfer process and indicates that Temkin adsorption (high O_2 coverage) conditions control electron transfer and the reaction is limited by the intermediates coverage of electrode. In contrast, in the region of high current density, the slope is equivalent to -2(2.303)RT/nF (=-2.3RT/0.5F) or about 120mV/decade and a Langmuir isotherm (low O_2 coverage)

determine overall adsorption conditions where the transfer of first electron can be considered as rate determining step. For example, α, transfer coefficient, can be decomposed to determine nature of the rate limiting step for ORR mechanism.[60c, 63]

$$\alpha = \frac{\gamma}{\upsilon} + \rho\beta$$

where γ is the number of electrons preceding the rate determining step (r.d.s), υ is the stoichiometric coefficient, ρ is 0 when r.d.s is a chemical step and 1 if the r.d.s is an electron transfer step, and β describes the symmetry of the activation barrier for the reaction, which is 0.5 for most systems of interest in which simple single electron exchange reactions are involved.[60c] Therefore, assuming a β value of 0.5, the smallest nonzero allowable values of α is 0.5, corresponding to ~120mV/decade of Tafel slope (=-2.3RT/0.5F), otherwise, assuming a β value of 1, corresponding Tafel slope is -2.3RT/F (~60mV/decade).[64] Some applications of transfer coefficient in determining r.d.s are fully described in previous literatures.[60a, 65]

2.2 Non-precious Catalysts for Zn-air Battery[66]

Transition-metal oxides have been widely used as an electrocatalysts as an alternative to noble metal catalysts such as platinum, Pt because of its high abundance, low cost, and environmental benignity. Although some of them suffer from its stability in acid electrolyte, generally they are quite durable in alkaline electrolyte, allowing them to be appropriate to electrocatalysts in alkaline solution. Brief histories of ORR catalysts to date are described in **Figure 2-7**.
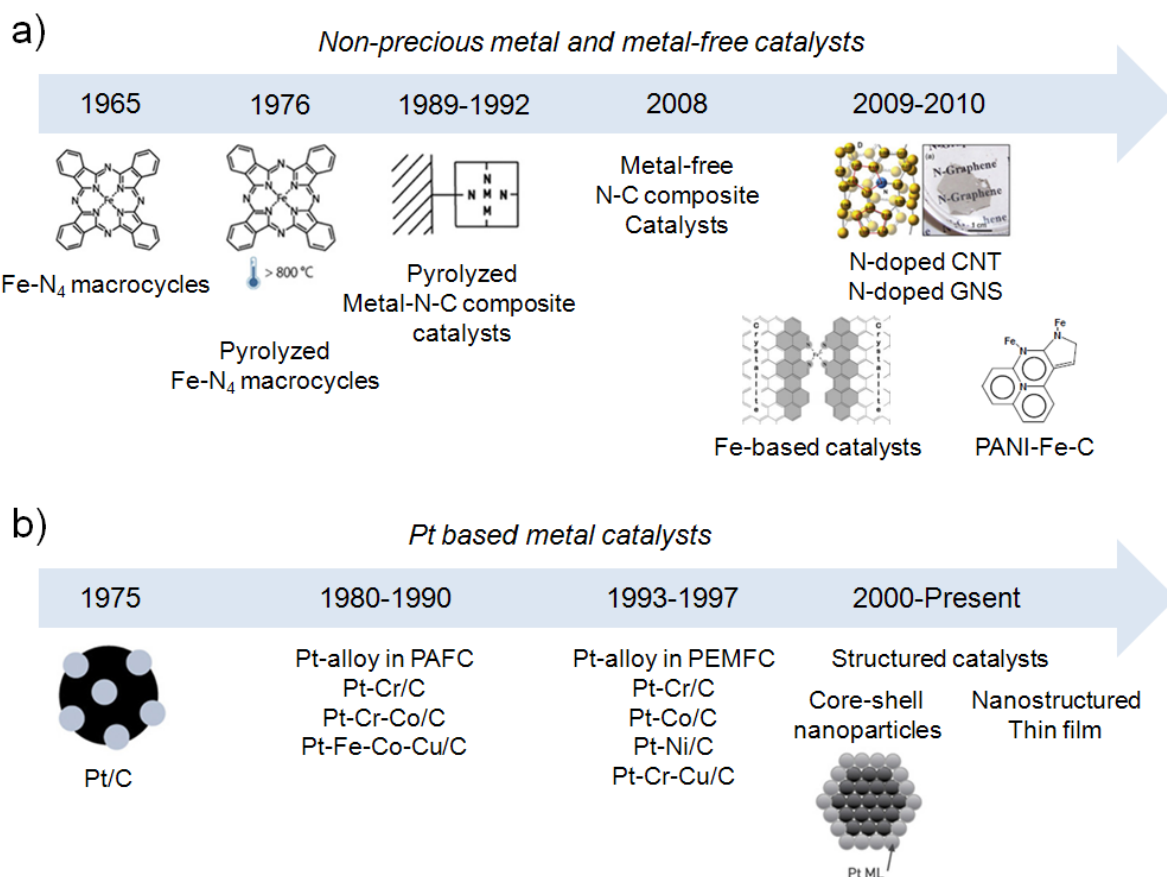
Figure 2-7. Brief history of ORR catalysts for (a) non-precious metal and metal-free catalysts and (b) Pt-based metal catalysts.[9]

2.2.1 Metal oxides

MnO$_x$-based ORR catalysts

Metal oxides, especially manganese oxides, are widely used as catalyst in Zn-air batteries. Since the study of MnO$_x$ for ORR reported by Zoltowski *et al.* in the early 1970s,[67] the electrocatalytic properties of MnO$_x$ toward ORR have been examined as functions of chemical composition, texture, morphology, oxidation state, and crystalline structure.[68] For example, the activity of MnO$_x$ with different composition was reported to follow the sequence of Mn$_5$O$_8$ < Mn$_3$O$_4$ < Mn$_2$O$_3$ < MnOOH,[68a, 68b] whereas the activity of MnO$_2$ with different crystal structure to follow the sequence of β- < λ- < γ- < α-MnO$_2$.[68f, 68g] In addition, the morphological structure, which was related to exposed facets and surface area, was an important factor to affect the catalytic activity of MnO$_x$ toward ORR.[68f, 69]

Although significant efforts have been devoted to the enhancement of activity and many studies have been done to show the good activity of MnO$_x$ in alkaline solutions, the detailed mechanism toward ORR of MnO$_x$ is still not very clear due primarily to the complexity of processes and the absence of computational simulation. Several studies revealed that the ORR mechanism of

MnO_x involved the reduction and oxidation of surface manganese species and the density of active sites (Mn^{4+}/Mn^{3+}) would dominate the ORR performance.[68b, 68d, 68g, 70] It was proposed that the materials with distorted structure such as amorphous manganese oxide would exhibit better performance for ORR since it could provide more active sites. *In-situ* XANES (X-ray absorption near edge structure) results demonstrated that the ORR process involved the reduction of Mn^{4+} to Mn^{3+}, followed by the electron transfer of Mn^{3+} to oxygen.[68d]

Since the doping of a low-valent element could enhance the catalytic activity of MnO_x toward ORR, MnO_x doped with a variety of elements (e.g., Ni, Mg and Ca) exhibited higher activity than non-doped materials.[71] Roche *et al.* proposed a four-electron ORR mechanism as follows:[71c]

$$MnO_2 + H_2O + e^- \leftrightarrow MnOOH + OH^-$$

$$2MnOOH + O_2 \leftrightarrow (MnOOH)_2\text{---}O_{2,ads}$$

$$(MnOOH)_2\text{---}O_{2,ads} + e^- \rightarrow MnOOH\text{---}O_{ads} + OH^- + MnO_2(rds)$$

$$MnOOH\text{---}O_{ads} + e^- \leftrightarrow MnO_2 + OH^-$$
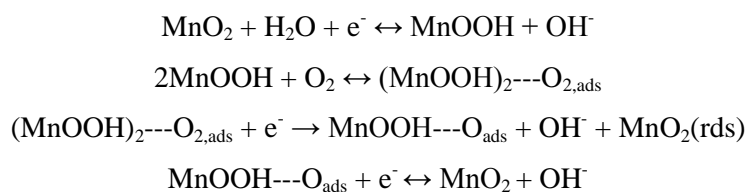
In this mechanism, Mn^{4+}/Mn^{3+} species act as oxygen mediator for oxygen reduction. The coexistence of Mn^{4+} and Mn^{3+} species was believed to assist the charge transfer to molecular oxygen and thus facilitate the ORR. The doping of divalent elements such as nickel and magnesium could stabilize the Mn^{4+} and Mn^{3+} species and accordingly enhanced the ORR activity of MnO_x.

The inherent low conductivity is one of the important drawbacks that limit the activity of MnO_x for ORR. To overcome this limitation, a variety of conducting substrates have been used as current collector for MnO_x catalysts, including different forms of carbons and conductive polymers.[72] Recently, we have devoted considerable efforts to improving the ORR activity of MnO_x in Zn-air batteries. Our strategy is to tailor the electronic property of MnO_x by crystal structure control to enhance the electrical conductivity using a unique composite design and to improve distribution of active sites through nano-fabrication. One example is to fabricate a composite electrode consisting of MnO_x and graphene.[72f] We proposed the introduction of ionic liquid moiety to reduced graphene oxide (rGO) nanosheets to increase not only interaction between graphene sheets and MnO_x nanoparticles, but also ORR catalytic activity based on enhanced utilization of oxygen molecules. This strategy was validated by electrochemical measurements performed on a rotating disk electrode (RDE). The rGO functionalized with ionic liquid moiety exhibited higher limiting current density and more positive onset potential than both graphene oxide (GO) and ionic liquid functionalized graphene oxide (GO-IL). Overloading of manganese oxides (Mn_3O_4) nanoparticles on this functionalized graphene sheet significantly hindered oxygen reduction and even changed the reaction mechanism from a direct four-electron pathway to an indirect two-electron pathway. The enhancement in catalytic activity of MnO_x toward ORR in an alkaline electrolyte is attributed to the increase in electrical conductivity of rGO and the enhanced oxygen molecules affinity by ionic liquid moiety. The result implies a synergic effect between manganese oxide and rGO substrate.

Recently, we developed another method to prepare Ketjenblack carbon (KB) supported amorphous manganese oxides nanowires (NWs) *via* polyol method for Zn-air battery.[73] In this approach, low-cost and highly conductive KB was used as substrate to support MnO_x and to promote the growth of amorphous NWs on KB. The unique structure of the composite electrode provide a large number of catalytically active sites for ORR, dramatically increasing the limiting current density and the onset potential in half measurements. The enhanced catalytic activity is resulted from the amorphous NWs structures, which are more accommodative to various geometrical configuration of dioxygen interacting with active metal sites than other crystalline structure. Zn-air batteries with the composite electrode exhibited a peak power density (~190 mW cm^{-2}), which was much better than those with commercial air cathodes (~120 mW cm^{-2}) and was comparable to those with Pt catalyst (~200 mW cm^{-2}).

More recently, we fabricated high power Zn-air batteries using composite electrodes with MnO_x and carbon nanotubes (CNTs) prepared by a facile electroless deposition method. As is shown in **Figure 2-8**, spontaneously electroless deposition resulted in a good distribution and a well-bonded attachment of MnOx on the surface of CNTs.
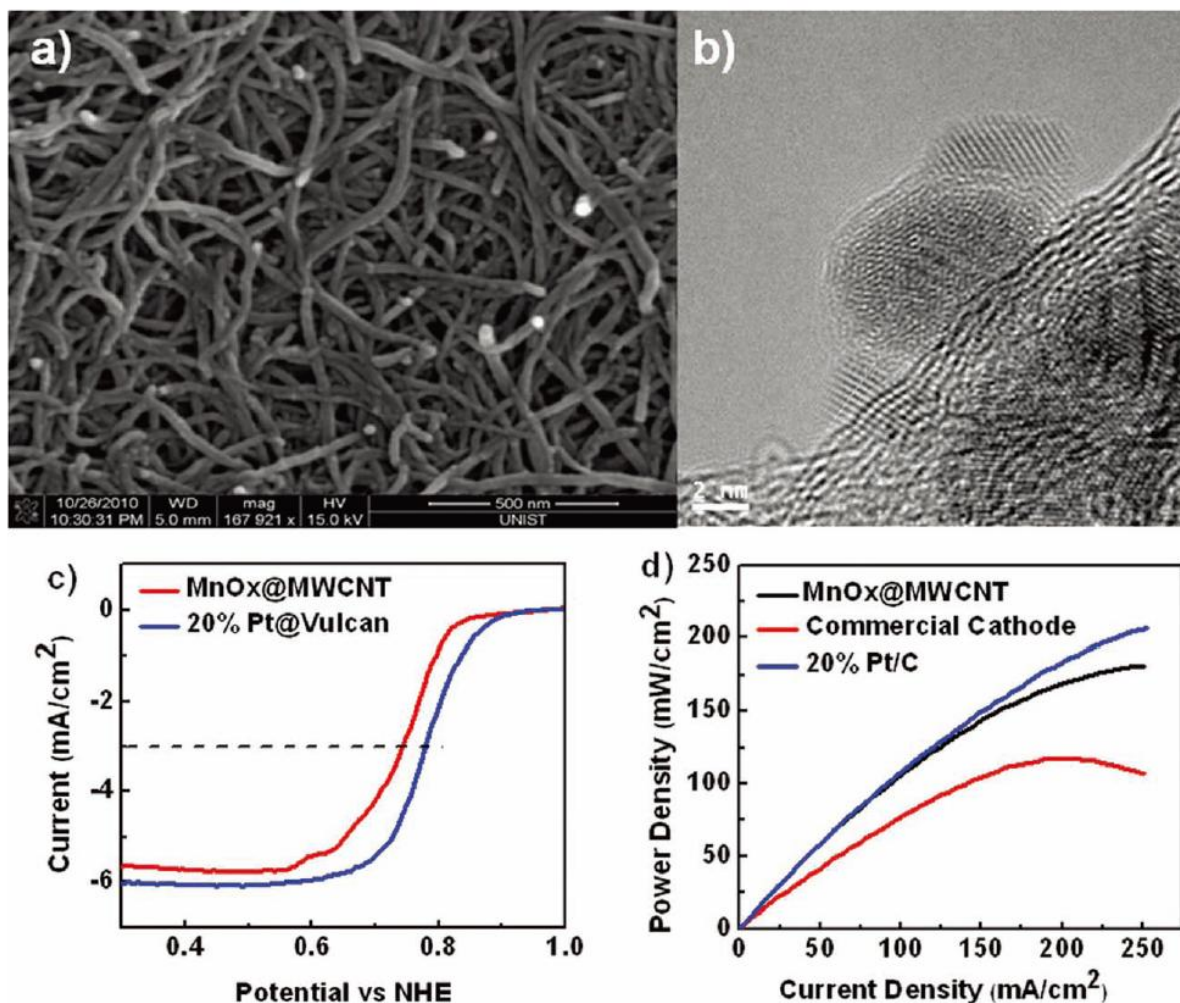
Figure 2-8. a) SEM and b) TEM images of MnOx/CNTs composite. c) Linear sweep voltammograms of MnOx composite and commercial Pt catalyst at a rotation speed of 1600 rpm and a scan rate of 10 mVs^{-1}, in an O$_2$-saturated 0.1 M KOH solution. d) Polarization curves of Zn-air batteries with MnOx/CNTs composite, commercial cathode, and commercial Pt catalysts, respectively.

MnO$_x$ was composed of birnessite crystalline structure, which contained coexistence of Mn^{4+} and Mn^{3+} species and was supposed to deliver very high catalytic activity toward ORR.[71c] In half-cell test measurements, the onset potential of MnO$_x$/CNTs is 0.86V (vs RHE), with a half-wave potential at 0.75V. At an ORR current density of 3 mA cm^{-2}, the potential for the MnO$_x$/CNT composite was 0.75V, only ~35mV away from that for the commercial platinum catalyst, which was the best performance comparing with recently summarized data.[74] A high peak power density (~180 mW cm^{-2}) was achieved for the zinc-air cell with the composite cathode, which was comparable to Pt catalyst (~200 mW cm^{-2}) and much higher than commercial air cathode (~117 mW cm^{-2}). The enhancement of catalytic activity is attributed to well-bounded interface between MnO$_x$ and CNTs, which decreases

interfacial resistance to facilitate electron transfer from electrode to active sites on the surface of MnO_x particles.

Spinel-type-based ORR catalysts

To build rechargeable Zn-air batteries, bifunctional catalysts for both ORR and OER in aqueous electrolyte are necessary. A conventional bifunctional catalyst is usually based on precious metals.[7] To develop a low-cost and high efficient bifunctional electrode is quite challenging owing to the large overpotential for both ORR and OER. A spinel structure with mixed valance oxides such as $(Mn,Co)_3O_4$ have been investigated extensively as electrocatalysts because it exhibits ORR catalytic activity and stability against corrosion for the ORR in alkaline conditions.[75] For Mn-based oxides, a high ratio of Mn^{4+}/Mn^{3+} favors the $4e^-$ ORR process, while a low ratio favors the $2e^-$ process.[70a, 76] For $(Mn,Co)_3O_4$, Co species facilitates to tune Mn oxidation state through an internal redox process, making it possible to control the ratio of Mn^{4+}/Mn^{3+}.[77] A bifunctional catalyst of nanostuctured Mn_3O_4 was developed by Jaramillo and co-workers.[74] The catalyst design was inspired from a cubane-like $CaMn_4O_x$ active site, the biological catalyst found in the oxygen evolving center in photosystem II in nature. Nanostructured Mn_3O_4 was prepared by a facile electrodeposition method and then calcined at 480 °C. Unlike other MnO_x, the catalytic activity of nanostructured Mn_3O_4 exhibited excellent performance for both ORR and OER, comparable to that of precious metals. The excellent catalytic activity is proposed to be stemmed from the nanostructured nature of the catalyst. Chen and co-workers developed another facile route to prepare bifunctional catalyst for Zn-air batteries.[75a] The nanocrystalline $Co_xMn_{3-x}O_4$ (M=divalent metals) spinels prepared by reduction-recrystallization of amorphous MnO_2 precursors exhibited enhanced catalytic activity towards both ORR and OER. DFT calculation implies the intrinsic electrocatalytic activity for ORR and OER is derived from the different binding energy between oxygen molecule and defect sites. Co_3O_4 is also a promising candidate of bifunctional ORR/OER catalyst owing to its high electrocatalytic activity and tunable composition.[78] The spinel type Co_3O_4 where Co^{2+} and Co^{3+} occupy the tetrahedral and octahedral sites, respectively, is demonstrated as a promising electrocatalysts for ORR[75a] and different morphologies of has a different catalytic activity for CO oxidation.[79] For ORR, Co^{3+} can produce surface electronic state and these can capture electrons from the bulk oxide to form excited states $[Co^{3+}-e]$, which can be considered as the active sites for ORR in alkaline.[80] Dai and co-workers developed a low-cost bifunctional catalyst based on a hybrid composite of Co_3O_4 nanocrystal and N-doped graphene.[81] The hybrid composite catalyst (Co_3O_4/N-rGO) outperformed its counterparts, including Co_3O_4, graphene oxide, Co_3O_4/rGO composite and commercial Pt catalyst, toward both ORR and OER. The improvement of catalytic activity is derived from the synergistic effect between catalyst and substrate. The k-edge XANES spectra implied the existence of interfacial Co–O–C and Co–N–C bonds in the Co_3O_4/N-rmGO, which affected the electronic structure of Co_3O_4. Recently, Xu *et al.* also revealed

29

the importance of tunable electronic structure of Co_3O_4 catalyst.[82] It was found that the ORR catalytic activity of Co_3O_4 catalysts was sensitive to the number and activity of surface-exposed Co^{3+} ions.

Perovskite-based ORR catalysts

Although significant efforts have been devoted to developing metal oxides catalysts for ORR/OER, most catalysts search is based on the method of trial-and-error.[83] It is very challenging, but desirable, to find a general principle to guide the material design and synthesis. As a successful example, high active ORR catalysts of Pt-based materials have been developed by following the Sabatier principle.[84] Inspired by the Sabatier principle, Shao-horn's group successfully identified an activity descriptor that governs the ORR activity of perovskite in alkaline solutions.[10] After assessing the ORR activity of 15 perovskite-based oxides using a methodology based on a thin-film rotating-disc electrode, it was found that the ORR activity for oxide catalysts primarily correlated to σ*-orbital (e_g) occupation and the extent of B-site transition-metal–oxygen covalency, which served as a secondary activity descriptor. Based on the findings, a volcano trend of the oxide ORR activity was demonstrated and the ORR mechanism on perovskite oxide catalysts was proposed in **Figure 2-9**.
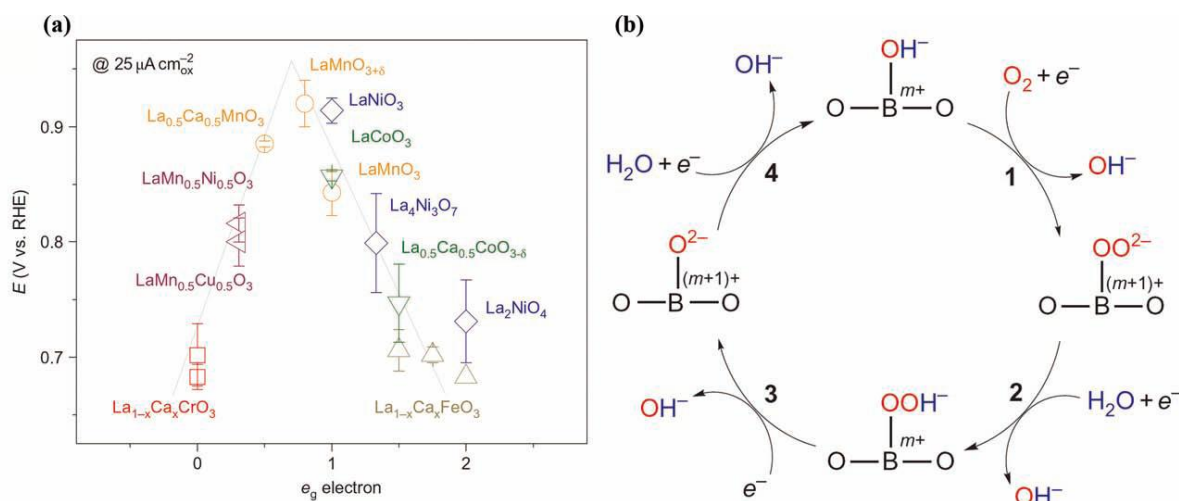
Figure 2-9. a) Volcano trend of ORR activity for perovskite-based oxides. b) the proposed ORR mechanism on perovskite oxide catalysts.[10] Reproduced with permission. [10] Copyright 2011, Nature Publishing Group.

This work provided a general principle to guide how to design perovskite catalysts and improve the ORR activity of future metal oxides catalysts. Soon later, the same group identified the descriptor, occupation of d states with e_g symmetry, for OER over metal oxide catalysts and induced a volcano-shaped activity relationship correlated to the 3d electron with an e_g symmetry of surface transition metal cations in an oxide.[85] Following the volcano plot, a good candidate, $Ba_{0.5}Sr_{0.5}Co_{0.8}Fe_{0.2}O_{3-\delta}$

(BSCF) perovskite, for OER was successfully predicted and prepared. The electrochemical validation of the selected perovskite totally matched the prediction. The catalytic activity of BCSF catalyst led by the design principle outperformed all oxides counterparts and the state-of-the-art iridium oxide catalyst in alkaline media. In a recent work, Sr_2CoMoO_6 exhibited relatively higher catalytic activity for ORR than Sr_2FeMoO_6, which is consistent with the volcano-shaped activity trend related to 3d electrons.[86]

2.2.2 Carbon-based Materials

Unlike carbon-based catalyst in non-aqueous electrolytes, pristine carbon materials without doping show considerably low catalytic activity for ORR/OER in aqueous solutions. Nitrogen-doping of carbon materials can enhance the catalytic activity for ORR in both acidic and basic electrolyte.[87] sp^2 carbon have abundant π electrons which is favorable to ORR requiring electrons. These π electrons, however, need to be activated before participating in ORR because they are so inert that it is hardly used itself. Therefore, putting more electrons into these π electrons systems can be the most practical method and it can be realized by doping carbon with nitrogen, N, increasing electron density and raising the highest occupied molecular orbital (HOMO) of sp^2 carbons. As a result, increased charge carrier facilitates the oxygen reduction reaction.[72a] Another activation method is doping carbon with electron deficient boron, B. For example, the vacant $2P_z$ orbital in B can withdraw electrons from carbon via conjugation, making B-doped carbon activated. Therefore, it can be used as catalysts for ORR.[88] Both the contents and lattice structure of nitrogen atoms in carbon materials dominate the catalytic activity toward ORR. Since Dai's group found nitrogen doped carbon nanotubes can activate ORR in an alkaline electrolyte, much efforts have been devoted to the promising metal-free ORR catalysts.[72a, 89] Learning from the knowledge of nitrogen-doped carbon nanotubes, the same group developed new metal-free catalyst of nitrogen-doped graphene for ORR.[90] The N-doped graphene film possesses remarkable electrocatalytic properties for ORR, similar to that of nitrogen-containing vertically aligned carbon nanotubes, implying the important role of N-doping in carbon materials for ORR. Recent studies demonstrated that carbon nanotubes (either in an aligned or nonaligned form) and graphene, functionalized with certain polyelectrolyte (e.g., Poly(diallyldimethylammonium chloride), PDDA), could also act as metal-free electrocatalysts for ORR.[91] It indicated that it was unnecessary for ORR activity whether the doped nitrogen atoms were in the carbon lattice. These findings indicate that the intermolecular charge-transfer can serve as a general approach to the cost-effective development of various carbon-based metal-free efficient ORR catalysts.

To develop metal-free catalysts for ORR, several approaches were demonstrated to synthesize nitrogen doped carbon materials. Nitrogen-doped carbon nanotube cups were prepared *via* chemical vapor deposition (CVD) using MeCN, EtOH and ferrocene as precursors, which performed high electrocatalytic activity ORR through combination of two-electron and four-electron

pathways.[89a] Another simple and efficient route was developed by Shanmugam *et al.* to synthesize nitrogen doped carbon nanocapsules (NCNCs) as a non-noble electrocatalyst for ORR.[92] The method was scalable and reproducible. The NCNCs displayed better performance as a metal-free electrode catalyst for the oxygen reduction in alkaline medium than commercial electrode catalyst with good stability and methanol tolerance.

An effective approach for the fabrication of graphene-based carbon nitride (G–CN) nanosheets was established using a nanocasting technology in **Figure 2-10**.[11]
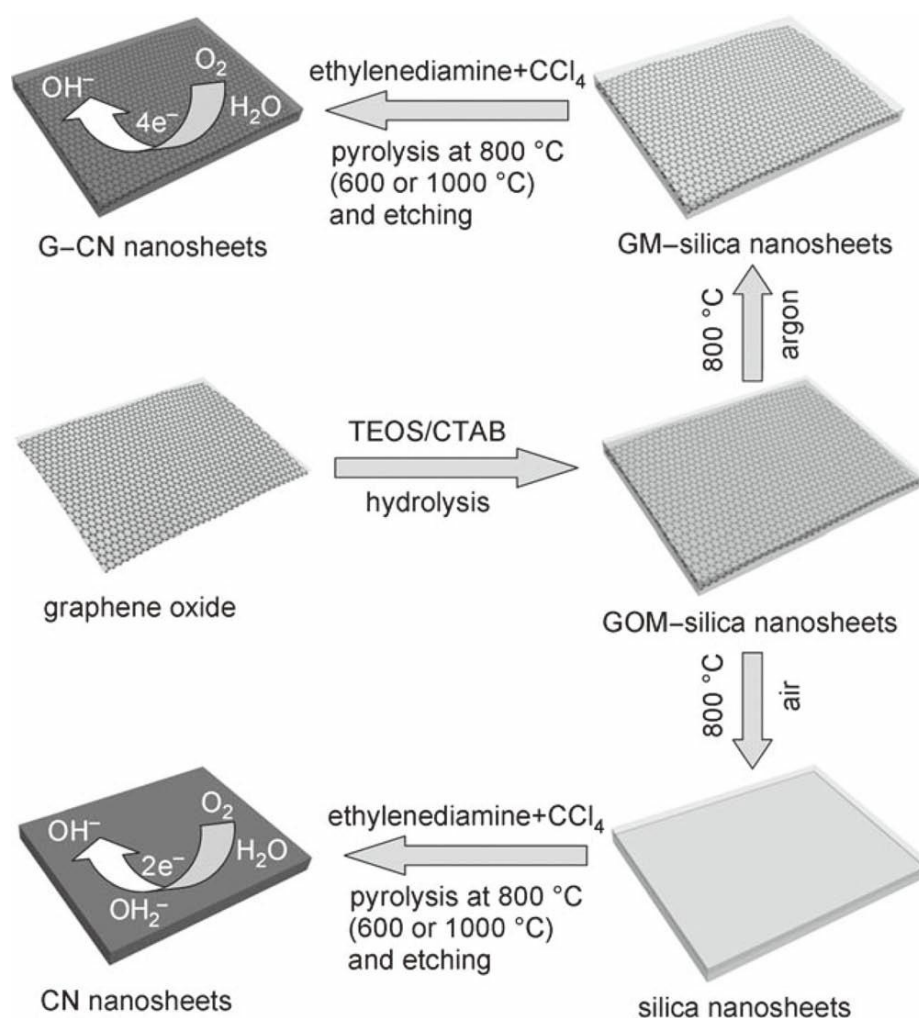
Figure 2-10. Fabrication of graphene-based carbon nitride (G–CN) and CN nanosheets for ORR. Reproduced with permission.[11]

The G-CN nanosheets contained high nitrogen content, thin thicknesses, high surface areas, and enhanced electrical conductivity. The G–CN nanosheets performed outstanding electrocatalytic activity, long durability, and high selectivity as metal-free catalysts for ORR. Both the electrical conductivity and the content of pyridinic nitrogen atoms are critical to achieve high-performance

nitrogen-doped carbon materials for ORR since the combination significantly affects the electron transportation in electrodes and active sites for ORR. A high-surface-area mesoporous nitrogen-doped carbon material was prepared through the carbonization of ionic liquids and nucleobases by using silica nanoparticles as hard templates.[93] The catalyst contained 12 wt % of nitrogen contents with narrow pore size distribution of *ca.* 12nm diameter. The mesoporous nitrogen-doped carbons exhibited very good electrocatalytic activity for ORR in an alkaline medium. This materials also showed a high methanol tolerance, compare with commercial Pt/C catalyst. In the full-cell tests, nitrogen-doped carbon nanotubes (N-CNTs) derived from ethylenediamine precursors were investigated as air cathode catalyst for zinc-air batteries and exhibited high activity for ORR.[94] A cell power density of ~70 mW cm^{-2} was achieved with an air-cathode catalyst loading of 0.2 mg cm^{-2} and an electrolyte of 6M KOH.

Heat-treatment is a widely-used strategy to improve the catalytic activity and stability of ORR catalysts. A large scale of nitrogen-doped graphene, consisting of both pyridine-like and pyrrole-like nitrogen atoms, was synthesized by heat-treatment of graphene with ammonia.[89d] The product annealed under 900℃ exhibited better performance for oxygen reduction than that under 800 ℃ and 1000 ℃, which contained more pyridine-like nitrogen atoms than others. The electrocatalytic activity and durability of this material were comparable or better than the commercial Pt/C.

Despite nitrogen doping for carbon materials, other elements such as boron and phosphorous doping for carbon materials also can enhance the catalytic activity of carbon materials for ORR. Boron-doped carbon nanotubes (BCNTs) prepared by CVD method exhibited good performance for ORR.[95] The electrocatalytic activity was improved progressively with increasing boron content. DFT calculations revealed that electron-deficient boron dopants were positively charged in the BCNT lattice and induced the chemisorptions of oxygen molecules on BCNTs. The electrocatalytic activity of BCNTs for ORR derived from the electron accumulation in the vacant $2p_z$ orbital of boron dopant from the π^* electrons of the conjugated system which then transfer to the chemisorbed oxygen molecules through boron as a bridge. The transferred charge weakened the O-O bonds and, as a result, facilitates the ORR on BCNTs. Carbon nanotubes doped with both boron and nitrogen (BCN nanotubes) can further enhance the catalytic activity toward ORR.[96] Comparing to carbon nanotubes doped with nitrogen atoms or boron atoms alone, the BCN nanotubes exhibited higher electrocatalytic activity in an alkaline medium. The better performance stemmed from the synergetic effect of co-doping with boron and nitrogen. Besides N and B, other elements such as S, I, and P have also used in preparing other heteroatom doped carbon materials as electrocatalysts for ORR.[97]

2.2.3 Other Non-precious Catalysts

For metal/N/C catalysts, macrocyclic structures containing nitrogen–transition metal coordination have been widely studied as catalysts for ORR since Jasinski's pioneer work in 1964.[98]

However, following works showed that these coordinated structures are not stable in acid media, making it inappropriate for PEMFC application. In the 1970s, additional heat treatment above 800°C can significantly improve both catalytic activities for ORR and durability.[99] Subsequent studies have been focused in finding optimized synthetic conditions for better heat-treated metal/N/C catalysts although intrinsic active sites remain unclear.[100]

Organic macrocycles, such as porphyrin and phthalocyanine, were widely used as electrochemical catalysts for ORR in fuel cells and metal-air batteries.[89h, 101] The main disadvantage of macrocycles is the poor durability and unclear active sites. Several strategies have been developed to enhance the activity and stability of macrocyclic catalysts for ORR. One of successful example is to construct a face-to-face structure of cobalt porphyrins.[102] The dicobalt face-to-face porphyrins can improve the activity and stability for oxygen reduction. Recently, Li *et al.* designed and synthesized a new highly durable iron phthalocyanine based non-precious ORR catalyst (Fe-SPc) in alkaline m edium.[103] The design of Fe-SPc catalyst was inspired by the structure of naturally occurring oxygen activation catalysts, enzymes with unique atomic structure and surface properties. By tuning the steric and electronic structure of catalysts, ORR stability of the Fe-SPc was significantly improved after modified by functional groups. Despite organic functionalization, pyrolysis is a widely used strategy to enhance the stability of metal macrocycles. The pyrolysis temperature is an important factor to affect the stability and activity of the complex catalysts. It was found that pyrolyzed pyrolyzed tetra methoxyphenyl porphyrin cobalt complex (CoTMPP) at 410 °C had higher catalytic activities than the catalyst pyrolyzed at 800 °C.[104] The pyrolyzed CoTMPP catalysts were tested as ORR catalysts in air electrode for a Zn-air battery. A current density of ~120mAcm^{-2} was reached at 1V cell voltage. A non-precious catalyst based on nitrogen chelated iron or cobalt (FeCo-EDA) has been noted to be a potential ORR catalysts for Zinc-air batteries.[105] The electrochemical stability of non-precious FeCo-EDA and commercial Pt/C cathode catalysts were compared in air electrodes for Zn-air batteries. The FeCo-EDA catalyst outperformed commercial Pt/C catalysts in both stability and mass activity. A higher peak power density (~232mWcm^{-2}) was achieved using FeCo-EDA, comparing to a power density (~196mWcm^{-2}) for commercial Pt/C. A variety of conductive polymers, such as polyaniline (PANI), polypyrrole (PPy) and polythiophen (Pth), have been found to have electrocatalytic activity for oxygen reduction.[106] Recently, a type of intrinsically conductive polymer (ICP), poly(3,4-ethylenedioxythiophen) (PEDOT), was found to have surprisingly high activity for oxygen reduction in alkaline medium.[107] An air electrode was fabricated by coating a PEDOT electro-active layer onto one side of a hydrophobic, porous membrane (Goretex), involving plasma polymerization of a binding layer to the polytetrafluoroethylene (PTFE) membrane, followed by polymerization of the 3,4-ethylenedioxythiophene monomer to form the PEDOT conducting polymer. The Goretex/PEDOT electrode was tested as an air electrode at various pH levels. As a result, the Goretex/PEDOT

electrode provided substantial oxygen reduction current densities at all of the pH conditions studied. For a full cell test, a Zn-air battery was constructed based on this PEDOT air-electrode and a 1M KOH electrolyte, which provided an open-circuit voltage of 1.44V. Based on a 48-hour continuous test, the PEDOT air electrode conducted a better performance than a Pt/Goretex air electrode under same test conditions.

Chapter 3. Ionic liquid modified graphene nanosheets anchoring manganese oxide nanoparticles as efficient electrocatalysts for Zn–air batteries[72f]

Adapted from ref. 72f with permission from RSC.

This article reports a systematic study of the surface engineering of graphene nanosheets by an ionic liquid moiety, demonstrating its utility in the controlled growth of nanoparticles as well as improving its conductivity and electrocatalytic activity in the oxygen reduction reaction (ORR), that is essential for potential applications in a Zn–air battery. Interestingly, based on the Koutecky–Levich plot, we find that the oxygen reduction pathway of these composites is tunable with the relative amount of Mn_3O_4 nanoparticles supported on the graphene sheets. For example, the ORR mechanism of the system with a lower Mn_3O_4 (19.2%) nanoparticles content is similar to the Pt/C electrode, i.e., a quasi-one-step, 4-electron transfer, unlike that with a higher Mn_3O_4 (52.5%) content which undergoes a classical two-step, 2-electron pathway. Most importantly, we demonstrate the potential of these hybrid rGO–IL/ Mn_3O_4 nanoparticles as efficient catalysts for the ORR in the Zn–air battery with a maximum peak power density of $120 mWcm^{-2}$, which is higher than that of commercial cathode catalysts. With its high surface area and combined catalytic activity with nanoparticles anchored on, we believe this study should present an important step forward in utilizing graphene in electrochemical catalysts and open new possibilities in applications as alternative low-cost catalysts for metal-air batteries and alkaline fuel cells.

Harvesting energy from green resources and developing suitable storage systems are the top priorities of current research in energy. Though the lithium-ion battery leads the market in the field of energy storage, it is still actively investigated as an alternative energy storage system with higher energy and power density to meet various energy demands.[1, 108] In that regard, Zn–air batteries have attracted much attention due to their high potential such as low-cost, relatively high capacity, facile nature of handling and processing, and environmental benignity.[19a] Among the many issues for the development of next generation Zn–air batteries, it is essential to develop highly efficient and low cost catalysts for oxygen reduction reaction (ORR).[57a] Although Pt-based electrocatalysts have been traditionally employed to catalyze the ORR with a high efficiency,[84a, 109] manganese oxides are particularly attractive candidates due to their high catalytic activity, high abundance of Mn, high stability, low cost, and lack of environmental issues.[71c] However, there are still obstacles in utilizing manganese oxides as an efficient ORR catalyst due to their intrinsically low electrical conductivity.[110] Graphene, a monolayer of aromatic carbon lattice, has recently drawn a tremendous amount of

interest due to its extraordinary electrical, optical, thermal, and mechanical properties.[111] Taking full advantage of its chemical stability and high conductivity along with its high specific surface area, the graphene nanosheet is an excellent substrate for hosting and growing functional nanomaterials for high-performance electrochemical and electrocatalytic devices.[112] To date, a number of examples have been reported to host a variety of metal,[113] metal oxide,[114] semiconducting,[115] and magnetic nanoparticles[116] on the surface of graphene; however, up to now, few papers have reported the utilization of metal nanoparticles anchored on graphene and its catalytic activity in a Zn–air battery. Herein, we present a simple approach of integrating manganese oxide nanoparticles into electrically conductive graphene sheets via a solution-based growth mechanism to afford hybrid graphene/Mn_3O_4 nanoparticles (**Figure 3-1**).
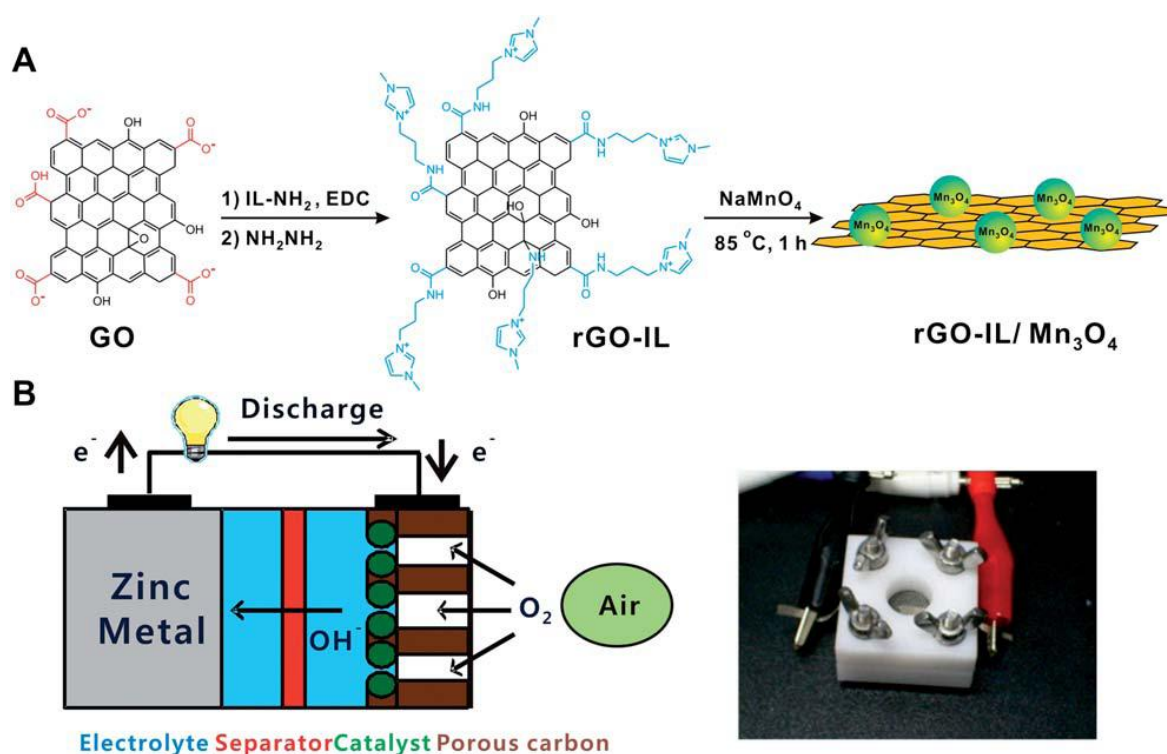

Figure 3-1. (a) Schematic representation of the functionalization of the surface of graphene oxide and subsequent formation of nanoparticles. (b) Diagram of a Zn–air battery cell with a photograph of the actual cell tested.

Furthermore, we investigated their potential as an efficient electrocatalyst for the ORR in a Zn–air battery. In this study, we introduced the ionic liquid moiety onto the surface of graphene oxide with the aim of introducing the manganese oxide precursor on the surface of graphene as well as benefiting from the many features of the ionic liquid moiety (i.e. high ion conductivity, wide electrochemical windows, and the low interfacial energy between the graphene and the nanoparticles) that play a key role in enhancing the electrochemical activity of the resulting hybrid nanostructure.[117]

According to the modified Hummers method, graphite oxide suspensions were initially prepared from a commercial graphite powder, followed by the sonication for the exfoliation of graphite oxide to graphene oxide (GO) nanosheets.[118] Carboxylic acid groups on the surface of GO were further reacted with 1-(3-aminopropyl)-3-methylimidazolium bromide (IL) through the N-ethyl-N'-(3-dimethyl aminopropyl)carbodiimide methiodide (EDC) mediated reaction to afford the ionic liquid moiety functionalized GO (GO–IL) (**Fig. 3.1**). As noted in other literature, the presence of the ionic liquid would enhance the solubility of graphene in a wide range of solvents,[119] facilitate its electrocatalytic activity and enhance its conductivity, hence improving overall the performance of the electrocatalyst. The successful functionalization of GO with the IL moiety was confirmed by zeta-potential measurements, which show a surface charge reversal from -52.0 mV to +45.2 mV upon functionalization. In addition, high-resolution X-ray photoelectron spectroscopy (XPS) further supported the presence of an IL moiety with the appearance of N1s 399.3 and 401.9 eV peaks from the imidazolium ring of ionic liquid in **Figure 3-2 and 3-3**.
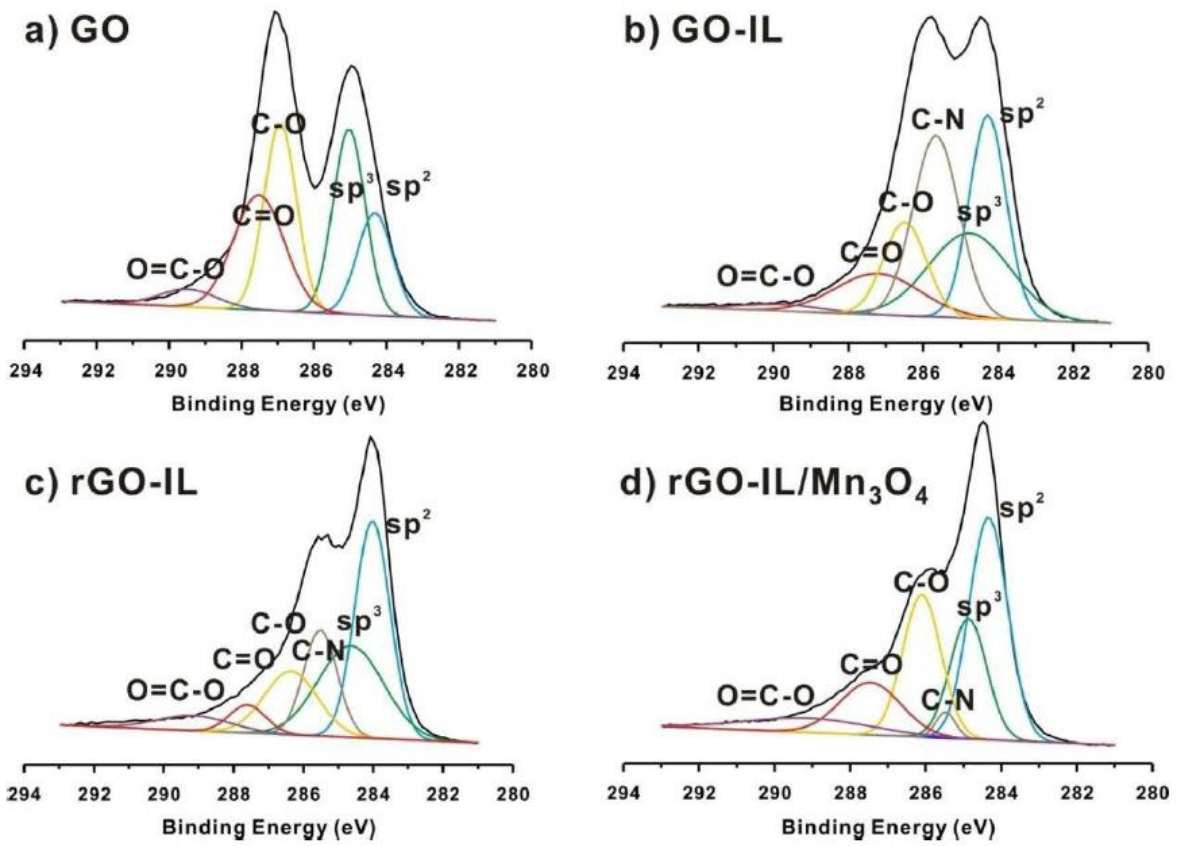
Figure 3-2. Deconvoluted high-resolution C1s XPS spectra of samples in this study. (a) GO, (b) GO-IL, (c) rGO-IL, and (d) rGO-IL/Mn$_3$O$_4$ (10:1).
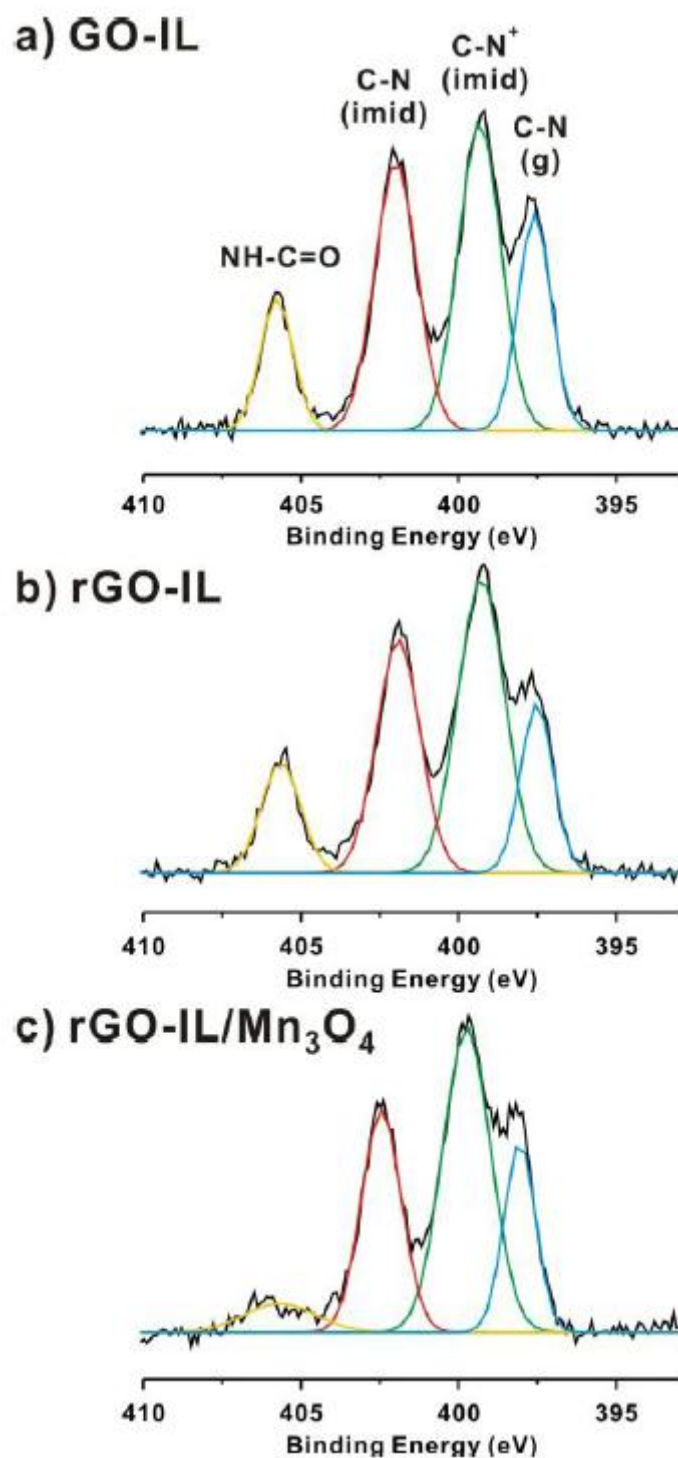
Figure 3-3. Deconvoluted high-resolution N1s XPS spectra of samples in this study. (a) GO, (b) rGO-IL and (c) rGO-IL/Mn_3O_4 (10:1).

In order to restore the electrical conductivity of the pristine GO, chemical reduction of the GO–IL

suspension was subsequently carried out by adding hydrazine to provide the reduced graphene oxide (rGO) nanosheets functionalized with the IL moiety (rGO–IL). In addition, manganese oxide nanoparticles were grown onto the above prepared rGO–IL nanosheets by a simple solution-based growth mechanism as shown in **Fig. 3-1**. Specifically, the manganese precursor, $NaMnO_4$, was mixed through the electrostatic interactions in various feeding ratios (the ratio of rGO–IL to Mn precursor ranges from 1 to 20), followed by heating at 85^oC for 1 h. The relatively mild conditions are proved to be important to control the hydrolysis of the manganese precursor, which precludes the formation of free nanoparticles in solution.

Figure 3-4. (a) SEM and (b) TEM images of rGO–IL/Mn_3O_4 composites with size distribution of Mn_3O_4 nanoparticles. (c) HR-TEM image of Mn_3O_4 nanoparticles with the inset of the corresponding SAED pattern and (d, e, f) STEM and the EDX elemental mapping images of hybrid rGO–IL/Mn_3O_4 (10 : 1) composites.
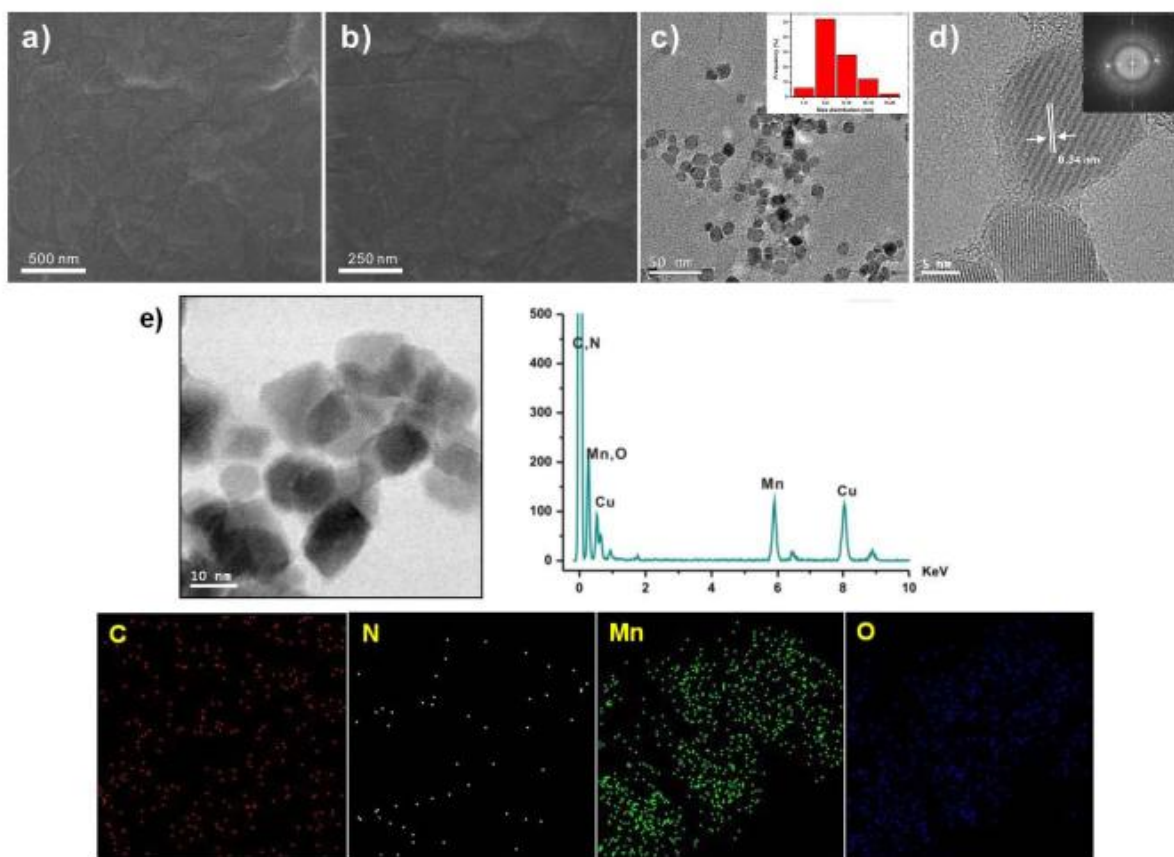
Figure 3-5. (a,b) High-magnification SEM images and (c) TEM image of rGO-IL/Mn$_3$O$_4$ (2:1) composites with size-distribution of Mn$_3$O$_4$ nanoparticles. (d) HRTEM image of Mn$_3$O$_4$ nanoparticles and the inset is the corresponding SAED pattern and (e) Elemental mapping image of hybrid rGO-IL/Mn$_3$O$_4$ (2:1).

The resulting rGO-IL/Mn$_3$O$_4$ composite was filtered and washed thoroughly with deionized water and dried in the oven at 50°C. The control experiment, carried out in the absence of rGO–IL under identical conditions, did not produce any nanoparticles that are redispersible in water. The morphological structures of the rGO–IL/Mn$_3$O$_4$ nanocomposites were characterized by scanning electron microscopy (SEM) and high-resolution transmission electron microscopy (HR-TEM). Based on the SEM and TEM images in **Figure 3-4**, we found non-uniform coating of Mn$_3$O$_4$ nanoparticles on the surface of graphene sheets possessing relatively spherical morphology with an average diameter of 9.45±1.72 nm. HRTEM images further reveal that crystal lattice fringes throughout the entire nanoparticles formed on the graphene sheet that matched with the major peaks of crystalline Mn$_3$O$_4$ nanoparticles. The crystalline phase of manganese oxide nanoparticles can be further revealed by the XRD spectrum, which clearly shows the formation of Mn$_3$O$_4$ in **Figure 3-6 and 3-7.**
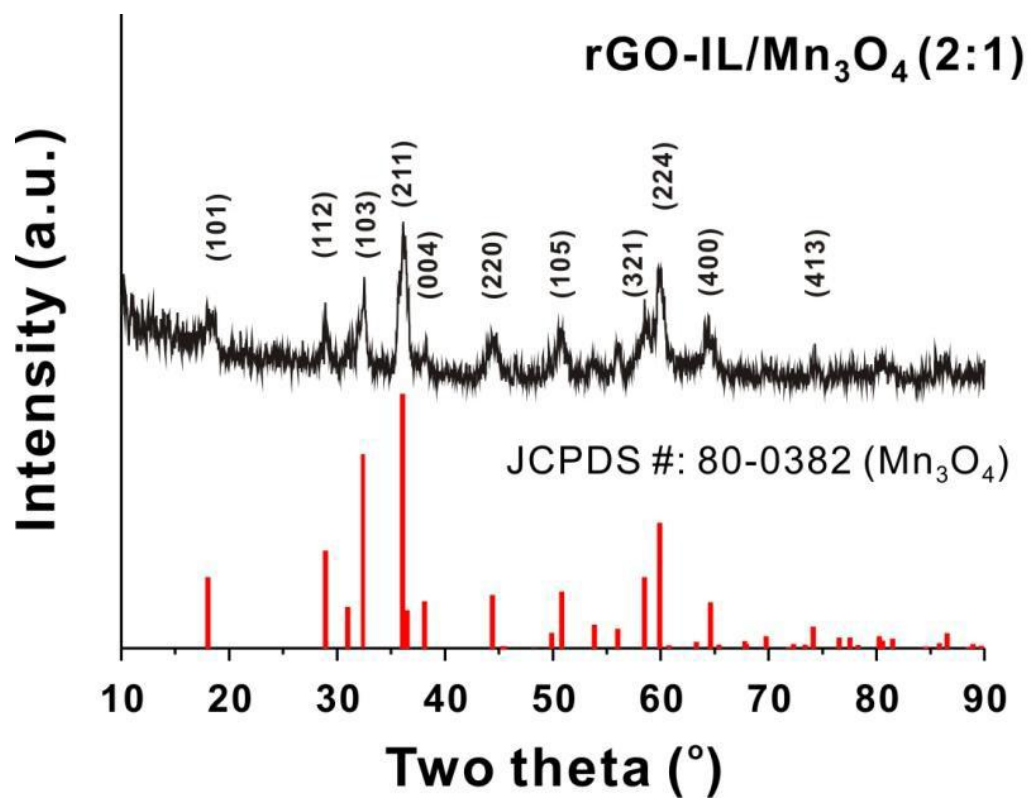
Figure 3-6. X-ray diffraction pattern of prepared hybrid rGO-IL/Mn$_3$O$_4$ (2:1) with the reference Mn$_3$O$_4$ diffraction pattern.
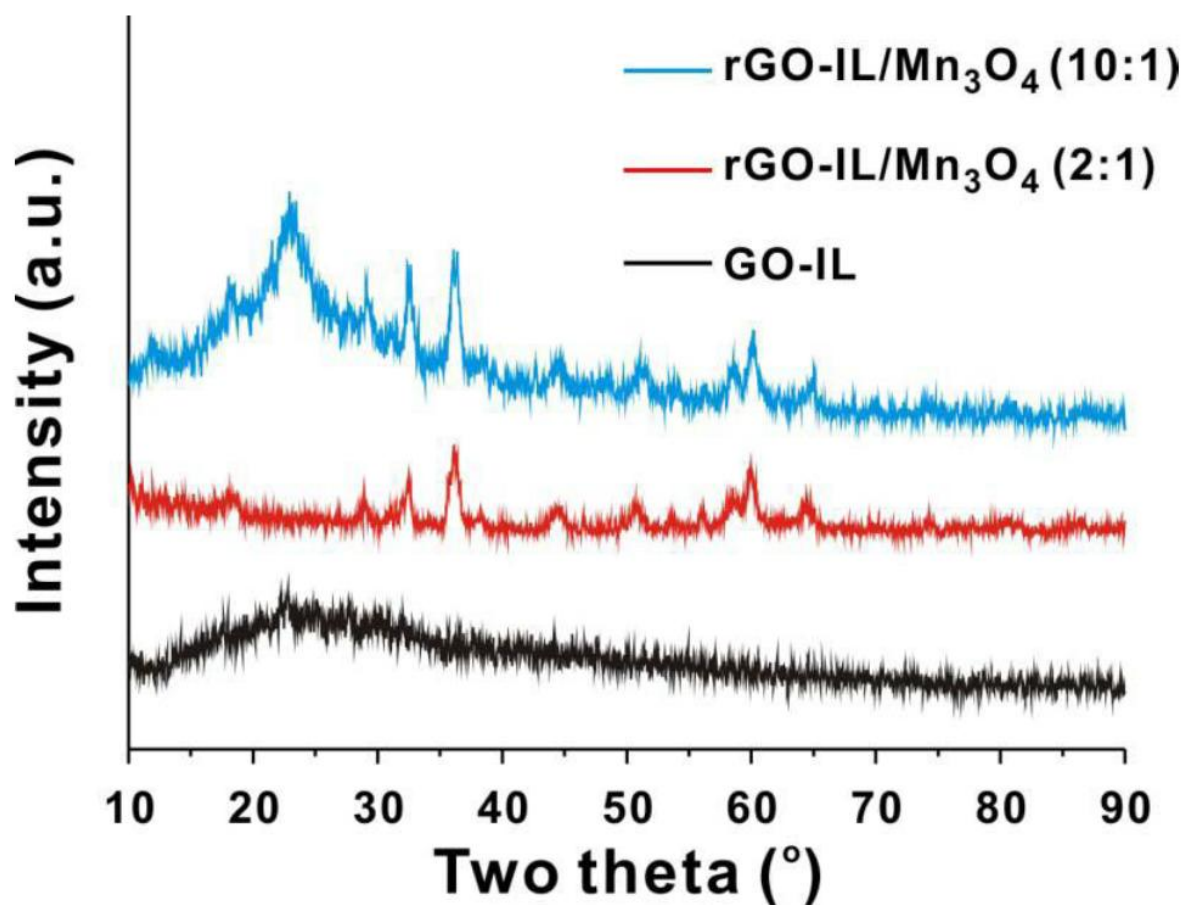
Figure 3-7. X-ray diffraction pattern of all samples used in this study.

Moreover, the selected area electron diffraction (SAED) of the nanoparticles displays the crystalline nature of the Mn_3O_4 nanoparticles that formed on the surface of the rGO–IL nanosheet. As shown in the elemental mapping of hybrid rGO–IL/Mn_3O_4, we observed the presence of the rGO–IL nanosheets by distinctive elements such as C, O and N as well as the presence of Mn_3O_4 nanoparticles by Mn and O elements (**Fig. 3-4f**).

Given the rather non-uniformly distributed Mn_3O_4 nanoparticles on the surface of rGO–IL, we postulate that the ionic linkage between the surface of rGO–IL and the manganese precursor are possibly not uniformly distributed on the surface of graphene nanosheets. The graphene–nanoparticles interaction, however, allows good dispersion of Mn_3O_4 nanoparticles grown on the rGO nanosheets thus avoiding the potential aggregation of nanoparticles during the electrocatalytic cycles.

With the hybrid nanoparticles prepared, we then performed the rotating-disk electrode (RDE) experiment to investigate the electrocatalytic activities of hybrid rGO–IL/ Mn_3O_4. Since the electrons resulting from the oxidation of zinc metal should flow efficiently to the nanoparticle-supporting carbon substrate to reduce the oxygen during the actual operation of a Zn–air battery, the electrical conductivity together with the catalytic activity of the nanoparticles are critical factors in designing

and developing the efficient catalyst.[120] Therefore, we employed two independent strategies to gain the insight on the catalytic activity: 1) chemical attachment of the ionic liquid moiety as well as chemical reduction of the graphene sheet to increase the conductivity of the system and electrocatalytic activity and 2) tuning the ratio of the Mn precursor with respect to the rGO-IL to determine the optimum ratio of our hybrid rGO–IL/Mn_3O_4 catalyst for enhanced ORR activity while preserving necessary electrical conductivity. As shown in the **Figure 3-8**, covalent attachment of the ionic liquid moiety onto the graphene nanosheet results in a higher limiting current and more positive onset potential than that of a plain, unmodified GO.
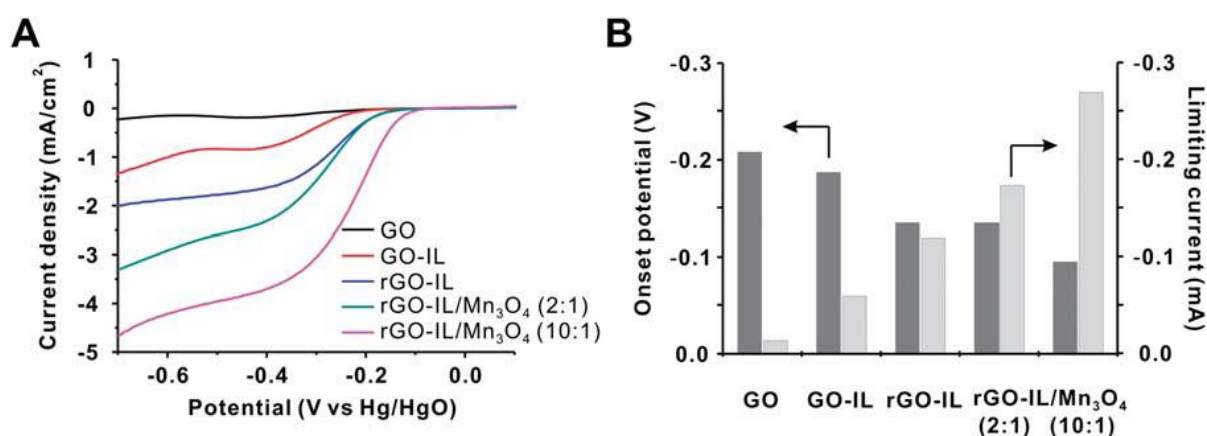
Figure 3-8. Rotating disk electrode (RDE) experiments of various samples prepared in this study. (a) Half-cell data and (b) comparison of the onset potential and limiting current of each sample of GO, GO–IL, rGO–IL, rGO–IL/Mn_3O_4 (2 : 1), and rGO–IL/Mn_3O_4 (10 : 1). The rotation rate is 3200 rpm and the scan rate is 10 mV s^{-1}; 0.10 M KOH is used as an electrolyte. Pt wire and Hg/HgO are used as counter and reference electrodes with a 3 mm diameter working electrode, respectively. Onset potential was measured at -0.002 mA and limiting current was measured at -0.45 V.

This is consistent with the previous reports that the presence of the ionic liquid moiety would facilitate the electrocatalytic activity between the metal and oxygen,[121] as well as increase the solubility of the oxygen which can affect the enhanced reduction rate of oxygen to perhydroxyl or hydroxyl ions.[122] Moreover, the chemically reduced graphene oxide (rGO-IL) has both a higher limiting current and more positive onset potential than GO–IL. Taken together, these data clearly support the critical role of the ionic liquid moiety as well as the enhanced conductivity gained upon the chemical reduction process of the GO nanosheet. Although electrical conductivity is another factor in determining ORR activity, the actual ORR activity of carbon materials is not sufficient to reduce oxygen effectively. When comparing the rGO–IL with rGO–IL/Mn_3O_4 composites, the latter has a higher ORR activity as expected, among which rGO–IL/Mn_3O_4 (10 : 1) has the highest catalytic activity. These results clearly show that Mn_3O_4 nanoparticles facilitate the reaction effectively;

however, higher Mn_3O_4 contents (rGO–IL/Mn_3O_4 (2 : 1), 52.5% Mn content as determined from TGA) can reduce ORR activity compared with a lower content of Mn_3O_4 (rGO–IL/Mn_3O_4 (10 : 1), 19.2% Mn content) in **Figure 3-9**.
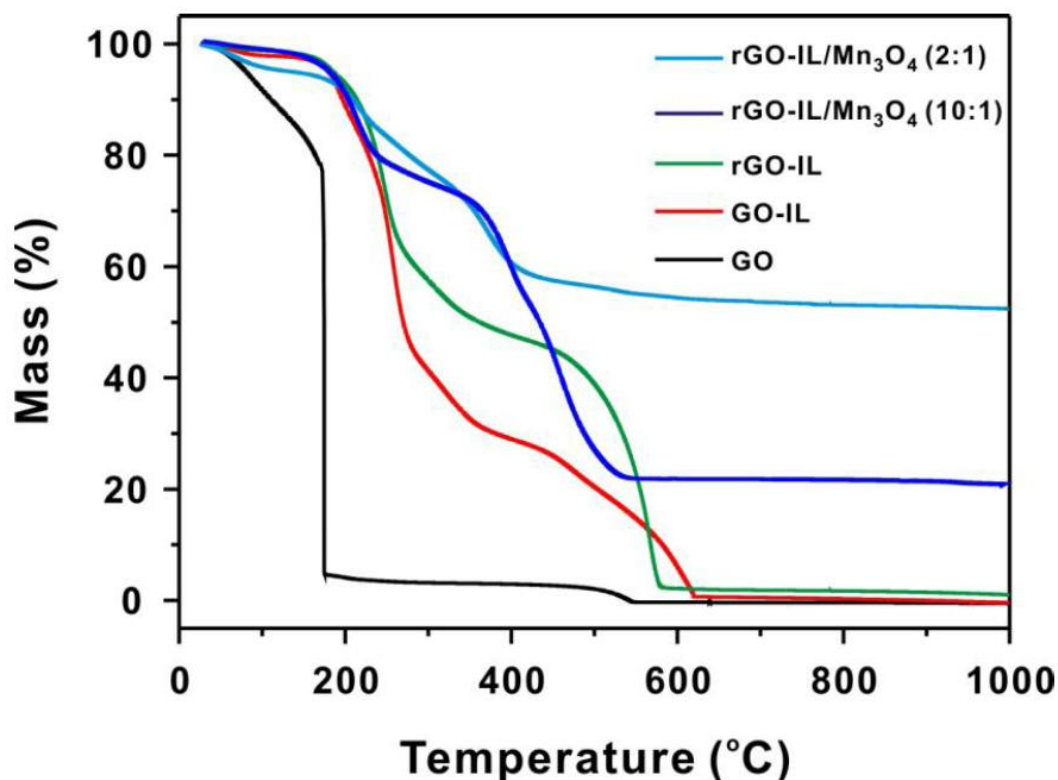
Figure 3-9. TGA thermograms of all samples used in this study. rGO-IL/Mn_3O_4 (2:1) and rGO-IL/ Mn_3O_4 (10:1) show the relative percentage of Mn_3O_4 within the composite is 52.5% and 19.2%, respectively. The thermograms were obtained at a scan rate of 10 ^{o}C/min under air.

We postulate that the relatively larger content of Mn_3O_4 with respect to the graphene sheet results in a lower electrical conductivity, which in turn, has an adverse effect on the ORR activity. This argument can be corroborated with the conductivity measurement with the 4-point probe. The sample with a lower content of Mn, rGO–IL/Mn_3O_4 (10 : 1), displays a lower surface resistance of 61.1 ohmsq^{-1} compared to 120.3 ohm sq^{-1} of rGO–IL/Mn_3O_4 (2 : 1). It is also of note that the absolute amount of Mn_3O_4 in the hybrid is not the major factor in governing the ORR activity, since the limiting current normalized to the effective mass of active Mn_3O_4 within the hybrid rGO–IL/Mn_3O_4 yields approximately 4 times higher mass activity for the rGO–IL/ Mn_3O_4 (10 : 1) sample (-233.9 mA/mg$_{Mn}$ at -0.45 V) than that of rGO–IL/Mn_3O_4 (2 : 1) (-55.2 mA/mg$_{Mn}$ at -0.45 V) in **Figure 3-10**.
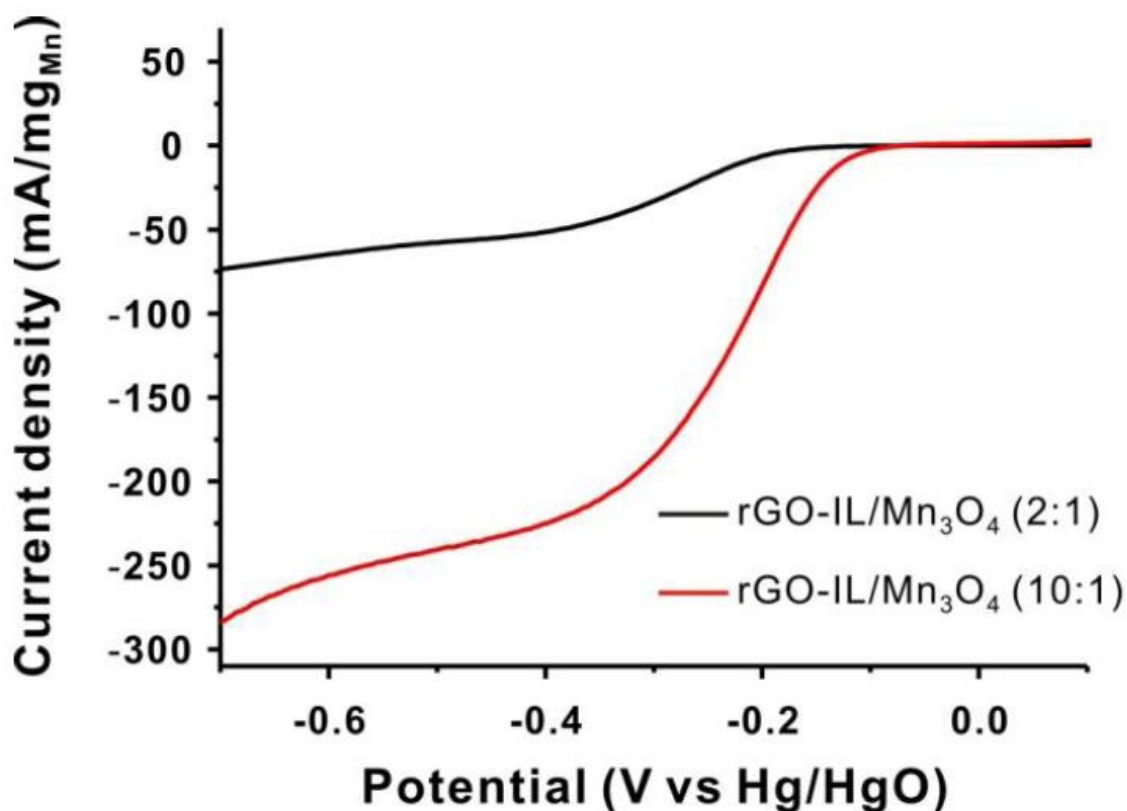
Figure 3-10. Half-cell data of rGO-IL/Mn$_3$O$_4$ samples with different Mn contents expressed by the normalization with the Mn content. Rotating disk electrode (RDE) experiments were conducted with the rotation rate 3200 rpm and the scan rate 10 mV/sec; 0.10 M KOH is used as an electrolyte. Pt wire and Hg/HgO is used as a counter and reference electrode with a 3-mm diameter working electrode, respectively.

To explore the ORR and the related kinetics in a more quantitative manner, we have further transformed the obtained RDE data based on the Koutecky–Levich equation (**Figure 3-11**).[8, 123]

$$\frac{1}{i} = \frac{1}{i_k} + \frac{1}{i_{dl}}$$

$$i_k = nFAkC_{O_2}$$

$$i_{dl} = 0.20nFAC_{O_2}D^{2/3}{}_{o_2}\nu^{-1/6}\omega^{1/2}$$

The Koutecky–Levich plot relates the current density (i) to the rotation rate of electrode (u) to determine both the kinetic current (i$_k$) and the number of transferred electrons (n) involved in the ORR. where i$_k$ represents the kinetic current; i$_{dl}$ is the diffusion limiting current; n is the number of electrons transferred per O$_2$ molecule; F is the Faraday constant (96485 C mol^{-1}); A is the geometric area of the disk electrode (7.06 X 10^{-6} m^2); k (m s^{-1}) is the rate constant for the ORR; C$_{O2}$ is the saturated

48

concentration of O_2 in solution (1.21 mol m^{-3} in 0.10 M KOH); n is the kinematic viscosity (1 X 10^{-6} m^2 s^{-1} in 0.10 M KOH); D_{O2} is the diffusion coefficient of O_2 in solution (1.87 X 10^{-9} m^2 s^{-1} in 0.10 M KOH); and u is the angular frequency of the rotation (rad s^{-1}). From the linear relationship between i^{-1} vs. $\omega^{-0.5}$ based on the Koutecky–Levich equation, we can obtain the number of electrons transferred (n) from the slope and compare the kinetic current (i_k) from the intercept. Given the RDE data, we calculated the average number of electrons transferred from the samples of two different Mn_3O_4 contents, particularly rGO–IL/Mn_3O_4 (2 : 1) and (10 : 1).
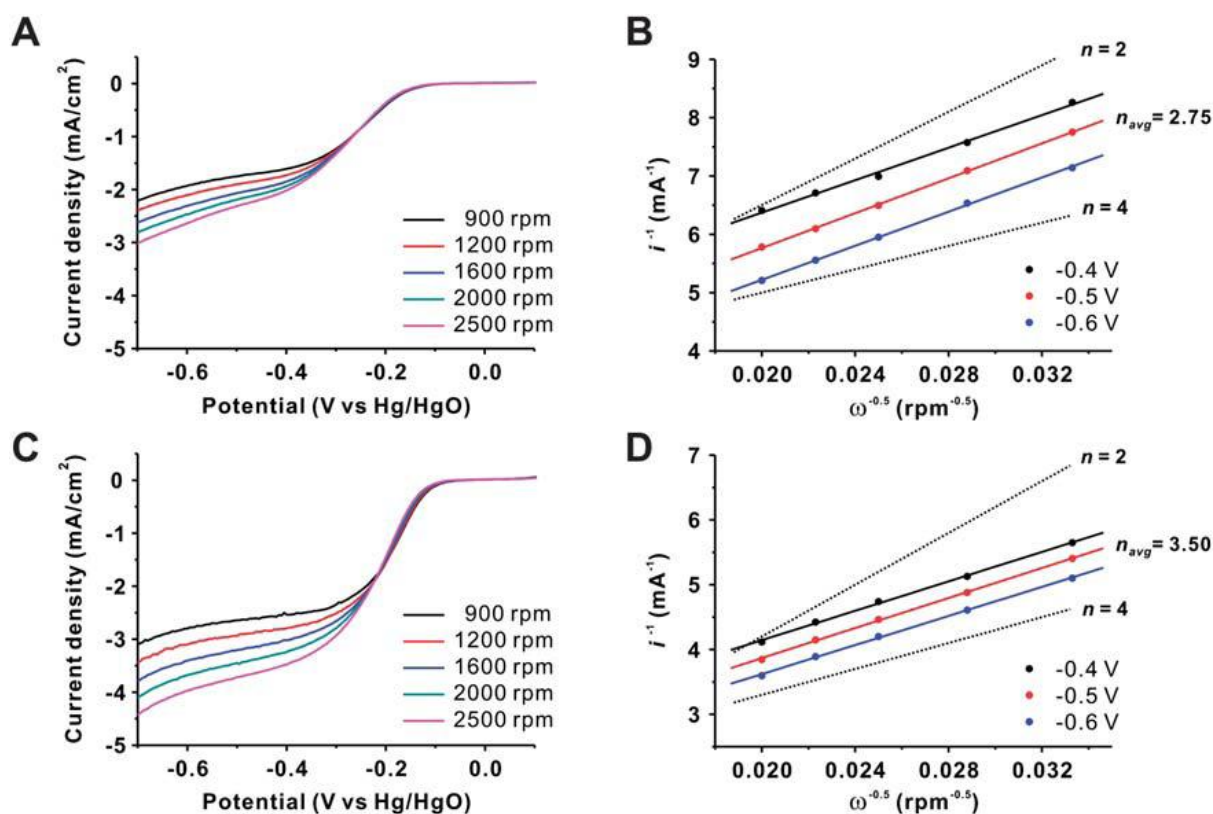
Figure 3-11. RDE experiments and the corresponding Koutecky–Levich plots of (a, b) rGO–IL/Mn_3O_4 (2 : 1) and (c, d) rGO–IL/Mn_3O_4 (10 : 1). The experiments were conducted at a scan rate of 10 mV s^{-1} in an O_2-saturated 0.10M KOH solution. Theoretical slopes for n = 2 and 4 are also constructed for comparison.

To our surprise, we found that the average number of transferred electrons (n) of rGO–IL/Mn$_3$O$_4$ (2 : 1) is 2.75 while it increased to 3.50 in the case of rGO–IL/Mn$_3$O$_4$ (10 : 1). With these results, it is reasonable to estimate that there exist two independent mechanisms depending on the contents of Mn$_3$O$_4$ in the hybrid rGO–IL/Mn$_3$O$_4$ catalyst. Specifically, the corresponding number of electrons (3.50) for rGO–IL/Mn$_3$O$_4$ (10 : 1) indicates an efficient one-step, quasi-4-electron transfer similar to the Pt/C electrode. On the other hand, the electron transfer number (2.75) of rGO–IL/Mn$_3$O$_4$ (2 : 1) is close to the classical two-step, 2-electron pathway, as is the case for many other carbon-based electrode materials (**Figure 3-12**).
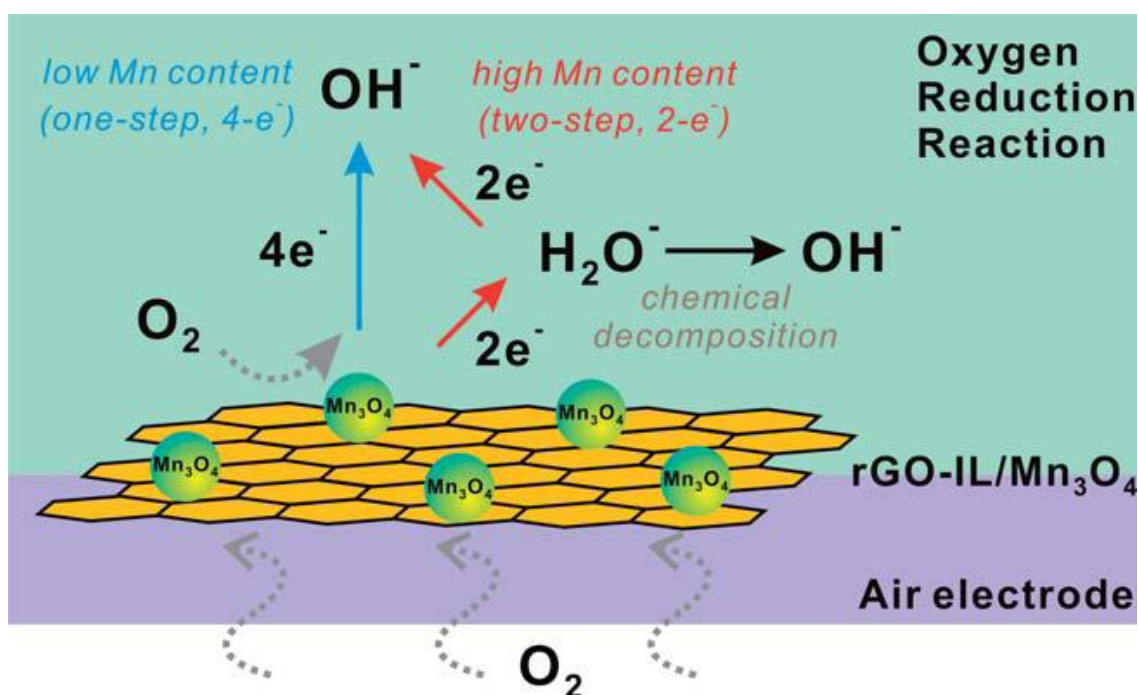
Figure 3-12. Schematic representation of the potential pathway of electrons during oxygen reduction reaction on the surface of rGO–IL/Mn$_3$O$_4$ electrocatalysts.

It is interesting to note that the reaction mechanism is tunable simply with the relative amount of nanoparticles supported onto the graphene sheets. Because the study on half-cell experiments such as RDE presents only the performance as a catalyst, we have to evaluate the actual ORR performance of catalysts in a Zn–air full cell. For that purpose, we have evaluated the electrochemical performance of a single Zn–air cell composed of an anode of zinc powder together with a hybrid rGO–IL/Mn$_3$O$_4$ electrocatalyst in the cathode electrode. Via a galvanodynamic method, the current density versus potential (reference to a Zn electrode) profile can be obtained under varying current density from 0 to 200 mA cm^{-2} and one can calculate the maximum peak power density from a polarization curve for the Zn–air cell (**Figure 3-13**).
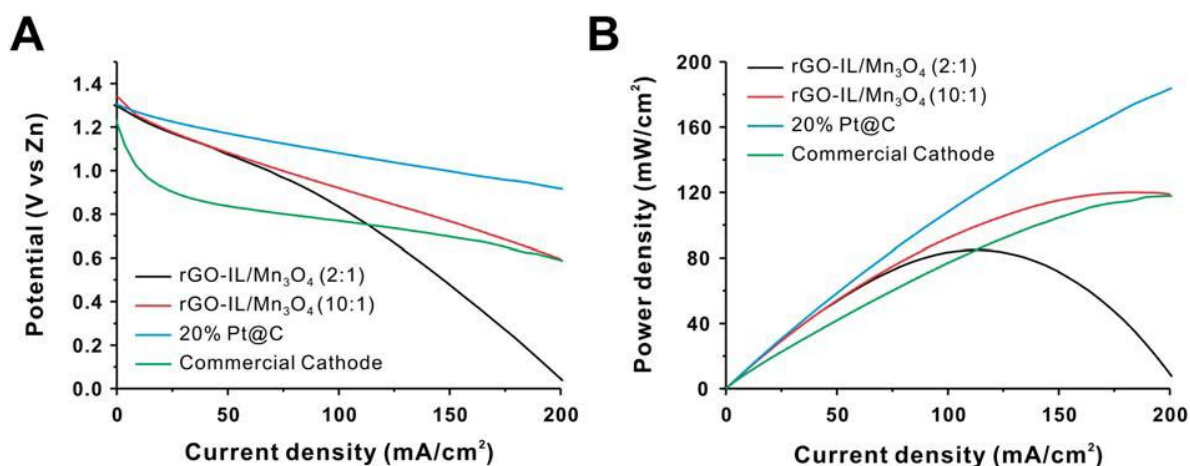
Figure 3-13. Single cell performance of the Zn–air battery assembled with hybrid rGO–IL/Mn3O4 electrocatalysts compared with 20% Pt/C and commercial cathode materials. (a) Polarization curve of zinc-air cell and (b) corresponding power density plot of (black) rGO–IL/Mn_3O_4 (2 : 1), (red) rGO–IL/Mn_3O_4 (10 : 1), (blue) 20% Pt/C, and (green) commercial cathode (MEET) under the current density from 0 to 200 mA cm^{-2}.

As shown in the discharge profile of Zn–air full cell, the voltage difference in two cells of different Mn contents rises significantly with the increase of current density. This result indicates that a resistance effect on a Zn–air cell is more dominant when high current density is applied to the cell and also coincides with the fact that the oxygen reduction reaction becomes very sluggish due to a high overpotential. When the power density plot is constructed, similar trends between RDE and actual cell performance are observed and maximum peak power density of 120 mW cm^{-2} can be obtained from the hybrid rGO–IL/Mn_3O_4 (10 : 1) sample. For comparison, identical procedures were applied to compare the efficiency of the air cathode with the commercial gas diffusion electrode (GDE) including MnOx (Meet Inc., Korea) and 20% Pt on Vulcan XC-72 (E-TEK). Although the 20% Pt/C exhibits the best electrochemical performance among various samples, our hybrid rGO–IL/Mn_3O_4 (10 : 1) still illustrates better efficiency in the overall Zn–air fuel cell performance than the commercial air cathode under the current density from 0 to 200 mA cm^{-2}. With further improvements, we believe this hybrid catalyst could be used as a potential candidate in low-cost electrocatalysts for metal-air batteries and alkaline fuel cells. For more practical application of our hybrid catalyst in various electrocatalytic reactions, our next endeavor should be focused more on addressing the stability and durability, as well as the product cost of the modified graphene nanosheet and hybrid catalyst.

In summary, we present a simple and facile approach of integrating manganese oxide nanoparticles into the electrically conductive graphene sheets via a solution-based growth mechanism to afford hybrid graphene/Mn_3O_4 nanoparticles. The ionic liquid moiety on the graphene nanosheet

was proven to be important in enhancing the electrocatalytic activity of the hybrid nanoparticles in oxygen reduction reaction with a one-step, quasi-4-electron transfer pathway. By utilizing the high activity of the graphene/Mn_3O_4 nanoparticles, we demonstrated their potential in the Zn–air battery, as they exhibit considerably high catalytic activity. By taking advantage of the facile synthetic nature of this hybrid nanoparticle with graphene nanosheet, we anticipate that the hybrid graphene/Mn_3O_4 nanoparticles will open new possibilities in applications as alternative low-cost catalysts for metal-air batteries and alkaline fuel cells.

Experimental

Procedures of graphene oxide (GO) nanosheets

Graphite oxide was synthesized from graphite (Aldrich, <20 mm) by the modified Hummers method and exfoliated to give a stable, brown dispersion of graphene oxide (GO, typical conc. of 0.50mg mL^{-1}) under ultrasonication for 40 min and then centrifuged at 4000 rpm for 10 min to remove any aggregates remained in the suspension.

Preparation of ionic liquid moiety (IL-NH2)

In the typical procedure according to the literature,47 3-bromopropylamine hydrobromide (1.1 g, 5.0 mmol) and 1-methylimidazole (0.395 mL, 5.0 mmol) were added to 15 mL ethanol, forming a colorless solution which was refluxed under nitrogen for 24 h. The resulting turbid mixture was purified by re-crystallization from ethanol, with ethyl acetate as an anti-solvent. Finally, the resulting white powder was dried under vacuum at 60 ^{o}C overnight and then purified. Preparation of ionic liquid modified graphene oxide nanosheet (GO–IL) and reduced graphene oxide nanosheet (rGO–IL) Ionic liquid modified GO nanosheets (GO–IL) were prepared by reacting GO with excess IL-NH2 (conc. 0.50 mg mL^{-1}) under stirring for 5 h in the presence of N-ethyl-N'-(3-dimethyl aminopropyl) carbodiimide methiodide (EDC, 98%, Alfa Aesar). The resulting suspension was dialyzed (MWCO 12000–14000, SpectraPore) for a few days to remove any by product and residuals during functionalization. The prepared GO–IL suspensions exhibited a fairly good colloidal stability over a wide span of pH conditions. Chemical reduction of the GO–IL to rGO–IL was carried out by adding hydrazine as reported previously. Preparation of catalyst ink for rotating disk electrode Catalyst ink was prepared by ultrasonically mixing 2.0 mg of asprepared sample with 1.0 mL of pure deionized water for 1 h in order to make a homogeneous suspension. Then, 3 mL of the prepared catalytic ink was transferred to the surface of the 3 mm diameter glassy carbon electrode using a micropipette. Finally, the ink was dried for 10 min under vacuum conditions at room temperature to form a thin catalyst film on the glassy carbon electrode as a working electrode.

Rotating disk electrode (RDE) experiments

All half cell experiments for the ORR using a rotating disk electrode (RDE) (ALS Co., Ltd) were carried out under the same conditions where Pt wire and Hg/HgO were used as a counter and a reference electrode respectively; 0.10 M KOH is used as an electrolyte; pure oxygen gas (99.9%) was purged for 30 min before each RDE experiment to make an electrolyte oxygen saturated condition. Rotation speeds were changed in this RDE measurement to deduce kinetic parameters related to ORR to construct the Koutecky–Levich plot. Electrochemical characterization of as-prepared catalysts were conducted using a single potentiostat (Ivium) with a scan rate of 10 mV s^{-1} and potential range from 0.15 V to -0.7 V.

Preparation of air electrode

All air electrodes used in this Zn–air full cell test are prepared with fixed weight composition; activated carbon (Darco G-60A, Sigma-Aldrich) is 62 wt% + poly-tetrafluoroethylene (PTFE) binder 30 wt% (60 wt% PTFE emulsion in water, Sigma-Aldrich) + as-prepared catalysts is 8 wt%. After sonicating each material in pure DI-water for 1 h, each suspension was then mixed ultrasonically for 1 h to form a homogeneous suspension. The excess water is removed by filtering the homogeneous suspension and then the slurry is dried at 60°C. By adding isopropyl alcohol to dried black powder, air electrodes were manufactured via a kneading and rolling process to make the desired thickness of air cathode. Finally, Ni-foam as a current collector was attached to the back side of the air electrode. The thickness of all air cathodes was set to 600 mm to minimize the thickness factor of electrodes to overall cell performance.

Zn–air full cell assembly

For the Zn–air full cell test, homemade Zn–air single cell were used in this experiments. 1 g of zinc powder (Umicore) was used as the anode electrode. Nylon net filter (Millipore) was used as a separator. A 16–pi air electrode is used as the cathode electrode. The galvanodynamic experiment is carried out with a multichannel potentiostat (WBCS 3000, WonA Tech, Korea) with various current densities from 0 mA cm^{-2} to 200 mA cm^{-2} to characterize the Zn–air single cell performance.

Chapter 4. Ketjenblack Carbon Supported Amorphous Manganese Oxides Nanowires as Highly Efficient Electrocatalyst for Oxygen Reduction Reaction in Alkaline Solutions[73]

A composite air electrode consisting of Ketjenblack carbon (KB) supported amorphous manganese oxides (MnOx) nanowires, synthesized via a ployol method, is highly efficient for oxygen reduction reaction (ORR) in a Zn-air battery. The low-cost and highly conductive KB in this composite electrode overcomes the limitations due to low electrical conductivity of MnOx while acting as a supporting matrix for the catalyst. The large surface area of the amorphous MnOx nanowires, together with other microscopic features (e.g., high density of surface defects), potentially offers more active sites for oxygen adsorption, thus significantly enhancing ORR activity. In particular, a Zn-air battery based on this composite air electrode exhibits a peak power density of ~190 mW/cm^2, which is far superior to those based on a commercial air cathode with Mn_3O_4 catalysts.

Batteries with higher energy density are needed to meet the ever-increasing demands of many emerging technologies, from portable electronics to electrical vehicles. The energy densities of the existing batteries are limited primarily by the low energy density of electrode materials used. To dramatically enhance the energy density of batteries, considerable efforts have been devoted to the development of new air electrodes for efficient utilization of oxygen from air in metal-air batteries. Among many metals that may be used as the anode (e.g., Ca, Al, Fe, Cd, Li and Zn) in a metal-air battery, Zn metal has received much attention due to its low cost, abundance, and environmental benignity. Additional advantages of Zn-air batteries include a flat discharge voltage and a long shelf-life.[1] To date, however, the performance of Zn-air battery is limited largely by the poor performance of the air electrode because the rate of ORR is much slower than that of zinc oxidation in **Figure 4-1**.
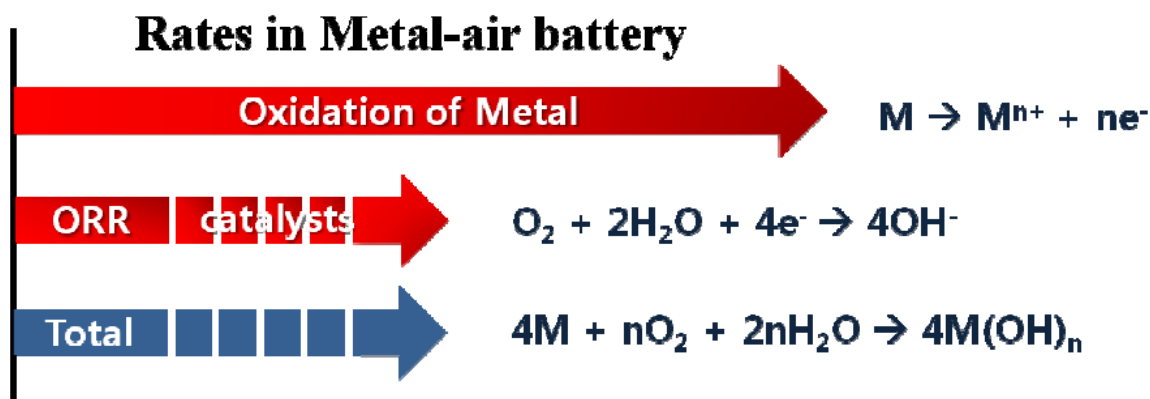
Figure 4-1. Schematic rates in general metal-air battery (also applied to Zinc-air battery).

Thus, the development of efficient catalyst for accelerating ORR in an air-electrode is vital to achieving high-performance zinc-air batteries.

Nanoparticles of precious metals and alloys with well-controlled facets are reported active and efficient catalysts for ORR in fuel cells and metal-air batteries.[109, 124] However, their high cost and scarcity severely hinder their applicability to broad commercialization. Accordingly, transition metal oxides and other less expensive catalysts have been used as alternative ORR catalysts in primary alkaline based fuel cells and metal-air batteries.[125] Among them, MnOx are particularly attractive because of their high catalytic activity, low cost, and minimum environmental impact. It has been reported that ORR catalytic activity of MnOx depends on its crystalline structure and oxidation state.[68d, 68g, 126] It also depends sensitively on the surface area and the available active sites exposed to oxygen molecules. Thus, the use of an amorphous structure as catalysts could be more favorable over crystalline manganese oxide structures. Yang et al. reported that nanoporous amorphous manages oxides, synthesized via low-temperature aqueous redox process, are efficient electrocatalysts for ORR in alkaline solutions,[5] due mainly to high surface area and large concentration of lattice defects in the amorphous structures. They also showed that this oxide significantly facilitates a 2-electron pathway in ORR.[68e]

However, full utilization of MnOx as an efficient ORR catalyst is still limited by the low electrical conductivity of MnOx,[127] to overcome this problem, conducting carbon materials, such as graphene and CNT, are usually used with MnOx.[72f] To reduce the cost, commercially available, less expensive, conducting materials such as ketjenblack can be used as an alternative way to prepare reliable ORR catalysts.

Here we report a simple approach to integration of amorphous MnOx nanowires with electrically conductive ketjenblack carbon materials via a polyol method (hereafter denoted as a-MnOx NWs on KB) and the electro-catalytic properties of the composite electrode for ORR in a Zn-air battery. In order to prepare a-MnOx NWs on KB, ethylene glycol and potassium permanganate

55

were used as the reducing agent and the precursor for manganese oxides, respectively.[128] Permanganate ion can be reduced to amorphous manganese oxides by ethylene glycol under the mild condition. A solution based-redox reaction for deposition of amorphous MnOx NWs onto the surface of ketjenblack carbon in a carbon matrix is schematically illustrated in **Figure 4-2 (a).**
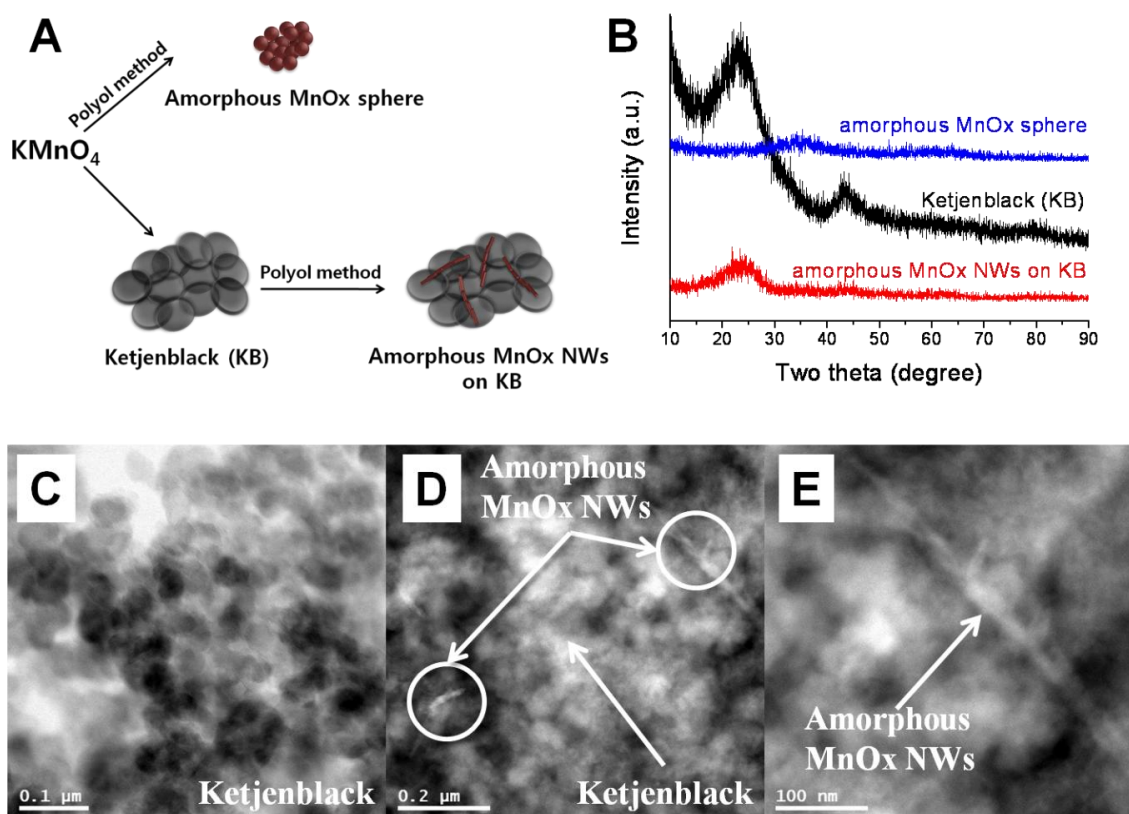
Figure 4-2. (a) Schematic description of amorphous MnOx particles (a-MnOx) and nanowires on ketjenblack composite (a-MnOx NWs on KB) (b) X-ray diffraction patterns of amorphous MnOx particle, ketjenblack (KB), and amorphous MnOx nanowires on Ketjenblack composites. TEM images of (c) pristine ketjenblack and (d) amorphous MnOx nanowires on Ketjenblack composites, and (e) magnified TEM image of (d).

Specifically, potassium permanganate, $KMnO_4$, was mixed with pristine ketjenblack carbon suspension in ethylene glycol under basic condition by adding small amount of 0.5M NaOH, followed by heating to 80^oC and kept for 2 h. The resulting amorphous manganese oxide on Ketjenblack composite was filtered and washed thoroughly with deionized water and ethanol, followed by drying in an oven at $60\,^o$C for 12 h. The MnOx content in this composite is ca. 10 wt%, as determined from inductively coupled plasma-atomic emission spectrometry. It is critical to optimize amount of manganese oxides in this MnOx catalyst and carbon composites because ORR pathway can be tunable with Mn contents based on the experimental fact that too much MnOx in this material decrease its overall electrical conductivity, deteriorating ORR activity.[72f] A control experiment was also performed in the absence of ketjenblack carbon under the same processing conditions (reaction temperatures and times), producing brown-black amorphous manganese oxides.

The X-ray diffraction (XRD) pattern from a sample of a-MnOx NWs on KB (**Figure 4-2b)** showed no distinct peaks (except those from ketjenblack), suggesting that the as-prepared MnOx was amorphous under this mild synthetic condition. TEM examination revealed that the amorphous MnOx on ketjenbalck carbon had a nanowire morphology with a diameter of ca. 10 nm (**Figure 4-2d and e**), which was further confirmed with line mapping in **Figure 4-3**.
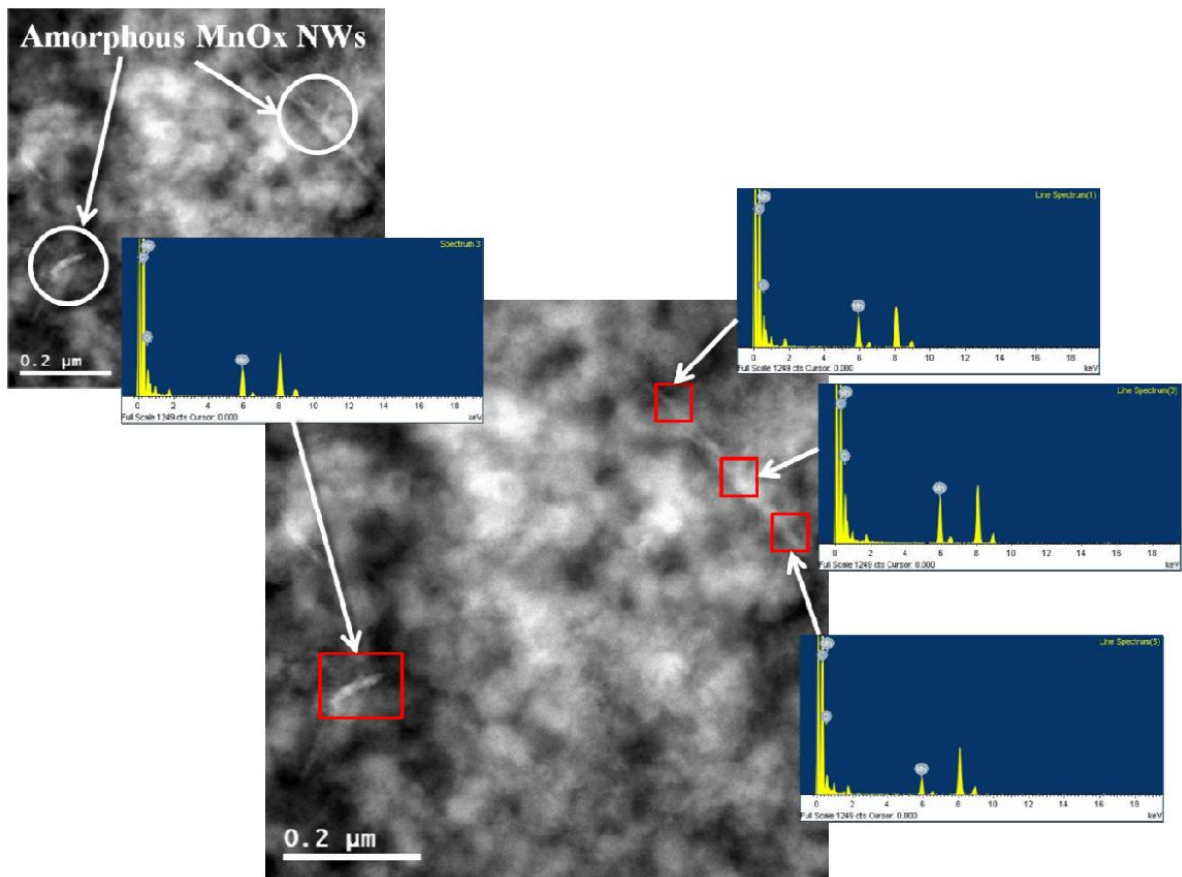
Figure 4-3. TEM images of amorphous MnOx nanowires on Ketjenblack and the corresponding EDAX spectra.

Since the NWs were obtained below 100°C, it is expected that they have many defects and rough surfaces. It is noted that the nanowire morphology of the amorphous MnOx on KB is very different from the particle shape of the amorphous MnOx without KB support, implying that the presence of KB matrix promoted the formation of MnOx nanowires in **Figure 4-4**.
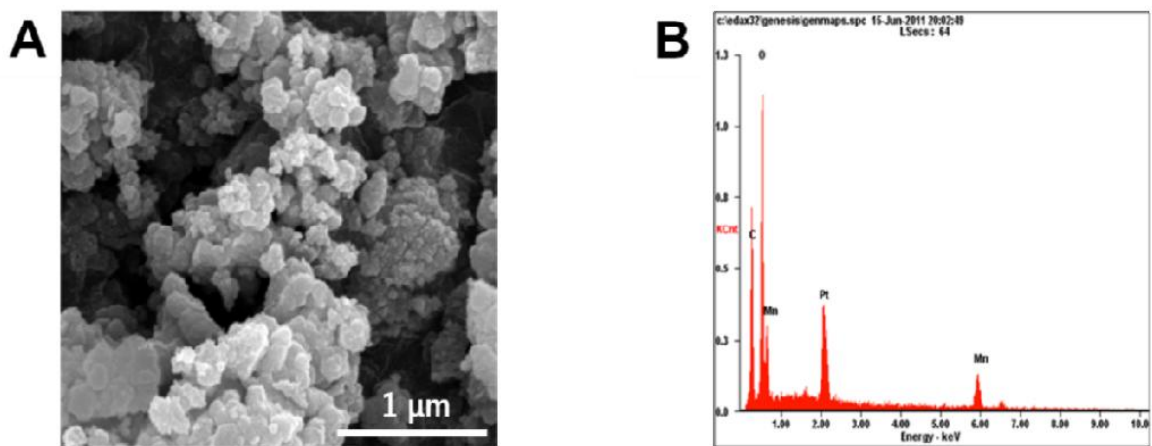
Figure 4-4. SEM image of as-prepared amorphous manganese oxides particles (A) and the corresponding EDS spectrum (B).

To the best of our knowledge, for the first time, we described facile route of growing amorphous manganese oxides nanowires along amorphous template, ketjenblack carbon. Because preparing amorphous structure is more cost effective and has larger surface area than other crystalline structure, we expect that it can be very promising candidates for ORR catalysts because catalytic reaction mostly occur onto surface. Therefore our question is how to keep amorphous MnOx structure on conducting carbon materials, preparing amorphous MnOx and carbon composites. This is why we use amorphous ketjenblack while expecting this carbon to act template in this synthetic condition. From this a point of view, we expect this innovative and simple approach to apply preparing amorphous catalysts on amorphous supporting materials, especially catalysts composites for metal-air and alkaline fuel cell.

To evaluate electrocatalytic activity for ORR of the a-MnOx NWs on KB, rotating disk electrode (RDE) experiments were performed with two MnOx samples prepared at 80 and 160°C, pristine KB, and *a*-MnOx NWs on KB composite (in **Figure 4-5**).
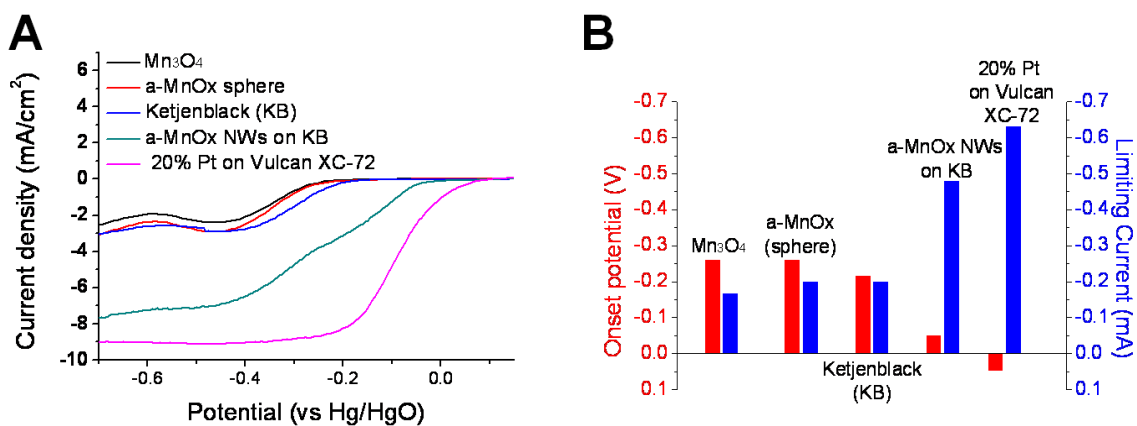
Figure 4-5. Rotating disk electrode (RDE) experiments of Mn_3O_4, amorphous MnOx particle (a-MnOx), ketjenblack (KB), amorphous MnOx nanowires on ketjenblack composites (a-MnOx NWs on KB), and 20% Pt on Vulcan XC-72 (E-tek) under oxygen saturation condition at 3200 rpm; scan rate was 10mV/sec; 0.10 M KOH was used as an electrolyte. Pt wire and Hg/HgO was used as a counter and reference electrode with a 3-mm diameter working electrode, respectively. Onset potential (red color) was measured at -0.002 mA and limiting current (blue color) was measured at -0.45 V.

While the MnOx sample was amorphous when prepared at $80\,^{o}C$, it turned to a crystalline phase of Mn_3O_4 when prepared at $160\,^{o}C$ in **Figure 4-6**.
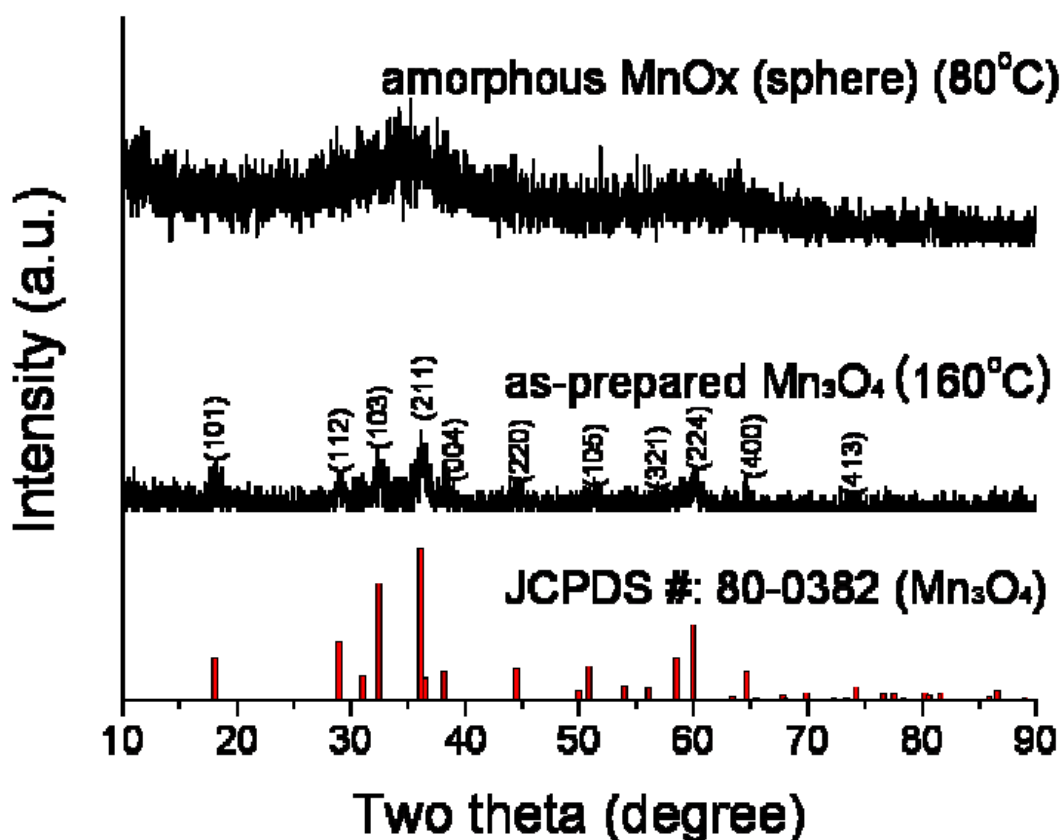
Figure 4-6. X-ray diffraction patterns of amorphous MnOx particles synthesized at 80°C and asprepared Mn_3O_4 at 160°C with the reference Mn_3O_4 diffraction pattern (JCPDS #: 80-0382).

The linear sweep voltammograms (**Figure 4-5a and b)** show that the onset potentials of the two samples are very similar, but the limiting current of the a-MnOx (prepared at 80°C) is higher than that of the Mn_3O_4 sample (prepared at 160°C). Because there is little difference in onset potential, the two samples have similar intrinsic ORR catalytic activity. Therefore, the improved limiting current of the a-MnOx sample may be attributed to the increased surface area or more adsorption sites for oxygen molecules. Brunaer, Emmet and Taller (BET) surface areas of the a-MnOx (80°C) and the Mn_3O_4 (160°C) are 273.5 and 97.8m²/g, respectively. Furthermore, although the limiting current for the pristine KB is similar to that for the a-MnOx, the onset potential of the KB is slightly more positive than that of the a-MnOx, implying that the intrinsic catalytic activity of the pristine KB is higher than that of the a-MnOx. Further, electrical conductivity of the MnOx may significantly impact the utilization of the ORR catalysts.

For the case of the a-MnOx NWs on KB, surprisingly, the onset potential was shifted to a more positive direction and the limiting current was increased considerably, demonstrating that the ORR activity of this composite is far better than those of the pristine KB and the two MnOx samples (**Figure 4-5a)** in a weak basic solution (0.1M KOH). Although electrical conductivity is another factor

affecting ORR activity, carbon materials itself has an insufficient to reduce oxygen effectively. Therefore, it clearly indicates that amorphous manganese oxides NWs in this composite facilitate ORR significantly.

However, the ORR activity of the *a*-MnOx NWs on KB composite appears to be less than that of a platinum based catalyst: 20 wt% Pt on Vulcan XC-72. Although the BET surface area of the a-MnOx NWs on KB is 637 m^2/g, the surface area alone cannot account for the improved ORR activity. Further, it is impossible that ideal comparison of our composite with just physical mixture composed of ketjenblack and MnOx NWs because MnOx NWs cannot be synthesized without ketjenblack carbon. It appears that significantly enhanced performance for ORR results from the unique nanowire morphology and microscopic features (e.g., high density of surface defects). Therefore, these reasons may play some role in enhancing the electrochemical performance by offering more active sites for adsorption of oxygen molecules.[68e] In other words, both electronic and geometric factor of catalysts can affect ORR catalytic activity. With an assumption that the bond strength between Mn metal and oxygen molecule is almost same as that in other previous literatures using MnOx because we use pure Mn metal oxides, not metal alloy, it is more reasonable to focus geometric factor of amorphous MnOx nanowires to elucidate enhanced ORR activity. Based on simple molecular orbital (MO) theory, s and p orbital of oxygen molecule should overlap with d-orbital of Mn metal to break O=O and these requirements has been illustrated with three possible configuration of oxygen molecule interaction with a metal in a complex such as Griffith, Pauling, Yeager's model[60c] in **Figure 4-7.**
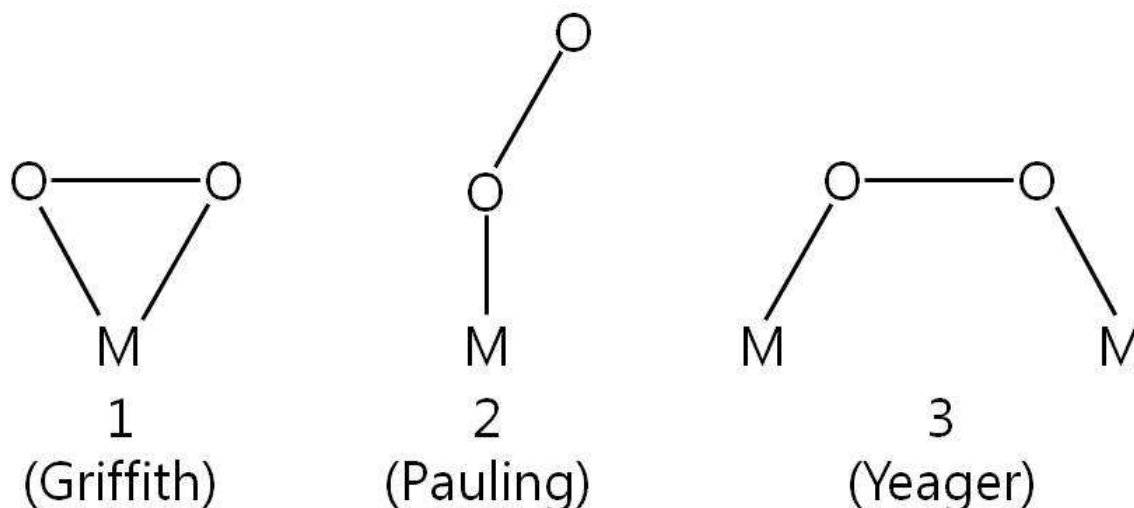
Figure 4-7. Possible configuration of oxygen molecule interaction with a metal: 1) Griffith, 2) Pauling, and 3) Yeager's model.

Therefore, how to bind effectively depends on physical surface structure of Mn oxides and thus amorphous MnOx NWs structure has less selectivity to certain one model mention above unlike other crystalline MnOx. It follows that we believe that amorphous MnOx NWs structures has more favorable in ORR, resulting in enhanced performance for ORR based on geometric factor of this composite and we hope that our suggestion in improved activity will be illuminated with time-resolved BB-SFG (Broad band sum frequency generation) spectroscopy and other advanced spectroscopic tool by tracking newly formed or broken bond and bond strength of oxygen within femto or nano second time scale during ORR.

It is noted, however, that the RDE (half-cell) measurements for ORR catalysts are insufficient in predicting the performance of this composite in a practical zinc-air battery because the typical electrolyte concentration for the RDE measurements (0.1 M KOH) was much lower than that usually used in full-cell measurements (6 M KOH). For example, oxygen solubility in 0.1M KOH is about 10 times higher than that in 6M KOH, which could considerably amplify the difference in ORR activity of the a-MnOx NWs on KB and 20% Pt on Vulcan XC-72 under our RDE experimental condition (0.1M KOH).[129] Therefore, it is necessary to characterize their ORR activity under the conditions similar to those for a practical zinc-air full cell using 6M KOH electrolyte, as schematically shown in **Figure 4-8a.**
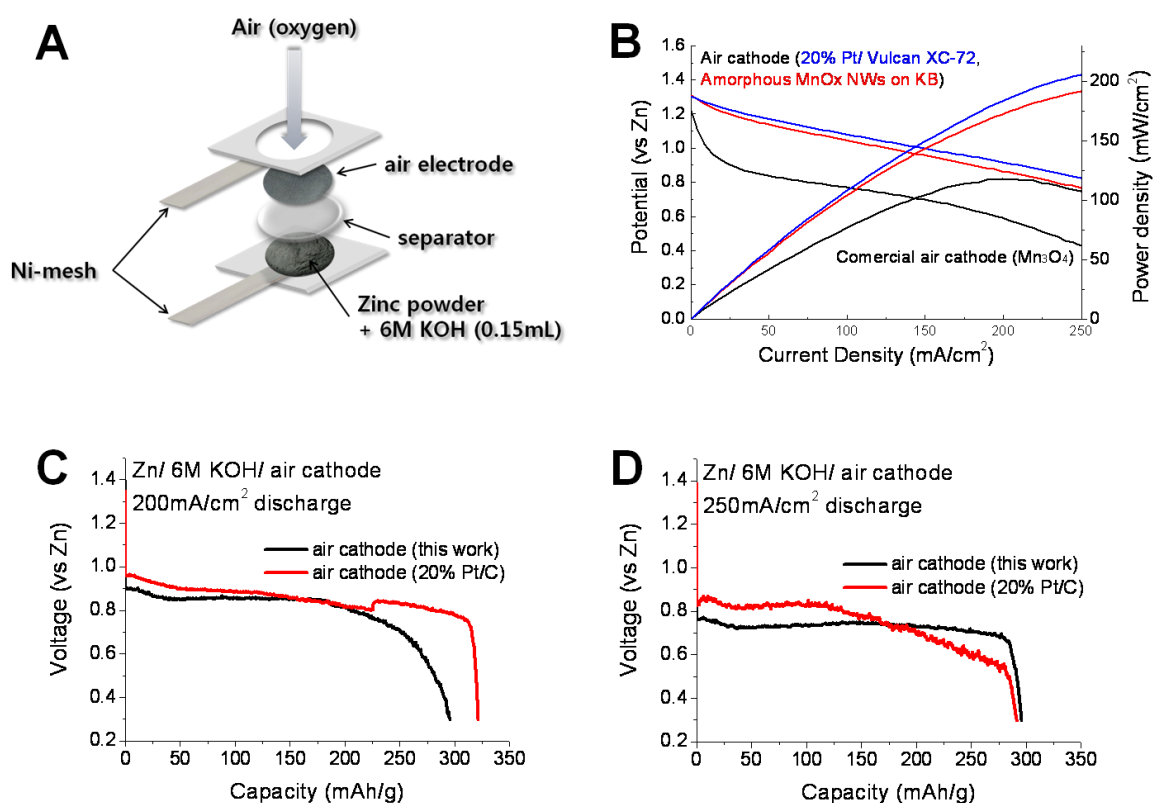
Figure 4-8. (a) A schematic of a zinc-air battery, (b) polarization and (c, d) discharge curve at 200 and 250 mA/cm^2, respectively, of zinc-air full cells with different air electrodes: amorphous MnOx nanowires on ketjenblack composites and 20% Pt on Vulcan XC-72 (E-tek). A commercial air electrode (Meet) was used for comparison.

The zinc-air battery composed of an air electrode, a separator, and a zinc anode. **Figure 4-8b** shows that a peak power density of ~ 190mW/cm^2 was obtained from a cell based on an air cathode of a-MnOx NWs on KB composite; the performance is much better than those obtained from cells based on a commercial air electrode with Mn_3O_4 catalysts (Meet Co.). Because the only difference between the test cells was the air electrode used in each zinc-air full cell assembly, the difference in overall electrochemical performance can be attributed to the difference in ORR activity of the air electrodes. The ORR activity of the a-MnOx NWs on KB composite electrode is very similar to that of a 20% Pt on Vulcan carbon XC-72.

In addition to enhanced power density, the activation loss of the a-MnOx NWs on KB was also significantly reduced compared to that of the commercial electrode with crystalline Mn_3O_4, as seen from the *i-v* curves. This result is also consistent with the RDE half-cell results (**Figure 4-5**). **Figure 4-8c and d** show some typical galvanic discharge curves of a zinc-air full cell at 200 and 250 mA/cm^2, respectively. These discharging current densities are much higher than those reported in the literature for practical Zn-air cells (e.g., 10 to 20 mA/cm^2).[75a]

The electrochemical performance of the as-prepared a-MnOx NWs on KB sample is very competitive to the commercial 20% Pt on Vulcan XC-72 catalysts under even higher current densities, which is also consistent with the *i-v* curves shown in Figure 3(b). However, the capacity of the Zn-air cell (typically normalized by the weight of zinc) decreased with   discharging rate (and lower than theoretical value of 820 mAh/g) due to the formation of insulating ZnO on pristine Zn particles at high discharging current densities.

Amorphous manganese oxide (MnOx) nanowires grown on commercial ketjenblack (KB) of high electrical conductivity and surface area display significantly enhanced catalytic activity toward oxygen reduction reaction in alkaline solutions. A Zn-Air battery based on a-MnOx on KB air cathode demonstrated a peak power density of ~190mW/cm^2, which is similar to the best performance of cells based on very expensive Pt catalysts (20% Pt/Vulcan carbon). Both the KB and the a-MnOx nanowires contributed to the improved catalytic activity for ORR. Especially, it appears that that amorphous MnOx NWs structures has more favorable in ORR, resulting in enhanced performance for ORR based on geometric factor of this composite and they can be a very promising electrode for ORR in alkaline solutions.

Experimental Section

Preparation of amorphous manganese oxide nanowires on ketenblack composites (a-MnOx NWs/KB)

0.28g of Ketjenblack (EC-300J) was dispersed in 20 mL of ethylene glycol (Sigma Aldrich), which was stirred vigorously with a magnetic bar and then 0.2mL of 0.5M NaOH (Samchun chemical) and 0.094mmol of KMnO4 (Sigma Aldrich) was added to this black suspension. This round bottom flaks was transferred to reflux condenser and heating up to 80oC and sustained for 2hr. The black powder was filtered and washed with distilled water and ethanol and dried at 60oC for 12hr. For comparison, amorphous MnOx was also prepared using the same procedure but without the addition of Ketjenblack.

Material characterization

The material morphology was examined using an SEM (Nanonova 230, FEI) operating at 10 kV and TEM (JEOL JEM-2100F) operating at 200 kV. Powder analysis was performed using an X-ray diffractometer (XRD) (D/Max2000, Rigaku).

Preparation of catalysts paste for rotating disk electrode

Catalyst paste was prepared by ultrasonically mixing 6.0 mg of as-prepared sample with 3.0 mL of pure deionized water for 1 h in order to make homogeneous suspension. Then, 3 μL of the prepared

catalytic paste was transferred to surface of glassy carbon electrode of 3 mm diameter using a micropipette. Finally, the ink was dried for 10 min under vacuum at room temperature to form a thin catalyst film on glassy carbon electrode as a working electrode.

Rotating disk electrode (RDE) experiments

All half cell experiment for ORR using rotating disk electrode (RDE) (ALS Co., Ltd) were carried out under the same conditions where Pt wire and Hg/HgO were used as a counter and reference electrode, respectively; 0.10 M KOH was used as an electrolyte; pure oxygen gas (99.9%) was purged for 30 min before each RDE experiment to make the electrolyte saturated with oxygen. Electrochemical characterization of as-prepared catalysts were conducted using single potentiostat (Ivium) with scan rate of 10 mV/sec and potential range from 0.15 V to -0.7 V.

Preparation of air electrode

All air electrodes used in this zinc-air full cell test were prepared with a fixed composition (in weight); activated carbon (Darco G-60A, Sigma Aldrich) was 62 wt.% + poly-tetrafluoroethylene (PTFE) binder 30 wt.% (60 wt.% PTFE emulsion in water, Sigma Aldrich) + as-prepared catalysts was 8 wt.%. After sonicating each material in pure DI-water for 1h, each suspension was then mixed ultrasonically for 1 h to form a homogeneous suspension. Excess water was removed by filtering the homogeneous suspension and then the slurry was dried at 60 ^{o}C. By adding isopropyl alcohol to dried black powder, air electrodes were manufactured via a kneading and rolling process to make the desired thickness of air cathode. Finally, Ni- foam as a current collector was attached to the back side of the air electrode. The thickness of all air cathodes was 600 μm to minimize thickness factor of electrode to overall cell performance.

Zinc-air full cell assembly

For the Zinc-air full cell test, homemade zinc-air single cell were used in this experiments. 1 g of zinc powder (Umicore) was used as the anode electrode. Nylon net filters (Millipore) were used as separators. A 16–pi Air electrode was used as the cathode electrode. The galvanodynamic experiment was carried out with multichannel potentiostat (WBCS 3000, WonA Tech, Korea) with current densities varied from 0 to 250 mA/cm^2 to characterize cell performance. The galvano discharge curves of zinc-air cells were recorded at 200 and 250mA/cm^2, respectively.

Chapter 5. A Highly Efficient Electrocatalyst for Oxygen Reduction Reaction: N-doped Ketjenblack Incorporated into Fe/Fe$_3$C Functionalized Melamine Foam[4]

The performance and operational life of metal-air batteries and fuel cells are often limited by the kinetics of oxygen reduction reactions (ORR) on the cathodes. While catalysts based on platinum and other precious metals are quite effective in facilitating the rate of ORR, their high cost and scarcity make them less competitive economically for broader commercialization, more so for higher power applications (due to lower efficiency and instability at higher discharge current densities). To overcome this problem, cost-effective catalysts must be developed that offer not only high catalytic activity but also unique architecture vital to high rate capability. Here we report a highly efficient, air-breathing electrode architecture derived from commercially available melamine foam and ketjenblack, inspired by the tetrapod structure of a breakwater. The nitrogen-doped ketjenblack (produced during pyrolysis) contributed significantly to the enhanced catalytic activity while the highly porous skeleton of melamine foam allowing dramatically increased mass transport of electroactive species to or away from the active sites. These unique air-breathing electrodes are a promising alternative for a new generation of low-cost and high-performance metal-air batteries and fuel cells.

Polarization due to oxygen reduction reaction (ORR) on the cathodes still contributes significantly to the energy efficiency loss of metal-air batteries and fuel cells.[1, 108, 130] Thus, how to increase the ORR kinetics while maintaining fast mass transfer represents a grand challenge in the development of a new generation of metal-air batteries and fuel cells. Catalysts based on platinum and other precious metals are found very effective in facilitating the rate of ORR in batteries and fuel cells [84b, 109, 124b, 131]. However, their high cost and low stability have hindered their practical applications in air breathing electrodes. Accordingly, much attention has been devoted to the development of non-precious metal or metal-free catalysts with desired catalytic activity[66, 125, 132]. For example, Jasinski and co-workers reported that metal/nitrogen/carbon- (M/N/C-) catalysts have high catalytic activity for ORR[98, 100]. These composite materials were synthesized by pyrolyzing proper precursors with nitrogen, carbon, and abundant transition metals such as iron and cobalt. While the superior catalytic activity for ORR are demonstrated[133], there is still debate on active sites for ORR of N-M-C catalysts

and their performance seems to be limited by mass transfer through the porous catalysts [134]. Further, the carbon-nitrogen precursors may be too expensive for commercial applications.

In addition to high catalytic activity and sufficient electronic conductivity, an efficient electrode architecture must allow fast transfer of other reactants (such as oxygen molecules) to and the reaction products (such as hydroxide ions) away from the catalytically active sites for ORR to minimize electrode polarization. To dramatically enhance mass transfer through porous oxygen-breathing electrodes, we have created some unique electrode architectures, similar to some breakwater seen at a coast composed of highly porous tetrapod structures (**Figure 5-1a**).
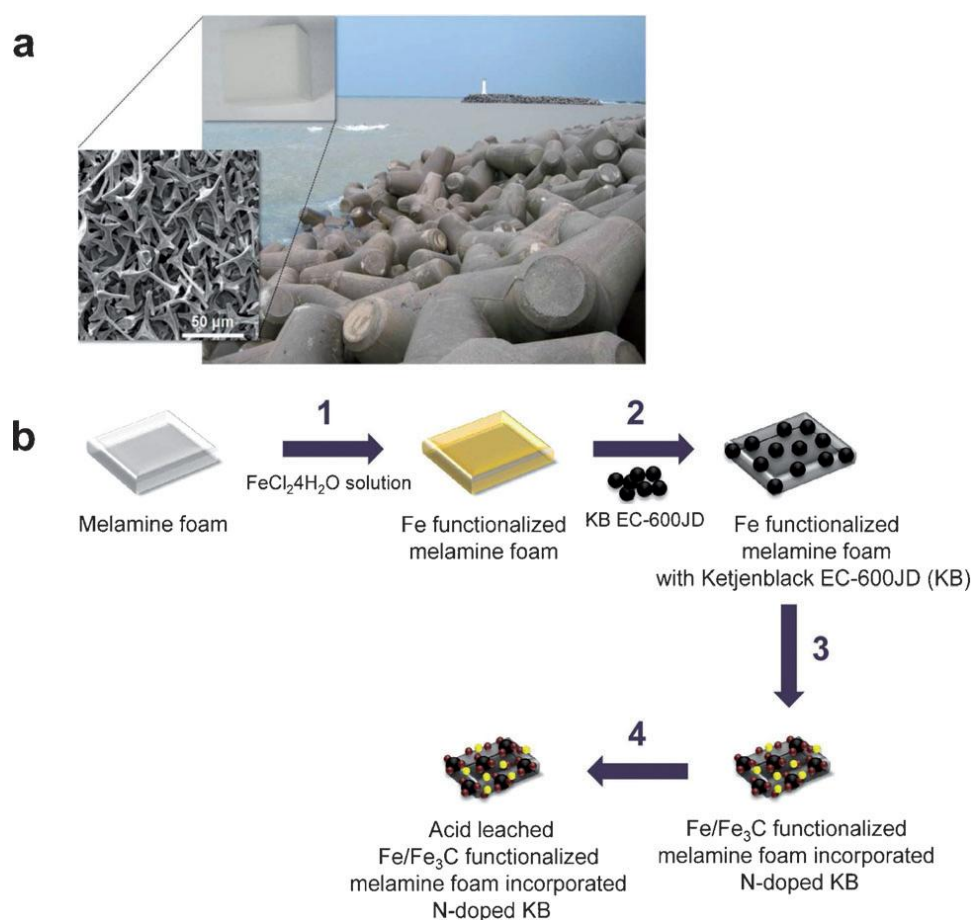
Figure 5-1. (a) Architectural features of tetrapod structures to minimize damage caused by a tsunami at a coast, commercially available melamine foam (inset), and an cross-sectional view (SEM image) of a fractured melamine foam after pyrolysis at 800°C in Ar for 2hr. It is noted that the interconnected large pores may facilitate fast mass transport. (b) Schematic scheme for the synthesis of Fe/Fe$_3$C functionalized melamine foam infiltrated with N-doped ketjenblack (KB). (1) Melamine foam was soaked with FeCl$_2$4H$_2$O solution. (2) Adding Ketjenblack EC-600JD and dry. (3) Heat treatment in Ar atmosphere for 2 hours at 800, 900, and 1000°C. (4) Acid leaching with 2M H$_2$SO$_4$.

To mimic this structure, we started with a commercially available melamine foam, formaldehyde-melamine-sodium bisulfite copolymer, which has been widely used for thermal insulation, sound absorption, and fire containment.[135] After pyrolysis, the open cell network structure of the carbonized melamine foam (**Figure 5-2**) becomes very fragile, easily broken to pieces by grinding with a mortar.
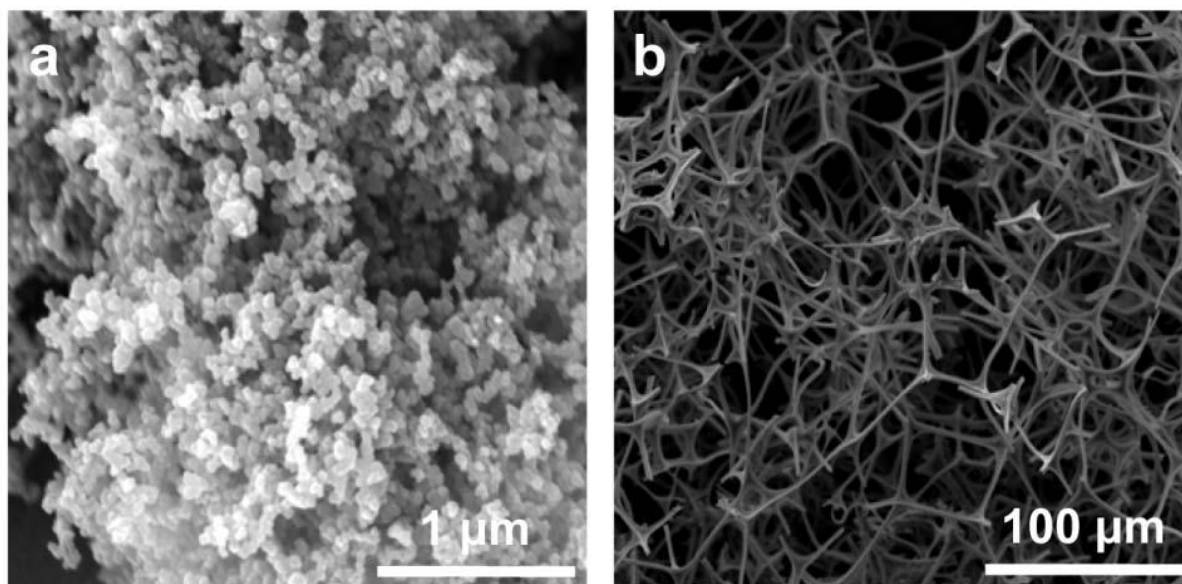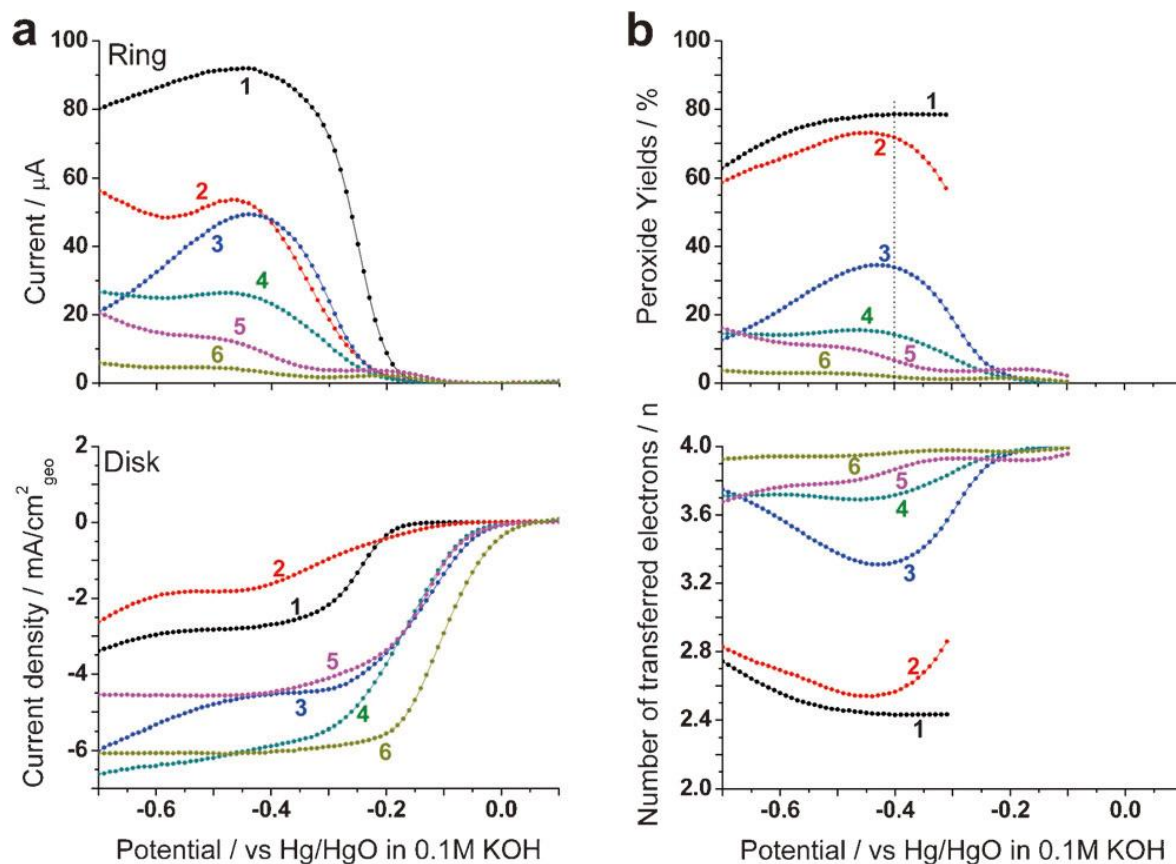

Figure 5-2. SEM images of (A) commercial ketjenblack carbon and (B) melamine foam pyrolyzed at 800°C under Argon.

Interestingly, the broken pieces appear similar to the tetrapod architecture (**Figure 5-1a**). In fact, our unique electrodes consist of carbonized melamine foam and nano-sized ketjenblack, offering high specific surface area, large number of active sites, and large amount of pore volume for fast mass transport. Although Lin et al. used melamine resin to prepare metal-free N-doped electrocatalysts for ORR[136], the unique architecture of carbonized melamine foam has not yet been used in synthesizing electrocatalysts for ORR.

We used commercially available melamine foam and ketjenblack carbon as precursor materials for synthesis of the catalysts. First, the interior surface of a porous melamine foam was infiltrated with a iron precursor solution for better catalytic activity. Then, commercially available ketjenblack carbon particles were infiltrated into the melamine foam using a liquid suspension. Third, the iron functionalized melamine foam with ketjenblack was fired at different temperatures in an inert atmosphere. Finally, the samples were leached with an acid to remove unstable and undesirable species and phases (**Figure 5-1b**).

Rotating ring-disk electrode (RRDE) experiments were used to characterize the electrocatalytic activity of the as-prepared Fe/Fe₃C-melamine/N-KB (Ar-800) (hereafter denoted as Ar-800 for brevity) (**Figure 5-3a**).

Figure 5-3. (a) Steady-state RRDE experiments of (1) ketjenblack EC-600JD, (2) carbonized melamine foam, (3) Fe/Fe₃C-melamine+ KB mixture, (4) Fe/Fe₃C-melamine/N-KB composite catalyst, (5) 9.55μg$_{Pt}$/cm², and (6) 28.6μg$_{Pt}$/cm², respectively, in O₂ saturated 0.1M KOH at 2000rpm. Non-precious metal catalysts loading are 0.286mg$_{cat}$/cm² and the Fe/Fe₃C-melamine was prepared at 800°C under Ar (denoted as Ar-800). Ring current (top) and disk (bottom) current density were separated for convenience. (b) Peroxide yields (%) (top) and the number of transferred electrons (n) (bottom) of as-prepared samples.

First, the carbonized melamine foam showed higher positive onset potential, but much lower limiting current density than pure ketjenblack EC-600JD (KB). This result clearly indicates the importance of C-N group on increased activity for ORR. However, carbonized melamine foam itself is ineffective because of very low surface area[137]. To confirm nitrogen doping effect on activity for ORR, we carefully separated N-doped carbon from the Ar-800 sample and performed XPS analysis. N1s peaks

confirmed that nitrogen was doped on KB, which had more positive onset potential and much higher current density than ketjenblack in **Figure 5-4**.
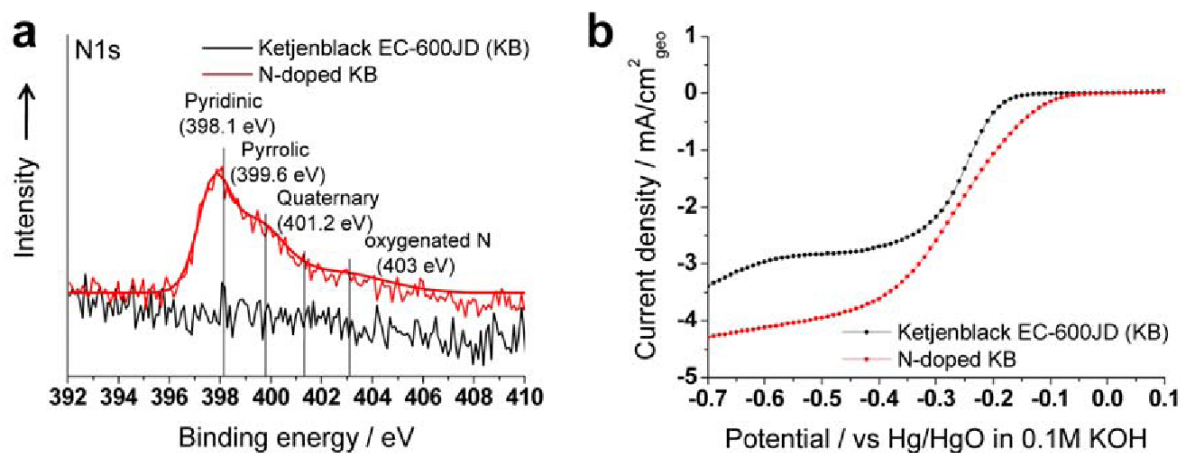
Figure 5-4. A) XPS high resolution N 1s and (B) Steady-state LSV curve of Ketjenblack EC-600JD (KB) and N-doped KB, in O_2 saturated 0.1M KOH at 2000rpm. The catalyst loading was $0.286mg_{cat}/cm^2$.

Apparently, the large active surface area from ketjenblack enhanced limiting current density. In the case of Ar-800, dramatic shift to positive direction of its onset potential and much higher limiting current density were observed. To confirm this synergic effect between iron carbide functionalized melamine foam and N-doped ketjenblack, we further examined two different samples, a composite electrode and an electrode consisting of physical mixture of the two phases. Although the two electrode samples had very similar onset potentials, the composite electrode had much higher current density than the one of physical mixture. Also, different current shapes were clearly observed around -0.4V for the two samples. The physical mixture had limiting current density from -0.3V to -0.45V and a further increase in current density beyond -0.45V, unlike that for the composite electrode. This means that the physical mixture had inferior performance to that of the composite sample and this flat current region is very similar to that for the pure Ketjenblack. Therefore, the flat limiting current at medium potential is attributed to the physical portion of ketjenblack in this mixture sample. With these results, it is reasonable to conclude that there are two types of active sites: the iron carbide functionalized melamine skeleton and the attached nitrogen doped ketjenblack. Proper combination of the two, as seen in the composite electrode, has a significant synergic effect on enhancing ORR activity.

To our pleasant surprise, the current density of the as-prepared sample are even slightly higher than that for Pt/C catalysts at high overpotentials, implying that the electrode architecture of

our as-prepared sample is more effective in facilitating oxygen transport to the active sites for ORR than the Pt/C catalysts under the testing conditions in **Table 5-1**.

Table 5-1. Summary of electrochemical performace for Ar-800 and Pt/C catalysts. (Data taken from Fig. 5-3a)

Catalyst	Potential at 0.1mA/cm^2 (V vs. Hg/HgO)	Current density at -0.45V (mA/cm^2)
Ketjenblack	-0.17	-1.793
Carbonized melamine foam	-0.11	-2.79
Fe/Fe$_3$C-melamine + KB mix.	-0.01	-4.62
Fe/Fe$_3$C-melamine/N-KB	-0.02	-6.03
9.55µg$_{Pt}$/cm^2	-0.01	-4.55
19.1µg$_{Pt}$/cm^2	0.025	-5.65
28.6µg$_{Pt}$/cm^2	0.035	-6.06

Further, the superior catalytic activity of the composite (Ar-800) over that of the physical mixture sample was also confirmed by the H_2O_2 yields and the number of electrons (n) transferred in the electrode reaction, as determined from the linear polarization curves (**Fig. 5-3b**). In particular, the number of electrons transferred is determined to vary from ~3.7 to ~3.85 (very close to 4) for our best catalysts (Ar-800), suggesting that it is an efficient 4-electron transfer pathway with peroxide yield of ~15% at -0.4V. These results indicate that the composite samples are very promising electrocatalysts for ORR in an alkaline solution, demonstrating highly competitive performance but at a much lower cost than the benchmarked Pt/C catalysts.

For practical applications, resistance to methanol crossover effect and durability of the catalysts are important considerations as well. The chronoamperometric response of the Ar-800 sample recovered quickly, about 150 s after methanol injection (**Figure 5-5a),** meaning that the catalyst was not influenced by methanol crossover.
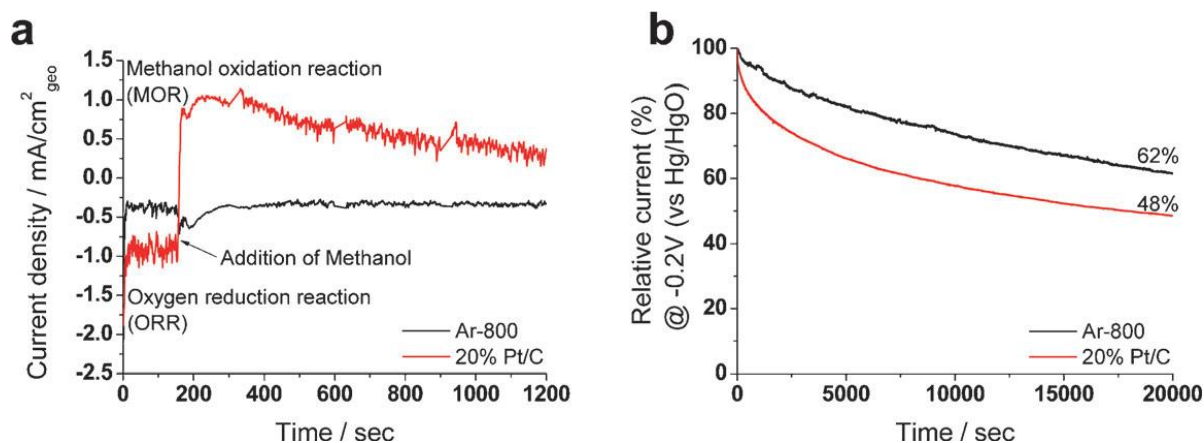
Figure 5-5. (a) chronoamperometric response with 10% (W/W) methanol (b) chronoamperometric response of Fe/Fe$_3$C-melamine/N-KB (Ar-800) and 20% Pt/C in O$_2$-saturated 0.1M KOH solution at -0.2V (vs Hg/HgO) and 1600 rpm. 10% (W/W). Methanol was injected into electrolyte at 150 sec and both catalysts loading density were 85μg/cm^2. Before both tests, linear sweep voltammetry was performed in the voltage range from 0.15V to -0.7V (vs Hg/HgO) for 4 times under the same above conditions. Data of (A) was constructed by adding each cycle data. 1 cycle was maintained for 300 sec and 4 cycles were tested under the same conditions.

In contrast, the chronoamperometric response of the Pt/C catalyst changed dramatically after methanol injection (**Fig. 5-5a**), suggesting that methanol oxidation reaction (MOR) initiated since the sign of current was changed from negative for ORR to positive for MOR. It clearly demonstrated that our catalyst has superior tolerance against methanol crossover effect. Further, the time-dependence data of performance suggested that the Ar-800 catalyst degraded in a slower rate than the Pt/C catalysts (**Fig. 5-5b**). This result implies that our catalysts are promising candidates for direct methanol and alkaline fuel cells as well. The stability and durability under real conditions of fuel cells and batteries may be further enhanced.

We also constructed Zn-air full cells using our catalysts and the Pt/C catalysts. Performance evaluation of these cells (**Figure 5-6a**) indicates that, at low current densities, there is a gap in power output between Ar-800 and Pt/C catalysts, consistent with the observations with the half cells discussed earlier. At higher current densities, however, the voltage of our catalysts became higher than that of the cell with Pt/C catalysts; the corresponding peak power density of the cell with our catalyst was ~200mW/cm^2, which is slightly higher than ~195mW/cm^2 for the cell with the Pt/C catalyst. These measurements are consistent with the RRDE results (**Fig. 5-3a**), suggesting that our catalysts have unique porous architecture for rapid mass and charge transfer.
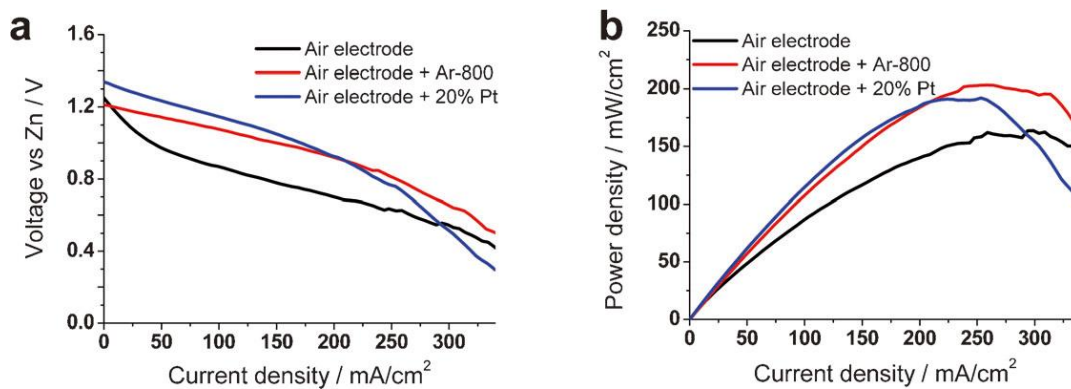
Figure 5-6. (a) Current-voltage and (b) power-voltage curves of Zn-air cells with as-prepared composite Fe/Fe$_3$C-melamine/N-KB (Ar-800) and 20% Pt/C catalysts. Gad diffusion layer without any catalysts was used as the baseline air-electrode for comparison. Catalysts loading density of Fe/Fe$_3$C-melamine/N-KB (Ar-800) and 20% Pt/C were 0.212mg$_{cat}$/cm^2 and 28.2μg$_{Pt}$/cm^2 (0.141mg$_{cat}$/cm^2), respectively.

To correlate the high performance with the microscopic features of the as-prepared samples, we examined the crystalline phases of Ar-800 using XRD analyses (**Fig. 5-7a),** which indicate that metallic Fe, Fe$_3$C, and graphitic carbon co-existed, according to diffraction data for α-Fe (JCPDS, NO. 87-0722) and Fe$_3$C crystalline species (JCPDS, NO. 89-2867)[134, 138].
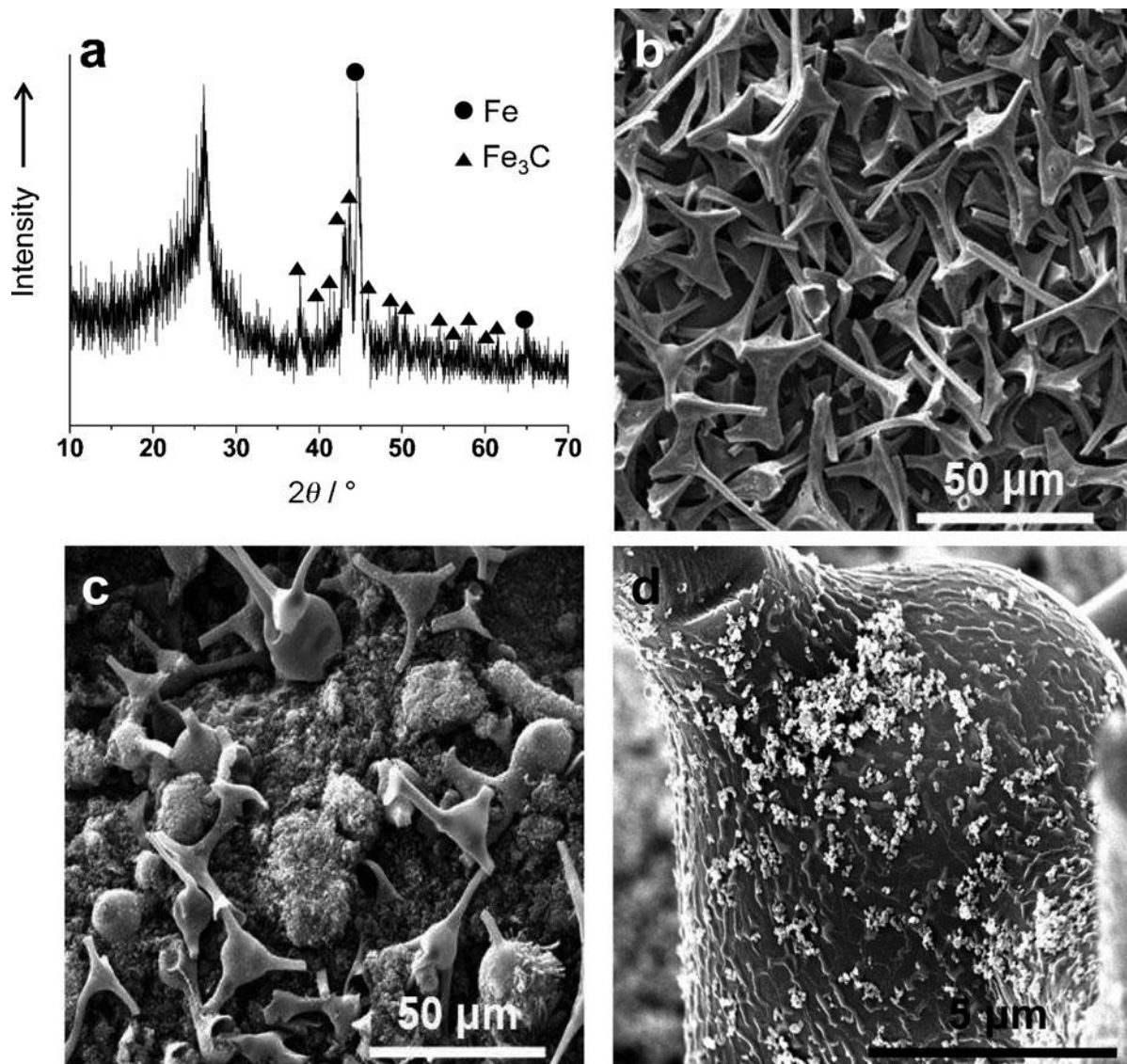
Figure 5-7. (a) X-ray diffraction patterns of a Fe/Fe$_3$C-melamine/N-KB (Ar-800) sample. (b) an SEM image of ground melamine foam structures after carbonization, (c) an SEM image of Fe/Fe$_3$C-melamine/N-KB (Ar-800) sample, and (d) a higher magnification of the image of (c).

Other samples heat treated at 900 and 1000°C for 2 hours also showed same diffraction patterns in **Figure 5-8**.
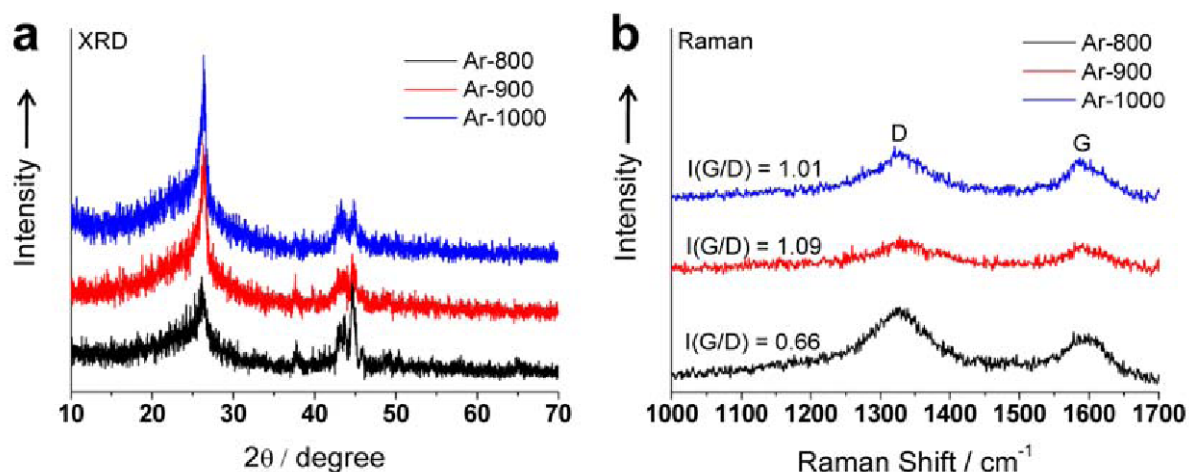
Figure 5-8. A) X-ray diffraction patterns and (B) Raman spectra of the composite Fe/Fe_3C-melamine/N-KB samples paralyzed at different temperatures (Ar-800, 900, and 1000^oC).

However, the intensities of the peaks related to iron species were low due to low iron content (~3.30wt. %) in the Ar-800 sample. Further, energy-dispersive X-ray spectroscopy (EDS) was used to analyze the elemental composition of the Ar-800 sample, which indicates that the sample was composed of 75.1 wt. % carbon, 14.2 wt. % nitrogen, 4.99 wt. % oxygen, 3.30 wt. % iron, and 2.30 wt. % sulfur, respectively in **Figure 5-9**.
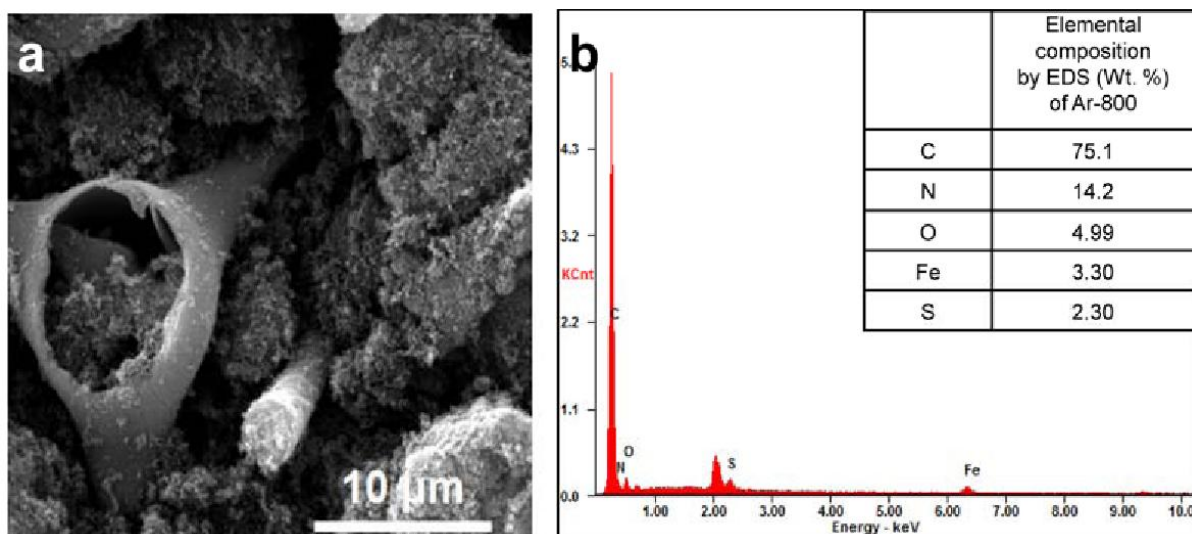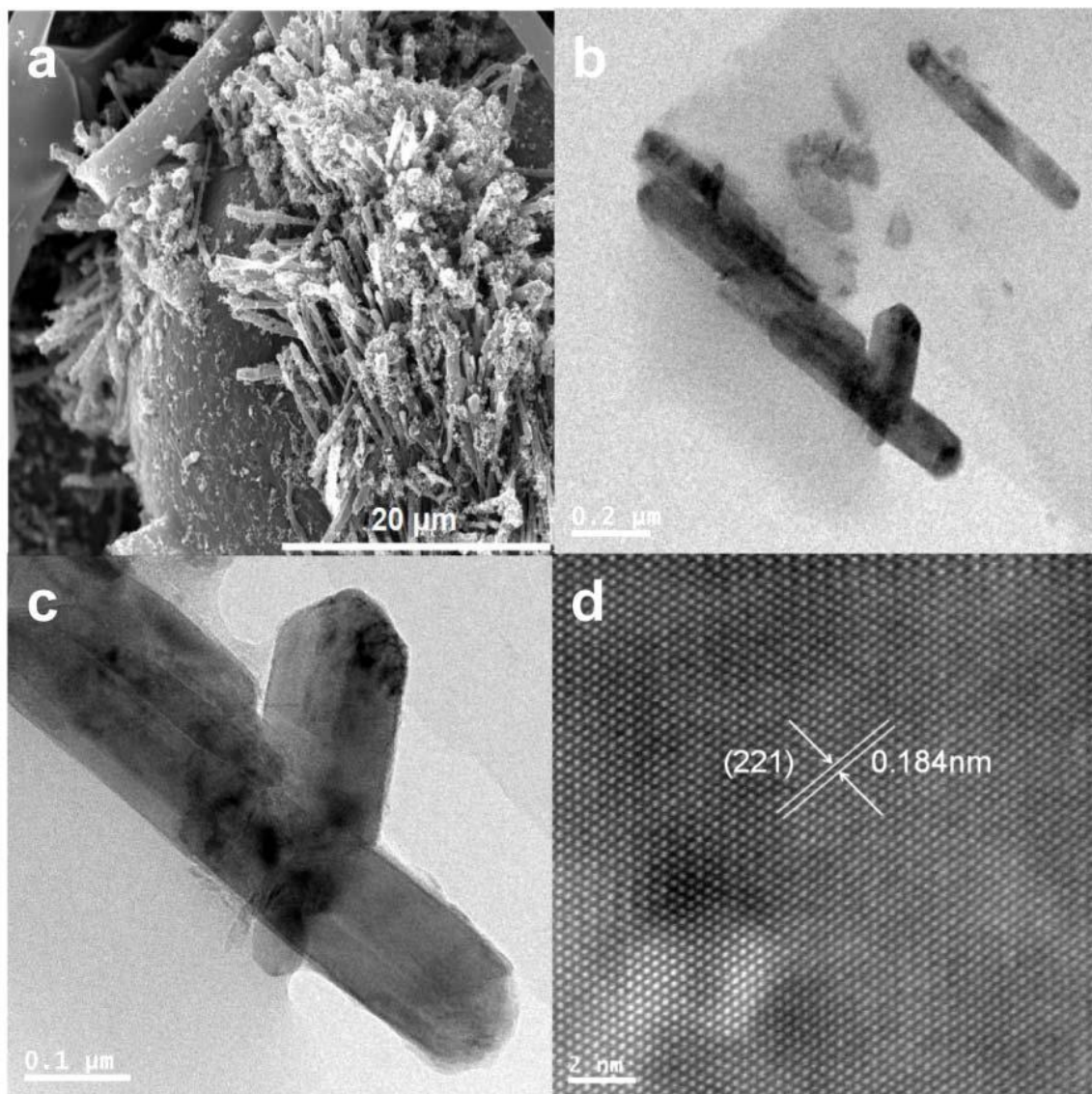
Figure 5-9. (A) A typical SEM image of a composite Fe/Fe3C-melamine/N-KB (Ar-800) and (B) the corresponding Energy-dispersive X-ray spectrum (EDS) (Fe peaks at about 0.71 and 6.39 KeV). Further, in energy-dispersive X-ray spectroscopy (EDS), the Ar-800 sample was composed of 75.1 wt. % carbon, 14.2 wt. % nitrogen, 4.99 wt. % oxygen, 3.30 wt. % iron, and 2.30 wt. % sulfur, respectively. The sulfur was originated from bisulfite group of the commercial melamine foam, formaldehyde-melamine-sodium bisulfite copolymer.

The sulfur was originated from bisulfite group of the commercial melamine foam.

The morphological features of the as-prepared sample (Ar-800), as characterized using a scanning electron microscope (SEM) under low magnifications, are similar to those of the melamine foam (**Fig. 5-7c**). Under higher magnifications (**Fig. 5-7d**), however, it becomes visible that the ketjenblack carbon is firmly and evenly attached onto the melamine foam surface (like moss grown there), creating high surface area and a large number of active sites for ORR within a highly porous architecture of melamine foam for fast mass transport. The nanorods have a diameter of about 100 nm with a length of around 0.6 to 1 mm. The well defined crystalline phase has a lattice fringe with d spacing of 0.184 nm, which is consistent with the (221) plane of Fe_3C in **Figure 5-10**.

Figure 5-10. A) A magnified SEM image of a composite Fe/Fe₃C-melamine/N-KB (Ar-800), (B) Typical TEM image of Ar-800, (C) a magnified TEM image of (B), and (D) corresponding HR-TEM image of Ar-800.

To examine the effect of pyrolysis temperature on catalytic activity for ORR, the samples were pyrolyzed under Ar atmosphere at 800, 900, and 1000°C. Linear sweep voltammetry curves (**Figure 5-11a**) for the three samples (Ar-800, 900, and 1000) indicate that Ar-800 had more positive onset potential and higher current density than the other two samples pyrolyzed at higher temperatures. In fact, the onset potential and current density for the Ar-800 electrode are comparable to those for the Pt/C catalyst with Pt loading of $19.1 \mu g_{Pt}/cm^2$ in the kinetic-controlled region. To gain more insight into the surface properties of the catalysts, we performed XPS analysis of the samples. High resolution XPS spectra suggest that, with increasing pyrolysis temperature, pyridinic moiety decreased (**Fig. 5-11b**) but quaternary N increased (in magnified N 1s peak, **Fig. 5-11c**). Thus, proper

combination of pyridinic N and pyrrolic N could be a key factor affecting the enhanced catalytic activity for ORR. This conclusion seems to contradict a previous report that graphite-like nitrogen atoms are more important in metal-free catalysts[139]. In our case, the iron precursor may be easily bounded to (and stabilized with) the nitrogen atom with lone pair electrons for further growth of Fe/Fe$_3$C particles. Therefore, our conclusion seems to be reasonable. On the other hand, sulfur was not affected by the heat treatment temperature (**Fig. 5-11d),** implying that sulfur may not significantly affect the catalytic activity for ORR.
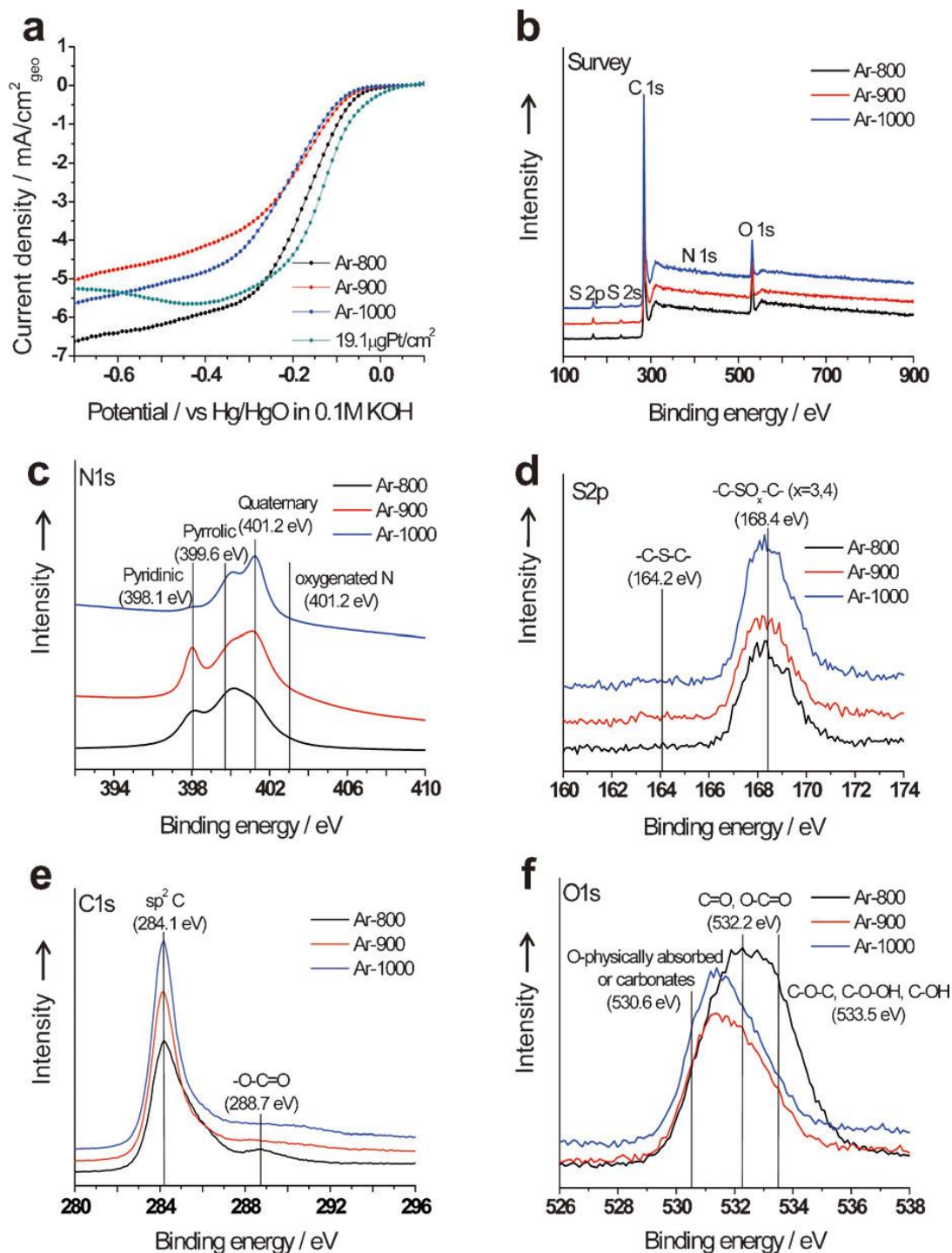
Figure 5-11. Dependence of ORR activity on pyrolysis temperature and chemical composition of the composite Fe/Fe$_3$C-melamine/N-KB ORR catalyst. (a) Steady-state LSV curves of composite Fe/Fe$_3$C-melamine/N-KB samples pyrolyzed at different temperatures: 800°C (Ar-800), 900°C (Ar-900), and 1000°C (Ar-1000), as compared to that for19.1μg$_{Pt}$/cm^2 catalyst, tested in O$_2$ saturated 0.1M KOH at 2000 rpm. Non-precious metal catalysts loading are 0.286mg$_{cat}$/cm^2. (b) XPS survey and high resolution (c) N 1s, (d) S 2p, (e) C 1s, and (f) O 1s spectra, respectively, of as-prepared samples.

One possible explanation is that sulfur exists as bisulfite in pristine melamine structure, not in the C-N skeleton of melamine. XPS data support our hypothesis. Sulfur does not exist as -C-S-C-, but as -C-SO$_x$-C-[97d, 140]. In this oxide moiety, sulfur would have little influence on the electronic structure of carbon plane directly, unlike the sulfur atom in –C-S-C. Thus, it is unlikely that sulfur doping may enhance ORR activity in our samples through some effect on electronic structures[97d]. However, it is worthy to note that the -C-SO$_x$-C- moiety may increase the hydrophilicity of carbon plane so that more electrolyte (together with dissolved oxygen) may gain easily access to the catalytic active sites. Meanwhile, oxygen gas may move along hydrophobic moiety. Therefore, proper combination of hydrophobic and hydrophilic property in catalyst design is vital to facilitating fast transport of reactants for ORR. Another origin of hydrophilicity is supported by C 1s and O 1s spectra. For the C 1s spectra, as expected, center peak of sp^2 C around 284.1 eV becomes more symmetric as heating temperature increase, implying that the degree of graphitization of the as-prepared samples increased with temperature (**Fig. 5-11e**). This result is also supported by XRD and Raman data. Obviously, graphitization could affect catalytic activity for ORR due to increased electrical conductivity and improved hydrophobicity. Further, the –O-C=O group was still present in Ar-800, which may increase the hydrophilicity of the sample and its affinity to aqueous electrolyte (as confirmed by O 1s of XPS). Clearly, the population of hydrophilic groups (e.g. C=O, and C-OH) decreased with synthetic temperature (**Fig. 5-11f**).

XPS analysis of the iron species was less successful; it was almost impossible to determine the exact oxidation state of Fe (Fe 2p, 702-740 eV) due to very week signal intensity (**Fig. 5-11b and Table 5-2**)[141].

Table 5-2. Elemental composition of the surface of the as-prepared samples examined by XPS.

Sample	Elemental composition by XPS (At. %)				
	C 1s	N 1s	O 1s	S 2p	Fe 2p
Ar-800	83.19	1.14	14.05	1.62	-
Ar-900	89.01	1.36	7.95	1.68	-
Ar-1000	88.27	1.56	7.17	1.99	0.21

While it is possible for the surface Fe to be in an oxidized form, a nitrogen coordinated iron, or hydroxide bound iron, most iron species exist as metallic Fe or iron carbide (Fe$_3$C), not iron oxide, as evident from XRD analysis. In addition, iron oxides (Fe$_2$O$_3$, Fe$_3$O$_4$) are hardly detected at 529.5 eV[142] in the O 1s spectra.   Also, no peaks related to the redox Fe$^{2+/3+}$ couple are observable in the ORR region of cyclic voltammetry curves, even at very high scan rates[60b]. Accordingly, it is reasonable to conclude that iron redox couple (Fe$^{2+/3+}$) might not play an important role in ORR in **Figure 5-12**.
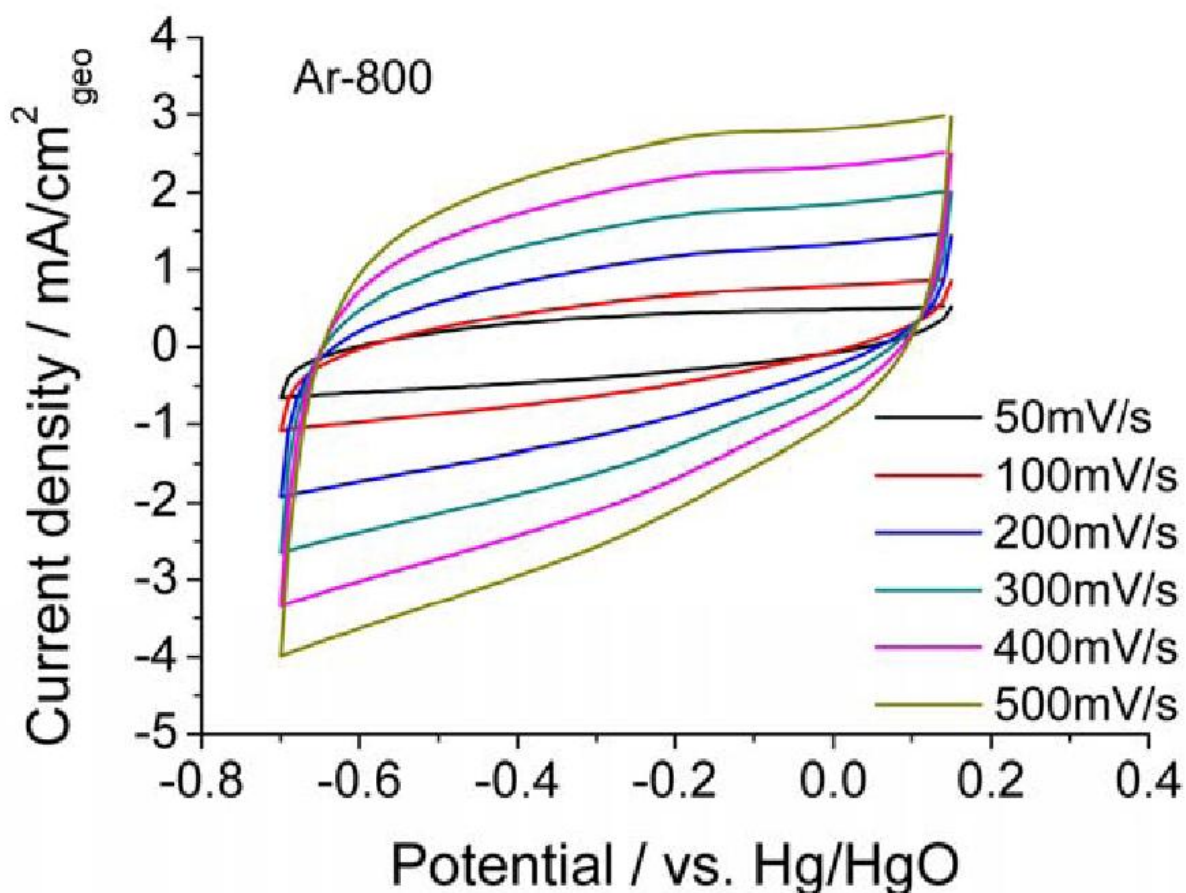
Figure 5-12. Cyclic voltammograms of the composite Fe/Fe$_3$C-melamine/N-KB (Ar-800) coated on a glassy carbon electrode tested in Ar saturated 0.1M KOH solution at different potential scan rates. This result is consistent with the physical characterization of our catalysts: they are composed of iron metal and iron carbide, not iron oxides.

This is consistent with the physical characterization of our catalysts: they composed of iron metal and iron carbide, not iron oxides.

Nano-sized ketjenblack clusters were successfully incorporated into commercially available melamine foam of micro-scale porous skeleton through a simple pyrolysis, creating unique catalyst architectures with a large number of active sites for ORR and large amount of pore volume for fast transport of oxygen gas and aqueous electrolyte to the active sites. Further, a simple solution based method was used to functionalize the melamine foam surface with iron precursors. The hydrophobic ketjenblack offers more active ORR sites by N-doping and enhances the electrical conductivity of the composite catalysts. Electrochemical performances of the low-cost catalysts are comparable to those of Pt-based catalysts at low overpotentials and even better at high overpotentials. XPS analysis suggests that –C- SO$_x$ – C, C=O, and C-OH in the as-prepared sample may increase hydrophilicity,

thus enhancing transport of oxygen gas and aqueous electrolyte through the porous catalysts. Performance measurements using RRDE and Zn-air cells suggest that large surface area of N-doped ketjenblack and Fe/Fe$_3$C of melamine carbon foam are responsible for the dramatically increased ORR activity. Good methanol tolerant and durability were also demonstrated. Since commercially available melamine foam and ketjenblack carbon are relatively inexpensive and the facile synthetic method is amendable to mass production, the non-precious metal catalysts are a promising alternative for a new generation of low-cost and high-performance metal-air batteries and fuel cells.

Experimental Section

Preparation of the composite Fe/Fe$_3$C-melamine/N-KB catalysts

In a typical experiment, 500mL 0.1MFeCl$_2$•4H$_2$O (from Sigma Aldrich) aqueous solution was prepared with pure distilled water, to which 0.5g commercial ketjenblack EC-600JD (KB) was dispersed to form a suspension. A slice (0.88g) of commercially available melamine foam (magic cleaner, Rainbow, KT trading, Made in Germany) was soaked with 500mL 0.1M FeCl$_2$•4H$_2$O solution and KB suspension. This melamine foam impregnated with FeCl$_2$ and ketjenblack was dried at 70°C for 24hr and then pyrolyzed under Ar atmosphere for 2hr at 800, 900, and 1000°C, respectively (with a heating rate of 5°C/min). Finally, the carbonized catalysts were leached with 2M H$_2$SO$_4$ at 80°C for 3hr to remove unstable species and excess metallic Fe and iron oxides.

Preparation of Fe/Fe$_3$C-melamine with KB mixture

The procedure was similar to that for the preparation of Fe/Fe$_3$C-melamine/N-KB as described above. Briefly, FeCl$_2$ impregnated melamine foam was pyrolyzed and then acid leached under the same conditions, but without the impregnation of ketjenblack. Instead, 0.5g commercial ketjenblack EC-600JD was physically mixed with carbonized Fe functionalized melamine foam to prepare a physical mixture of the two.

Preparation of catalysts ink and working electrode

The carbonized foam catalysts were grinded to powder with a mortar for better dispersion in aqueous solution. Desired catalyst ink was prepared by ultrasonically mixing 12 mg of the catalyst powder with 2 mL of 0.05 % Nafion (Aldrich) solution in distilled water for at least 1 hr to form homogeneous catalysts ink. Then, 6μL of the catalysts ink was carefully dropped onto a polished glassy carbon (GC) electrode of 4 mm diameter (RRDE Pt Ring/GC Disk Electrode, cat. NO. 011162, ALS Co., Ltd.). Glassy carbon electrodes were polished with 0.05 µm polishing alumina to maintain a good condition of working electrode (PK-3 Electrode Polishing kit, ALS Co., Ltd.). Catalyst-coated GC electrodes were then dried under vacuum at room temperature for at least 1hr.

Electrochemical characterization of the composite Fe/Fe₃C-melamine/N-KB ORR catalyst

Typical loading of the non-precious metal catalysts is 0.286 mg_{cat}/cm^2. For comparison, 20% Pt on Vulcan XC-72 catalysts (Premetek Co.) was used to prepare catalyst inks with desired concentration. For the 19.1$\mu g_{Pt}/cm^2$ catalyst, 4 $mg_{cat(Pt+carbon)}$ was dispersed in 2 mL of 0.05 % Nafion (Aldrich) solution in distilled water. Other 20%Pt/C catalyst inks (such as 9.55$\mu g_{Pt}/cm^2$ and 28.6$\mu g_{Pt}/cm^2$) were prepared using similar procedures. The detail procedure for application of catalyst inks to an electrode was the same as described above.

Rotating Ring Disk Electrode (RRDE) experiment

Rotating ring disk electrode (RRDE) (ALS Co., Ltd) experiments were carried out using the as-prepared catalysts film (deposited on GC electrode) as the working electrode in 0.1M KOH alkaline electrolyte. Pt wire and Hg/HgO is used as counter and reference electrode, respectively. Before RRDE test, 0.1 M KOH electrolyte was bubbled with pure oxygen gas (99.9%) for 30 min. Elecrochemical characterization was conducted using bi-potentiostat (IviumStat). 10mV of scan rate was swept from 0.15V to -0.7V and sufficient ring potential of 0.4Vwas biased to oxdizeintermidiate during ORR. The collection efficiency (N) was determined under Ar atmosphere using 10mM $K_3[Fe(CN)_6]$, which is around 0.41.This value is very close to its theoretical value, 0.42.

Hydrogen peroxide yields and the number of transferred electrons were calculated using the equations below

$$HO_2(\%) = 200 \frac{I_r/N}{I_d + I_r/N}$$

$$n = 4 \frac{I_d}{I_d + I_r/N}$$

and the experimentally determined collection efficiency (N) was 0.41.

The origin and a copyright of tetrapod structure of a breakwater

This digital photo was taken in *Jung-Ja* harbor in Ulsan, Korea. A tetrapod structure of a breakwater is constructed to minimize damage caused by a tsunami at a coast. The melamine foam in SEM image was prepared with pyrolysis at 800^oC in Ar for 2hr.

Characterization of methanol tolerance and stability of the composite Fe/Fe₃C-melamine/N-KB ORR catalyst

To test methanol tolerance, 10% (W/W) methanol was injected into electrolyte at 150 sec and both catalysts (Ar-800 and Pt/C) loading density were 85$\mu g/cm^2$. Before both tests, linear sweep voltammetry was performed in the voltage range from 0.15V to -0.7V (vs Hg/HgO) for 4 times under

the same above conditions. Data of (A) was constructed by adding each cycle data. 1 cycle was maintained for 300 sec and 4 cycles were tested under the same conditions.

Electochemical performance of Zn-air battery with the composite Fe/Fe$_3$C-melamine/N-KB ORR catalyst

The gas diffusion layer (GDL)was prepared from a mixture of activated carbon (Darco G-60A, Sigma Aldrich) and PTFE binder (60 wt% PTFE emulsion in water, Sigma Aldrich) at a weight ratio of 7 to 3.[S1] The thickness of the GDL was kept at ~350 µm to ensure proper gas distribution and sufficient current collection. This GDL (without catalyst) was used as the baseline reference for comparison. To prepare a catalyst layer on the GDL, 3 mg of an as-prepared Fe/Fe$_3$C-melamine/N-KB catalyst powder was dispersed in 1 mL ethanol to form a homogeneous suspension; then, 200 µL of the catalyst suspension was carefully transferred to the surface of the GDL to form a catalyst layer after drying under vacuum for 30 minutes. Similarly, to prepare a Pt-based catalyst layer, 2 mg of 20% Pt/C catalyst powder was dispersed in 1 mL ethanol and then 200 µL of the Pt catalyst ink was carefully transferred to the surface of a GDL, followed by drying under vacuum for 30 minutes. Catalyst loading for the Fe/Fe$_3$C melamine/N-KB (Ar-800) was 0.3mg$_{cat}$/cm^2 whereas that for 20% Pt/C catalyst was 40µg$_{Pt}$/cm^2 (0.2mg$_{cat(Pt+carbon)}$/cm^2).

Sulfur effect on catalytic activity for ORR

From S2p of XPS result (Figure 6d), in this oxide moiety, sulfur would have little influence on the electronic structure of carbon plane directly, unlike the sulfur atom in -C-S-C. Thus, it is unlikely that sulfur doping may enhance ORR activity in our samples through some effect on electronic structures.

Characterization

The material morphology wasexamined using a SEM (Nanonova 230, FEI) operating at 10 kV. Powderanalysis was performed using an X-ray diffractometer (XRD)(D/Max2000, Rigaku). Oxidation state of elements was analyzed using XPS (Thermo Fisher, UK) and surface carbon state was examined using micro-Raman (WITec).

Chapter 6. Facile synthesis of hybrid graphene and carbon nanotubes as a metal-free electrocatalysts with active dual interfaces for efficient oxygen reduction reaction[56]

Adapted from ref. 56 with permission from RSC.

We report metal-free electrocatalysts to enhance utilization of dissolved and gaseous oxygen during oxygen reduction reaction (ORR). Proper balance between hydrophobicity and hydrophilicity is achieve using reduced graphene oxide (rGO) and polyelectrolyte functionalized multiwalled carbon nanotubes (pMWNTs). In this unique architecture, both two- and three-phase reactions in ORR can be maximized with a quasi-four-electron pathway.

Oxygen reduction is a vital reaction for energy conversion systems in which oxygen can be used as the cathode active material.[1] Since oxygen undergoes a reduction process with high overpotential in both acidic and alkaline media, the electrocatalysts to facilitate the oxygen reduction reaction (ORR) is signicant. In particular, compared to its behavior in acidic media, the ORR in an alkaline environment is more facile and can be catalyzed by a broader range of materials.[143] For that reason, the development of efficient ORR electrocatalysts is essential for improving electrochemical performance of alkaline fuel cells and metal–air batteries.[55a, 84a, 144] In general, the utilization of oxygen at the cathode interface for the three-phase (i.e. catalyst (solid), electrolyte (liquid), and oxygen (gas)) reaction should be improved. Furthermore, despite its relatively low efficiency, two-phase ORR, involving dissolved oxygen, also needs to be considered particularly for the design of high performance metal-free electrocatalysts.[66] With its unique structures to alleviate the mass transport effect, it maximizes the utilization of available gas phase and dissolved oxygen. It leads to our key idea of developing more efficient electrocatalysts to maximize both gaseous and dissolved oxygen involved during the ORR through the appropriate combination of hydrophobicity and hydrophilicity. In order to realize this design principle, it is critical to balance the hydrophilic and hydrophobic properties of catalysts for a large number of active reaction sites to participate. For this purpose, we suggest a unique model system which can offer insight into the importance of dual interfaces by using hybrid nanomaterials. Although many noble metal catalysts, such as Pt and Pt based alloys, have been employed as ORR catalysts with excellent efficiency, the high cost and poor long-term durability intrinsically associated with the Pt group ORR catalysts have restricted their use for large-scale applications.[109, 145] The recent development of non-precious metal-based or metal-free catalysts for effective ORR has thus generated considerable interest.[90, 133a, 133c, 139] In particular, metal-free nitrogen-doped carbon materials have been demonstrated to exhibit good electrocatalytic

activities for ORR which are comparable to commercial Pt/C.[146] The design of many of these metal-free electrocatalysts, however, mainly focused on the electronic interaction between oxygen and carbon materials doped by heteroatoms or adsorbed with polyelectrolytes without addressing the phase boundary structures of electrocatalysts within the electrode. Herein, a unique design for the synthesis of 3D-metal-free electrocatalysts by controlled hybridization of one-dimensional (1D) multiwalled carbon nanotubes (MWNTs) and two-dimensional (2D) reduced graphene oxide (rGO) nanosheets is reported. Specially, we combined poly(diallyldimethylammonium chloride) (PDAC)-functionalized hydrophobic MWNTs (pMWNTs) with hydrophilic rGO nanosheets having a large surface area for the construction of metal-free carbon electrocatalysts to allow effective oxygen access in both gas and aqueous forms (**Figure 6-1**).
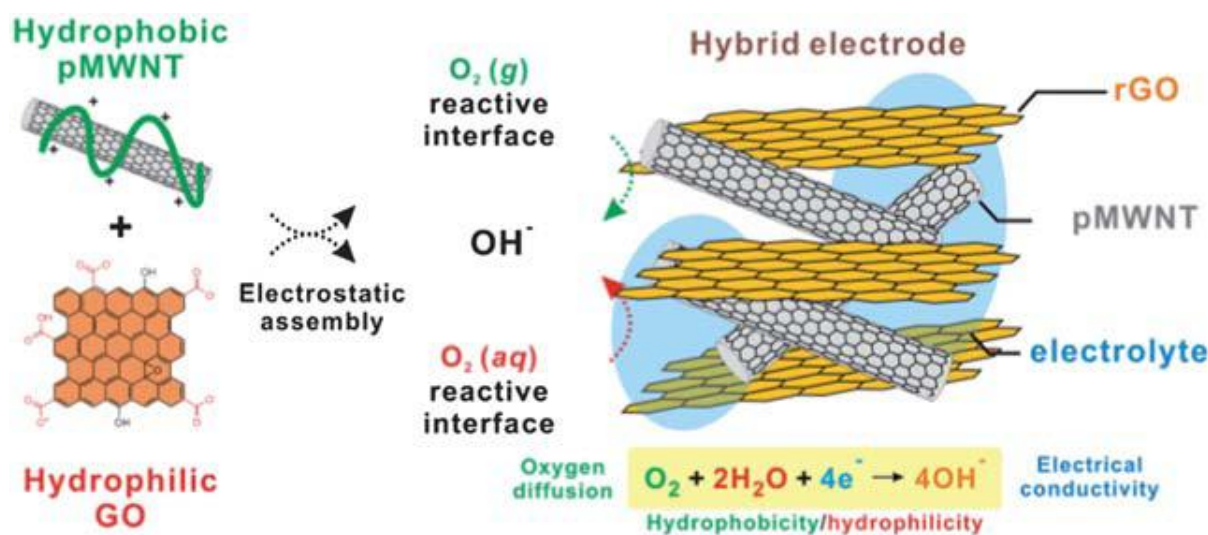
Figure 6-1. Schematic representation of a randomly stacked 3D hybrid structure of polyelectrolyte functionalized multiwalled carbon nanotubes (pMWNTs) with reduced graphene oxide (rGO) nanosheets.

In a typical experiment, we dispersed the hydrophobic MWNTs in an aqueous solution of PDAC with NaCl by sonication. The filtered suspension of pMWNTs exhibited good colloidal stability with a zeta-potential of +29.9 mV, which is constant over the entire pH range tested (pH 3–11). This confirms the presence of a positively charged strong polyelectrolyte PDAC coating layer on pMWNTs. High-resolution X-ray photoelectron spectroscopy (XPS) and FT-IR measurements further supported the successful adsorption of PDAC chains onto the MWNTs (see **Figure 6-2 and 6-3**).
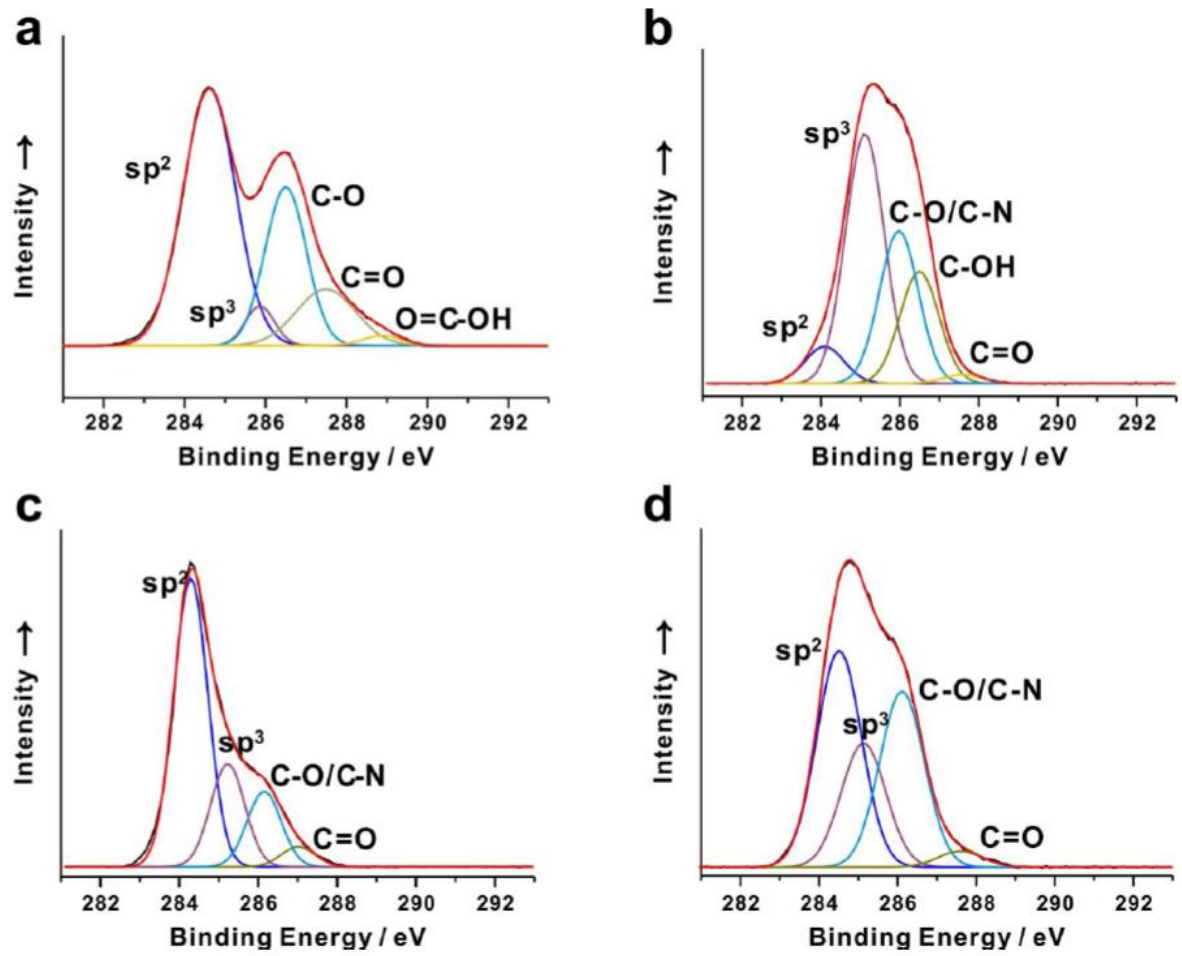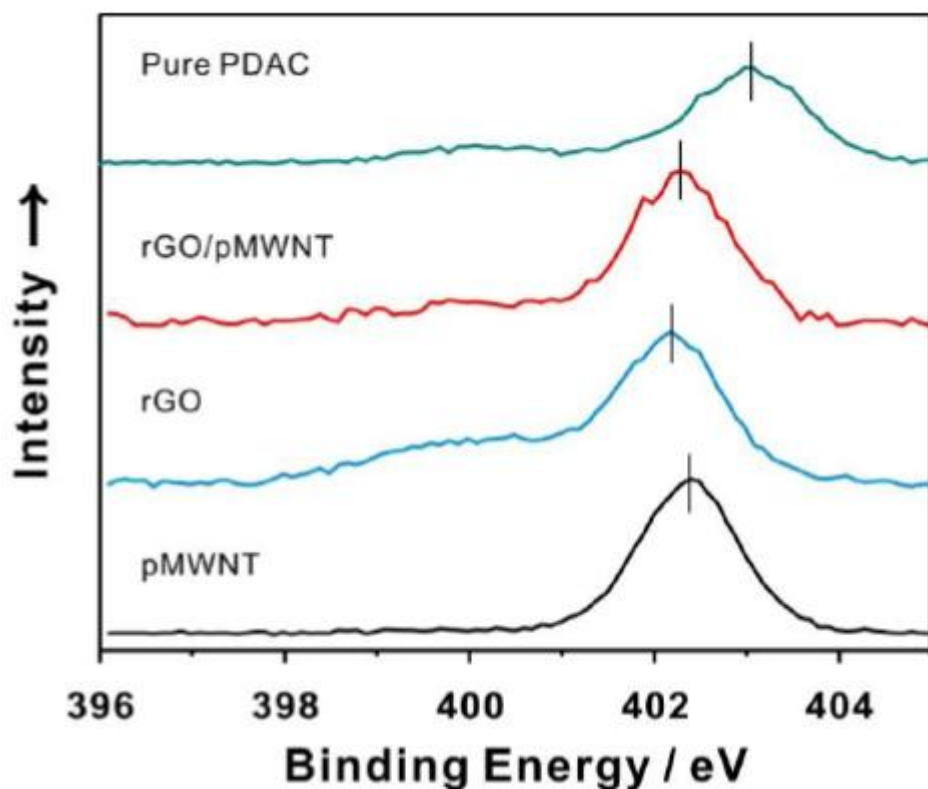
Figure 6-2. High-resolution C 1s XPS spectra of all samples used in the study. (a) GO, (b) pMWNT, (c) rGO/pMWNT(0.5:1), and (d) rGO.
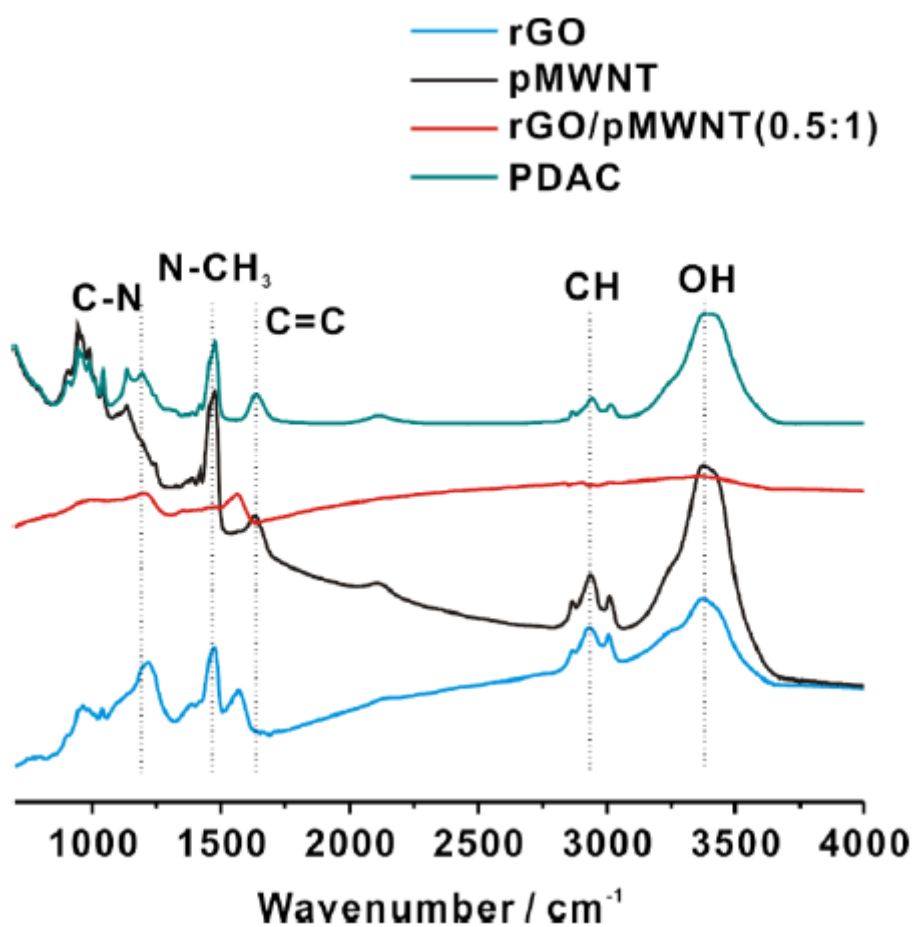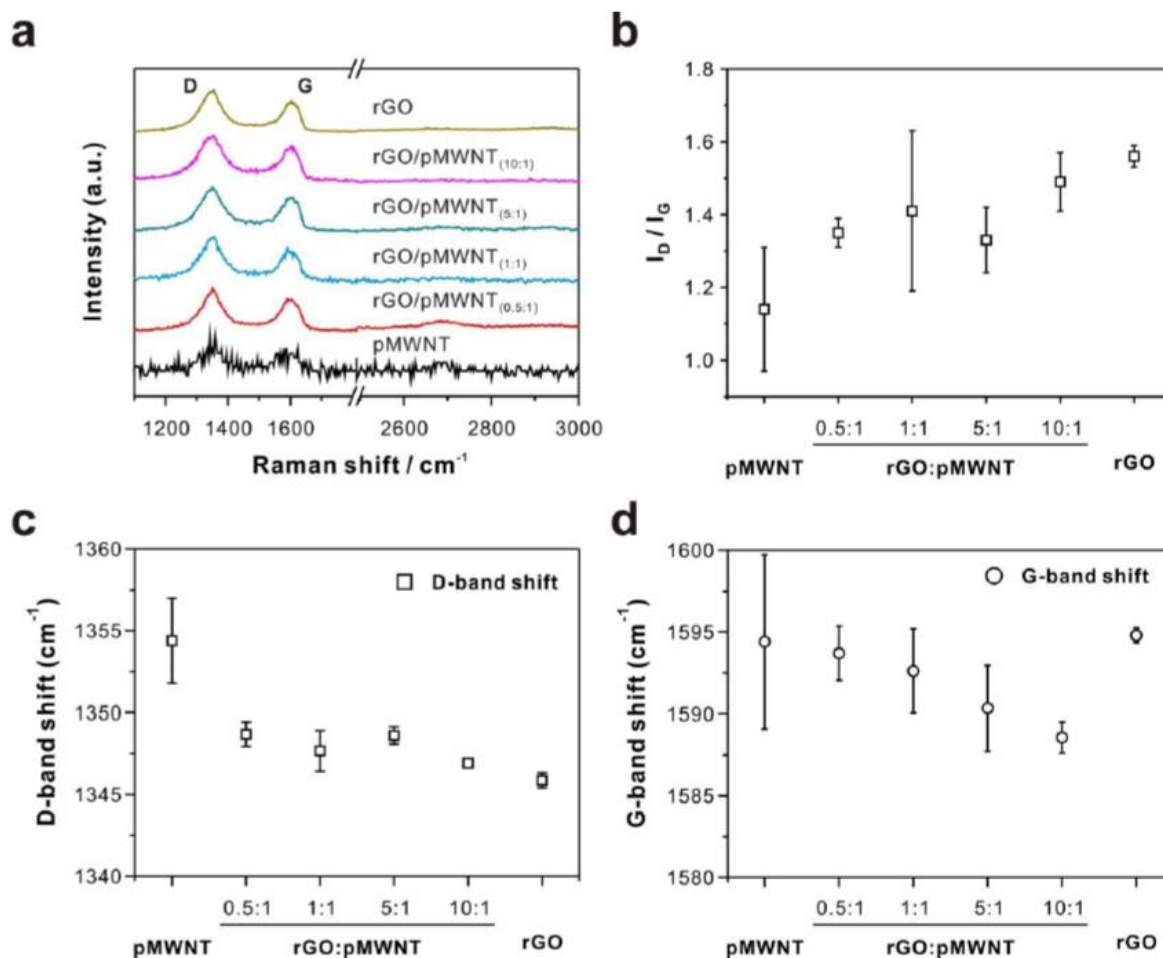
Figure 6-3. FT-IR spectra of rGO, pMWNT, rGO/pMWNT(0.5:1), and pure PDAC. All peaks are assigned with the data of previous literature.

In particular, the intermolecular charge transfer from MWNTs to electron-deficient quaternary ammonium nitrogen atoms of the adsorbed PDAC was evident from the negative shift of the N1s peak from 402 (pure PDAC) to 401.5 eV (pMWNTs) (see **Figure 6-4**).[91b]

Figure 6-4. High-resolution N 1s XPS spectra of all samples used in the study. Negative shift of N 1s peak from 402 eV (pure PDAC) to 401.5 eV (pMWNT) can be attributed to intermolecular charge-transfer of quaternary ammonium nitrogen.

Consistent with the XPS results, Raman spectroscopy also revealed the charge transfer effect needed to enhance ORR activities of the hybrid rGO/pMWNTs. As reported previously, the up-shift of G bands from 1594.2 cm^{-1} in pMWNTs to 1588.6 cm^{-1} in rGO/pMWNT(10:1) illustrated the charge transfer between rGO and pMWNTs. Concomitantly, the I_D/I_G ratio increased from 1.14 for pMWNTs to 1.35 for rGO/pMWNT(0.5:1) and even to 1.49 for rGO/pMWNT(10:1), indicating the presence of disordered graphitic structures in the hybrid electrocatalysts (see **Figure 6-5**).

Figure 6-5. (a) Raman spectra of all samples used in the study, (b) ratio of I_D/I_G, (c) D-band shift, and (d) G-band shift of all samples. The ID/IG ratio increased from 1.14 in pMWNT to 1.35 in rGO/pMWNT(0.5:1) and even to 1.49 in rGO/pMWNT(10:1), indicating the disordered graphitic structures of hybrid electrocatalysts upon introduction of rGO into pMWNT. The I_D/I_G ratio was measured at least 5 different points of each sample. Up-shift of G bands from 1594.2 cm-1 in pMWNT to 1588.6 cm-1 in rGO/pMWNT(10:1) illustrated the charge transfer between rGO and pMWNT.

This partial positive charge developed along the backbone of pMWNTs is known to play a key role in regulating the oxygen adsorption modes and in facilitating electron transfer for enhanced ORR activity.[91b] Using the prepared stable suspension of pMWNTs, we started preparing hybrid electrodes by mixing pMWNTs with the GO suspension generated by employing the modified Hummers method (typically, ratios of GO/pMWNTs = 0.5–10).[72f, 118] After the hybrid nanostructures were formed via electrostatic interactions between the two oppositely charged constituent components, the GO was subsequently reduced to rGO using the reducing agent hydrazine to restore structural pathways to transport charges needed for ORR.[147] The excess hydrazine and unbound free PDAC were then

removed by filtration, followed by extensive rinsing. The resulting hybrid electrocatalysts of rGO/pMWNTs with varying ratios were readily redispersed in water and remained stable without any noticeable aggregation for several months (see **Figure 6-6**).
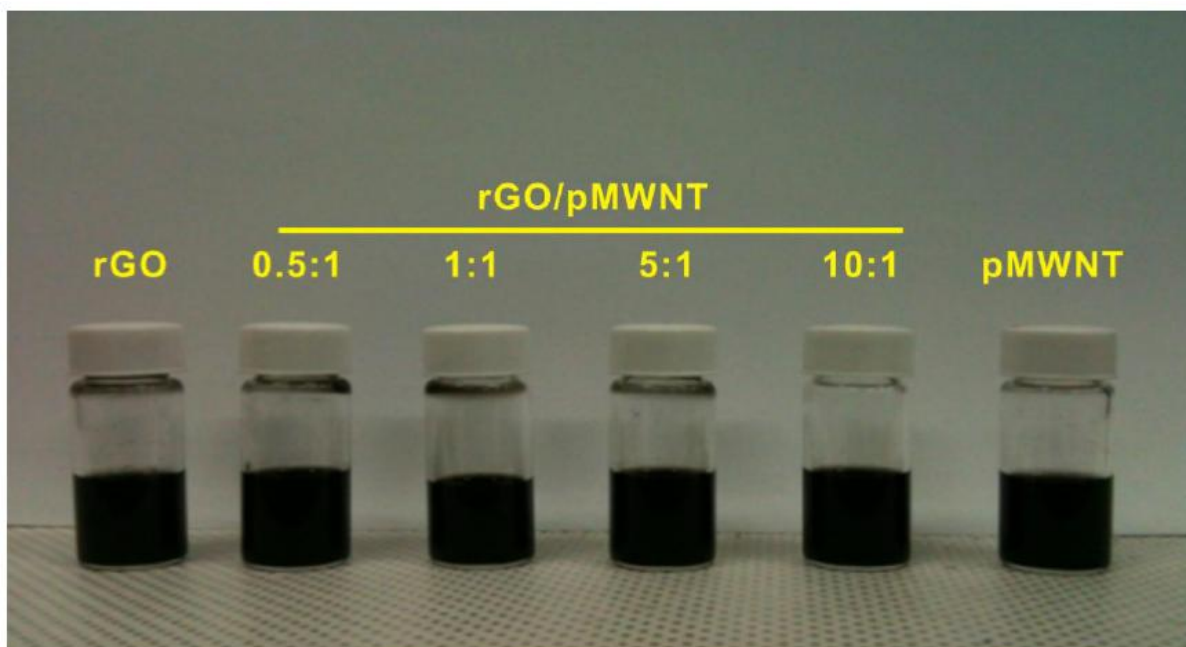
Figure 6-6. Photograph of each suspension prepared in this study at a concentration of 0.50 mg/mL. The stability of the suspension remained over 8 months.
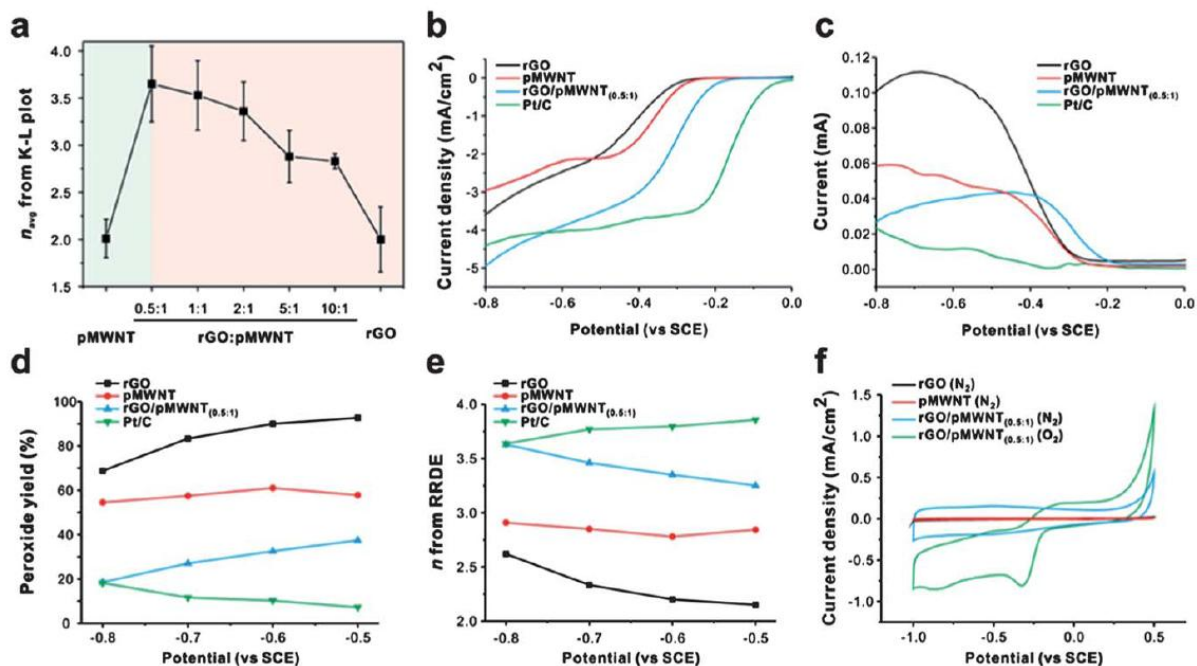
It should be noted that the rGO was additionally functionalized with PDAC as a control. The structure and morphology of rGO/pMWNTs were examined by scanning electron microscopy (SEM) and transmission electron microscopy (TEM). The representative SEM image revealed 3D interconnected network structures of pMWNTs with interdispersed rGO nanosheets driven from electrostatic stacking between oppositely charged carbon nanomaterials (**Figure 6-7**).
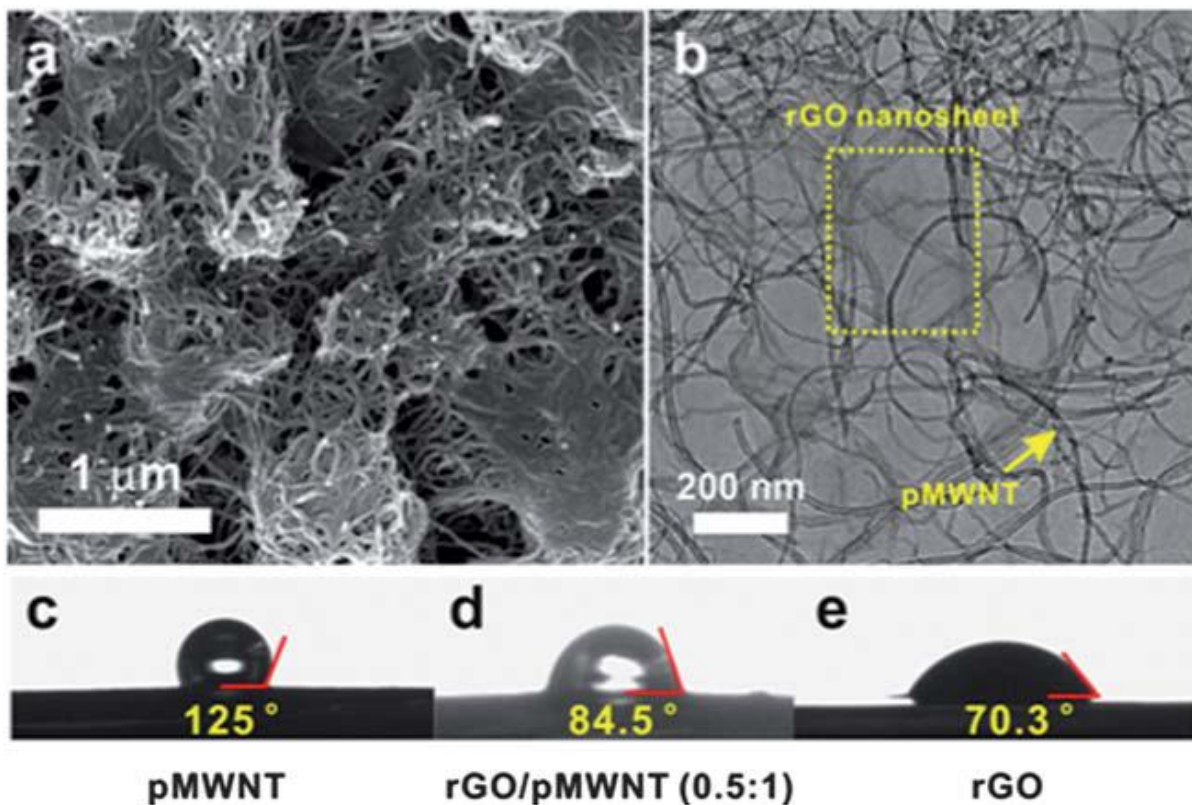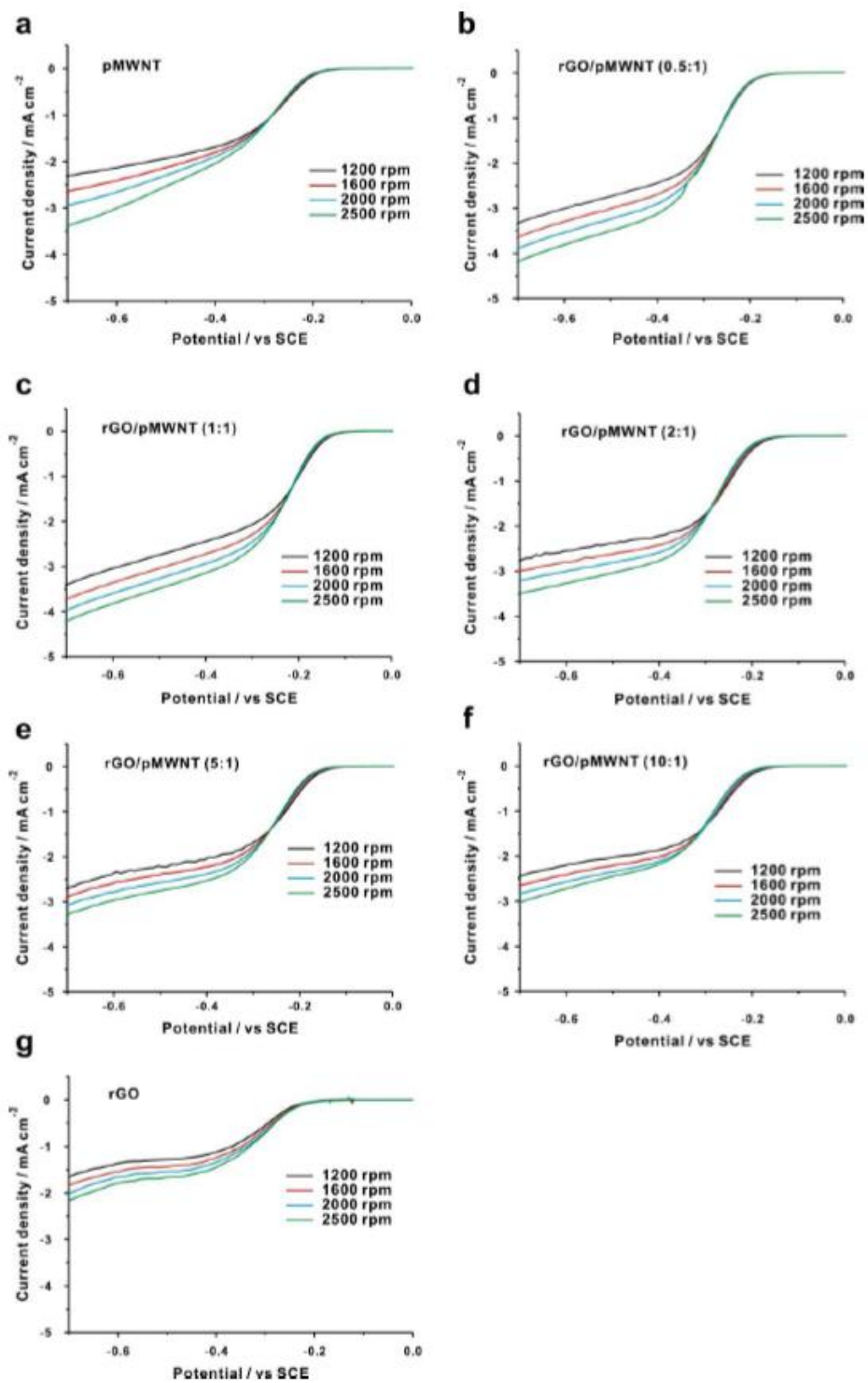
Figure 6-7. Representative (a) SEM and (b) TEM images of rGO/pMWNT(0.5:1). (c–e) Contact angle images of a water droplet on (c) pMWNT, (d) rGO/pMWNT(0.5:1), and (e) rGO films.

The TEM image further validated the thin layer of graphene sheet stacked with pMWNTs (**Fig. 6-7b**). Furthermore, it was found that thin films of pMWNTs and rGO showed the sessile contact angles of 125° and 70.3^o, respectively, while their hybrid rGO/pMWNT(0.5:1) exhibited an intermediate value of 84.5^o (**Fig. 6-7c–e**). These results show that our unique hybrid composite has dual interfaces that can balance the hydrophobic and hydrophilic nature for efficiently catalyzing ORR using both gaseous and dissolved oxygen molecules. By measuring the average number of electrons transferred (n_{avg}) per oxygen molecule derived from the slope of the Koutecky– Levich plot (i^{-1} vs. $\omega^{-0.5}$) (**Fig. 6-8a**),[148] we first explored the optimization of the rGO/pMWNT ratio (see also **Figure 6-9**).

Figure 6-8. (a) Average number of electrons (n_{avg}) transferred per O_2 molecule at different rGO/pMWNT ratios, measured at -0.4, -0.5, and -0.6 V using the Koutecky–Levich plot. A comparison with control sets of pMWNTs and rGO is also presented. (b–e) Steady-state RRDE experiments of pMWNTs, rGO, hybrid rGO/pMWNT(0.5:1) and Pt/C, respectively, in O_2-saturated 0.1 M KOH at 2000 rpm. (b) Disk current density and (c) ring current were separated for convenience. (d) Peroxide yields (%) and (e) the number of electrons (n) transferred from as-prepared samples. (f) CV curves of pMWNTs, rGO, and hybrid rGO/pMWNT(0.5:1) in N_2- and O_2-saturated 0.1Maqueous KOH electrolyte solution at a scan rate of 50 mV s^{-1}.

Figure 6-9. Linear sweep voltammetry (LSV) curves of (a) pMWNT, (b) rGO/pMWNT(0.5:1), (c) rGO/pMWNT(1:1), (d) rGO/pMWNT(2:1), (e) rGO/pMWNT(5:1), (f) rGO/pMWNT(10:1), and (g) rGO measured in O$_2$-saturated 0.1 M KOH solution.

As can be seen in **Fig. 6-8a**, the ORR activity was considerably affected by the relative amounts of pMWNTs and rGO within the hybrids. While pMWNTs provided the majority of the catalytic active sites due to their hydrophobic nature and the induced partial positive charge on their surface, introduction of rGO into their hybrid materials also improves the utility of both dissolved and gaseous oxygen and facilitates electron transfer during ORR due to its hydrophilic nature. Interestingly, however, pure pMWNTs without rGO displayed significantly lower ORR activity similar to that of pure rGO. Among all samples investigated in this study, rGO/pMWNT(0.5:1) demonstrated the highest n_{avg} value of 3.6$\pm$0.40 for an efficient onestep, quasi-four-electron process. To gain further insight into the ORR activity of hybrid rGO/pMWNTs, we performed linear sweep voltammetry (LSV) measurements using a rotating ring-disk electrode (RRDE) in O_2-saturated electrolyte solution of 0.1 M KOH, which revealed that ORR at the hybrid rGO/pMWNT(0.5:1) electrode exhibited a relatively high limiting current density and more positive onset potential with respect to its single-component counterparts (i.e., rGO and pMWNTs) (**Fig. 6-8b**). For example, the limiting current density of the hybrid rGO/pMWNT(0.5:1) electrode at -0.8 V reached -5.0 mA cm^{-2}, whereas the corresponding values for the rGO and pMWNT electrodes were -3.6 and -3.0 mA cm^{-2}, respectively. In addition, the onset potential of the rGO/pMWNT electrode up-shifted considerably toward -0.23 V compared to those of rGO (-0.35 V) and pMWNTs (-0.32 V) at a constant current density of -0.5 mA cm^{-2}. Further, the superior catalytic activity of the hybrid rGO/pMWNT(0.5:1) over that of the respective single-component was also confirmed by the hydrogen peroxide yields (%) and the number of electrons (n) transferred during the ORR, as determined from disk and ring currents (**Fig. 6-8b and c**). In particular, the number of electrons transferred was measured to be 3.3–3.6 (very close to 3.6 in **Fig. 6-8a**) for the hybrid rGO/pMWNT(0.5:1), suggesting that it is an efficient 4-electron transfer pathway with its peroxide yield of ~25% at -0.75 V (**Fig. 6-8d and e**). Furthermore, it is noteworthy that the current density of the hybrid rGO/pMWNT(0.5:1) was even slightly higher than that of Pt/C catalysts in high overpotential regions; this observation indicates that more active sites could participate in ORR due to its unique architecture which can facilitate both aqueous and gaseous oxygen transport to active sites. Though it was fabricated via an extremely facile way, these results demonstrate that the catalytic activity of this hybrid rGO/pMWNT(0.5:1) is comparable to that of other metal-free catalysts which were synthesized through harsh treatments in an alkaline solution. The high ORR activity of the hybrid resulted from the proper balance of hydrophilicity and hydrophobicity and the unique catalyst structures of the dual interface. The significance of the dual interface was further confirmed by evaluating its charge per loading which is proportional to active surface area by measuring non-faradaic current under inert N_2 conditions (**Fig. 6-8f**). In this study, we chose measuring total charges of unit mass instead of BET because the dual interfaces of gaseous and dissolved oxygen species involved during mixed phase ORR can be better addressed with this method. The charge per unit loading was 2.66 C g^{-1} for rGO, 2.16 C g^{-1} for pMWNTs and 62.9 C g^{-1} for rGO/pMWNT(0.5:1),

respectively. As expected, rGO/pMWNT(0.5:1) had about 30 times higher surface area than those of pMWNTs and rGO, clearly supporting that a fine hydrophobic–hydrophilic balance was established in the hybrid electrode, which resulted in an increase in the active surface area by facilitating the access of the electrolyte and dissolved and gaseous oxygen. Taken together, with the above physio-chemical and electrochemical analyses, it is reasonable to conclude that factors more crucial than simple charge transfer play a role in improving ORR activities of the 3D hybrid rGO/pMWNT electrocatalysts. Further, the rational design of the hydrophobic and hydrophilic dual interfaces within the hybrid electrode is critical to optimize the catalytic activity for reducing gaseous and dissolved oxygen at the electrode.

Finally, in order to evaluate the advantages of hybrid carbonbased electrochemical catalysts over conventional Pt-based electrocatalysts for potential practical applications, current–time chronoamperometric response was used to examine the methanol crossover effect and long-term stability. No crossover effect was observed in the hybrid rGO/pMWNT(0.5:1) composite upon the addition of 3.0 M methanol, while Pt/C showed a sharp current decrease under identical conditions (see **Figure 6-10**).
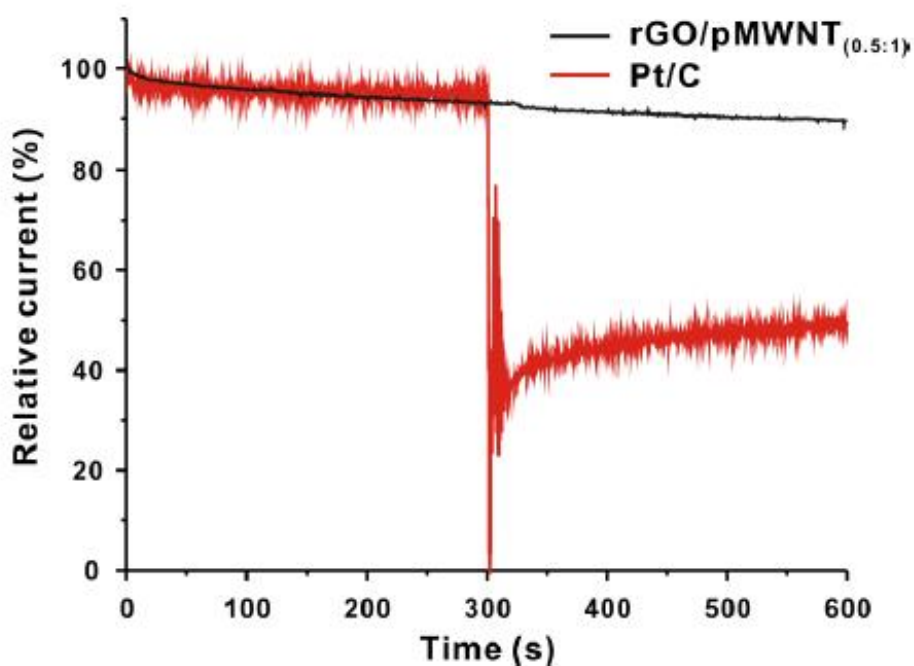
Figure 6-10. Current-time (i-t) chronoamperometric response of rGO/pMWNT(0.5:1) in O_2-saturated 0.1 M KOH at -0.4 V (vs. SCE). 3 M of methanol was added at about 300 s to show crossover effect does not occur.

The chronoamperometric durability response for 20000 s verified that the hybrid rGO/pMWNT(0.5:1) exhibited very slow attenuation with a high current retention of 61%, a value higher than that of Pt/C (see **Figure 6-11**).
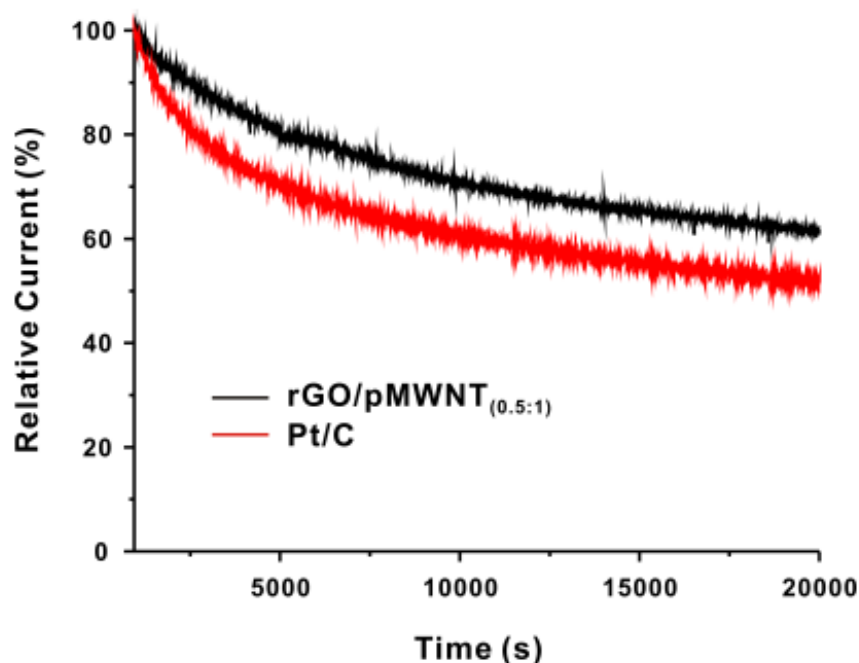
Figure 6-11. The chronoamperometric durability response for 20000 s verified that the rGO/pMWNT(0.5:1) composite exhibited a very slow attenuation with high current retention of 61%, a value which is higher than that of Pt/C in the O2-saturated 0.1 M KOH solution at -0.25 V (vs. SCE). Electrode rotation rate: 1600 rpm.

In conclusion, we have developed electrostatic force driven randomly stacked three-dimensional hybrid electrocatalysts to maximize the utility of oxygen during the oxygen reduction reaction (ORR). The newly developed carbon electrodes formed using multiwalled carbon nanotubes hybridized with reduced graphene oxide nanosheets exhibited a remarkably enhanced ORR activity without extreme conditions for synthesis. The observed improvement in the ORR performance can be attributed to the increased number of active reaction sites and to enhanced mass transport associated with the well-established hydrophobic and hydrophilic dual interfaces and the porosity within the electrode. The high catalytic activity combined with the extremely facile synthetic nature of this electrocatalyst with dual interface active sites makes its development an important step forward in designing and utilizing carbon nanomaterials in electrocatalysts, and opens up new possibilities for carbon materials to be used as alternative cost-effective catalysts for metal–air batteries and alkaline fuel cells.

Experimental sections

Preparation of PDAC functionalized multi-walled carbon nanotubes (pMWNT) and graphene oxide (GO) to synthesize the hybrid rGO/pMWNT electrode.

pMWNT were prepared by following method. 50 mg of MWNT (10 - 15 nm diameter, Hanwha Nanotech Corp.) were mixed with 2 wt. % of poly(diallyldimethylammonium chloride) (PDAC) in 100 mL of water in the presence of 3 wt. % of NaCl. Then, stable pMWNT suspension was prepared by ultrasonication for 1 h.S3 Graphene oxide (GO) was prepared from a commercial graphite (Aldrich) by modified Hummers method and exfoliated using ultrasonication. The resulting brown solution was mixed with pMWNT suspension at a specific ratio (GO:pMWNT = 0.5:1 - 10:1). GO in a mixed solution was reduced into reduced graphene oxide (rGO) by adding hydrazine (35 wt. % in water, Aldrich) followed by heating at 100 oC for 2 hours. Finally, the suspension of rGO/pMWNT was filtered by Nylon membrane filter (pore size of 0.2m, Corning) and redispersed at a concentration of 0.50 mg/mL of rGO. rGO sheets were stabilized by PDAC functionalization to prevent restacking. PDAC Functionalized rGO was written as rGO for simple notation.

Preparation of rGO, pMWNT and rGO/pMWNT(0.5:1) thin films for contact angle measurement.

rGO, pMWNT and rGO/pMWNT(0.5:1) solutions were filtered with anodic aluminum oxide (AAO) membrane. After several times washing with deionized water, uniform films were formed on the membrane. To measure contact angle, a water droplet was dropped on each film and the contact angle image was captured immediately after forming the contact interface.

Preparation of catalysts ink and working electrode.

Actual concentrations of each solution were 2.3 mg/ml for rGO, 2.8 mg/ml for pMWNT and 1.5 mg/ml for rGO/pMWNT(0.5:1), respectively. For comparison, 20% Pt on Vulcan XC-72 catalysts (Premetek Co.) ink was prepared by ultrasonically mixing 2 mg of the catalyst powder with 2 mL in distilled water at least 1 h. Then, 6μL of each solution including Pt/C catalyst was loaded on the polished glassy carbon (GC) electrode of 4 mm diameter (RRDE Pt Ring/GC Disk Electrode, cat. NO. 011162, ALS Co., Ltd.). Corresponding loading densities were 109 μgCat/cm2 for rGO, 133 μgCat/cm2 for pMWNT, 71.2 μgCat/cm2 for rGO/pMWNT(0.5:1), and 20 μgPt/cm2 for Pt, respectively. Before applying each catalyst, glassy carbon electrodes were polished with 0.05 μm polishing alumina to maintain a good condition of working electrode (PK-3 Electrode Polishing kit, ALS Co., Ltd.). Catalyst-coated GC electrodes were then dried under vacuum at room temperature for at least 20 min.

Rotating Ring Disk Electrode (RRDE) experiment.

Rotating ring disk electrode (RRDE) (ALS Co., Ltd) experiments were carried out using the as-prepared catalysts film (deposited on GC electrode) as the working electrode in 0.1 M KOH alkaline electrolyte. Pt wire and SCE are used as a counter and a reference electrode, respectively. Before RRDE test, 0.1 M KOH electrolyte was bubbled with pure oxygen gas (99.9%) for 30 min. Electrochemical characterization was conducted using bi-potentiostat (IviumStat). 10 mV of scan rate was swept from 0.15 to -0.8 V and sufficient ring potential of 0.4 V was biased to oxidize intermediate during ORR. The collection efficiency (N) was determined under Ar atmosphere using 10 mM K3[Fe(CN)6], which is around 0.41. This value is very close to its theoretical value of 0.42. Hydrogen peroxide yields and the number of electrons transferred (n) were calculated using the equations below. Furthermore, rotating disk electrode (RDE) (ALS Co., Ltd) experiments were carried out under aforementioned condition to construct the Koutecky–Levich plot.

$$H_2O_2(\%) = 100\frac{2I_r/N}{I_d + I_r/N} \tag{1}$$

$$n = 4\frac{I_d}{I_d + I_r/N} \tag{2}$$

Calculating the number of transferred electrons (n) of the as-prepared catalysts from the slope of the Koutecky–Levich plot. Koutecky-Levich plot relates the current density (i) to the rotation rate of electrode and allows one to determine both kinetic current (ik) and number of transferred electrons (n) involved in ORR.

$$\frac{1}{i} = \frac{1}{i_k} + \frac{1}{i_{dl}} = \frac{1}{i_k} + \frac{1}{B\omega^{0.5}} \tag{3}$$

$$i_k = nFAkC_{O_2} \ \text{(Kinetic current)} \tag{4}$$

$$i_{dl} = 0.62nFAC_{O_2}D_{O_2}{}^{2/3}v^{-1/6}\omega^{1/2} \ \text{(Diffusion current)} \tag{5}$$

$$= 0.620(\frac{2\pi}{60})^{1/2}nFAC_{O_2}(\omega' = \text{rpm number})^{1/2}D_{O_2}{}^{2/3}v^{-1/6}$$

$$= 0.2nFAC_{O_2}(\omega' = \text{rpm number})^{1/2}D_{O_2}{}^{2/3}v^{-1/6}$$

where i_k represents the kinetic current; i_{dl} is diffusion limiting current; n is the number of electrons transferred per O_2 molecule; F is the Faraday constant (96485 C/mol); A is the geometric area of the disk electrode (7.06 × 10⁻⁶ m²); k (m/s) is the rate constant for the ORR; C_{O_2} is the saturated concentration of O_2 in solution (1.21 mol/m³ in 0.10 M KOH); v is the kinematic viscosity (1 × 10⁻⁶

m^2/s in 0.10 M KOH); D_{O_2} is the diffusion coefficient of O_2 in solution (1.87×10^{-9} m^2/s in 0.10 M KOH). ω and ω ' are the angular frequency of the rotation (rad/s) and electrode rotation rate in rpm, respectively. 0.2 is a constant when the rotation speed is expressed in rpm. From the linear relationship between i^{-1} vs $\omega^{-1/2}$ based on the Koutecky-Levich equation, we can obtain the electrons transferred (n) from the slope.

Chapter 7. Metal-Free Ketjenblack Incorporated Nitrogen-doped Carbon Sheets derived from Gelatine as Oxygen Reduction Catalysts

Electrocatalysts facilitating oxygen reduction reaction (ORR) are vital components in advanced fuel cells and metal-air batteries. Here we report ketjenblack incorporated nitrogen-doped carbon sheets derived from gelatine and apply these easily scalable materials as metal-free electrocatalysts for ORR. These carbon nanosheets demonstrate highly comparable catalytic activity for ORR as well as better durability than commercial Vulcan carbon supported Pt catalysts in alkaline media. physico-chemical analysis suggest that proper combination of quaternary and pyridinic nitrogen species with more exposed edge sites, increasing catalytic activities for ORR. Our results demonstrate a novel strategy to expose more nitrogen doped edge sites by irregular stacked small sheets in developing better electrocatalysts for Zn-air batteries. These desirable architectures are embodied by amphiphlilic gelatine mediated compatible synthetic strategy between hydrophobic carbon and aqueous water.

Zinc-air battery has been attracted as next generation energy storage and conversion devices due to its larger energy density than that of Li-ion battery, environmental benignity, safety, and low cost[1, 149]. As a cathode reaction in Zinc-air battery, oxygen reduction reaction (ORR) is a vital reaction, but very sluggish[150]. Therefore, how to facilitate ORR with proper catalysts has been a key issue to date. In spite of the lack of understanding of details mechanisms for ORR, a formation of superoxide though a one electron transfer, $(O_2 + e^- \leftrightarrow [O_{2(ad)}]^-)$, is considered as the first step for ORR[151]. Pt-based electrocatalysts have been widely used in fuel cell operated in acid electrolyte[152], but various non-precious metal or metal-free catalysts can speed up ORR in alkaline media due to its better stability of materials and facilitated kinetics for ORR in alkaline solution[6, 66, 101c, 143a, 153]. Another advantage of using non-Pt based catalysts in alkaline media can avoid unnecessary zinc corrosion caused by hydrogen evolution reaction (HER) catalysed with Pt metal-based catalysts deposited at Zn anode coming from air electrodes due to its instability under ORR potential range during discharge[154]. However, compared to Pt catalysts, it is still challenging to develop not only a high efficient catalyst for ORR, but also better durability with low cost.

Recently, nitrogen doped carbons have been significantly attracted as efficient metal-free electrocatalysts due to the disordered carbon nanostructures and their higher surface polarity that are induced from electron donation from nitrogen to adjacent carbon[72a, 90, 155]. For example, the graphene edge defects induced by nitrogen could enable the edge sites to have higher catalytic activity rather than the graphene plane because oxygen adsorption at the edge sites is more favourable than in basal plane[151]. Although various nitrogen doping into carbon methods are available, pyrolyzing precursors

with nitrogen is the effective way to synthesize nitrogen-doped carbon materials[156]. Gelatine as nitrogen source contains about 16 wt % of nitrogen compared with 45 wt % of melamine[157] and gelatine could be more desirable precursors than melamine because too much nitrogen contents in precursors can decrease its carbonization yields after pyrolysis[137, 158]. As far as we are concerned, there are only three previous studies reported gelatine and its applications including the anode in Li-ion battery, supercapacitor, and catalysts for ORR in fuel cell[157a, 159]. For instance, Schnepp et al. used gelatine as nitrogen source in preparing trimodal porous materials as catalysts for ORR in fuel cell[159b]. However, sole usage of gelatine as nitrogen doped carbon precursor without any other carbons could decrease productivity and effective nitrogen doped carbon active sites density. In this regard, commercial carbon black composed of small and aggregated graphitic carbon sheets can be a proper supporting materials in preparing catalysts for ORR[133a, 133c, 160]. However, intrinsic hydrophobic character of carbon can limit its potential application in aqueous water without further oxidation onto carbon surface[161]. When it comes to how to fully utilize hydrophobic carbon in water, it should be noted that gelatine has amphiphilic character (both hydrophilic and hydrophobic)[162], rendering effective interaction between carbon and gelatine possible in aqueous media. Accordingly, in spite of this advantage that makes easily scalable process, these amphiphilic characters of gelatine as nitrogen-carbon precursors, however, have not been fully utilized simultaneously with commercial hydrophobic carbon black.

Herein, we synthesized ketjenblack incorporated into irregular stacked nitrogen-doped carbon sheets and apply these easily scalable materials as metal-free electrocatalysts for ORR in alkaline media. Introduced gelatine functioned as not only nitrogen-carbon sheet precursor, but also a mediator which can increase interaction between aqueous water and hydrophobic ketjenblack. During high temperature pyrolysis, nitrogen-doped carbon sheet derived from gelatine are grown in dispersed Ketjenblack nanoparticles, thus forming irregular stacked small sheets morphology with more exposed edge sites. As-prepared stacked sheets like structures show comparable catalytic activity for ORR, durability under ORR potential in both half-cell testing condition and Zn-air battery compared with that of commercial Vulcan carbon supported Pt catalysts.

We synthesized GKs catalysts via aqueous water based mixing of commercial gelatine and Ketjenblack carbon, followed by pyrolysis under inert atmosphere (**Figure 7-1 and 7-2**).
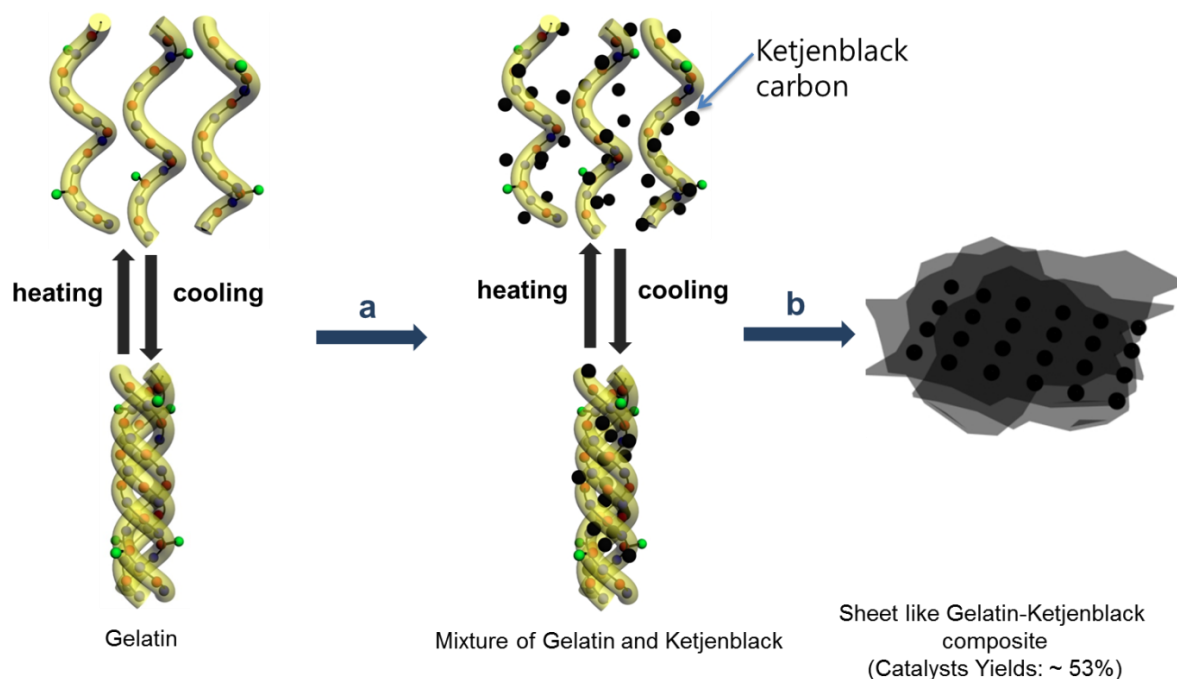
Figure 7-1. Schematic view of the synthesis of Ketjenblack incorporated nitrogen doped irregular stacked carbon sheets. (a) Mixing Ketjenblack with gelatin solution via simple aqueous solution, and (b) Pyrolysis at high temperature above 800°C under inert atmosphere. Note that as-prepared catalysts yields are above 50 wt % and large scale synthesis is possible.
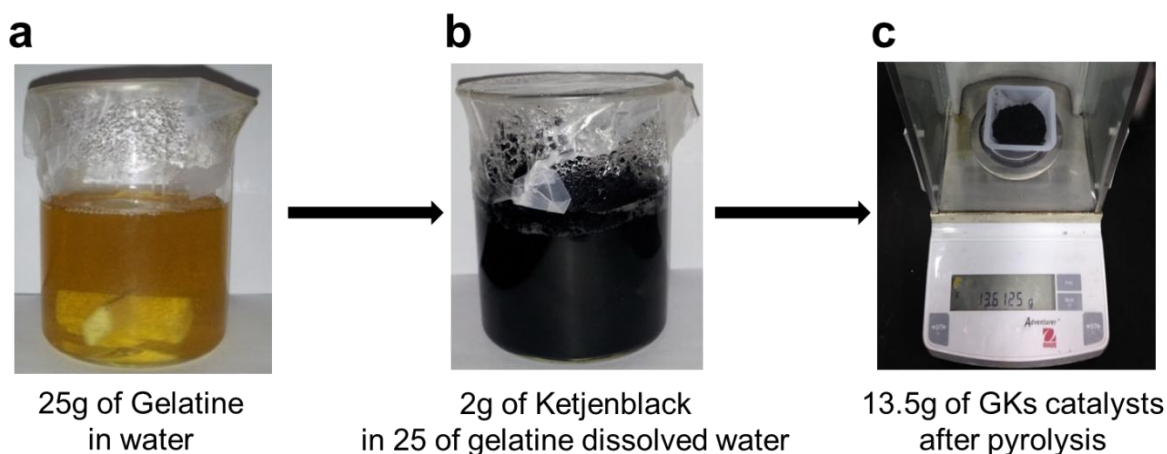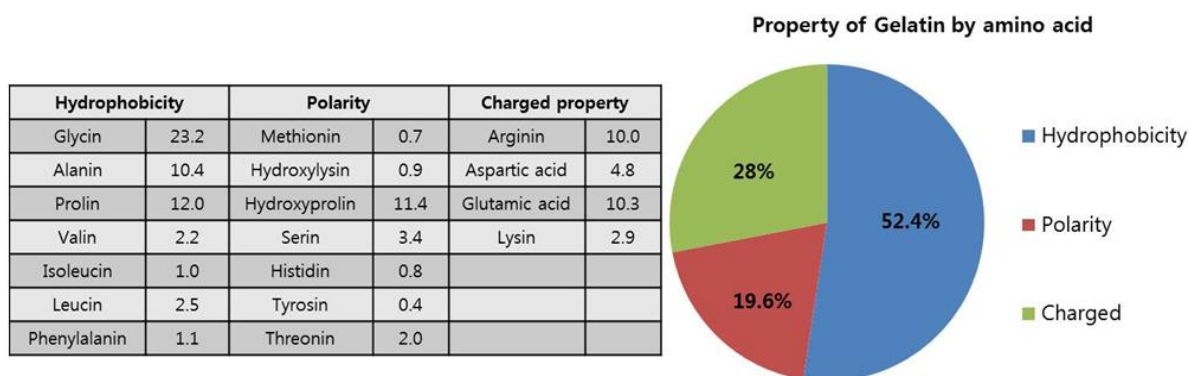

Figure 7-2. Pictures for synthetic process of GK-series. (a) Gelatin solution, (b) Gelatine-Ketjenblack jelly, (c) After pyrolysis process at 900 ℃, GK-900 catalyst on weighing machine.

In this synthetic approach, it is worthy to note that introduced gelatine makes it possible that commercial hydrophobic carbon can be well dispersed in aqueous water through two types of interactions below even without any surface oxidation[161]. The one comes from amphiphilic character (both hydrophilic and hydrophobic) of gelatine so that Ketjenblack interacts with hydrophobic Glycin

and Prolin amino acids of gelatine with its polar and charged groups interacting with aqueous water[162] in **Table 7-1**.

Table 7-1. Gelatine amino acid composition (The table were reconstructed based on the previous literature data)

Hydrophobicity		Polarity		Charged property	
Glycin	23.2	Methionin	0.7	Arginin	10.0
Alanin	10.4	Hydroxylysin	0.9	Aspartic acid	4.8
Prolin	12.0	Hydroxyprolin	11.4	Glutamic acid	10.3
Valin	2.2	Serin	3.4	Lysin	2.9
Isoleucin	1.0	Histidin	0.8		
Leucin	2.5	Tyrosin	0.4		
Phenylalanin	1.1	Threonin	2.0		

Property of Gelatin by amino acid

- Hydrophobicity: 52.4%
- Polarity: 19.6%
- Charged: 28%

The other results from a folding and unfolding of three polymer chains composed of a triple helix during cooling and heating process, allowing gelatine to hold Ketjenblack tightly. Therefore, introduced Ketjenblack and gelatine can be distributed evenly each other through above two mediated interaction in aqueous media, forming uniform solidified jelly block as precursors for nitrogen-doped carbons composites.

The morphological structures of the GK were characterized by high-resolution transmission electron microscopy (HR-TEM). Based on the HR-TEM images (**Figure 7-3**), we found that irregular carbon sheets were closely stacked each other along with random directions, allowing more edge sites to be exposed (**Fig. 7-3a,d**) and its corresponding FFT represents these stacked carbon sheets are disordered structures. (**Inset of Fig. 7-3d**)
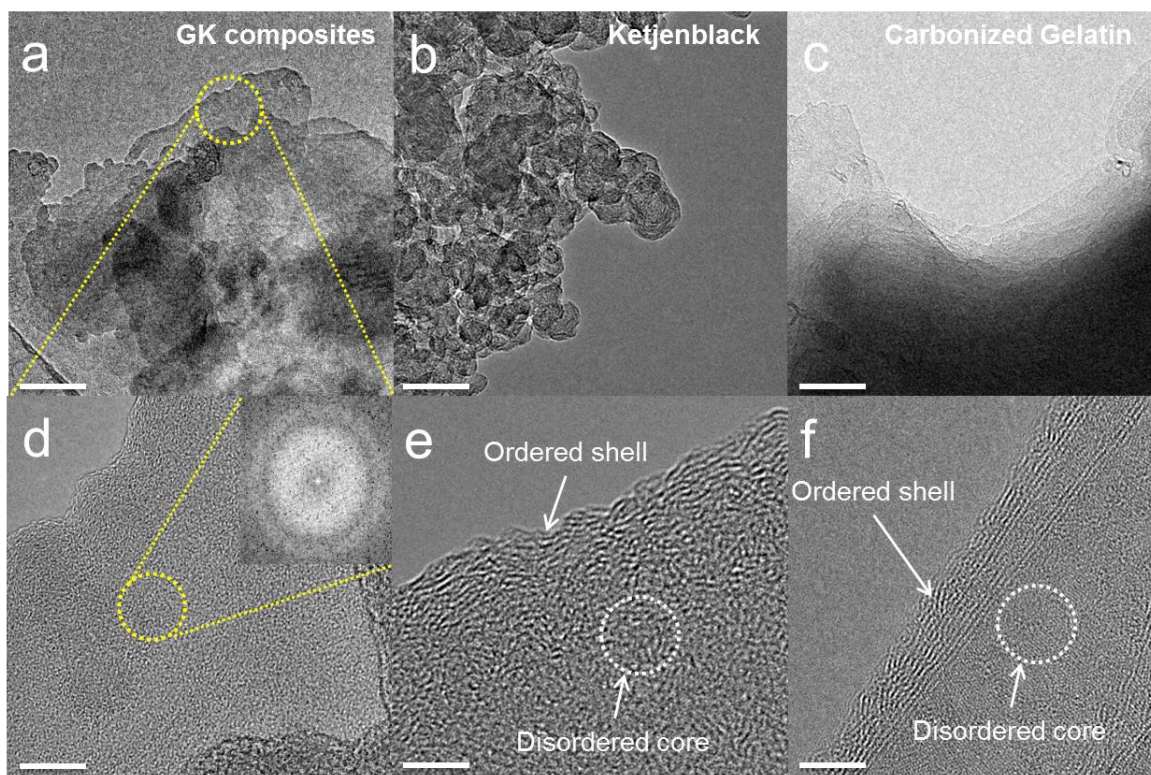
Figure 7-3. Physical morphology of nitrogen-doped gelatin with Ketjenblack carbon composites (GK). TEM images of GK composites (a), Ketjenblack nanoparticles (b), carbonized gelatin (c) and respective magnified images of a, b, and c (d, e, and f), respectively. Inset is FFT of (d). Scale bars for (a-c) and (d-f) are 100 nm and 5 nm, respectively.

These disordered characters were further confirmed in its XRD data in **Figure 7-4**.
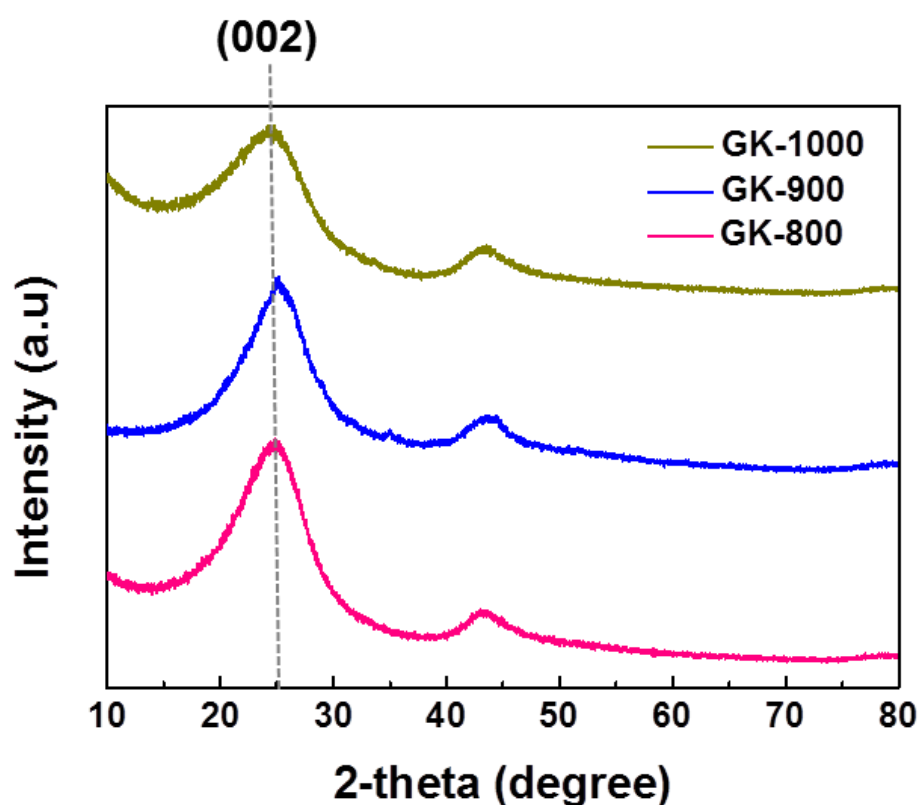
Figure 7-4. XRD data of GKs samples.

There are broad two kinds of peaks at 24.6° and 42.3° which indicate (002) and (100) planes, respectively. These broad (002) basal plane diffraction peaks can be a mixed phase of crystalline and disordered carbon[163]. Furthermore, it should be noted that as-prepared catalysts show a negative shift in the broad (002) peaks compared with the 2θ peak of general graphite powder at about 26.5°[163b], indicating increased interplanar distance between (002) planes. This effect could facilitate a mass transport, thus increasing a kinetic for ORR. To gain the insight into the origin of these randomly oriented stacked carbon sheets structures, each microstructure of ketjenblack nanoparticles and carbonized gelatine was examined. HR-TEM images (**Figure 7-3b,c,e, and f**) show that each of them are composed of outer shell (ordered graphitic) and core (more disordered structures) parts like a morphology acquired from pyrolysis of nitrogen containing precursors[155, 164]. Especially, it is clearly shown that gelatine derived nitrogen doped carbon morphology forms stacked small sheets by random directions. Although apparent morphology of as-prepared GK catalysts is hardly distinguishable from each ketjenblack and carbonized gelatine due to its quite similarity in morphology (**Fig. 7-3a-c**), it is believed that ketjenblack with relatively low contents of precursors (ca. 13 times lower than gelatine in synthetic procedure described in method) are incorporated into carbonized gelatine sheets and the origin of these overall stacked sheets structured comes from carbonized gelatine, not ketjenblack carbon. Therefore, it can be possible to conclude that gelatine derived disordered carbon sheets grow

randomly and tightly along aggregated Ketjenblack carbon with exposed ordered graphitic edge sites due to effective interaction between Ketjenblack and gelatine. Furthermore, these exposed edges along with the outline of gelatine derived carbon sheets could be much favourable to oxygen adsorption as initial step for ORR. Along with these unique physical properties, X-ray photoelectron spectroscopy (XPS) was used to figure out the nitrogen chemical state of the catalysts (**Figure 7-5**).
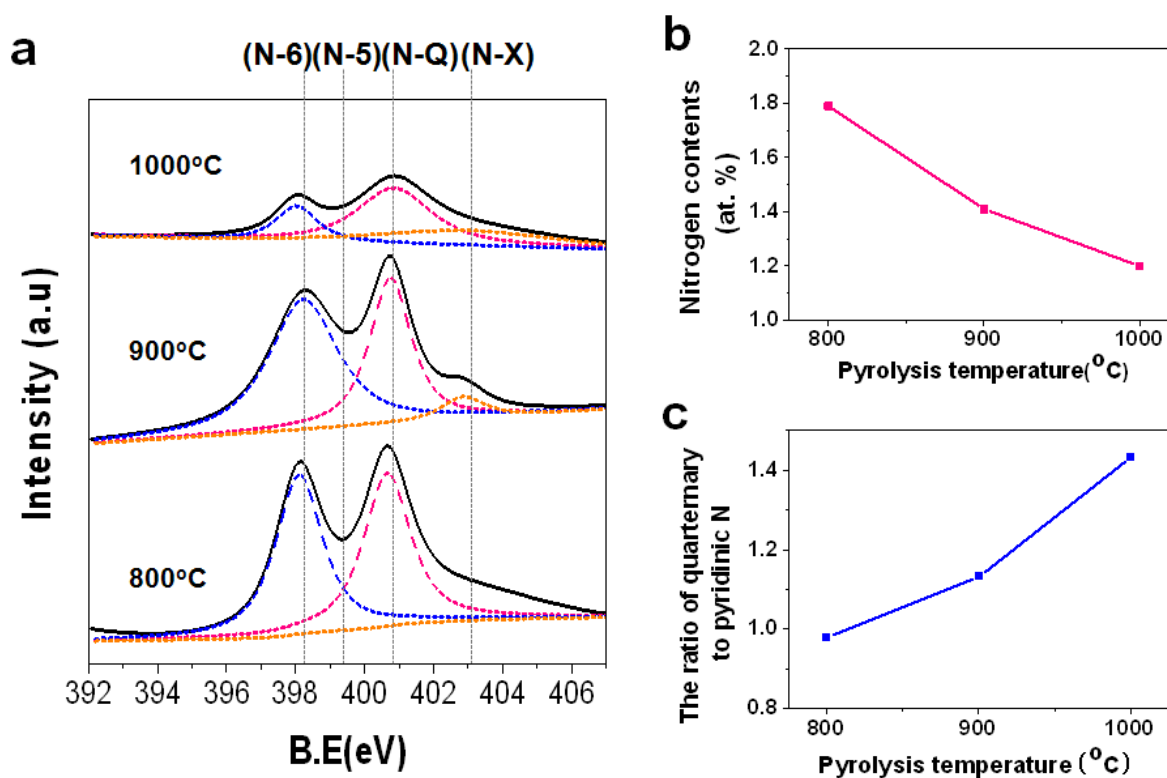
Figure 7-5. Chemical state of nitrogen species in GKs catalysts using XPS analysis. (a) N1s XPS analysis of GK-900. Labeled pyridinic nitrogen as (N-6), pyrrolic as (N-5), quarternary as (N-Q), and oxidized nitrogen as (N-X), (b) Overall nitrogen contents and (c) the ratio of Quarternary N to Pyridinic N depends on pyrolysis temperature.

As shown in **Figure 7-5**, the N 1s spectrum of GKs (pyrolysis above 800°C) can be deconvoluted into four components at 398.1, 399.6, 401.2, and 403.0 eV, corresponding to N-6 (pyridinic), N-5 (pyrrolic), N–Q (quaternary), and N–X (oxidized nitrogen), respectively[156a]. In high resolution spectra of N 1s, predominant peaks are pyridinic and quaternary nitrogen species, otherwise, a contribution of pyrrolic nitrogen, especially, is minor or even negligible due to a decomposition of pyrrolic and pyridone nitrogen into either pyridinic or quaternary N above 800 °C[156a]. The ratio of quaternary (N-Q) to pyridinic (N-6) increases from 0.98 to 1.43 with increasing pyrolysis temperature. Simultaneously, however, overall nitrogen contents decreases from 1.79 to 1.19 at. %) (**Fig. 7-5b, c and Table 7-2**).

Table 7-2. Atomic percent of various samples by XPS.

Sample	C 1s	N 1s	O 1s
	Elemental composition by XPS (At. %)		
GK-800	93.29	1.79	4.92
GK-900	93.90	1.41	4.69
GK-1000	94.15	1.19	4.66

Furthermore, by careful analysis for the C1s spectra, graphitic carbon peak (sp^2 carbon) around 284.1 eV became more symmetric from GK-800 to GK-1000, indicating that the degree of graphitization of the GKs depends on heating temperature, which is also supported by Raman data in **Figure 7-6**.
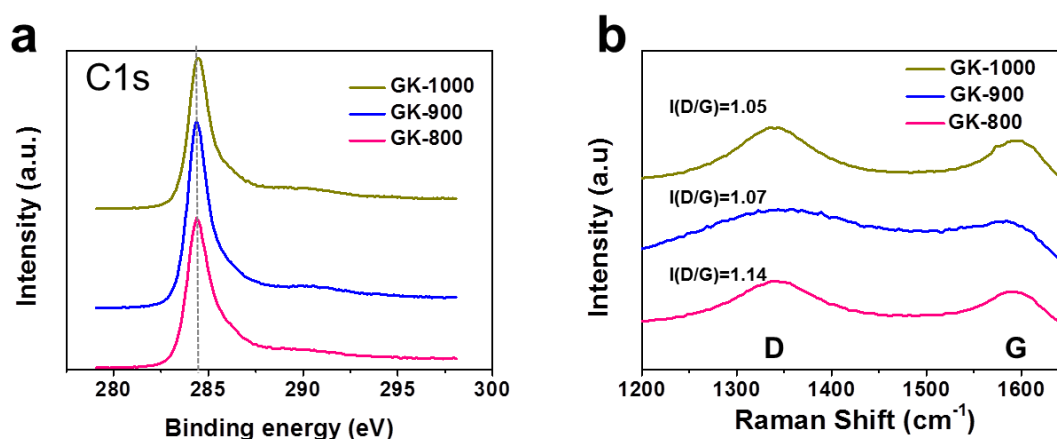
Figure 7-6. (a) XPS high resolution spectrums of C1s and (b) Raman data of GKs samples.

These trends can imply that the ORR activity for N-doped GKs catalysts prepared >800°C well correlates with the ratio of quaternary to pyridinic although the intrinsic role for each nitrogen species for enhanced activity for ORR is on debate[165].

To gain further insight into the ORR activity of GKs, we performed linear sweep voltammetry (LSV) measurements using a rotating ring-disk electrode (RRDE) in O_2-saturated electrolyte solution of 0.1 M KOH at 24°C (**Figure 7-7a,b**).
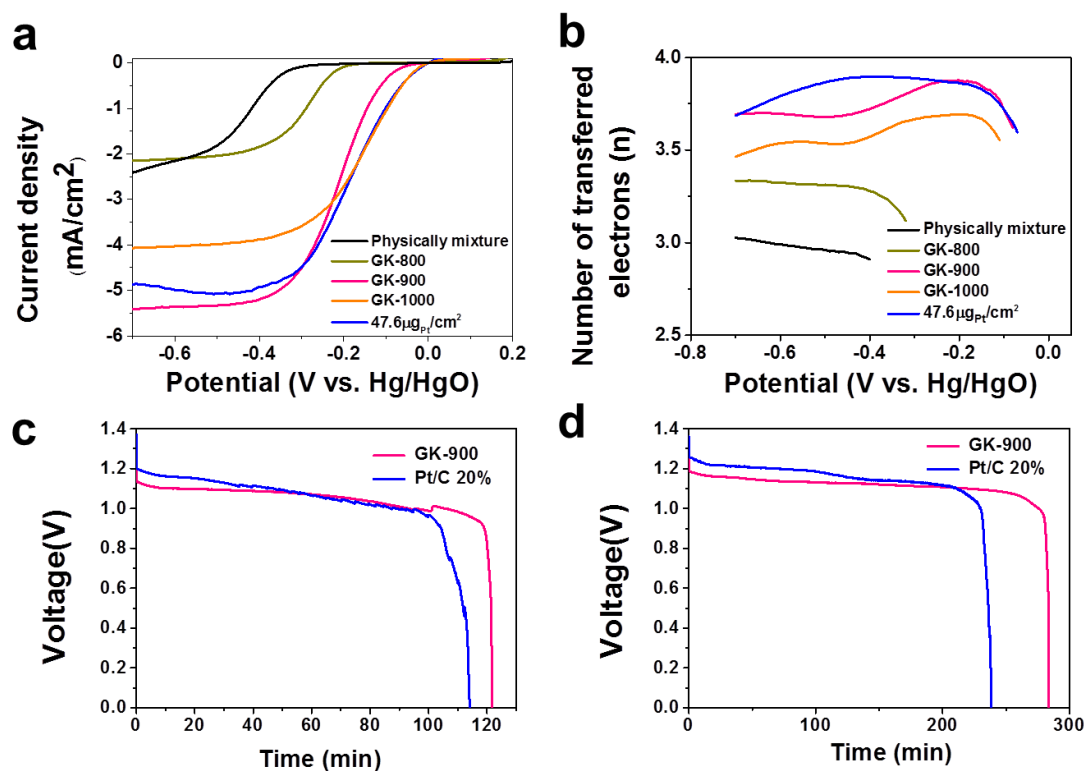
Figure 7-7. Electrochemical characterization for GKs catalysts. (a) Steady-state RRDE experiments of GKs ($0.238mg_{cat}/cm^2$) and Pt/C 20% ($47.6\mu g_{pt}/cm^2$) in O_2-saturated 0.1M KOH at 1600 rpm and 10mV/s scan rate. (b) The number of transferred electrons (n) of GKs, physically mixture of gelatin and KB, and Pt/C catalysts. (c), (d) Zn-air full cell discharge curve for discharge current density at $50mA/cm^2$ and $25mA/cm^2$, respectively.

Before discussion on temperature effect on GKs, it is worthy to note that all GKs shows much better catalytic activity than physical mixture of Ketjenblack and carbonized gelatine (**Fig. 7-7a**). With understanding about the good interaction between gelatine and KB in aqueous solution, these results could be explained due to closely stacked sheet structures. Obviously, introduced Ketjenblack affords better electrical conductivity to carbonized nitrogen doped gelatine carbon sheets in this tightly each other aggregated sheet like architecture. Besides this reason, during pyrolysis, nitrogen species in gelatine could be partially decorated onto KB surface, preparing nitrogen doped KB which also can act as catalysts for ORR[158]. Therefore, this unique GK morphology contributes enhanced catalytic activity for ORR compared to physical mixture without good adhesion, which is also supported by these stacked sheet architectures (**Fig. 7-3**). To reveal reaction pathway for ORR, the number of electrons for GK-900 was determined from disk and ring currents in RRDE results. The calculated value is from 3.7 to 3.85, indicating that oxygen is reduced on this catalyst most likely through a direct four-electron pathway rather than two-electron pathway (**Fig. 7-7b**). This highly stable

110

selectivity for OH$^-$ of GK electrode is comparable to recent metal-free carbon-based catalysts[97a, 166]. Furthermore, this high selectivity to direct conversion from O_2 to OH$^-$ for GK-900 electrode is also supported by much lower peroxide yields than other GKs such as GK-800 and-1000 and even highly comparable to state-of art Pt/C catalysts in **Figure 7-8**.
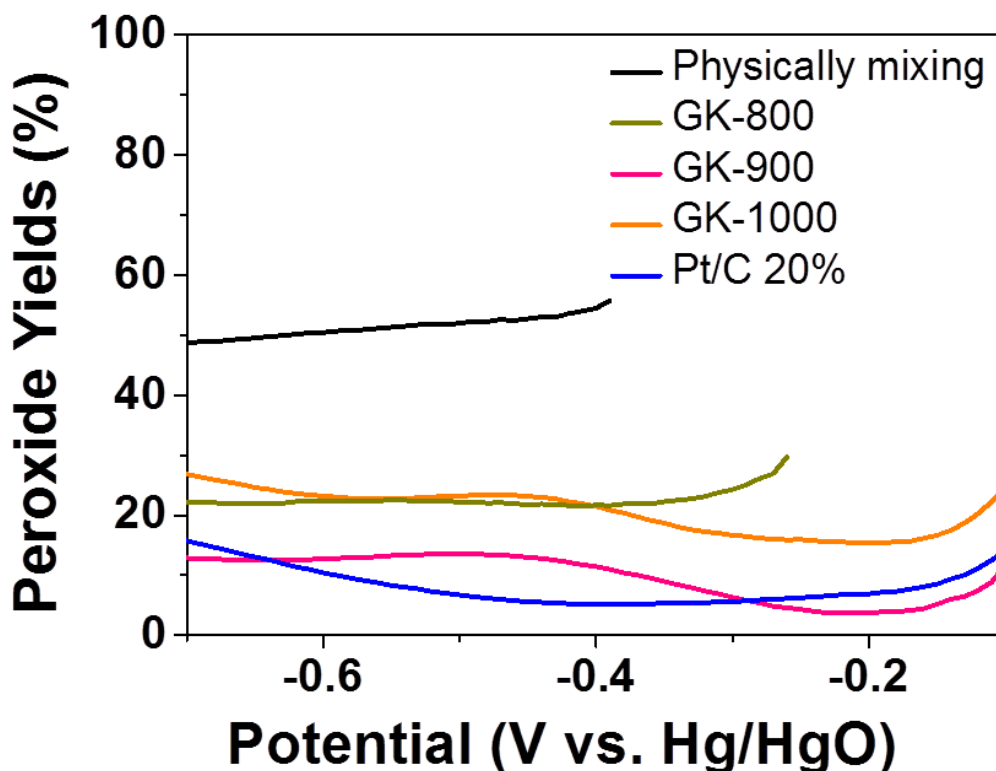
Figure 7-8. Calculated peroxide yields (H$_2$O$^-$) of GKs samples.

When it comes to heating temperature effect, GK-900 and 1000 composites has superior catalytic activity than GK-800 based on a relatively high limiting current density and more positive onset potential, even highly comparable to Pt catalysts at $0.238mg_{cat}/cm^2$ and $47.6\mu g_{pt}/cm^2$ ($0.238mg_{(20\% Pt/C)}/cm^2$) of loading density, respectively, indicating that the as-prepared GK catalyst can be a very promising electrocatalysts for ORR in alkaline media. Furthermore, in detail analysis on GK-900 and 1000, although GK-1000 is more positive onset potential than GK-900, the latter has higher limiting current density. For the GKs samples, the amount of the pyridinic type of nitrogen decreases whereas those of the quaternary nitrogen increases from GK-800 to GK-1000 (**Fig. 7-5**). These results conclude that the ratio of pyridinic to quaternary N could be a primary indicator affecting enhanced catalytic activity for ORR in our system with beyond required portion of quaternary N between GK-900 and GK-1000 compared to GK-800. Furthermore, these catalytic activities of GKs electrodes clearly depend on the total amount of nitrogen. For example, GK-800 (1.79 at. %) has inferior activity to other GK-900 (1.41 at. %) or GK-1000 (1.19 at. %). Therefore, it is believed that the proper

combination of pyridinic and quaternary-nitrogen groups with optimized nitrogen contents can be a key factor affecting enhanced ORR activity in our system.

As shown in **Fig. 7-7c and d**, we carried out zinc-air cell test correlate with enhanced catalytic activity measured in half-cell condition at 25 and 50 mA/cm^2. It should be note that testing Zn-air cell under ambient static air condition is much more practical than under intentionally oxygen blowing and even water vapour saturated ideal condition because both intrinsic activity and architecture of a catalysts sensitive to oxygen and electrolyte diffusion can contribute overall cell performance.[149a] As expected, acquired voltage profile is almost flat, indicating that only oxygen and zinc participate in cell reaction constantly without any chemical redox reaction of active materials in electrode like a chemistry of Li-ion battery. According to those data, our catalyst observe improved performance in discharge capacity compared to that catalyzed by 20% Pt catalysts both at 25 to 50 mA/cm^2 and much more enhanced electrochemical improvement of Zn-air cell compared to those without catalysts and even highly comparable to Pt catalysts. For example, the peak power density of the cell with GK-900 was about 193 mWcm^{-2} (**Fig. 7-7c, d and 7-9 and Table 7-3**), which is slightly higher than about 188 mWcm^{-2} for the cell with the Pt/C catalyst although there is slight voltage drop caused by activation loss at initial stage of discharge also shown in slightly more positive onset potential of Pt than GK-900 in our RRDE results (**Fig. 7-7a**).
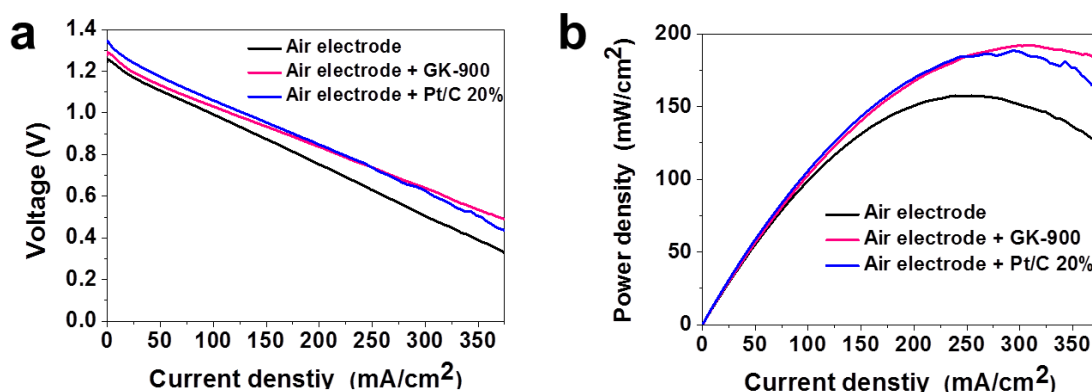
Figure 7-9. (**a**) Current-voltage and (**b**) power-current curves of Zn-air cells with GK-900, 20% Pt/C catalysts and air electrode without any catalyst.

Table 7-3. Survey of Zinc-air full cell activity of Metal-free catalyst and Non-precious metal catalyst of previous works.

Sample	method	Electron transferred number (n)	Peak power density at Zinc-air battery (mW/cm^2)	Reference
GK-900	Pyrolyzed Gelatine-KB jelly at 900°C	3.74	193	**This work**
CoO/N-CNT[167]	Multiwalled CNT and Co(OCH$_2$CH$_3$)$_2$ were stirred in NH$_4$OH solution then annealed at 400°C	-	265[a]	[167]
Amorphous MnO$_x$ NWs on KB[73]	Ketjenblack carbon supported amorphous MnO$_x$	-	190	[73]
rGO-IL/Mn$_3$O$_4$[72f]	Mn$_3$O$_4$ on reduced-Graphene Oxide by a simple facile solution method	3.5	120	[72f]

a. Blowing pure oxygen gas for Zn-air full cell test.

The chronoamperometric (*i-t*) response shows the response for ORR for GK-900 and Pt/C electrodes in **Figure 7-10**.
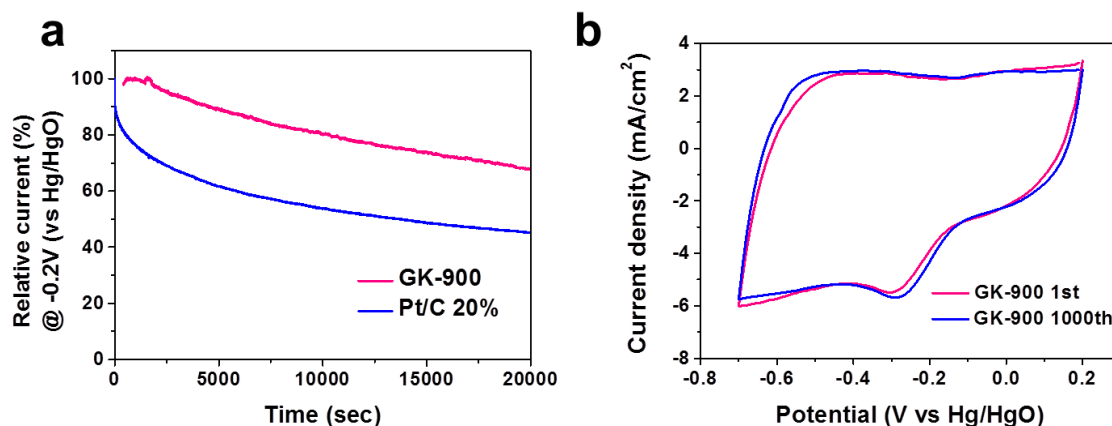
Figure 7-10. Chronoamperometric response of (**a**) GK-900 and 20% Pt/C in O_2-saturated 0.1M KOH solution at -0.2 V (vs Hg/HgO) at 1600 rpm each. (**b**) CV curves at initial and after 1000 cycle at 50 mV/s of scan rate in O_2-saturated 0.1M KOH solution.

As can be seen, the continuous ORR at -0.2V (vs. Hg/HgO) showed that a remaining relative current density for GK-900 (68% at 20000s) is higher than that of Pt/C electrodes (45% at 20000s). This enhanced durability is also supported by almost unchanged cyclic voltammetry curves of GK-900 even after 1000 cycles. These results clearly indicate that the active sites of the GK are not affected under ORR potential range unlike commercial Pt/C[154b], thus rendering N-C active sites much more stable. Furthermore, in methanol posing test, the current response of GKs catalysts is insensitive to the added methanol in **Figure 7-11**.
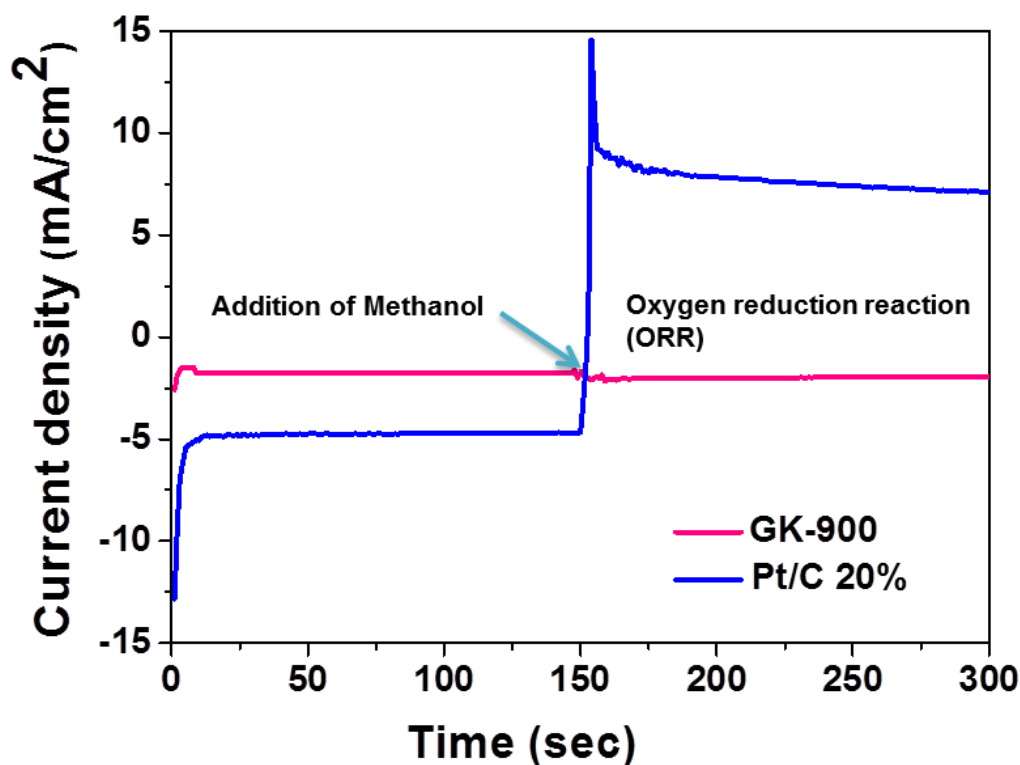
Figure 7-11. Chronoamperometric response of 10% (w/w) methanol of GK-900 and 20% Pt/C in O_2-saturated 0.1M KOH solution at -0.2 V (vs Hg/HgO) at 1600 rpm and 10mV/s scan rate.

In contrast, Pt/C catalysts showed a sharp fluctuation upon the addition of methanol. Therefore, it follows that our developed GKs indicate a better methanol tolerance than Pt/C catalysts, enabling it to be applied for DMFC (direct methanol fuel cell) as well as efficient and durable cathode catalysts for Zn-air batteries.

In conclusion, we established easily scalable irregular stacked nitrogen-doped carbon sheets catalysts for efficient metal free electrocatalysts for ORR in alkaline solution. In this work, efficient utilization of hydrophobic Ketjenblack in aqueous media is possible due to enhanced interaction by amphiphilic character of gelatine mediator as nitrogen doped carbon precursors, thus making mass production possible. Its comparable catalytic activity and better durability with Vulcan carbon supported Pt catalysts was demonstrated and synthesized catalysts were also effectively applied to Zn-air battery. In physiochemical analysis, it revealed that as-prepared GK catalysts composed of proper combination of quaternary and pyridinic nitrogen species around more exposed edge sites by irregular stacked sheets increasing catalytic activities for ORR.

Experimental Section

Catalyst preparation

For preparation of catalysts precursors, 25g of commercial gelatine powder (purchased from Geltech Co.,Ltd. Korea) were fully dissolved in 50mL of distilled water at 60°C under magnetic stirring for about 3 hours. When gelatine was completely dissolved in water, and 2g of commercial Ketjenblack EC-600JD (KB) was added into the gelatine solution with stirring for uniform dispersion of KB. Finally, this gelatine-KB solution was kept in the refrigerator about 30mins below 3°C, and were pyrolyzed under Ar atmosphere (flow rate of 50ml/min) at 800, 900, and 1000°C for 1hr.

Preparation of catalysts ink and working electrode

The formulation of catalyst ink is a mixture of 12 mg of the GKs catalyst powder, 400μl of 0.05 % Nafion (Aldrich) solution and 1600μl of ethanol. Briefly, desired catalyst ink was prepared by ultrasonically mixing in distilled water for at least 1 hr to form homogeneous catalysts ink. 5μl of ink was loaded on the surface of working electrode, resulting in 0.238mg$_{cat}$/cm^2. For the physical mixture catalysts, 24mg of carbonized gelatine at 900°C was mixed well with 2mg of ketjenblack carbon using mortar and then the ink was prepared to 0.238mg$_{cat}$/cm^2 of loading density with above mentioned procedure. For the 47.6μg$_{pt}$/cm^2 catalysts, 12mg of Pt/C 20% powder was dissolved in 400μl of 0.05% Nafion (Aldrich) solution and 1600μl of ethanol. This desired catalyst ink was ultrasonically mixed at least 1hr to get homogeneous catalysts ink. Then 5μl of ink was loaded on the surface of working electrode, resulting in 0.238mg$_{(20\%\ Pt/C)}$/cm^2, corresponding to 47.6μg$_{pt}$/cm^2 with above mentioned same methods.

Electrochemical measurements

Rotating ring disk electrode (RRDE) (ALS Co., Ltd) experiments were carried out using the GK-series catalysts film (deposited on GC electrode) as the working electrode in 0.1 M KOH alkaline electrolyte with saturated O$_2$. Pt wire and Hg/HgO are used as a counter and a reference electrode, respectively. Electrochemical characterization was conducted using bi-potentiostat (IviumStat). 10 mV/s of scan rate was swept from 0.2 to -0.7 V and sufficient ring potential of 0.4 V was biased to oxidize intermediate during ORR. The collection efficiency (N) was determined under Ar atmosphere using 10 mM K$_3$[Fe(CN)$_6$], which is around 0.41. This value is very close to its theoretical value of 0.42. The number of electrons transferred (n) and peroxide yields (H$_2$O$^-$) were calculated using the equations below.

$$H_2O^- (\%) = 100\frac{2I_r/N}{I_d + I_r/N} \quad (1)$$

$$n = 4\frac{I_d}{I_d + I_r/N} \quad (2)$$

Zn-air full cell tests

Full-cell test of our catalysts, we prepared 0.75g zinc powder as an anode, and 200μl of 6M KOH was used for electrolyte. Nylon membrane was used for a separator. The air cathode was prepared by uniformly casting the catalyst ink on the prepared gas diffusion layer (the catalyst ink formulation: 10mg of catalyst, 100ul of 5wt% of Nafion in mixture of lower aliphatic alcohols and H_2O (Sigma-Aldrich), and 400ul of ethanol) (Supplementary Figure S8). Assembled full-cell was tested at discharge current densities 25mA/cm^2 and 50mA/cm^2. The gas diffusion layer (GDL) was prepared from a mixture of activated carbon (Darco G-60A, Sigma Aldrich) and PTFE binder (60 wt% PTFE emulsion in water, Sigma Aldrich) at a weight ratio of 7 to 3 with about 350 μm of thickness to ensure proper gas distribution and sufficient current collection[158]. This as-prepared GDL was used as the reference for comparison to confirm enhanced performance of catalyzed air electrode in polarization curve of Zn-air battery.

Physical characterization

The material morphology was examined using a high-resolution transmission electron microscopy (HR-TEM) (JEOL JEM-2100F) operating at 200 kV. Powder analysis was performed using an X-ray diffractometer (XRD) (D/Max2000, Rigaku). Oxidation state of elements was analyzed using X-ray photoelectron spectroscopy (XPS) (Thermo Scientific Kα spectrometer, 1486.6eV) and surface carbon state was examined using micro-Raman (WITec).

Chapter 8. Ligand effect on oxygen reduction in alkaline solution: [Fe(phen)₂L₂] (L= CN or NCS) complexes as electrocatalysts

The different strength filed ligands (weak and strong field ligands, NCS and CN, respectively) are introduced to reveal the ligand induced Fe effect on ORR. This approach, allows us to investigate the Fe active sites with a different point of view. Herein, we selected [Fe(II)(phen)₂(CN)₂]·3.5H₂O (Fe-CN) and [Fe(II)(phen)₂(NCS)₂]·H₂O (Fe-NCS) and introduced metal organic framework-5 (MOF-5) to stabilize the Fe-CN complex (MOF[Fe-CN]). Regarding the electrochemical properties, the activity for ORR increases as the amount of Fe increases, indicating that Fe is still active sites in this hexa-coordinated system. Furthermore, NCS induced Fe facilitates ORR, but MOF[Fe-CN] suppress ORR. From the possible molecular orbital overlap in this structure, introduced NCS and CN can clearly interact with central Fe species, making coordinated Fe be active or inactive for ORR.

The tremendous efforts made in the design of advanced non-precious metal electrocatalysts with unique architectures have been devoted to enhancing the catalytic activity dramatically for the oxygen reduction reaction (ORR).[4] For example, metal coordinated nitrogen-carbon (metal/N/C) electrocatalysts have been studied as efficient non-precious metal electrocatalysts since Jasinski's pioneering work and subsequent studies.[98, 168] While superior catalytic activity for ORR has already been demonstrated, there is still debate on the exact catalytic active sites during high temperature pyrolysis and on the intrinsic role of the active sites. So far only limited synthetic approaches have been used in the development of heat treated Fe-based catalysts in spite of the fact that the intrinsic properties of Fe are governed by the surrounding environments. Recently, Li et al. introduced the CN⁻ as a blocking ligand of Fe/N/C catalysts and studied the effect on the ORR.[169] They showed that a coordinated Fe can clearly participate in this catalytic process using Fe-CN interaction and further TOF-SIMS negative and positive ion imaging. This method results in a deterioration of the catalytic activity for the ORR, which enables us to identify that coordinated iron can be considered as an actual active site. Other evidence showed coordinated Fe can act as the heart of intrinsic catalytic activity for ORR by examining that remained Fe(II)N₄/C and Fe(II)N₂₊₂···N$_{prot}$/C has catalytic activity for ORR after acid washing from Mössbauer spectroscopy.[170] Furthermore, the amount of Fe in Fe/N/C catalysts can alter the ORR mechanism from an indirect 2-electron transfer pathway to a 4-electron transfer dominated process and the best ORR performance was achieved at the optimized Fe contents. This study clearly indicates that coordinated iron can be also considered as an actual active site.[60b] From above results, although an iron N$_x$ chelate complexes could deeply participate in ORR as catalysts, the only nitrogen coordinated Fe catalysts (Fe-N₂ or N₄) could limit the full utilization of Fe

active sites because of limited ligand effect on Fe. Therefore, in this regard, studying different strength filed ligand effects on Fe can be a significant milestone in the development of next generation iron based catalysts beyond conventional Fe/N/C catalyst approach, which is the subject of this present study. Based upon this point of view, the fully coordinated Fe system, hexacoordinated iron (II) systems, can be good reference materials because additional ligand can be introduced. Accordingly, it is possible to confirm that even fully saturated system still has catalytic activity for ORR and the same approach about iron active site in conventional Fe/N/C catalysts still can be extended to these fully saturated system.[171]

Our study started with nearly the same molecular structures, i.e., two different strengths ligand-coordinated Fe/N/C complex and reports the ligand effect on ORR and intrinsic active site with more systematic manner in fully saturated hexacoordinated iron (II) systems. Fully coordinated Fe in hexacoordinated iron (II) systems can still act as active sites for ORR like conventional square N4 coordinated Fe system.[168b] The introduced Fe can act as catalysts, while it hinders ORR. These clearly showed that this ligand effect cannot be negligible and rather determine which Fe is active or inactive for ORR. Therefore, these valuable different views in Fe/N/C catalysts will afford more systematic approaches to the development of next-generation iron based catalysts for fuel cells and metal-air batteries.

We selected $[Fe(II)(phen)_2(CN)_2]\cdot 3.5H_2O$ (S=0, $t_{2g}^6 e_g^0$) and $[Fe(II)(phen)_2(NCS)_2]\cdot H_2O$ (S=2, $t_{2g}^4 e_g^2$) with a low and high spin state, respectively, (hereafter denoted as the Fe-CN and -NCS complex for brevity, respectively) as the model compounds in this work (**Figure 8-1a**).[172]
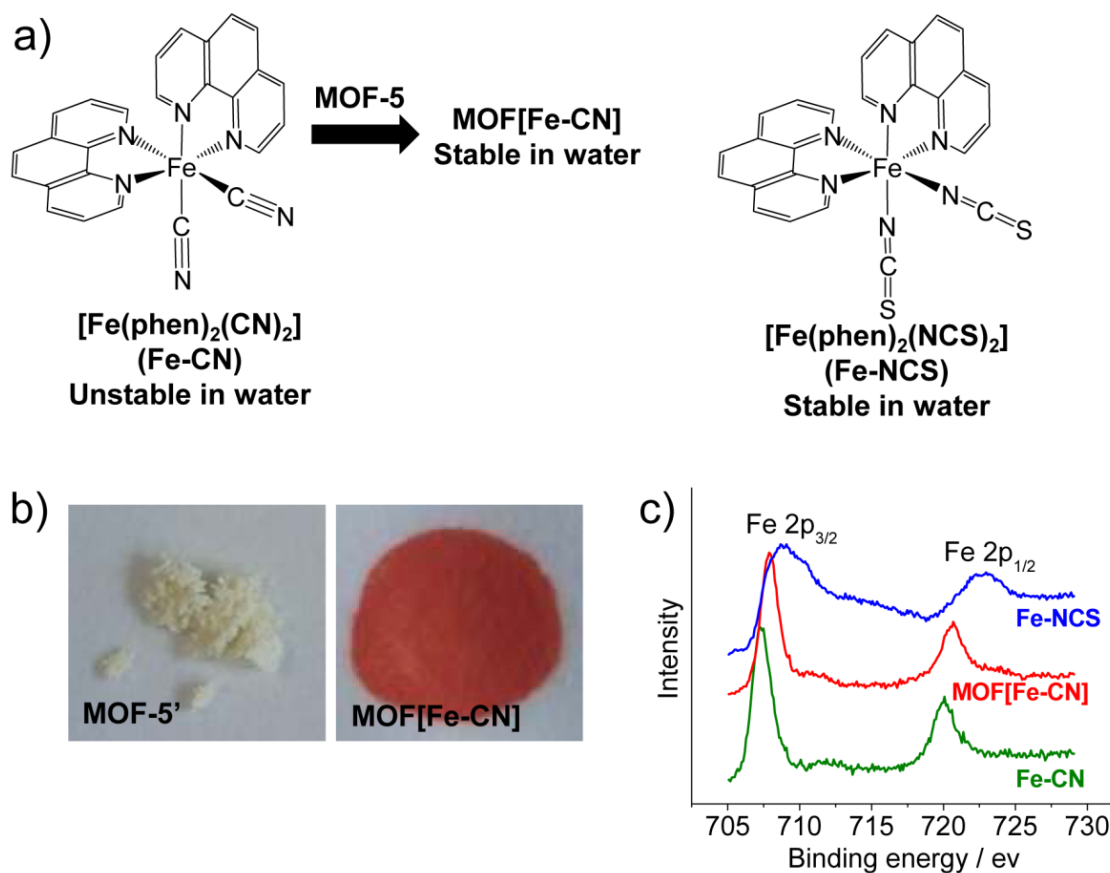
Figure 8-1. (a) [Fe(II)(phen)$_2$(CN)$_2$]·3.5H$_2$O (Fe-CN), Fe-CN stabilized with MOF-5 (MOF[Fe-CN]), and [Fe(II)(phen)$_2$(NCS)$_2$]·H$_2$O (Fe-NCS) complex in this study. Note that Fe-CN complex is encapsulated with MOF-5 to prevent from dissolving in water. (b) Digital photograph of MOF-5' and MOF[Fe-CN]. (c) High resolution XPS of Fe2p for Fe-NCS, MOF[Fe-CN], and Fe-CN.

The Fe-CN complex, however, is easily soluble in water, while Fe-NCS is insoluble, indicating that it is impossible to apply this catalyst in an aqueous based solution to gain the electrochemical properties for an oxygen reduction reaction. Therefore, we newly introduce metal organic framework-5 (MOF-5) as a stabilizer for the Fe-CN complex (**Fig. 8-1a**). Interestingly, MOF-5 exposed to air generates a hydroxyl group (-OH) within the MOF-5 itself, resulting in a stabilized MOF-5' in air and water (hereafter, we designate MOF-5 exposed to air as MOF-5')[173] in **Figure 8-2**.
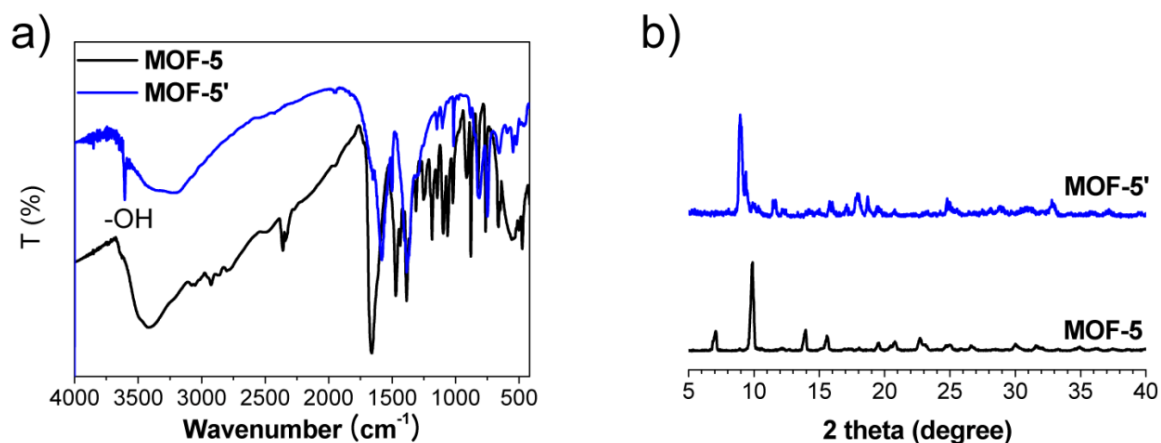
Figure 8-2. IR data (a) and PXRD patterns (b) of as-synthesized MOF-5 and MOF-5'.

In **Fig 8-2**, XRD patterns of MOF-5' is different from those of MOF-5. The important feature of XRD pattern of MOF-5' is the missing of the peak $2\theta = 7.0°$, probably due to disruption of periodicity induced by solvent molecules that fill the mesopores of MOF-5. A new splitting of the peaks at $2\theta = 8.9$ and 9.4 appear in MOF-5', which is correlated with the distortion of lattice structure of MOF-5 (cubic system).[4] MOF-5 is very sensitive of air and water, but MOF-5' is very stable in air and water. We initially performed physical and chemical characterizations of a MOF-5' encapsulated Fe-CN (hereafter denoted as MOF[Fe-CN] for brevity) and Fe-NCS complex used in this study. Infrared spectroscopy and PXRD clearly indicate that the two samples were prepared successfully and that the Fe-CN complex can be inserted into MOF-5' in **Figure 8-3**.
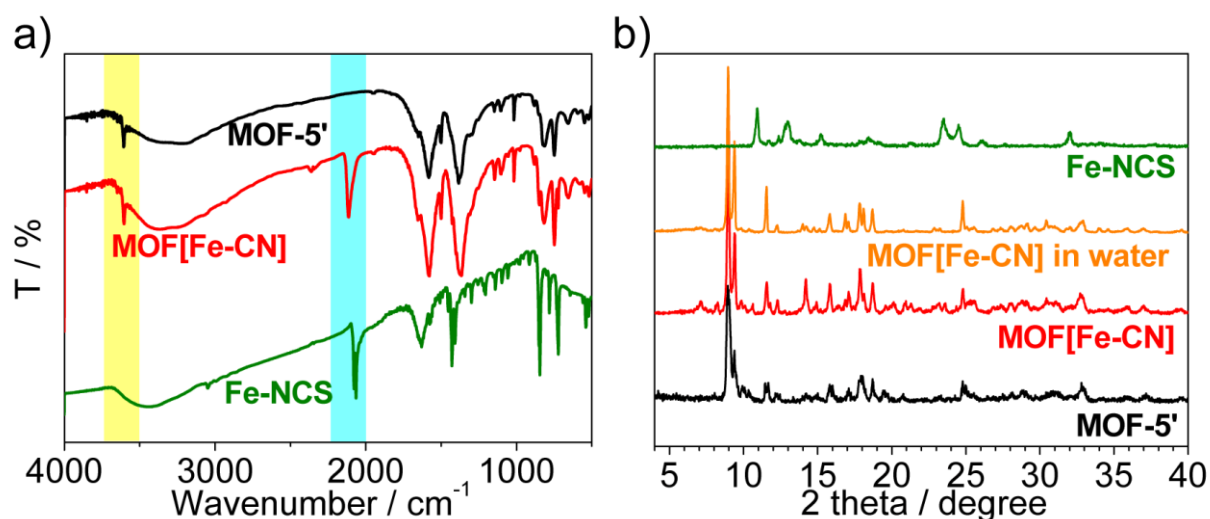
Figure 8-3. IR data (a) and PXRD patterns (b) of $[Fe(II)(phen)_2(CN)_2]\cdot3.5H_2O$ (Fe-CN), Fe-CN stabilized with MOF-5 (MOF[Fe-CN]), and $[Fe(II)(phen)_2(NCS)_2]\cdot H_2O$ (Fe-NCS).

In the IR spectra, the OH vibration peaks of MOF-5' (3606 cm^{-1}) and MOF[Fe-CN] (3604 cm^{-1}) have sharp signals, which can be assigned as free-OH group vibration (**Fig.8-2**). This indicates that the OH group was newly formed in MOF-5 and was retained after the insertion process, which makes it possible to assume that deformed MOF-5 (MOF-5') can stabilize the Fe-CN complex. The CN peaks for Fe-CN complex are 2078 and 2065 cm^{-1}, which are the symmetrical and antisymmetrical stretching mode, respectively, whereas the CN peak for MOF[Fe-CN] shows only antisymmetrical stretching and has a higher wavenumber at 2115 cm^{-1}. This suggests that there could be interaction via the OH group between MOF-5' and the CN of Fe-CN; therefore, MOF[Fe-CN] can be stabilized for this reason. The powder X-ray diffraction (PXRD) pattern of the as-synthesized MOF[Fe-CN] is very similar to that of MOF-5', indicating that Fe-CN has little effect on the MOF-5 structures during this spontaneous insertion process. Furthermore, the PXRD peaks of the water exposed to MOF[Fe-CN] are very similar to the pristine Fe-CN peaks. Besides, the color changes also indicate Fe-CN complex can be inserted into MOF. It is worthy noted that the color of pristine Fe-CN is purple, but MOF[Fe-CN] is red because of a change in surrounding environments (**Fig. 8-1b**). In a XPS study, it clearly indicated that MOF[Fe-CN] and Fe-NCS exhibit a low and high spin state of Fe, respectively, according to the high resolution Fe2p XPS results (**Fig.8-1c**). The XPS of Fe-CN and MOF[Fe-CN] are the almost same, not exact identical, indicating that this slight difference explain there are a little interaction between MOF-5 and Fe-CN complex. A spin energy of Fe-CN is ca. 12.5 eV between 2p3/2 and Fe 2p1/2 in Fe2p. Otherwise, the difference between two major peaks in Fe2p of Fe-NCS is about 13.6 eV, which agrees with the reports very well.[174] Obviously, these introduced different strength filed ligands can affect a spin state of coordinated Fe metal in these complexes.

To gain insight into the ligand effect on the ORR activity, we first prepared a catalyst ink by adding Ketjenblack carbon to maintain a sufficient electrical conductivity in the as-prepared samples. We controlled each ligand induced Fe portion in these complexes by physically mixing a proper amount of MOF[Fe-CN] and Fe-NCS each other to reveal both the total Fe amount and each ligand effect on ORR simultaneously in **Table 8-1 and 8-2**.

Table 8-1. Preparation of desired catalyst inks.

Sample	MOF-5	MOF[Fe-CN]	Fe-NCS	KB	Sample Notation
1	-	-	-	5.5mg	KB
2	3.3mg	-	-	5.5mg	MOF+KB
3	-	3mg	-	5.5mg	3-MOF[Fe-CN] + KB
4	-	2mg	1mg	5.5mg	2-MOF[Fe-CN]+ 1-Fe-NCS + KB
5	-	1mg	2mg	5.5mg	1-MOF[Fe-CN]+ 2-Fe-NCS + KB
6	-	-	3mg	5.5mg	3-Fe-NCS + KB

Table 8-2. Calculation of total amount of Fe, Fe-CN and NCS portion within the samples.

Samples	Total amount of Fe (wt. %)	Fe-CN portion (wt. %)	Fe-NCS portion (wt %)
3-MOF [Fe-CN]	0.83	0.83	0
2-MOF[Fe-CN] + 1-Fe-NCS	9.83	0.55	9.28
1-MOF[Fe-CN] + 2-Fe-NCS	19.93	0.28	19.65
3-Fe-NCS	29.47	0	29.47

Then, linear sweep voltammetry (LSV) measurements were carried out on a rotating ring disk electrode (RRDE) in an O_2-saturated electrolyte solution of 0.1 M KOH (**Figure 8-4**).
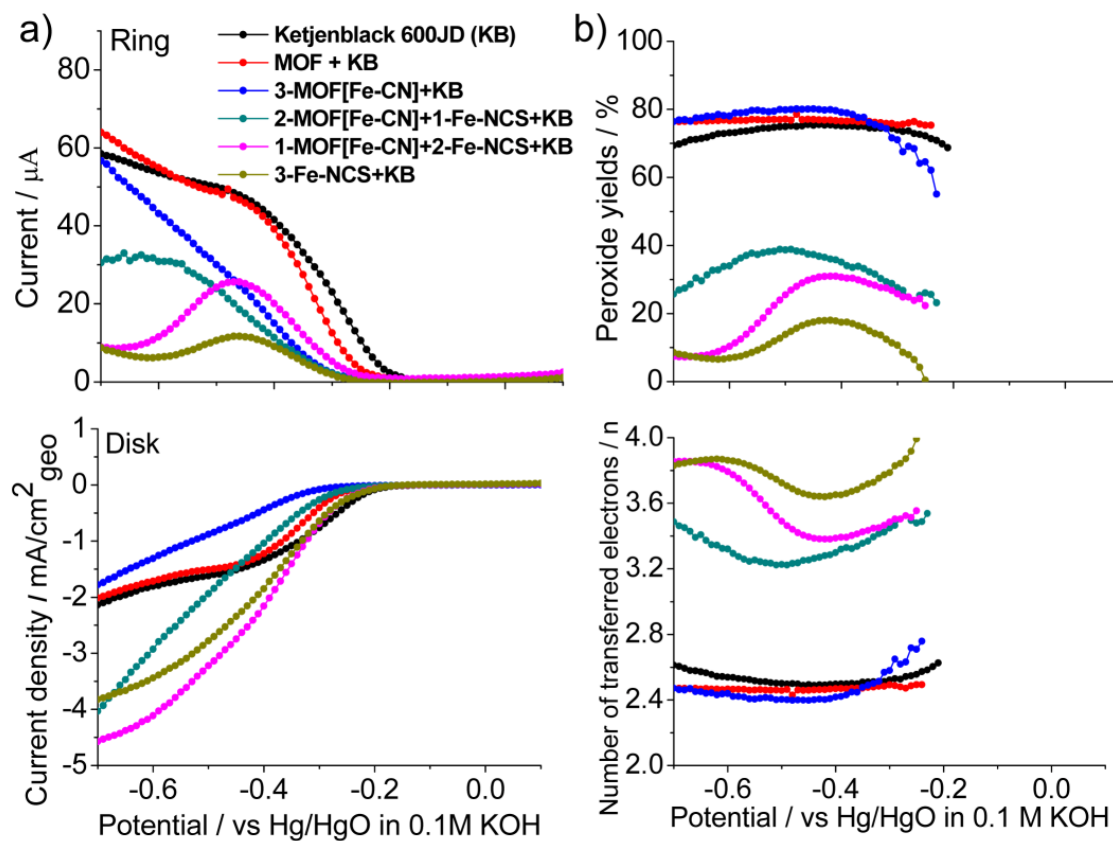
Figure 8-4. Steady-state RRDE experiments of as-prepared samples in O_2 saturated 0.1M KOH at 2000 rpm. (a) Ring current (top) and disk (bottom) current density were separated for convenience. (b) Its peroxide yields (%) (top) and the number of electrons (n) transferred (bottom).

When comparing MOF-5' blended with carbon (MOF+KB) and pure Ketjenblack carbon (KB), very similar activity and current shape for the ORR was observed, although the KB had a slightly positive onset potential. It is believed that a majority activity for ORR resulted from KB, not MOF-5 because of an insulating properties of MOF. Besides, as the total amount of Fe increases in the mixture sample of MOF[Fe-CN] and Fe-NCS from 0.83 to 29.47 wt% of Fe, the onset potential shifts to more positive direction and a higher disk current, a lower ring current and peroxide yield, and nearly four transferred electrons for ORR are gained, which resulting in a direct ORR pathway. Besides, electrochemical impedance spectroscopy showed that charge transfer resistances sharply decrease as increasing the total amount of Fe species in **Figure 8-5**.
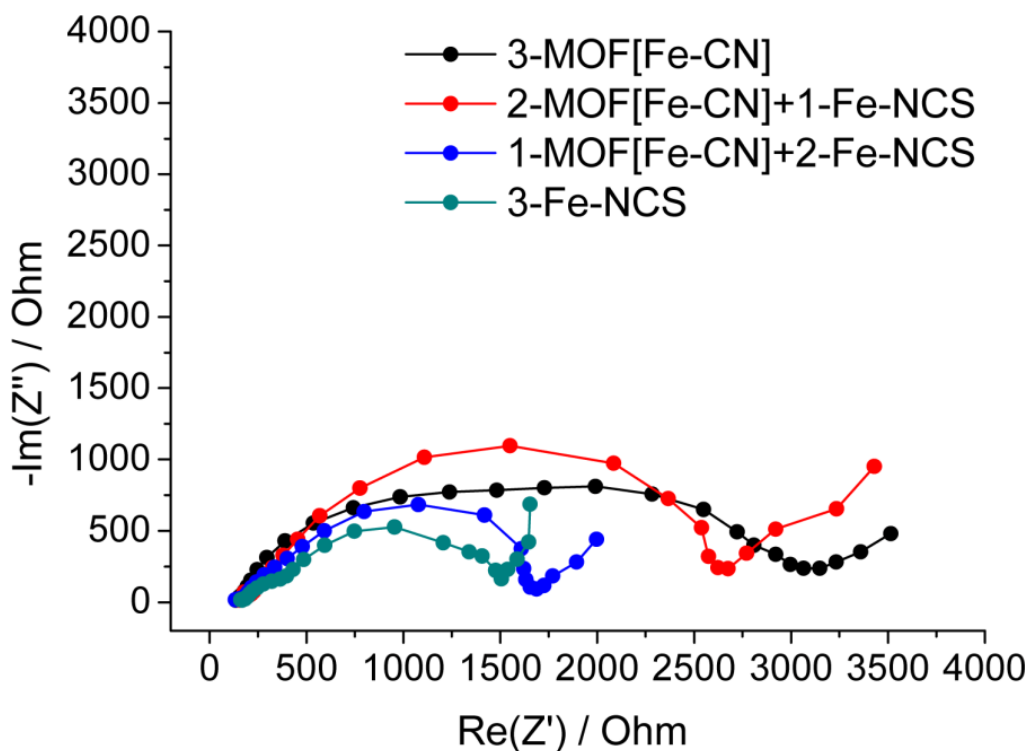
Figure 8-5. Nyquist plots for 3-MOF[Fe-CN], 2-MOF[Fe-CN] + 1-Fe-NCS, 1-MOF[Fe-CN] + 2-Fe-NCS, 3-Fe-NCS. Impedance spectra were taken at -0.4 vs. Hg/HgO in O_2-saturated 0.1 M KOH at 2000 rpm from 10 kHz to 0.01 Hz with 10 mV of single sine wave.

Based on these experimental results, the ORR performance is closely related with the amount of Fe and it follows that coordinated Fe species in hexacoordinated iron (II) systems still can act as the heart of catalytic activity sites during ORR like a conventional Fe/N/C catalysts. When it comes to ligand effects, interestingly, as increasing in the portion of Fe-NCS, ORR performance also increase. These activity trends are correspondence to those according to the total amount of Fe.

This result indicates that enhanced ORR activity can nearly result from the increased portion for Fe-NCS from 9.28 to 29.47 wt% Fe. Otherwise, when the CN induced Fe (Fe-CN) is introduced; the activity for ORR is inferior to that in both KB and MOF+KB. Obviously, this result cannot be explained because the coordinated Fe can act as catalysts for ORR in hexacoordinated system. Therefore, it is logically concluded that the CN induced Fe suppress ORR performance together with the introduced MOF-5 although the hindrance of MOF is a little effect on overall performance for ORR compared to KB and MOF + KB. Therefore, the NCS and CN ligands coordinated iron active sites can be activated or deactivated according to which ligand binds to Fe, resulting in totally different overall ORR performance. Therefore, selecting which ligands induced Fe in a hexacoordinated Fe complex can determine whether Fe act as catalysts or inhibitor for ORR, which can be a much more systematic approach in designing advanced Fe/N/C catalysts.

Based on the experimental results, ORR performance is closely related with both the amount of Fe and which ligand coordinated Fe, which corresponds to our conclusion that ligand coordinated Fe can affect ORR performance. These results indicate that there are very close relationship between ligand coordinated Fe and introduced oxygen molecules. From this point of view, it is worthy noted that this interaction can be only possible in hexacoordinated Fe complex through the indirect π-overlap via ligand, Fe-ligand$\cdots$O$_2$ (**Figure 8-6**). Especially, π-overlap is much more favorable than σ-overlap when considering orbital symmetry of Fe, ligand, and oxygen. This assumption can be clearly supported with the previous report of a significant contribution of the π orbital of the CN and SCN to the central Fe species in the almost same system to our reference materials.[175] This means that introduced ligand determines the available orbital of Fe that can interact with outer oxygen molecule, which can make coordinated Fe active or inactive for ORR. Therefore, a molecular overlap between Fe and oxygen molecules via ligand is significant as a critical step for ORR in a hexacoordinated Fe complex.
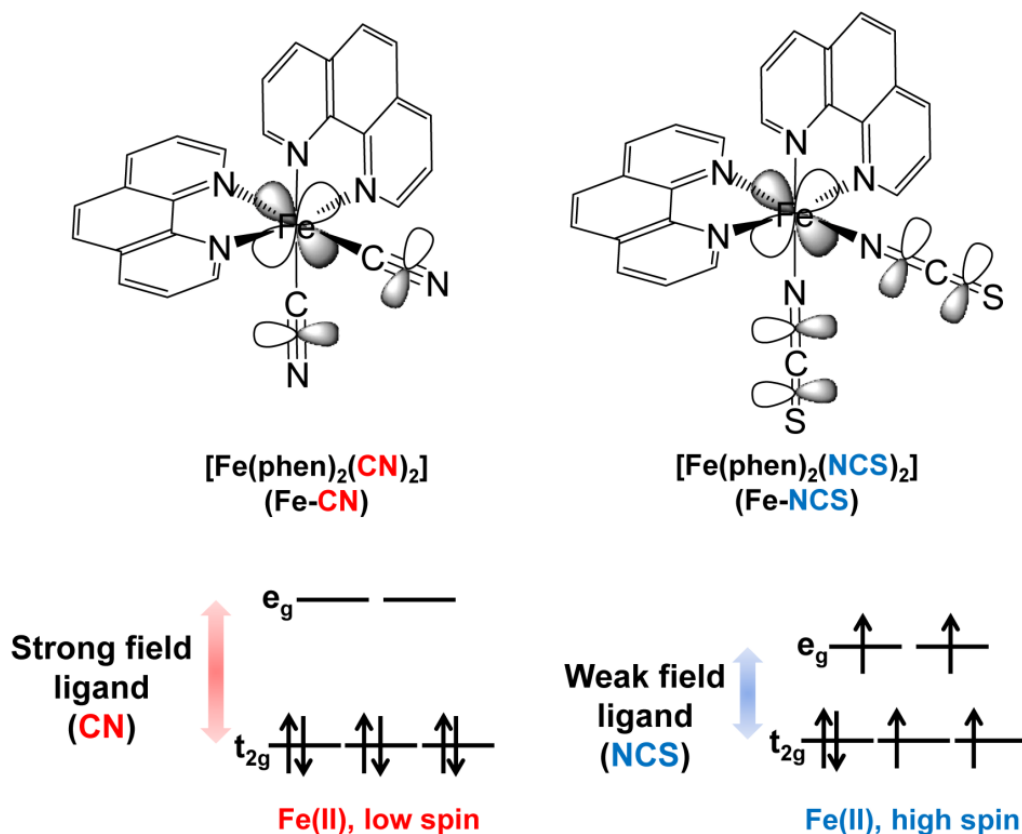
Figure 8-6. Possible π-orbital overlap between central Fe and additional different strength field ligands, CN and NCS, and its induced low and high spin state of coordinated Fe, respectively.

Regarding this orbital interaction between central Fe and outer oxygen molecule, these arguments can be extended to the relationship between the spin state of Fe and ORR activity because absolutely introduced ligand change the spin state of Fe. Therefore, it is possible to say that a NCS induced high spin of Fe facilitate ORR. Otherwise, CN induced low spin of Fe has a negative effect on ORR. Interestingly, when considering the number of lone pair electrons in each Fe state, it is likely that the difference in ORR performance could be linked to Fe spin state because oxygen coverage on noble metals are closely related to the number of unpaired d electrons.[176] Besides, these arguments can be supported with the previous literature that an increase in electron density on Fe in Fe-N$_4$ catalysts facilitates ORR.[177] However, further electrochemical and characterization studies are required before correlating the spin state of Fe and ORR clearly with the insoluble ligand coordinated Fe complex which are totally free from additional effect of MOF-5 and its induced different amount of Fe. Obviously, this should be desirable for better logical discussion on spin state effect on ORR.

We selected two reference materials, [Fe(II)(phen)$_2$(CN)$_2$]·3.5H$_2$O(S=0, $t_{2g}^6 e_g^0$) and [Fe(II)(phen)$_2$(NCS)$_2$]·H$_2$O (S=2, $t_{2g}^4 e_g^2$), and found that the coordinated Fe species in hexacoordinated iron (II) systems could still act as the heart of catalytic activity sites during ORR like conventional square N$_4$ coordinated Fe system. Furthermore, the chelated iron can be activated or deactivated according to which ligand binds to Fe, indicating that ligand induced Fe makes totally different catalytic activity for ORR. Therefore, this valuable insight into the additional ligand effect on the ORR can provide more valuable insight in the development of advanced Fe-based catalysts for fuel cells and metal-air batteries given this novel knowledge of how to alleviate the charge transfer resistance during the ORR process beyond the conventional Fe/N/C catalyst approach.

Experimental Section

Preparation of HS-[Fe(phen)$_2$(NCS)$_2$]·H$_2$O and LS-[Fe(phen)$_2$(CN)$_2$]·3.5H$_2$O

HS-[Fe(phen)$_2$(NCS)$_2$]·H$_2$O and LS-[Fe(phen)$_2$(CN)$_2$]·3.5H$_2$O were prepared by the previous literature. Briefly, for the [Fe(phen)$_2$(NCS)$_2$]·H$_2$O, proper amount of FeCl$_2$·7H$_2$O, 3phen (1,10-phenanthroline), and 2KSCN were dissolved and kept in methanol for 1 day and then reflux in methylcyclohexane at 180°C for 2 days to gain [Fe(phen)$_2$(NCS)$_2$]·H$_2$O. For the [Fe(phen)$_2$(CN)$_2$]·3.5H$_2$O, all procedure were exactly same except 2NaCl as ligand. All chemical reagents were purchased from commercial sources and were used without further purification. From EA analysis, for [Fe(phen)$_2$(NCS)$_2$]·H$_2$O (C$_{26}$H$_{20}$N$_6$O$_2$S$_2$Fe); Calc.: C, 54.39; H, 3.55; N, 14.78; S, 11.28 %. Found: C, 54.64; H, 3.01; N, 14.95; S, 11.59 %. Mw: 568.45 g/mol. For [Fe(phen)$_2$(CN)$_2$]·3.5H$_2$O (C$_{26}$H$_{23}$N$_6$O$_{3.5}$Fe); Calc.: C, 58.77; H, 4.36; N, 15.82 %. Found: C, 58.64; H, 4.11; N, 15.63 %. Mw: 531.34 g/mol.

Preparation of [Zn$_4$O(BDC)$_3$(H$_2$O)$_2$] $\cdot$3H$_2$O$\cdot$1.5DMF (MOF-5')

[Zn$_4$O(BDC)$_3$(H$_2$O)$_2$]$\cdot$3H$_2$O$\cdot$1.5DMF (MOF-5') was prepared by the previous literature (Figure 1a). Terephthalic acid (2.83 g, 15.4 mmol) and triethylamine (4.3 mL) are dissolved in 200 mL of DMF. Zn(NO$_3$)$_2$$\cdot$2H$_2$O (10.10 g, 38.7 mmol) is dissolved in 250 mL of DMF. The zinc salt solution is added to the organic solution with stirring over 15 min, forming a precipitate, and the mixture is stirred for 1.5 h. The precipitate (MOF-5) is filtered and washed with DMF/MeOH and then dried in air for 1 day.　Yield = 5.20 g, 56.0 %. Elemental analysis (EA) for C$_{28.5}$H$_{22.5}$N$_{1.5}$O$_{19.5}$Zn$_4$ (Mw = 959.62 g/mol), Calc.: C, 35.67; H, 2.36; N, 2.19 %. Found: C, 35.70; H, 2.08; N, 2.38 %. IR (KBr, cm^{-1}): 3606 (m), 3357-3212 (m, b), 1652 (w), 1581 (vs), 1558 (w), 1500 (m), 1403 (w), 1384 (vs), 1309 (w), 1292 (w), 1251 (w), 1147 (w), 1103 (w), 1060 (vw),　1016 (m), 975 (vw), 881 (w), 854 (vw), 813 (s), 714 (s), 667 (w), 592 (vw), 547 (w), 520 (w), 493 (vw), 458 (vw), 420 (vw).

Preparation of [Fe(phen)$_2$(CN)$_2$]$_{0.04}$@[Zn$_4$O(BDC)$_3$(H$_2$O)$_2$]$_{0.77}$$\cdot$1.03H$_2O\cdot$2.1DMF (MOF-5'[LS-Fe])

MOF-5' (200 mg, 0.210 mmol) was added to LS-[Fe(phen)$_2$(CN)$_2$]$\cdot$3.5H$_2$O (100 mg, 0.188 mmol) solution of　DMF 5 mL in a 10 mL galss vial. The materials were sonicated for 5 min and then the vial sealed at RT for 1 day. The resulting orange color powder was collected and washing with DMF and then dried in air for 1 day. Elemental analysis (EA) for C$_{25.82}$H$_{29.72}$N$_{2.34}$O$_{14.68}$Fe$_{0.04}$Zn$_{3.08}$ (Mw = 811.42 g/mol), Calc.: 38.22; H, 3.69; N, 4.04 %. Found: C, 37.78; H, 3.03; N, 4.56 %. IR (KBr, cm^{-1}): 3604 (m), 3380-3290 (m, b), 1645 (w), 1579 (vs), 1498 (m), 1425 (w), 1396 (w), 1363 (vs), 1305 (w), 1247 (w), 1143 (w), 1101 (w), 1061 (m), 997 (w), 879 (w), 846 (m), 813 (m), 748 (s), 723 (m), 665 (w), 578 (w), 545 (w), 518 (w), 464 (vw).

Material characterization

Elemental analyses (C, H, and N) were performed using a Thermo Scientific Flash 2000 elemental analyzer. Metal ions (Fe and Zn) were analyzed using a Varian 720-ES inductively coupled plasma atomic emission spectrometer (ICP-AES). FT–IR spectra were recorded in the range 4000 ~ 400 cm^{-1} using a Varian 670 FT–IR spectrophotometer. Powder X-ray diffraction (PXRD) data was recorded using a Rigaku D/M 2500T automated diffractometer at room temperature with a step size of 0.02° in 2θ angle. The material morphology was examined using a SEM (Nanonova 230, FEI) operating at 10 kV and spin state of Fe was analyzed using XPS (Thermo Fisher, UK).

Preparation of catalysts ink and RRDE measurements

Detail method for catalysts ink and RRDE procedure are described in our previous report (See Table S1).[3] Briefly, for 3-MOF[Fe-CN] + KB, 3 mg of MOF[LS-Fe] were dispersed in 1 mL of 0.05 % Nafion (Aldrich) solution in distilled water and 5.5 mg of ketjenblack 600JD (KB) were

dispersed in 3 mL of 0.05 % Nafion (Aldrich) solution in distilled water. Then, two inks were mixed by ultrasonically for at least 1 hr to form homogeneous catalysts ink. Then, 6 µL of the catalysts ink was carefully dropped onto a polished glassy carbon (GC) electrode of 4 mm diameter (RRDE Pt Ring/GC Disk Electrode, cat. NO. 011162, ALS Co., Ltd.). Glassy carbon electrodes were polished with 0.05 µm polishing alumina to maintain a good condition of working electrode (PK-3 Electrode Polishing kit, ALS Co., Ltd.). Catalyst-coated GC electrodes were then dried under vacuum at room temperature for at least 1hr.

Rotating ring disk electrode (RRDE) (ALS Co., Ltd) experiments were carried out using the as-prepared catalysts film (deposited on GC electrode) as the working electrode in 0.1 M KOH alkaline electrolyte. Pt wire and Hg/HgO is used as counter and reference electrode, respectively. Before RRDE test, 0.1 M KOH electrolyte was bubbled with pure oxygen gas (99.9 %) for 30 min. Electrochemical characterization was conducted using bi-potentiostat (IviumStat). 10mV of scan rate was swept from 0.15 V to -0.7 V and sufficient ring potential of 0.4 V was biased to oxidize intermediate during ORR. The collection efficiency was determined under Ar atmosphere using 10 mM $K_3[Fe(CN)_6]$, which is around 0.41.This value is very close to its theoretical value, 0.42. Hydrogen peroxide yields and the number of transferred electrons were calculated using the equations below

$$HO_2(\%) = 200\frac{I_r/N}{I_d + I_r/N}$$

$$n = 4\frac{I_d}{I_d + I_r/N}$$

Determination of Fe contents using Inductively Coupled Plasma (ICP) analysis

The contents of Fe are 1) 0.83 wt % in 3-MOF[Fe-CN], 2) 0.55 wt % (Fe-CN) + 9.28 wt% (Fe-NCS) in 2-MOF[Fe-CN] + 1-Fe-NCS, 3) 0.28 wt % (Fe-CN) + 19.65 wt % (Fe-NCS) 1-MOF-[Fe-CN] + 2-Fe-NCS, and 4) 29.47 wt % (Fe-NCS) of 3-Fe-NCS, respectively (See Table S2). It is noted that insertion of Fe-CN into MOF-5' is difficult so that the contents of Fe-CN in MOF-5' is relatively much lower than Fe-NCS complex.

Appendix 1: Permission from all cited journal papers in this thesis

All cited materials in this thesis are properly adapted with permission from following

1. **Figure 1-1.** and **1-2.** and **chapter 1** (from "Metal–Air Batteries with High Energy Density: Li–Air versus Zn–Air." Advanced Energy Materials 2011, 1 (1), 34-50)

2. **Figure 1-4.** (from "Revised pourbaix diagrams for zinc at 25–300 ℃." Corrosion Science 1997, 39 (1), 107-114.)

3. **Figure 1-5.** and **chapter 5** (from "A Highly Efficient Electrocatalyst for the Oxygen Reduction Reaction: N-Doped Ketjenblack Incorporated into Fe/Fe₃C-Functionalized Melamine Foam", Angewandte Chemie International Edition, 2011, 52(3), pp 1026–1030.)

4. **Figure 2-1.** (from "Determination of the kinetic parameters of the oxygen reduction reaction using the rotating ring-disk electrode: Part I. Theory." *Journal of Electroanalytical Chemistry and Interfacial Electrochemistry* **1987,** *229* (1–2), 305-316)

133

5. **Figure 2-2.** (from "Metal-air batteries: from oxygen reduction electrochemistry to cathode catalysts." Chemical Society Reviews 2012, 41 (6), 2172-2192.) Adapted from ref. 6 with permission from RSC. (This is RSC policy and recommend format.)

6. **Chapter 2** (from "Non-Precious Catalysts: Recent Progress in Non-Precious Catalysts for Metal-Air Batteries" Advanced Energy Materials 2012, 2 (7), 701-701.)

7. **Chapter 3** (from "Ionic liquid modified graphene nanosheets anchoring manganese oxide nanoparticles as efficient electrocatalysts for Zn-air batteries." Energy & Environmental Science 2011, 4 (10), 4148-4154.) *Adapted from ref. 72f with permission from RSC.* (This is RSC policy and recommend format.)

*Recommend format is "For reproduction of material from all other RSC journals and books: Reproduced from Ref. XX with permission from The Royal Society of Chemistry."

8. **Chapter 4** (from "Ketjenblack Carbon Supported Amorphous Manganese Oxides Nanowires as Highly Efficient Electrocatalyst for Oxygen Reduction Reaction in Alkaline Solutions." Nano Letters 2011, 11 (12), 5362-5366.) *Reprinted with permission from Ref.73. Copyright © 2011 American Chemical Society.*

Appendix 2: Experimental section for RRDE technique

1. Non-electrochemical kinetic parameters for RDE data analysis in 0.1M KOH, 25°C, 1atm O$_2$.

D_0 (diffusion coefficient of O$_2$ in solution): **1.87×10^{-9} m$^2 \cdot$s^{-1} in 0.1 M KOH**

C_0 (saturation concentration of O$_2$ in solution): **1.21 mol$\cdot$m^{-3} in 0.1 M KOH**

V (kinematic viscosity): **1×10^{-6}m$^2 \cdot$s^{-1} for 0.1 M KOH**

A (geometric are of the disk electrode=RDE glassy carbon electrode):

      Φ 3mm (diameter: 0.3cm) for RDE glassy carbon electrode

      Radios: 0.15cm = 1.5×10^{-3}m

      Area: $(1.5 \times 10^{-3}$m$)^2 \times 3.14 =$ **7.06×10^{-6}m^2 (= 0.070cm^2)**

      Φ 4mm (diameter: 0.4cm) for RRDE glassy carbon electrode

      (Disk: 4mm; Ring ID:5mm; Ring OD:7mm)

      Theoretical collection efficiency (N) = 0.42

      Radios: 0.2cm = 2×10^{-3}m

      Area: $(2.0 \times 10^{-3}$m$)^2 \times 3.14 =$ **0.1256cm^2**

ω (the angular frequency of the rotation) (rad$\cdot$s^{-1})

2. Calculation of B using above parameters in Koutecky-Levich(K-L) plot

$$I_d = 0.20nFAc^0(\omega' = \text{rpm number})^{1/2}D^{2/3}v^{-1/6} = Bn\omega'^{1/2}$$

$$B = 0.20FAc^0D^{2/3}v^{-1/6}$$

B= 1000 * 0.20 * 96500C/mol (F) * $(1.87 \times 10^{-9}$ m$^2 \cdot$s$^{-1})$^(2/3) (D$_0$) * $(1 \times 10^{-6}$m$^2 \cdot$s$^{-1})$^(-1/6) (v) * 1.21 mol$\cdot$m^{-3}(C$_0$) * 7.06×10^{-6}m^2 (A) = 2.5×10^{-3}mA$\cdot$rpm$^{-1/2}$

$$I_d = 0.20nFAc^0\omega'^{1/2}D^{2/3}v^{-1/6} = 2.5 \times 10^{-3}n\omega'^{1/2}$$

$$1/(\text{slope in K-L plot}) = 2.5 \times 10^{-3} \text{ mA} \times \text{rpm}^{-1/2} \times n$$

3. Preparation of electrodes for RDE

      The detail method of thin-film rotating disk electrode is described in previous Shao-Horn's group paper.[58a] A weighed mass of the catalysts powder was dispersed using ultrasonication in 0.05wt% Nafion of distilled water solvent to form a catalysts ink. A measured volume of the ink was then casted onto polished glassy carbon electrode by means of micropipette. After loading aqueous volume of catalysts ink, catalysts thin-film can be prepared using vacuum drying for at least 30mintes in **Appendix Figure 2-1, 2-2, and 2-3**.

Appendix Figure 2-1. Loaded aqueous catalyst ink onto glassy carbon electrode.

Appendix Figure 2-2. Vacuum drying for the preparation of catalysts films.

Appendix Figure 2-3. As-prepared catalysts thin-film.

4. Determination of RRDE collection efficiency

Although manufacture provides collection efficiency in **Appendix Figure 2-4**,[12] modified electrodes can be different from bare-electrodes. Therefore, the flow dynamic can be modified, affecting the collection efficiency. It is required to determine the collection efficiency at catalysts loaded electrodes using well-known redox couple such as $K_3[Fe(CN)_6]$. In this system, we can expect that $Fe^{3+} + e^- \rightarrow Fe^{2+}$ at disk, otherwise, $Fe^{2+} \rightarrow Fe^{3+} + e^-$ at ring electrode. Therefore, it is possible to calculate collection efficiency using the equation, $N = -I_R/I_D$, where I_R is ring current and I_D is disk current at a specific potential in **Appendix Figure 2-5.**

RRDE Efficiency Calculator

This Microsoft Excel Worksheet provides an easy way to predict the theoretical collection efficiency for any Rotated Ring-Disk Electrode (RRDE).
The equations used by this worksheet are taken from the classic text Electrochemical Methods, by Alan Bard and Larry Faulkner (John Wiley & Sons, 1980).
(See equation 8.4.16 in section 8.4.2 of the text for more information.)

Note that Pine actually machines electrodes using English units. The metric dimensions in the following table are nearest Metric equivalent.

Standard Pine RRDE Designs

	Metric Diameters				Metric Radii					Metric Areas (sq. cm)		Collection Efficiency
	disk OD	ring ID	ring OD	shroud OD	disk	ring	ring	disk-ring	shroud	disk	ring	(%)
	(mm)	(mm)	(mm)	(mm)	outer radius	inner radius	outer radius	gap	thickness			
E6 Series	5.00	6.50	7.50	15.00	2.50	3.25	3.75	0.75	7.50	0.1963	0.1100	25.6%
E6HT Series	5.50	6.50	8.50	15.00	2.75	3.25	4.25	0.50	6.50	0.2376	0.2356	38.3%
E7R8 Series	4.57	4.93	5.38	15.00	2.29	2.47	2.69	0.18	9.62	0.1640	0.0364	21.8%
E7R9 Series	5.61	6.25	7.92	15.00	2.81	3.13	3.96	0.32	7.08	0.2472	0.1859	37.0%
Older Style Pine RRDE Designs												
MT28 Series	4.57	4.93	5.38	13.50	2.29	2.47	2.69	0.18	8.12	0.1640	0.0364	21.8%
MT29 Series	5.61	6.25	7.92	13.50	2.81	3.13	3.96	0.32	5.58	0.2472	0.1859	37.0%
MTI34 Series	6.00	7.50	8.50	15.00	3.00	3.75	4.25	0.75	6.50	0.2827	0.1257	24.0%
MTI36 Series	5.00	7.50	8.50	15.00	2.50	3.75	4.25	1.25	6.50	0.1963	0.1257	22.5%
Enter Your Own Dimensions Here												
custom												
custom												

Appendix Figure 2-4. Collection efficiency of the RRDE supplied by Pine Inc.[12] (Data was taken from supplied sheets)
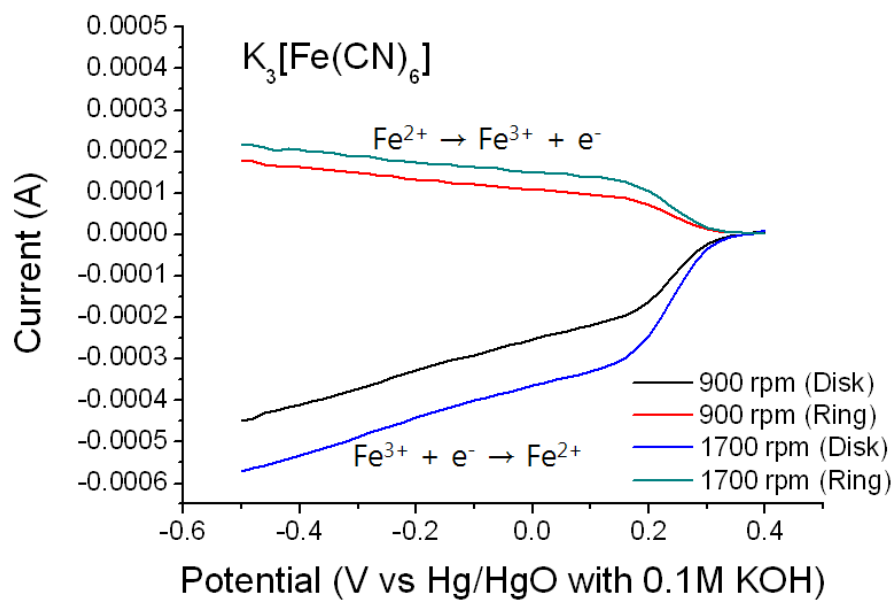
Appendix Figure 2-5. Determination of collection efficiency of the RRDE using catalysts modified electrode. All measurements were conducted in Ar-saturated electrolyte.

Appendix 3: Construction of pourbaix diagram of zinc

1. Construction pourbaix diagram of zinc in aqueous electrolyte (Figure 1-4)[24]

Taking the general equation for a half-cell reaction as,

$$aA + mH^+ + ze^- = bB + H_2O$$
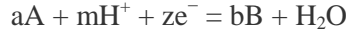
the Nernst equation becomes

$$E_e = E^0 - \frac{2.303RT}{zF} \log \frac{[reduced]}{[oxidised]}$$

or

$$E_e = E^0 + \frac{0.0591}{z} \log \frac{[A]^a}{[B]^b} - \frac{m}{z} 0.0591 pH$$

For the case that oxygen dissolved in water is in equilibrium with water.

$O_2 + 4H^+ + 4e^- = 2H_2O$
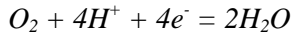
$$E_e = E^0 + \frac{0.0591}{4} \log \frac{[O_2]^1}{[H_2O]^2} - \frac{4}{4} 0.0591 pH$$

$$E_e = 1.223 + \frac{0.0591}{4} \log \frac{[O_2]^1}{[H_2O]^2} - \frac{4}{4} 0.0591 pH$$

$$E_e = E^0 - 0.0591 pH$$

For the case that water is in equilibrium with gaseous hydrogen.

$2H^+ + 2e^- = H_2$
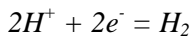
$$E_e = E^0 - \frac{2}{2} 0.0591 pH$$

$$E_e = 0 - \frac{2}{2} 0.0591 pH$$

$$E_e = -0.0591 pH$$

$Zn^{2+} + 2e^- = Zn$ (reaction i)
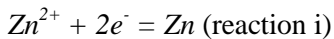
$$E_e = E^0 + \frac{0.0591}{2} \log \frac{[Zn^{2+}]^1}{[Zn]^1}$$

$$For\ reaction\ on\ i : E_e = -0.763 + 0.02951 \log[Zn^{2+}]$$

$Zn(OH)_2 + 2H^+ + 2e^- = Zn + 2H_2O$ (reaction ii)
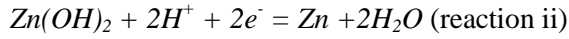
$$E_e = E^0 + \frac{0.0591}{2} log \frac{[Zn(OH)_2]^1}{[Zn]^1} - \frac{2}{2} 0.0591 pH$$

$$For\ reaction\ on\ ii : E_e = -0.439 - 0.0591 pH$$

$HZnO_2^- + 3H^+ + 2e^- = Zn + 2H_2O$ (reaction iii)
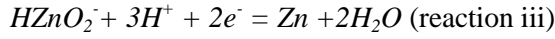
$$E_e = E^0 + \frac{0.0591}{2} log \frac{[HZnO_2^-]^1}{[Zn]^1} - \frac{3}{2} 0.0591 pH$$

$$For\ reaction\ on\ iii : E_e = 0.054 - 0.0886 pH + 0.02951 log[HZnO_2^-]$$

$ZnO_2^{2-} + 4H^+ + 2e^- = Zn + 2H_2O$ (reaction iv)
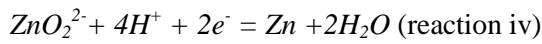
$$E_e = E^0 + \frac{0.0591}{2} log \frac{[ZnO_2^{2-}]^1}{[Zn]^1} - \frac{4}{2} 0.0591 pH$$

$$For\ reaction\ on\ iv : E_e = 0.441 - 0.1182 pH + 0.02951 log[ZnO_2^{2-}]$$

Assuming $[Zn(aq)]_{tot} = 10^{-6}$ molal,[3] we can construct above pourbaix diagram for Zinc in aqueous electrolyte.
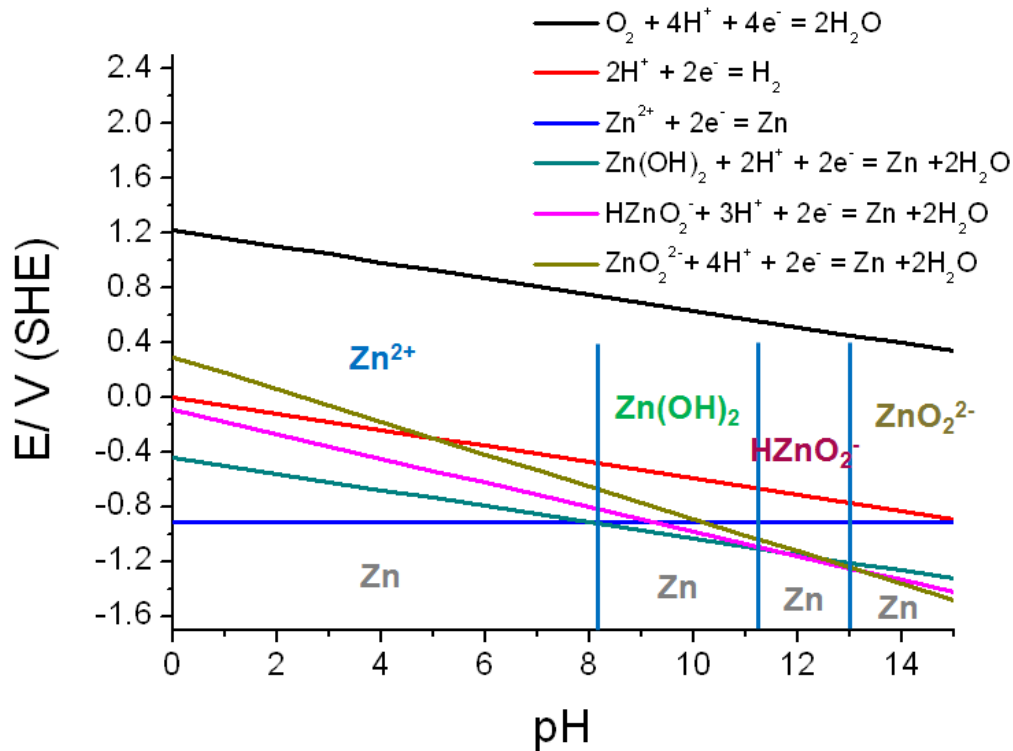
Appendix Figure 3-1. Pourbaix diagram for zinc at 25°C and $[Zn(aq)]_{tot} = 10^{-6}$ molal.
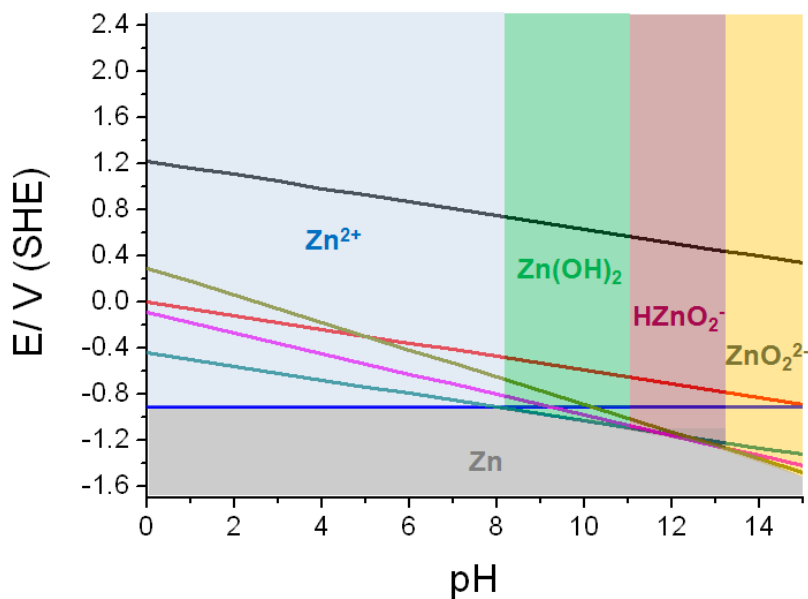
Appendix Figure 3-2. Stable chemical species in Pourbaix diagram for zinc at 25℃ and $[Zn(aq)]_{tot} = 10^{-6}$ molal.

In constructed pourbaix diagrams, it is worth to note following three lines:

1) Horizontal lines. The reactions on these lines depend on electrons, not pH. Therefore, neither H nor OH ions participate in these reactions.

For example,

$Zn^{2+} + 2e^- = Zn$ (reaction i)
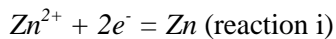
2) Diagonal lines with slope. The reactions on these lines depend on both electrons and pH.

For example,

$O_2 + 4H^+ + 4e^- = 2H_2O$

$2H^+ + 2e^- = H_2$

$Zn(OH)_2 + 2H^+ + 2e^- = Zn + 2H_2O$ (reaction ii)

$HZnO_2^- + 3H^+ + 2e^- = Zn + 2H_2O$ (reaction iii)

$ZnO_2^{2-} + 4H^+ + 2e^- = Zn + 2H_2O$ (reaction iv)
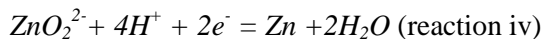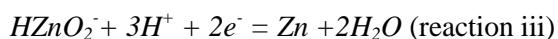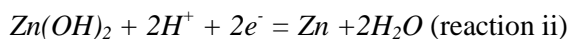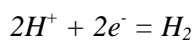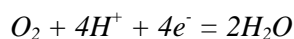
3) Vertical lines. The reactions on these lines depend on either H or OH ions, not potential. In these reactions, electrons do not participate in the reactions.

For example,

$Zn(OH)_2 + 2H^+ = Zn^{2+} + 2H_2O$ *(at pH 8.5)*

$Zn(OH)_2 = HZnO_2^- + H^+$ *(at pH 10.7)*

$HZnO_2^- = ZnO_2^{2-} + H^+$ *(at pH 13.1)*
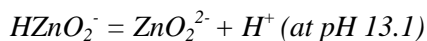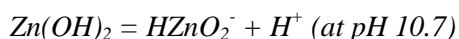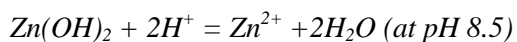
Appendix 4: Zinc utilization (%) in Zn-air battery

It is important to calculate the zinc utilization (%) in studying Zn-air battery to maximize the intrinsic potential of metal-air battery such as high capacity. Usually, zinc utilization (%) is below 60% so that the theoretical capacity ($820mAh/g_{Zn}$) can be significantly reduced. In this regard, generally constant current discharge for already charged zinc-air battery has been widely used and is much more practical than C-rate discharge used in Li-ion battery.[14, 73] Therefore, how to increase zinc utilization can be a critical issues in advanced zinc-based batteries beyond commercial Li-ion battery.

1. Zinc utilization (%) using C-rate discharge

Appendix Table 4-1. Taken results for Zn-air cell at different discharge rates in the previous literature.[14]

Parameter	Discharge rate		
	C/5 (0.2C)	C/10 (0.1C)	C/20 (0.05C)
Theoretical capacity (mAh)	1560 (820mAh/g * 1.90g= 1560mAh)	1560	1560
Discharge current (mA)	300 (1560/5=312)	150 (1560/10=156)	75 (1560/20=78)
Discharge time (h)	4.31	9.35	19.08
Real capacity (mAh)	1293 (300 * 4.31=1293)	1402.5 (150 * 9.35=1293)	1431 (75 * 19.08=1293)
Zinc Utilization (%)	**82.88 (1293/1560 *100=82.88)**	**89.90 (1402.5/1560 *100=89.90)**	**91.73 (1431/1560 *100=91.73)**

1) Zn utilization (%) = Practical capacity (mAh)/ Theoretical capacity (mAh) * 100

  Practical capacity (mAh) = applied current (mA) (or from C-rate based on theoretical capacity) * measured discharge time (h)

  Theoretical capacity (mAh) = 820mAh/g * initial Zn mass (g)

2) Specific capacity of Zinc-air battery was was normalized to the mass of consumed Zn.

2. Calculation of driving distance using Zn-air battery

Note: all calculation was based on the previous presentation by MEET inc. Korea.[178]

1) Calculation of theoretical specific energy density (Wh/Kg$_{Zn}$) of Zn-air battery

Assuming that all zinc metal can be consumed and average working potential is ca. 1.2V,

$$Zn \rightarrow Zn^{2+} + 2e^-$$
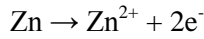
$$\frac{2\text{mol e}^-}{1\text{mol Zn}} \times \frac{1\text{mol Zn}}{65.38\text{g}} \times \frac{9.64 * 10^4 \text{C}(\text{A}\cdot\text{s})}{1\text{mol e}^-} \times \frac{\text{mAh}}{3.6\text{C}} = 820\text{mAh/g}_{Zn}$$

$$\frac{820\text{mAh}}{\text{g}_{Zn}} \times 1.2V = \frac{0.984Wh}{\text{g}_{Zn}} = 984\text{Wh/Kg}_{zn}$$

Or

$$\frac{820\text{mAh}}{\text{g}_{Zn}} \times \frac{65.38\text{g}_{Zn}}{1\text{mol Zn}} = 53611\text{mAh/mol}_{Zn} = 53.611\text{Ah/mol}_{Zn}$$

$$\frac{53.611\text{Ah}}{\text{mol}_{Zn}} \times 1.2V = 64.33\text{Wh/mol}_{Zn}(\text{ca.}\frac{57\text{Kcal}}{\text{mol}})$$

About 57Kcal/mol of Zn is more efficient than 37Kcal/mol(=43.7Wh/mol) delivered by thermal power generation if 40 % of energy conversion efficiency of thermal power is assumed.

2) Calculation of practical specific energy density (Wh/Kg$_{Zn}$) of Zn-air battery

Assuming that 60% of zinc metal can be consumed because of side reactions in Zn electrode and average working potential is ca. 1.2V,

$$\frac{984\text{Wh}}{\text{Kg}_{zn}} \times 0.6 = 590\text{Wh/Kg}_{Zn}$$

Therefore, arithmetically specific energy density (Wh/Kg$_{Zn}$) of Zn-air battery is larger than those in long-term goal of USABC.

Appendix Table 4-2. Power and energy density in USABC long-term goal.[15]

USABC long-term goal	
Power density (W/Kg)	400 W/Kg
Energy density (Wh/Kg)	200 Wh/Kg

3) Calculation of theoretical generated energy per zinc

Assuming that 8kWh of energy is required for 64km (40miles) by car,
125 Wh/km is needed.

$$\frac{8000\text{Wh}}{64\text{Km}} = 125\text{Wh/km}$$

Therefore, required Zinc metal per 1km is,

$$\frac{984\text{Wh}}{\text{Kg}_{zn}} \times \text{ x Kg}_{Zn} = 125\text{Wh (127g of zinc is required)}$$

$$\frac{53.611\text{Ah}}{\text{mol}_{Zn}} \times 1.2\text{V} = \frac{64.33\text{Wh}}{\text{mol}_{Zn}} = \sim 1\text{Wh/g}_{Zn}$$

In other words, 1Wh of energy can be generated with 1g of zinc. Furthermore, 1Mwh electricity can be stored in 1tone of zinc, which is 140L of zinc spelter or 250L of zinc ball assuming that specific gravity of Zn is 7.14 g/cm^3. (1L=1000cm^3)

$$\frac{7.14\text{g}}{\text{cm}^3} \times \frac{1000\text{cm}^3}{1\text{L}} = \frac{7140\text{g}}{\text{L}}$$

Also, 127g of Zinc has 15.5cm^3 of volume, which is much smaller than 50~100cm^3 of gasoline.

4) Calculation of theoretical required zinc metal for 450Km distance by car.
Required energy for 450Km is,

$$450\text{Km} \times \frac{125\text{Wh}}{\text{Km}} = 56250\text{Wh}$$

1g of Zinc can generate 1Wh,

$$\sim 1\text{Wh/g}_{Zn}$$

Required Zinc metal for 450Km distance are 56.250kg$_{Zn}$.

$$56250\text{Wh} \times \frac{\text{g}_{Zn}}{1\text{Wh}} = 56250\text{g}_{Zn} = 56.250\text{Kg}_{Zn}$$

Appendix 5: Research flow of Zinc-air battery
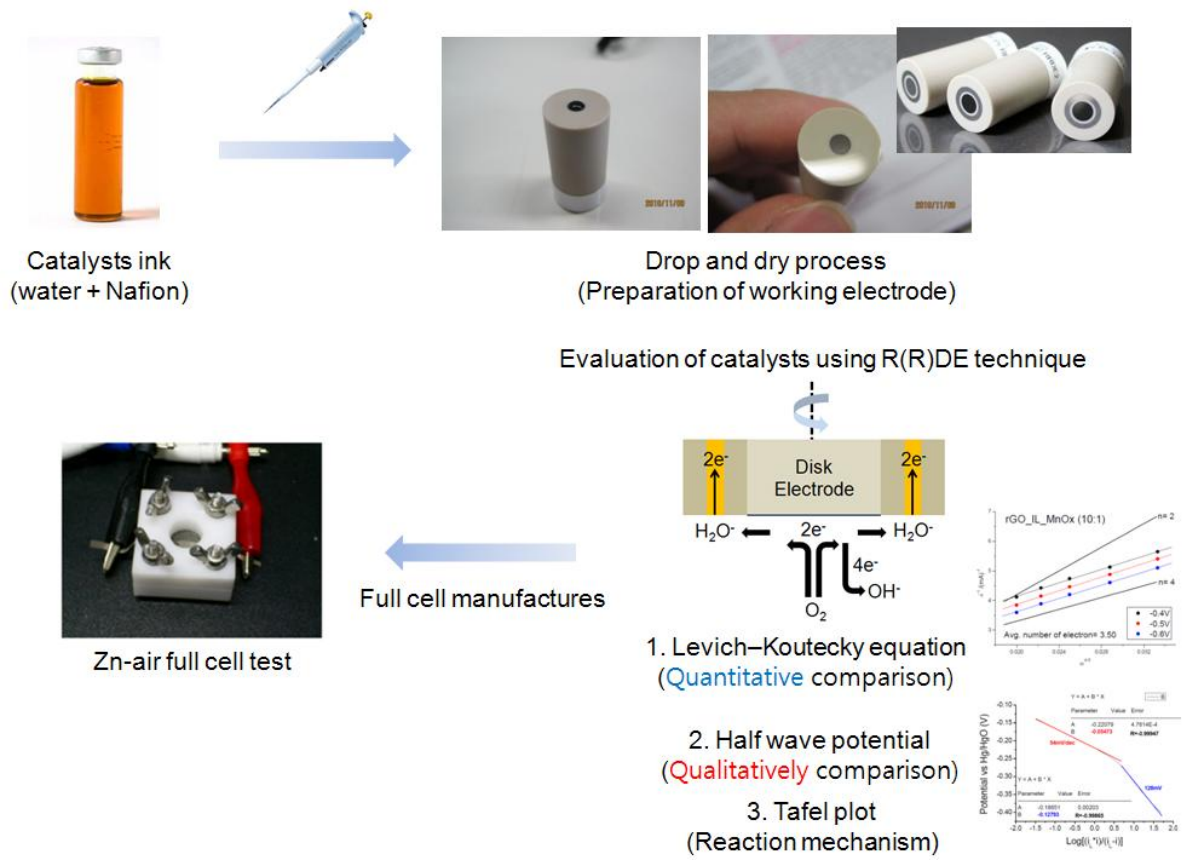
Appendix Figure 5-1. Schematic research flow of zinc-air battery.

1. Preparation of gas diffusion layer (GDL)

Gas diffusion layer (GDL)

Activated carbon (Darco G-60A, Sigma Aldrich) and PTFE binder (60 wt% PTFE emulsion in water, Sigma Aldrich) at a ratio of 7 to 3.

2. Catalysts ink for preparation of catalysts layer and preparation of air electrode

Catalysts ink

Gas diffusion layer (GDL)

Dry

Catalysts layer

Gas diffusion layer (GDL)

3. Zinc-air Full cell assembly

A

Air (oxygen)

air electrode

Ni-mesh

separator

Zinc powder + 6M KOH (0.15mL)

Zinc + KOH

Separator

Gas diffusion layer (GDL)

Catalysts layer

air

air electrode = catalysts layer + GDL
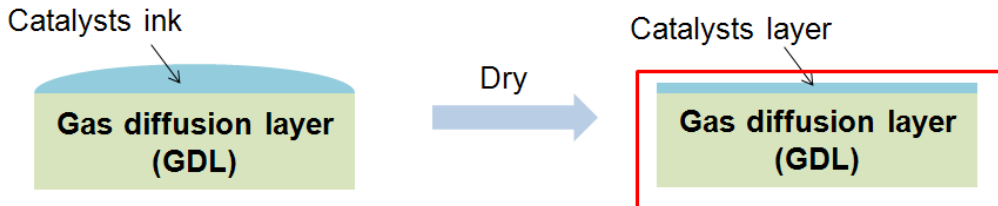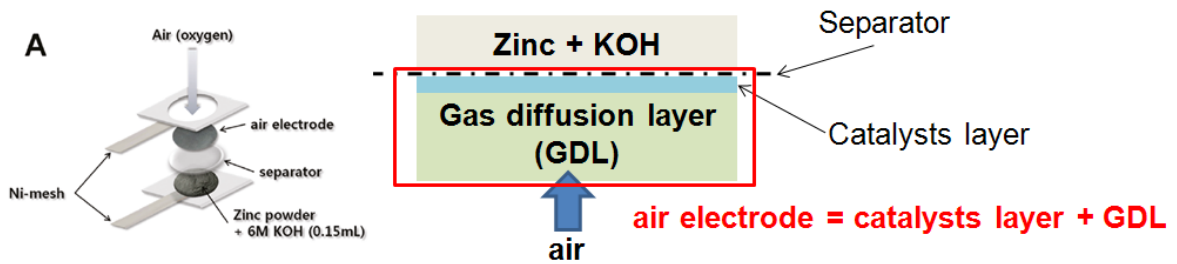
Appendix Figure 5-2. Schematic description of zinc-air full cell manufactures.

Appendix 6: Current Interrupt Technique for Zinc-air battery

To discriminate ohmic and activation loss from overall resistance loss, current interrupt technique can be used because both ohmic and activation loss as resistances exists in zinc-air battery.[13, 179] This method is based on each different time scale.[7] For example, the time scale in the buildup and decay of activation loss is 10^{-2} -10^{-4}s, otherwise, ohmic resistance instantaneously appears and disappear ($<10^{-6}$ s). Therefore, after ceasing current, instantaneously recovered voltage gap can be considered as IR drop ($\eta=IR$) from ohmic loss. In contrast, slowly recovered voltage gap can be activation polarization following the Tafel equation ($\eta= A\ ln\ (i/i_0)$), where A is Tafel constant and i_o is exchange current density. Typically, activation loss is more dominant than ohmic drop in zinc-air battery. Therefore, to reduce activation loss, following solutions can be effective: 1) increasing cell temperature, 2) using highly active catalysts, and 3) increasing active surface area of electrodes.
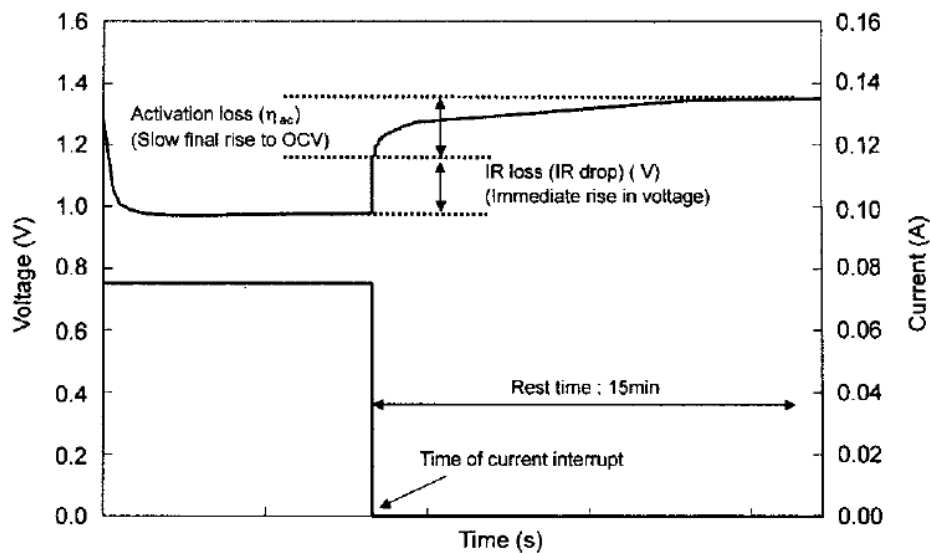
Appendix Figure 6-1. Voltage and current profile according to time before and after current interrupt.[13] (This figure was directly taken from previous literature.)

REFERENCES

1.   Lee, J.-S.; Tai Kim, S.; Cao, R.; Choi, N.-S.; Liu, M.; Lee, K. T.; Cho, J., Metal–Air Batteries with High Energy Density: Li–Air versus Zn–Air. *Advanced Energy Materials* **2011,** *1* (1), 34-50.

2.   Huggins, R. A., Principles Determining the Potentials and Capacities of Electrochemical Cells. In *Materials for Lithium-Ion Batteries*, Julien, C.; Stoynov, Z., Eds. Springer Netherlands: 2000; Vol. 85, pp 21-46.

3.   Beverskog, B.; Puigdomenech, I., Revised pourbaix diagrams for zinc at 25–300 ℃. *Corrosion Science* **1997,** *39* (1), 107-114.

4.   Lee, J.-S.; Park, G. S.; Kim, S. T.; Liu, M.; Cho, J., A Highly Efficient Electrocatalyst for the Oxygen Reduction Reaction: N-Doped Ketjenblack Incorporated into Fe/Fe_3C-Functionalized Melamine Foam. *Angewandte Chemie International Edition* **2013,** *52* (3), 1026-1030.

5.   Anastasijević, N. A.; Vesović, V.; Adžić, R. R., Determination of the kinetic parameters of the oxygen reduction reaction using the rotating ring-disk electrode: Part I. Theory. *Journal of Electroanalytical Chemistry and Interfacial Electrochemistry* **1987,** *229* (1–2), 305-316.

6.   Cheng, F.; Chen, J., Metal-air batteries: from oxygen reduction electrochemistry to cathode catalysts. *Chemical Society Reviews* **2012,** *41* (6), 2172-2192.

7.   Winter, M.; Brodd, R. J., What Are Batteries, Fuel Cells, and Supercapacitors? *Chemical Reviews* **2004,** *104* (10), 4245-4270.

8.   A.J. Bard, L.R. Faulkner, Electrochemical Methods, Wiley, New York, **2001**.

9.   Lee, J.; Jeong, B.; Ocon, J. D., Oxygen electrocatalysis in chemical energy conversion and storage technologies. *Current Applied Physics* **2013,** *13* (2), 309-321.

10.   Suntivich, J.; Gasteiger, H. A.; Yabuuchi, N.; Nakanishi, H.; Goodenough, J. B.; Shao-Horn, Y., Design principles for oxygen-reduction activity on perovskite oxide catalysts for fuel cells and metal–air batteries. *Nat Chem* **2011,** *3* (7), 546-550.

11.   Yang, S.; Feng, X.; Wang, X.; Müllen, K., Graphene-Based Carbon Nitride Nanosheets as Efficient Metal-Free Electrocatalysts for Oxygen Reduction Reactions. *Angewandte Chemie International Edition* **2011,** *50* (23), 5339-5343.

12.   RRDE   Efficiency   Calculator. http://webcache.googleusercontent.com/search?q=cache:3BxZuPSMMu4J:www.pineinst.com/echem/files/RRDE_EFFICIENCY.XLS+&cd=3&hl=ko&ct=clnk&gl=kr.

13.   Jee Hoon Kim, S. W. E., Seong In Moon, Mun Soo Yun, Ju Yong Kim, Gyeong Chang Yug, Jeong Hoo Park Effect of the Conducting Agent on Characteristics of Cathode for Zn/Air Batteries *Journal of the Korean Electrochemical Society* **2002,** *5* (2), 74-78.

14.	Yang, C.-C.; Lin, S.-J., Alkaline composite PEO–PVA–glass-fibre-mat polymer electrolyte for Zn–air battery. *Journal of Power Sources* **2002,** *112* (2), 497-503.

15.	http://www.uscar.org/guest/view_team.php?teams_id=12.

16.	Zhang, T.; Tao, Z.; Chen, J., Magnesium-air batteries: from principle to application. *Materials Horizons* **2014**.

17.	Reddy, D. L. a. T. B., *HANDBOOK OF BATTERIES*. Third Edition ed.; McGraw-Hill.

18.	Sapkota, P.; Kim, H., Zinc-air fuel cell, a potential candidate for alternative energy. *Journal of Industrial and Engineering Chemistry* **2009,** *15* (4), 445-450.

19.	(a) McLarnon, F. R.; Cairns, E. J., The Secondary Alkaline Zinc Electrode. *Journal of the Electrochemical Society* **1991,** *138* (2), 645-656; (b) Zhang, P. A. a. Z. J., Battery Separators. *Chem. Rev* **2004,** *104*, 4419-4462.

20.	(a) Zhu, W. H.; Poole, B. A.; Cahela, D. R.; Tatarchuk, B. J., New structures of thin air cathodes for zinc–air batteries. *Journal of Applied Electrochemistry* **2003,** *33* (1), 29-36; (b) Dirkse, T. P.; Kroon, D. J., Effect of ionic strength on the passivation of zinc electrodes in KOH solutions. *Journal of Applied Electrochemistry* **1971,** *1* (4), 293-296.

21.	Balaish, M.; Kraytsberg, A.; Ein-Eli, Y., Realization of an Artificial Three-Phase Reaction Zone in a Li–Air Battery. *ChemElectroChem* **2013**, n/a-n/a.

22.	Abraham, K. M., A Brief History of Non-Aqueous Metal-Air Batteries. *Meeting Abstracts* **2006,** *MA2006-02* (6), 388.

23.	(a) Cheng, F. Y.; Chen, J.; Gou, X. L.; Shen, P. W., High-Power Alkaline Zn–MnO2 Batteries Using γ-MnO2 Nanowires/Nanotubes and Electrolytic Zinc Powder. *Advanced Materials* **2005,** *17* (22), 2753-2756; (b) Xu, C.; Li, B.; Du, H.; Kang, F., Energetic Zinc Ion Chemistry: The Rechargeable Zinc Ion Battery. *Angewandte Chemie International Edition* **2012,** *51* (4), 933-935.

24.	http://www.doitpoms.ac.uk/tlplib/pourbaix/pourbaix_construction.php.

25.	Urry, L. F., Zinc anode for an electochemical cell. *US 6,022,639* **1996**.

26.	Tang, Electrode for an electrochemical cell including ribbons *US 6,221,527* **1998**.

27.	(a) Goldstein, J., Enhanced performance zinc *US 6,015,636* **2000**; (b) Yang, C.-C.; Lin, S.-J., Improvement of high-rate capability of alkaline Zn-MnO2 battery. *Journal of Power Sources* **2002,** *112* (1), 174-183.

28.	Zhang, X. G., Fibrous zinc anodes for high power batteries. *Journal of Power Sources* **2006,** *163* (1), 591-597.

29.	Minakshi, M.; Appadoo, D.; Martin, D. E., The Anodic Behavior of Planar and Porous Zinc Electrodes in Alkaline Electrolyte. *Electrochemical and Solid-State Letters* **2010,** *13* (7), A77-A80.

30.	Coates, G.; Hampson, N. A.; Marshall, A.; Porter, D. F., The anodic behaviour of porous zinc electrodes. II. The effects of specific surface area of the zinc compact material. *Journal of Applied*

Electrochemistry **1974,** *4* (1), 75-80.

31.   COMPANY, T. G., ZINC/AIR CELL *WO01/056098* **2002**.

32.   Burchardt, T., ZINC ELECTRODE COMPRISING AN ORGANIC GELLING AGENT AND AN ORGANIC BINDER. *WO/2006/111835* **2006**.

33.   Müller, S.; Holzer, F.; Haas, O., Optimized zinc electrode for the rechargeable zinc–air battery. *Journal of Applied Electrochemistry* **1998,** *28* (9), 895-898.

34.   Othman, R.; Basirun, W. J.; Yahaya, A. H.; Arof, A. K., Hydroponics gel as a new electrolyte gelling agent for alkaline zinc-air cells. *Journal of Power Sources* **2001,** *103* (1), 34-41.

35.   Kim, K.; Cho, Y.-H.; Eom, S. W.; Kim, H.-S.; Yeum, J. H., Anions of organic acids as gas suppressants in zinc-air batteries. *Materials Research Bulletin* **2010,** *45* (3), 262-264.

36.   (a) Devyatkina, T. I.; Gun'ko, Y. L.; Mikhalenko, M. G., Development of Ways To Diminish Corrosion of Zinc Electrode. *Russian Journal of Applied Chemistry* **2001,** *74* (7), 1122-1125; (b) Lee, C. W.; Sathiyanarayanan, K.; Eom, S. W.; Yun, M. S., Novel alloys to improve the electrochemical behavior of zinc anodes for zinc/air battery. *Journal of Power Sources* **2006,** *160* (2), 1436-1441.

37.   Zhang, C.; Wang, J. M.; Zhang, L.; Zhang, J. Q.; Cao, C. N., Study of the performance of secondary alkaline pasted zinc electrodes. *Journal of Applied Electrochemistry* **2001,** *31* (9), 1049-1054.

38.   Cho, Y.-D.; Fey, G. T.-K., Surface treatment of zinc anodes to improve discharge capacity and suppress hydrogen gas evolution. *Journal of Power Sources* **2008,** *184* (2), 610-616.

39.   Zhu, L.; Zhang, H.; Li, W.; Liu, H., New modification procedure of zinc powder in neodymium nitrate solution for improving the electrochemical properties of alkaline zinc electrodes. *Journal of Physics and Chemistry of Solids* **2009,** *70* (1), 45-54.

40.   Ein-Eli, Y.; Auinat, M.; Starosvetsky, D., Electrochemical and surface studies of zinc in alkaline solutions containing organic corrosion inhibitors. *Journal of Power Sources* **2003,** *114* (2), 330-337.

41.   Lee, C. W.; Sathiyanarayanan, K.; Eom, S. W.; Kim, H. S.; Yun, M. S., Novel electrochemical behavior of zinc anodes in zinc/air batteries in the presence of additives. *Journal of Power Sources* **2006,** *159* (2), 1474-1477.

42.   David Linden, T. B. R., Handbook of batteries, third edition.

43.   (a) Renuka, R.; Ramamurthy, S.; Srinivasan, L., Interaction of zincate with additives turbidimetric, IR and Raman spectral analyses. *Journal of Power Sources* **2000,** *89* (1), 70-79; (b) Arise, I.; Fukunaka, Y.; McLarnon, F. R., Ionic Mass Transfer Accompanying Anodic Dissolution of Zinc in Alkaline Solution. *Journal of the Electrochemical Society* **2006,** *153* (1), A69-A74; (c) Dirkse, T. P., The Behavior of the Zinc Electrode in Alkaline Solutions. *Journal of the Electrochemical Society* **1981,** *128* (7), 1412-1415; (d) Cachet, C.; Saidani, B.; Wiart, R., The Behavior of Zinc Electrode in Alkaline Electrolytes. *Journal of the Electrochemical Society* **1992,** *139* (3), 644-654.

44.   (a) Wen, Y.-h.; Cheng, J.; Zhang, L.; Yan, X.; Yang, Y.-s., The inhibition of the spongy electrocrystallization of zinc from doped flowing alkaline zincate solutions. *Journal of Power Sources* **2009,** *193* (2), 890-894; (b) Sharifi, B.; Mojtahedi, M.; Goodarzi, M.; Vahdati Khaki, J., Effect of alkaline electrolysis conditions on current efficiency and morphology of zinc powder. *Hydrometallurgy* **2009,** *99* (1-2), 72-76; (c) Peng, W.-j.; Wang, Y.-y., Mechanism of zinc electroplating in alkaline zincate solution. *Journal of Central South University of Technology* **2007,** *14* (1), 37-41; (d) Simicic, M. V.; Popov, K. I.; Krstajic, N. V., An experimental study of zinc morphology in alkaline electrolyte at low direct and pulsating overpotentials. *Journal of Electroanalytical Chemistry* **2000,** *484* (1), 18-23; (e) Trigueros, P. P.; Claret, J.; Mas, F.; Sagués, F., Pattern morphologies in zinc electrodeposition. *Journal of Electroanalytical Chemistry* **1991,** *312* (1-2), 219-235; (f) Einerhand, R. E. F.; Visscher, W. H. M.; Barendrecht, E., Hydrogen production during zinc deposition from alkaline zincate solutions. *Journal of Applied Electrochemistry* **1988,** *18* (6), 799-806; (g) Hendrikx, J.; van der Putten, A.; Visscher, W.; Barendrecht, E., The electrodeposition and dissolution of zinc and amalgamated zinc in alkaline solutions. *Electrochimica Acta* **1984,** *29* (1), 81-89; (h) Popov, K. I.; Pavlović, M. G.; Spasojević, M. D.; Nakić, V. M., The critical overpotential for zinc dendrite formation. *Journal of Applied Electrochemistry* **1979,** *9* (4), 533-536; (i) Diggle, J. W.; Fredericks, R. J.; Reimschuessel, A. C., Crystallographic and morphological studies of electrolytic zinc dendrites grown from alkaline zincate solutions. *Journal of Materials Science* **1973,** *8* (1), 79-87.

45.   Sapkota, P.; Kim, H., An experimental study on the performance of a zinc air fuel cell with inexpensive metal oxide catalysts and porous organic polymer separators. *Journal of Industrial and Engineering Chemistry* **2010,** *16* (1), 39-44.

46.   (a) Hsu, L.-C.; Sheibley, D. W., Inexpensive Cross-Linked Polymeric Separators Made from Water-Soluble Polymers. *Journal of the Electrochemical Society* **1982,** *129* (2), 251-254; (b) Sheibley, D. W.; Manzo, M. A.; Gonzalez-Sanabria, O. D., Cross-Linked Polyvinyl Alcohol Films as Alkaline Battery Separators. *Journal of the Electrochemical Society* **1983,** *130* (2), 255-259; (c) Lewandowski, A.; Skorupska, K.; Malinska, J., Novel poly(vinyl alcohol)-KOH-H$_2$O alkaline polymer electrolyte. *Solid State Ionics* **2000,** *133* (3-4), 265-271; (d) Yang, C.-C.; Lin, S.-J., Alkaline composite PEO-PVA-glass-fibre-mat polymer electrolyte for Zn-air battery. *Journal of Power Sources* **2002,** *112* (2), 497-503; (e) Dewi, E. L.; Oyaizu, K.; Nishide, H.; Tsuchida, E., Cationic polysulfonium membrane as separator in zinc-air cell. *Journal of Power Sources* **2003,** *115* (1), 149-152.

47.   Kiros, Y., Separation and permeability of zincate ions through membranes. *Journal of Power Sources* **1996,** *62* (1), 117-119.

48.   Wu, G. M.; Lin, S. J.; You, J. H.; Yang, C. C., Study of high-anionic conducting sulfonated microporous membranes for zinc-air electrochemical cells. *Materials Chemistry and Physics* **2008,** *112* (3), 798-804.

49.   Chakkaravarthy, C.; Waheed, A. K. A.; Udupa, H. V. K., Zinc--air alkaline batteries -- A

review. *Journal of Power Sources* **1981,** *6* (3), 203-228.

50.   Jindra, J.; Mrha, J.; Musilová, M., Zinc-air cell with neutral electrolyte. *J Appl Electrochem* **1973,** *3* (4), 297-301.

51.   Jörissen, L., Bifunctional oxygen/air electrodes. *Journal of Power Sources* **2006,** *155* (1), 23-32.

52.   Nam-In Kim, K.-H. P., Yong-Kook Choi and Woo-Tae Lee, Effect of Carbon Dioxide in the Air on Zinc-air Cell. *Journal of the Korean Industrial and Engineering Chemistry* **1999,** *10* (2), 177 - 182.

53.   Drillet, J. F.; Holzer, F.; Kallis, T.; Muller, S.; Schmidt, V. M., Influence of CO_2 on the stability of bifunctional oxygen electrodes for rechargeable zinc/air batteries and study of different CO2 filter materials. *Physical Chemistry Chemical Physics* **2001,** *3* (3), 368-371.

54.   Cheng, H.-H.; Tan, C.-S., Reduction of CO_2 concentration in a zinc/air battery by absorption in a rotating packed bed. *Journal of Power Sources* **2006,** *162* (2), 1431-1436.

55.   (a) Lee, J.-S.; Park, G. S.; Kim, S. T.; Liu, M.; Cho, J., A Highly Efficient Electrocatalyst for the Oxygen Reduction Reaction: N-Doped Ketjenblack Incorporated into Fe/Fe_3C-Functionalized Melamine Foam. *Angewandte Chemie International Edition* **2012**, n/a-n/a; (b) Kaisheva, A., METAL-AIR BATTERIES: RESEARCH, DEVELOPMENT, APPLICATION. *Proceedings of the International Workshop "Portable and Emergency Energy Sources – from Materials to Systems"* **2005**, 16 – 22.

56.   Lee, J.-S.; Jo, K.; Lee, T.; Yun, T.; Cho, J.; Kim, B.-S., Facile synthesis of hybrid graphene and carbon nanotubes as a metal-free electrocatalyst with active dual interfaces for efficient oxygen reduction reaction. *Journal of Materials Chemistry A* **2013**.

57.   (a) K. Kinoshita, Electrochemical Oxygen Technology; Wiley & Sons: New York, **1992**.; (b) Song, C.; Zhang, J., Electrocatalytic Oxygen Reduction Reaction. In *PEM Fuel Cell Electrocatalysts and Catalyst Layers*, Zhang, J., Ed. Springer London: 2008; pp 89-134.

58.   (a) Suntivich, J.; Gasteiger, H. A.; Yabuuchi, N.; Shao-Horn, Y., Electrocatalytic Measurement Methodology of Oxide Catalysts Using a Thin-Film Rotating Disk Electrode. *Journal of The Electrochemical Society* **2010,** *157* (8), B1263-B1268; (b) Bonakdarpour, A.; Lefevre, M.; Yang, R.; Jaouen, F.; Dahn, T.; Dodelet, J.-P.; Dahn, J. R., Impact of Loading in RRDE Experiments on Fe–N–C Catalysts: Two- or Four-Electron Oxygen Reduction? *Electrochemical and Solid-State Letters* **2008,** *11* (6), B105-B108.

59.   Song, C.; Tang, Y.; Zhang, J. L.; Zhang, J.; Wang, H.; Shen, J.; McDermid, S.; Li, J.; Kozak, P., PEM fuel cell reaction kinetics in the temperature range of 23–120℃. *Electrochimica Acta* **2007,** *52* (7), 2552-2561.

60.   (a) Li, X.; Qu, W.; Zhang, J.; Wang, H., Electrocatalytic Activities of $La_{0.6}Ca_{0.4}CoO_3$ and $La_{0.6}Ca_{0.4}CoO_3$-Carbon Composites Toward the Oxygen Reduction Reaction in Concentrated Alkaline

Electrolytes. *Journal of The Electrochemical Society* **2011,** *158* (5), A597-A604; (b) Zhang, L.; Lee, K.; Bezerra, C. W. B.; Zhang, J.; Zhang, J., Fe loading of a carbon-supported Fe–N electrocatalyst and its effect on the oxygen reduction reaction. *Electrochimica Acta* **2009,** *54* (26), 6631-6636; (c) Mustain, W. E.; Prakash, J., Kinetics and mechanism for the oxygen reduction reaction on polycrystalline cobalt–palladium electrocatalysts in acid media. *Journal of Power Sources* **2007,** *170* (1), 28-37.

61.   Parthasarathy, A.; Srinivasan, S.; Appleby, A. J.; Martin, C. R., Temperature Dependence of the Electrode Kinetics of Oxygen Reduction at the Platinum/Nafion® Interface—A Microelectrode Investigation. *Journal of The Electrochemical Society* **1992,** *139* (9), 2530-2537.

62.   (a) Damjanovic, A.; Genshaw, M. A., Dependence of the kinetics of O2 dissolution at Pt on the conditions for adsorption of reaction intermediates. *Electrochimica Acta* **1970,** *15* (7), 1281-1283; (b) Gasteiger, H. A.; Ross, P. N., Oxygen Reduction on Platinum Low-Index Single-Crystal Surfaces in Alkaline Solution: Rotating Ring Disk Pt(*hkl*) Studies. *The Journal of Physical Chemistry* **1996,** *100* (16), 6715-6721.

63.   (a) Taylor, R. J.; Humffray, A. A., Electrochemical studies on glassy carbon electrodes: II. Oxygen reduction in solutions of high pH (pH 10). *Journal of Electroanalytical Chemistry and Interfacial Electrochemistry* **1975,** *64* (1), 63-84; (b) Taylor, R. J.; Humffray, A. A., Electrochemical studies on glassy carbon electrodes: III. Oxygen reduction in solutions of low pH (pH 10). *Journal of Electroanalytical Chemistry and Interfacial Electrochemistry* **1975,** *64* (1), 85-94.

64.   Wang, J. X.; Markovic, N. M.; Adzic, R. R., Kinetic Analysis of Oxygen Reduction on Pt(111) in Acid Solutions: Intrinsic Kinetic Parameters and Anion Adsorption Effects. *The Journal of Physical Chemistry B* **2004,** *108* (13), 4127-4133.

65.   http://catalysis.eprints.iitm.ac.in/1121/1/Electrocatalysi1.pdf.

66.   Cao, R.; Lee, J.-S.; Liu, M.; Cho, J., Non-Precious Catalysts: Recent Progress in Non-Precious Catalysts for Metal-Air Batteries (Adv. Energy Mater. 7/2012). *Advanced Energy Materials* **2012,** *2* (7), 701-701.

67.   Żółtowski, P.; Dražić, D. M.; Vorkapić, L., Carbon-air electrode with regenerative short time overload capacity: Part 1. Effect of manganese dioxide. *J Appl Electrochem* **1973,** *3* (4), 271-283.

68.   (a) Mao, L.; Sotomura, T.; Nakatsu, K.; Koshiba, N.; Zhang, D.; Ohsaka, T., Electrochemical Characterization of Catalytic Activities of Manganese Oxides to Oxygen Reduction in Alkaline Aqueous Solution. *J. Electrochem. Soc.* **2002,** *149* (4), A504; (b) Mao, L., Mechanistic study of the reduction of oxygen in air electrode with manganese oxides as electrocatalysts. *Electrochim. Acta* **2003,** *48* (8), 1015-1021; (c) Ohsaka, T.; Mao, L.; Arihara, K.; Sotomura, T., Bifunctional catalytic activity of manganese oxide toward O2 reduction: novel insight into the mechanism of alkaline air electrode. *Electrochem. Commun.* **2004,** *6* (3), 273-277; (d) Lima, F. H. B.; Calegaro, M. L.; Ticianelli,

E. A., Investigations of the catalytic properties of manganese oxides for the oxygen reduction reaction in alkaline media. *Journal of Electroanalytical Chemistry* **2006,** *590* (2), 152-160; (e) Yang, J.; Xu, J. J., Nanoporous amorphous manganese oxide as electrocatalyst for oxygen reduction in alkaline solutions. *Electrochemistry Communications* **2003,** *5* (4), 306-311; (f) Cheng, F.; Su, Y.; Liang, J.; Tao, Z.; Chen, J., MnO$_2$-Based Nanostructures as Catalysts for Electrochemical Oxygen Reduction in Alkaline Media†. *Chem. Mater.* **2010,** *22* (3), 898-905; (g) Cao, Y. L.; Yang, H. X.; Ai, X. P.; Xiao, L. F., The mechanism of oxygen reduction on MnO$_2$-catalyzed air cathode in alkaline solution. *J. Electroanal. Chem.* **2003,** *557*, 127-134.

69.   (a) Benbow, E. M.; Kelly, S. P.; Zhao, L.; Reutenauer, J. W.; Suib, S. L., Oxygen Reduction Properties of Bifunctional α-Manganese Oxide Electrocatalysts in Aqueous and Organic Electrolytes. *J. Phys. Chem. C* **2011,** *115* (44), 22009-22017; (b) Cheng, F.; Shen, J.; Ji, W.; Tao, Z.; Chen, J., Selective synthesis of manganese oxide nanostructures for electrocatalytic oxygen reduction. *ACS Appl. Mater. Interfaces* **2009,** *1* (2), 460-6; (c) Ominde, N.; Bartlett, N.; Yang, X.-Q.; Qu, D., Investigation of the oxygen reduction reaction on the carbon electrodes loaded with MnO$_2$ catalyst. *J. Power Sources* **2010,** *195* (13), 3984-3989.

70.   (a) Lima, F. H. B.; Calegaro, M. L.; Ticianelli, E. A., Electrocatalytic activity of manganese oxides prepared by thermal decomposition for oxygen reduction. *Electrochimica Acta* **2007,** *52* (11), 3732-3738; (b) J.P, B., Electrochemical behaviour of metallic oxides. *J. Power Sources* **1979,** *4* (3), 183-190.

71.   (a) Bezdička, P.; Grygar, T.; Klápště, B.; Vondrák, J., MnOx/C composites as electrode materials. I. Synthesis, XRD and cyclic voltammetric investigation. *Electrochim. Acta* **1999,** *45* (6), 913-920; (b) Klápště, B.; Vondrák, J.; Velická, J., MnOx/C composites as electrode materials II. Reduction of oxygen on bifunctional catalysts based on manganese oxides. *Electrochim. Acta* **2002,** *47* (15), 2365-2369; (c) Roche, I.; Chaînet, E.; Chatenet, M.; Vondrák, J., Carbon-Supported Manganese Oxide Nanoparticles as Electrocatalysts for the Oxygen Reduction Reaction (ORR) in Alkaline Medium: Physical Characterizations and ORR Mechanism. *The Journal of Physical Chemistry C* **2006,** *111* (3), 1434-1443; (d) Roche, I.; Scott, K., Carbon-supported manganese oxide nanoparticles as electrocatalysts for oxygen reduction reaction (orr) in neutral solution. *J. Appl. Electrochem.* **2008,** *39* (2), 197-204.

72.   (a) Gong, K.; Du, F.; Xia, Z.; Durstock, M.; Dai, L., Nitrogen-Doped Carbon Nanotube Arrays with High Electrocatalytic Activity for Oxygen Reduction. *Science* **2009,** *323* (5915), 760-764; (b) Qian, Y.; Lu, S.; Gao, F., Synthesis of manganese dioxide/reduced graphene oxide composites with excellent electrocatalytic activity toward reduction of oxygen. *Mater. Lett.* **2011,** *65* (1), 56-58; (c) Gong, K.; Yu, P.; Su, L.; Xiong, S.; Mao, L., Polymer-Assisted Synthesis of Manganese Dioxide/Carbon Nanotube Nanocomposite with Excellent Electrocatalytic Activity toward Reduction of Oxygen. *J. Phys. Chem. C* **2007,** *111* (5), 1882-1887; (d) Yang, Z.; Zhou, X.; Nie, H.; Yao, Z.;

Huang, S., Facile Construction of Manganese Oxide Doped Carbon Nanotube Catalysts with High Activity for Oxygen Reduction Reaction and Investigations into the Origin of their Activity Enhancement. *ACS Appl. Mater. Interfaces* **2011,** *3* (7), 2601-2606; (e) Lee, J.-S.; Park, G. S.; Lee, H. I.; Kim, S. T.; Cao, R.; Liu, M.; Cho, J., Ketjenblack Carbon Supported Amorphous Manganese Oxides Nanowires as Highly Efficient Electrocatalyst for Oxygen Reduction Reaction in Alkaline Solutions. *Nano Lett.* **2011,** *11* (12), 5362-5366; (f) Lee, J.-S.; Lee, T.; Song, H.-K.; Cho, J.; Kim, B.-S., Ionic liquid modified graphene nanosheets anchoring manganese oxide nanoparticles as efficient electrocatalysts for Zn-air batteries. *Energy Environ. Sci.* **2011,** *4* (10), 4148-4154.

73.   Lee, J.-S.; Park, G. S.; Lee, H. I.; Kim, S. T.; Cao, R.; Liu, M.; Cho, J., Ketjenblack Carbon Supported Amorphous Manganese Oxides Nanowires as Highly Efficient Electrocatalyst for Oxygen Reduction Reaction in Alkaline Solutions. *Nano Letters* **2011,** *11* (12), 5362-5366.

74.   Gorlin, Y.; Jaramillo, T. F., A Bifunctional Nonprecious Metal Catalyst for Oxygen Reduction and Water Oxidation. *J. Am. Chem. Soc.* **2010,** *132* (39), 13612-13614.

75.   (a) Cheng, F.; Shen, J.; Peng, B.; Pan, Y.; Tao, Z.; Chen, J., Rapid room-temperature synthesis of nanocrystalline spinels as oxygen reduction and evolution electrocatalysts. *Nat Chem* **2011,** *3* (1), 79-84; (b) Ríos, E.; Reyes, H.; Ortiz, J.; Gautier, J. L., Double channel electrode flow cell application to the study of HO_2^- production on $Mn_xCo_{3-x}O_4$ (0≤x≤1) spinel films. *Electrochimica Acta* **2005,** *50* (13), 2705-2711.

76.   Restovic, A.; Ríos, E.; Barbato, S.; Ortiz, J.; Gautier, J. L., Oxygen reduction in alkaline medium at thin $Mn_xCo_{3-x}O_4$ (0≤x≤1) spinel films prepared by spray pyrolysis. Effect of oxide cation composition on the reaction kinetics. *Journal of Electroanalytical Chemistry* **2002,** *522* (2), 141-151.

77.   (a) Yang, B. L.; Chan, S. F.; Chang, W. S.; Chen, Y. Z., Surface enrichment in mixed oxides of Cu, Co, and Mn, and its effect on CO oxidation. *Journal of Catalysis* **1991,** *130* (1), 52-61; (b) Joy, P. A.; Date, S. K., Unusual magnetic hysteresis behavior of oxide spinel $MnCo_2O_4$. *Journal of Magnetism and Magnetic Materials* **2000,** *210* (1–3), 31-34.

78.   Lu, B.; Cao, D.; Wang, P.; Wang, G.; Gao, Y., Oxygen evolution reaction on Ni-substituted Co3O4 nanowire array electrodes. *Int. J. Hydrogen Energy* **2011,** *36* (1), 72-78.

79.   Xie, X.; Li, Y.; Liu, Z.-Q.; Haruta, M.; Shen, W., Low-temperature oxidation of CO catalysed by Co3O4 nanorods. *Nature* **2009,** *458* (7239), 746-749.

80.   Compton, R. G., Comprehensive Chemical Kinetics. *Elsevier* **1987**.

81.   Liang, Y.; Li, Y.; Wang, H.; Zhou, J.; Wang, J.; Regier, T.; Dai, H., Co_3O_4 nanocrystals on graphene as a synergistic catalyst for oxygen reduction reaction. *Nat Mater* **2011,** *10* (10), 780-786.

82.   Xu, J.; Gao, P.; Zhao, T. S., Non-precious Co_3O_4 nano-rod electrocatalyst for oxygen reduction reaction in anion-exchange membrane fuel cells. *Energy Environ. Sci.* **2012,** *5* (1), 5333.

83.   (a) Nikolova, V.; Iliev, P.; Petrov, K.; Vitanov, T.; Zhecheva, E.; Stoyanova, R.; Valov, I.; Stoychev, D., Electrocatalysts for bifunctional oxygen/air electrodes. *J. Power Sources* **2008,** *185* (2),

727-733; (b) Vojvodic, A.; Nørskov, J. K., Optimizing Perovskites for the Water-Splitting Reaction. *Science* **2011,** *334* (6061), 1355-1356; (c) Thiele, D.; Züttel, A., Electrochemical characterisation of air electrodes based on La$_{0.6}$Sr$_{0.4}$CoO$_3$ and carbon nanotubes. *J. Power Sources* **2008,** *183* (2), 590-594; (d) Hammouche, A.; Kahoul, A.; Sauer, D. U.; De Doncker, R. W., Influential factors on oxygen reduction at La$_{1-x}$Ca$_x$CoO$_3$ electrodes in alkaline electrolyte. *J. Power Sources* **2006,** *153* (2), 239-244; (e) Yuasa, M.; Shimanoe, K.; Teraoka, Y.; Yamazoe, N., Preparation of carbon-supported nano-sized LaMnO$_3$ using reverse micelle method for energy-saving oxygen reduction cathode. *Catal. Today* **2007,** *126* (3-4), 313-319.

84.   (a) Stamenkovic, V. R.; Fowler, B.; Mun, B. S.; Wang, G.; Ross, P. N.; Lucas, C. A.; Marković, N. M., Improved Oxygen Reduction Activity on Pt$_3$Ni(111) via Increased Surface Site Availability. *Science* **2007,** *315* (5811), 493-497; (b) GreeleyJ; Stephens, I. E. L.; Bondarenko, A. S.; Johansson, T. P.; Hansen, H. A.; Jaramillo, T. F.; RossmeislJ; ChorkendorffI; Nørskov, J. K., Alloys of platinum and early transition metals as oxygen reduction electrocatalysts. *Nat. Chem.* **2009,** *1* (7), 552-556.

85.   Suntivich, J.; May, K. J.; Gasteiger, H. A.; Goodenough, J. B.; Shao-Horn, Y., A perovskite oxide optimized for oxygen evolution catalysis from molecular orbital principles. *Science* **2011,** *334* (6061), 1383-5.

86.   Cheriti, M.; Kahoul, A., Double perovskite oxides Sr$_2$MMoO$_6$ (M=Fe and Co) as cathode materials for oxygen reduction in alkaline medium. *Mater. Res. Bull.* **2012,** *47* (1), 135-141.

87.   Song, M.-K.; Park, S.; Alamgir, F. M.; Cho, J.; Liu, M., Nanostructured electrodes for lithium-ion and lithium-air batteries: the latest developments, challenges, and perspectives. *Materials Science and Engineering: R: Reports* **2011,** *72* (11), 203-252.

88.   Yang, L.; Jiang, S.; Zhao, Y.; Zhu, L.; Chen, S.; Wang, X.; Wu, Q.; Ma, J.; Ma, Y.; Hu, Z., Boron-Doped Carbon Nanotubes as Metal-Free Electrocatalysts for the Oxygen Reduction Reaction. *Angewandte Chemie International Edition* **2011,** *50* (31), 7132-7135.

89.   (a) Tang, Y.; Allen, B. L.; Kauffman, D. R.; Star, A., Electrocatalytic Activity of Nitrogen-Doped Carbon Nanotube Cups. *J. Am. Chem. Soc.* **2009,** *131* (37), 13200-13201; (b) Su, D. S.; Zhang, J.; Frank, B.; Thomas, A.; Wang, X.; Paraknowitsch, J.; Schlogl, R., Metal-free heterogeneous catalysis for sustainable chemistry. *ChemSusChem* **2010,** *3* (2), 169-80; (c) Calle-Vallejo, F.; Martinez, J. I.; Rossmeisl, J., Density functional studies of functionalized graphitic materials with late transition metals for Oxygen Reduction Reactions. *Phys. Chem. Chem. Phys.* **2011,** *13* (34), 15639-43; (d) Geng, D.; Chen, Y.; Chen, Y.; Li, Y.; Li, R.; Sun, X.; Ye, S.; Knights, S., High oxygen-reduction activity and durability of nitrogen-doped graphene. *Energy Environ. Sci.* **2011,** *4* (3), 760; (e) Geng, D.; Liu, H.; Chen, Y.; Li, R.; Sun, X.; Ye, S.; Knights, S., Non-noble metal oxygen reduction electrocatalysts based on carbon nanotubes with controlled nitrogen contents. *Journal of Power Sources* **2011,** *196* (4), 1795-1801; (f) Kim, H.; Lee, K.; Woo, S. I.; Jung, Y., On the mechanism of enhanced oxygen

reduction reaction in nitrogen-doped graphene nanoribbons. *Phys. Chem. Chem. Phys.* **2011,** *13* (39), 17505-10; (g) Li, H.; Liu, H.; Jong, Z.; Qu, W.; Geng, D.; Sun, X.; Wang, H., Nitrogen-doped carbon nanotubes with high activity for oxygen reduction in alkaline media. *International Journal of Hydrogen Energy* **2011,** *36* (3), 2258-2265; (h) Liu, G.; Li, X.; Lee, J.-W.; Popov, B. N., A review of the development of nitrogen-modified carbon-based catalysts for oxygen reduction at USC. *Catal. Sci. Technol.* **2011,** *1* (2), 207; (i) Ni, S.; Li, Z.; Yang, J., Oxygen molecule dissociation on carbon nanostructures with different types of nitrogen doping. *Nanoscale* **2011**; (j) Qiu, Y.; Yu, J.; Shi, T.; Zhou, X.; Bai, X.; Huang, J. Y., Nitrogen-doped ultrathin carbon nanofibers derived from electrospinning: Large-scale production, unique structure, and application as electrocatalysts for oxygen reduction. *J. Power Sources* **2011,** *196* (23), 9862-9867.

90.   Qu, L.; Liu, Y.; Baek, J.-B.; Dai, L., Nitrogen-Doped Graphene as Efficient Metal-Free Electrocatalyst for Oxygen Reduction in Fuel Cells. *ACS Nano* **2010,** *4* (3), 1321-1326.

91.   (a) Xiong, W.; Du, F.; Liu, Y.; Perez, A.; Supp, M.; Ramakrishnan, T. S.; Dai, L.; Jiang, L., 3-D Carbon Nanotube Structures Used as High Performance Catalyst for Oxygen Reduction Reaction. *J. Am. Chem. Soc.* **2010,** *132* (45), 15839-15841; (b) Wang, S.; Yu, D.; Dai, L.; Chang, D. W.; Baek, J.-B., Polyelectrolyte-Functionalized Graphene as Metal-Free Electrocatalysts for Oxygen Reduction. *ACS Nano* **2011,** *5* (8), 6202-6209.

92.   Shanmugam, S.; Osaka, T., Efficient electrocatalytic oxygen reduction over metal free-nitrogen doped carbon nanocapsules. *Chem. Commun.* **2011,** *47* (15), 4463-5.

93.   Yang, W.; Fellinger, T.-P.; Antonietti, M., Efficient Metal-Free Oxygen Reduction in Alkaline Medium on High-Surface-Area Mesoporous Nitrogen-Doped Carbons Made from Ionic Liquids and Nucleobases. *J. Am. Chem. Soc.* **2010,** *133* (2), 206-209.

94.   Zhu, S.; Chen, Z.; Li, B.; Higgins, D.; Wang, H.; Li, H.; Chen, Z., Nitrogen-doped carbon nanotubes as air cathode catalysts in zinc-air battery. *Electrochim. Acta* **2011,** *56* (14), 5080-5084.

95.   Yang, L.; Jiang, S.; Zhao, Y.; Zhu, L.; Chen, S.; Wang, X.; Wu, Q.; Ma, J.; Ma, Y.; Hu, Z., Boron-doped carbon nanotubes as metal-free electrocatalysts for the oxygen reduction reaction. *Angew. Chem. Int. Ed.* **2011,** *50* (31), 7132-5.

96.   Wang, S.; Iyyamperumal, E.; Roy, A.; Xue, Y.; Yu, D.; Dai, L., Vertically Aligned BCN Nanotubes as Efficient Metal-Free Electrocatalysts for the Oxygen Reduction Reaction: A Synergetic Effect by Co-Doping with Boron and Nitrogen. *Angew. Chem. Int. Ed.* **2011,** *50* (49), 11756-60.

97.   (a) Liu, Z.-W.; Peng, F.; Wang, H.-J.; Yu, H.; Zheng, W.-X.; Yang, J., Phosphorus-Doped Graphite Layers with High Electrocatalytic Activity for the O_2 Reduction in an Alkaline Medium. *Angewandte Chemie International Edition* **2011,** *50* (14), 3257-3261; (b) Yang, D.-S.; Bhattacharjya, D.; Inamdar, S.; Park, J.; Yu, J.-S., Phosphorus-Doped Ordered Mesoporous Carbons with Different Lengths as Efficient Metal-Free Electrocatalysts for Oxygen Reduction Reaction in Alkaline Media. *Journal of the American Chemical Society* **2012,** *134* (39), 16127-16130; (c) Yao, Z.; Nie, H.; Yang,

Z.; Zhou, X.; Liu, Z.; Huang, S., Catalyst-free synthesis of iodine-doped graphenevia a facile thermal annealing process and its use for electrocatalytic oxygen reduction in an alkaline medium. *Chemical Communications* **2012,** *48* (7), 1027-1029; (d) Yang, Z.; Yao, Z.; Li, G.; Fang, G.; Nie, H.; Liu, Z.; Zhou, X.; Chen, X. a.; Huang, S., Sulfur-Doped Graphene as an Efficient Metal-free Cathode Catalyst for Oxygen Reduction. *ACS Nano* **2011,** *6* (1), 205-211.

98.   Jasinski, R., A New Fuel Cell Cathode Catalyst. *Nature* **1964,** *201* (4925), 1212-1213.

99.   Alt, H.; Binder, H.; Sandstede, G., Mechanism of the electrocatalytic reduction of oxygen on metal chelates. *Journal of Catalysis* **1973,** *28* (1), 8-19.

100.   Bezerra, C. W. B.; Zhang, L.; Lee, K.; Liu, H.; Marques, A. L. B.; Marques, E. P.; Wang, H.; Zhang, J., A review of Fe–N/C and Co–N/C catalysts for the oxygen reduction reaction. *Electrochimica Acta* **2008,** *53* (15), 4937-4951.

101.   (a) Bezerra, C.; Zhang, L.; Lee, K.; Liu, H.; Marques, A.; Marques, E.; Wang, H.; Zhang, J., A review of Fe–N/C and Co–N/C catalysts for the oxygen reduction reaction. *Electrochim. Acta* **2008,** *53* (15), 4937-4951; (b) Chen, Z.; Higgins, D.; Yu, A.; Zhang, L.; Zhang, J., A review on non-precious metal electrocatalysts for PEM fuel cells. *Energy & Environmental Science* **2011,** *4* (9), 3167-3192; (c) Neburchilov, V.; Wang, H.; Martin, J. J.; Qu, W., A review on air cathodes for zinc–air fuel cells. *Journal of Power Sources* **2010,** *195* (5), 1271-1291.

102.   (a) Kadish, K. M.; Frémond, L.; Shen, J.; Chen, P.; Ohkubo, K.; Fukuzumi, S.; El Ojaimi, M.; Gros, C. P.; Barbe, J.-M.; Guilard, R., Catalytic Activity of Biscobalt Porphyrin-Corrole Dyads Toward the Reduction of Dioxygen. *Inorg. Chem.* **2009,** *48* (6), 2571-2582; (b) Kadish, K. M.; Frémond, L.; Ou, Z.; Shao, J.; Shi, C.; Anson, F. C.; Burdet, F.; Gros, C. P.; Barbe, J.-M.; Guilard, R., Cobalt(III) Corroles as Electrocatalysts for the Reduction of Dioxygen: Reactivity of a Monocorrole, Biscorroles, and Porphyrin−Corrole Dyads. *J. Am. Chem. Soc.* **2005,** *127* (15), 5625-5631; (c) Chang, C. J.; Loh, Z.-H.; Shi, C.; Anson, F. C.; Nocera, D. G., Targeted Proton Delivery in the Catalyzed Reduction of Oxygen to Water by Bimetallic Pacman Porphyrins. *J. Am. Chem. Soc.* **2004,** *126* (32), 10013-10020.

103.   Li, W.; Yu, A.; Higgins, D. C.; Llanos, B. G.; Chen, Z., Biologically Inspired Highly Durable Iron Phthalocyanine Catalysts for Oxygen Reduction Reaction in Polymer Electrolyte Membrane Fuel Cells. *J. Am. Chem. Soc.* **2010,** *132* (48), 17056-17058.

104.   Li Zhu, A.; Wang, H.; Qu, W.; Li, X.; Jong, Z.; Li, H., Low temperature pyrolyzed cobalt tetramethoxy phenylporphyrin catalyst and its applications as an improved catalyst for metal air batteries. *J. Power Sources* **2010,** *195* (17), 5587-5595.

105.   Chen, Z.; Choi, J.-Y.; Wang, H.; Li, H.; Chen, Z., Highly durable and active non-precious air cathode catalyst for zinc air battery. *J. Power Sources* **2011,** *196* (7), 3673-3677.

106.   Khomenko, V. G.; Barsukov, V. Z.; Katashinskii, A. S., The catalytic activity of conducting polymers toward oxygen reduction. *Electrochim. Acta* **2005,** *50* (7-8), 1675-1683.

107. Winther-Jensen, B.; Winther-Jensen, O.; Forsyth, M.; Macfarlane, D. R., High rates of oxygen reduction over a vapor phase-polymerized PEDOT electrode. *Science* **2008,** *321* (5889), 671-4.

108. Armand, M.; Tarascon, J. M., Building better batteries. *Nature* **2008,** *451* (7179), 652-657.

109. Lim, B.; Jiang, M.; Camargo, P. H. C.; Cho, E. C.; Tao, J.; Lu, X.; Zhu, Y.; Xia, Y., Pd-Pt Bimetallic Nanodendrites with High Activity for Oxygen Reduction. *Science* **2009,** *324* (5932), 1302-1305.

110. Kim, H.; Popov, B. N., Synthesis and Characterization of MnO_2-Based Mixed Oxides as Supercapacitors. *Journal of The Electrochemical Society* **2003,** *150* (3), D56-D62.

111. (a) Novoselov, K. S.; Geim, A. K.; Morozov, S. V.; Jiang, D.; Zhang, Y.; Dubonos, S. V.; Grigorieva, I. V.; Firsov, A. A., Electric Field Effect in Atomically Thin Carbon Films. *Science* **2004,** *306* (5696), 666-669; (b) Geim, A. K.; Novoselov, K. S., The rise of graphene. *Nat Mater* **2007,** *6* (3), 183-191.

112. Guo, S.; Wen, D.; Zhai, Y.; Dong, S.; Wang, E., Platinum Nanoparticle Ensemble-on-Graphene Hybrid Nanosheet: One-Pot, Rapid Synthesis, and Used as New Electrode Material for Electrochemical Sensing. *ACS Nano* **2010,** *4* (7), 3959-3968.

113. (a) Scheuermann, G. M.; Rumi, L.; Steurer, P.; Bannwarth, W.; Mülhaupt, R., Palladium Nanoparticles on Graphite Oxide and Its Functionalized Graphene Derivatives as Highly Active Catalysts for the Suzuki−Miyaura Coupling Reaction. *Journal of the American Chemical Society* **2009,** *131* (23), 8262-8270; (b) Fang, Y.; Guo, S.; Zhu, C.; Zhai, Y.; Wang, E., Self-Assembly of Cationic Polyelectrolyte-Functionalized Graphene Nanosheets and Gold Nanoparticles: A Two-Dimensional Heterostructure for Hydrogen Peroxide Sensing. *Langmuir* **2010,** *26* (13), 11277-11282.

114. Wang, D.; Choi, D.; Li, J.; Yang, Z.; Nie, Z.; Kou, R.; Hu, D.; Wang, C.; Saraf, L. V.; Zhang, J.; Aksay, I. A.; Liu, J., Self-Assembled TiO2–Graphene Hybrid Nanostructures for Enhanced Li-Ion Insertion. *ACS Nano* **2009,** *3* (4), 907-914.

115. Williams, G.; Kamat, P. V., Graphene−Semiconductor Nanocomposites: Excited-State Interactions between ZnO Nanoparticles and Graphene Oxide†. *Langmuir* **2009,** *25* (24), 13869-13873.

116. He, H.; Gao, C., Supraparamagnetic, Conductive, and Processable Multifunctional Graphene Nanosheets Coated with High-Density Fe3O4 Nanoparticles. *ACS Applied Materials & Interfaces* **2010,** *2* (11), 3201-3210.

117. MacFarlane, D. R.; Tachikawa, N.; Forsyth, M.; Pringle, J. M.; Howlett, P. C.; Elliott, G. D.; Davis, J. H.; Watanabe, M.; Simon, P.; Angell, C. A., Energy applications of ionic liquids. *Energy & Environmental Science* **2014,** *7* (1), 232-250.

118. Hummers, W. S.; Offeman, R. E., Preparation of Graphitic Oxide. *Journal of the American Chemical Society* **1958,** *80* (6), 1339-1339.

119. Yang, H.; Shan, C.; Li, F.; Han, D.; Zhang, Q.; Niu, L., Covalent functionalization of

polydisperse chemically-converted graphene sheets with amine-terminated ionic liquid. *Chemical Communications* **2009,** (26), 3880-3882.

120. Zhang, Y.; Shen, Y.; Yuan, J.; Han, D.; Wang, Z.; Zhang, Q.; Niu, L., Design and Synthesis of Multifunctional Materials Based on an Ionic-Liquid Backbone. *Angewandte Chemie International Edition* **2006,** *45* (35), 5867-5870.

121. Li, B.; Cao, H.; Shao, J.; Qu, M.; Warner, J. H., Superparamagnetic Fe_3O_4 nanocrystals@graphene composites for energy storage devices. *Journal of Materials Chemistry* **2011,** *21* (13), 5069-5075.

122. Snyder, J.; Fujita, T.; Chen, M. W.; Erlebacher, J., Oxygen reduction in nanoporous metal–ionic liquid composite electrocatalysts. *Nat Mater* **2010,** *9* (11), 904-907.

123. Treimer, S.; Tang, A.; Johnson, D. C., A Consideration of the Application of Koutecký-Levich Plots in the Diagnoses of Charge-Transfer Mechanisms at Rotated Disk Electrodes. *Electroanalysis* **2002,** *14* (3), 165-171.

124. (a) Lee, K.; Kim, M.; Kim, H., Catalytic nanoparticles being facet-controlled. *Journal of Materials Chemistry* **2010,** *20* (19), 3791-3798; (b) Stamenkovic, V. R.; Fowler, B.; Mun, B. S.; Wang, G.; Ross, P. N.; Lucas, C. A.; Markovic, N. M., Improved Oxygen Reduction Activity on $Pt_3Ni(111)$ via Increased Surface Site Availability. *Science* **2007**, 1135941.

125. Chen, Z.; Higgins, D.; Yu, A.; Zhang, L.; Zhang, J., A review on non-precious metal electrocatalysts for PEM fuel cells. *Energy & Environmental Science* **2011**.

126. (a) Mao, L.; Sotomura, T.; Nakatsu, K.; Koshiba, N.; Zhang, D.; Ohsaka, T., Electrochemical Characterization of Catalytic Activities of Manganese Oxides to Oxygen Reduction in Alkaline Aqueous Solution. *Journal of The Electrochemical Society* **2002,** *149* (4), A504-A507; (b) Cheng, F.; Su, Y.; Liang, J.; Tao, Z.; Chen, J., MnO2-Based Nanostructures as Catalysts for Electrochemical Oxygen Reduction in Alkaline Media†. *Chemistry of Materials* **2009,** *22* (3), 898-905; (c) Xiao, W.; Wang, D.; Lou, X. W., Shape-Controlled Synthesis of MnO_2 Nanostructures with Enhanced Electrocatalytic Activity for Oxygen Reduction. *The Journal of Physical Chemistry C* **2009,** *114* (3), 1694-1700.

127. (a) Kim, H.; Popov, B. N., Synthesis and Characterization of MnO_2-Based Mixed Oxides as Supercapacitors. *Journal of the Electrochemical Society* **2003,** *150* (3), D56-D62; (b) Zhang, L. L.; Wei, T.; Wang, W.; Zhao, X. S., Manganese oxide-carbon composite as supercapacitor electrode materials. *Microporous and Mesoporous Materials* **2009,** *123* (1-3), 260-267.

128. Ragupathy, P.; Park, D. H.; Campet, G.; Vasan, H. N.; Hwang, S.-J.; Choy, J.-H.; Munichandraiah, N., Remarkable Capacity Retention of Nanostructured Manganese Oxide upon Cycling as an Electrode Material for Supercapacitor. *The Journal of Physical Chemistry C* **2009,** *113* (15), 6303-6309.

129. Davis, R. E.; Horvath, G. L.; Tobias, C. W., The solubility and diffusion coefficient of

oxygen in potassium hydroxide solutions. *Electrochimica Acta* **1967,** *12* (3), 287-297.

130.   Bruce, P. G.; Freunberger, S. A.; Hardwick, L. J.; Tarascon, J.-M., Li-O2 and Li-S batteries with high energy storage. *Nat Mater* **2012,** *11* (1), 19-29.

131.   (a) Gasteiger, H. A.; Kocha, S. S.; Sompalli, B.; Wagner, F. T., Activity benchmarks and requirements for Pt, Pt-alloy, and non-Pt oxygen reduction catalysts for PEMFCs. *Appl. Catal. B-Environ.* **2005,** *56* (1-2), 9-35; (b) Antolini, E.; Salgado, J. R. C.; Giz, M. J.; Gonzalez, E. R., Effects of geometric and electronic factors on ORR activity of carbon supported Pt–Co electrocatalysts in PEM fuel cells. *International Journal of Hydrogen Energy* **2005,** *30* (11), 1213-1220.

132.   Jaouen, F.; Proietti, E.; Lefevre, M.; Chenitz, R.; Dodelet, J.-P.; Wu, G.; Chung, H. T.; Johnston, C. M.; Zelenay, P., Recent advances in non-precious metal catalysis for oxygen-reduction reaction in polymer electrolyte fuel cells. *Energy & Environmental Science* **2011,** *4* (1).

133.   (a) Wu, G.; More, K. L.; Johnston, C. M.; Zelenay, P., High-Performance Electrocatalysts for Oxygen Reduction Derived from Polyaniline, Iron, and Cobalt. *Science* **2011,** *332* (6028), 443-447; (b) Proietti, E.; Jaouen, F.; Lefèvre, M.; Larouche, N.; Tian, J.; Herranz, J.; Dodelet, J.-P., Iron-based cathode catalyst with enhanced power density in polymer electrolyte membrane fuel cells. *Nat Commun* **2011,** *2*, 416; (c) Lefèvre, M.; Proietti, E.; Jaouen, F.; Dodelet, J.-P., Iron-Based Catalysts with Improved Oxygen Reduction Activity in Polymer Electrolyte Fuel Cells. *Science* **2009,** *324* (5923), 71-74; (d) Choi, J.-Y.; Hsu, R. S.; Chen, Z., Highly Active Porous Carbon-Supported Nonprecious Metal−N Electrocatalyst for Oxygen Reduction Reaction in PEM Fuel Cells. *The Journal of Physical Chemistry C* **2010,** *114* (17), 8048-8053.

134.   Wen, Z.; Ci, S.; Zhang, F.; Feng, X.; Cui, S.; Mao, S.; Luo, S.; He, Z.; Chen, J., Nitrogen-Enriched Core-Shell Structured Fe/Fe$_3$C-C Nanorods as Advanced Electrocatalysts for Oxygen Reduction Reaction. *Advanced Materials* **2012,** *24* (11), 1399-1404.

135.   Powerair PDF.

136.   Lin, Z.; Song, M.-k.; Ding, Y.; Liu, Y.; Liu, M.; Wong, C.-p., Facile preparation of nitrogen-doped graphene as a metal-free catalyst for oxygen reduction reaction. *Physical Chemistry Chemical Physics* **2012,** *14* (10), 3381-3387.

137.   Kodama, M.; Yamashita, J.; Soneda, Y.; Hatori, H.; Kamegawa, K., Preparation and electrochemical characteristics of N-enriched carbon foam. *Carbon* **2007,** *45* (5), 1105-1107.

138.   Dong, X. L.; Zhang, Z. D.; Xiao, Q. F.; Zhao, X. G.; Chuang, Y. C.; Jin, S. R.; Sun, W. M.; Li, Z. J.; Zheng, Z. X.; Yang, H., Characterization of ultrafine γ-Fe(C), α-Fe(C) and Fe$_3$C particles synthesized by arc-discharge in methane. *Journal of Materials Science* **1998,** *33* (7), 1915-1919.

139.   Liu, R.; Wu, D.; Feng, X.; Müllen, K., Nitrogen-Doped Ordered Mesoporous Graphitic Arrays with High Electrocatalytic Activity for Oxygen Reduction. *Angewandte Chemie International Edition* **2010,** *49* (14), 2565-2569.

140.   (a) Choi, C. H.; Park, S. H.; Woo, S. I., Heteroatom doped carbons prepared by the pyrolysis

of bio-derived amino acids as highly active catalysts for oxygen electro-reduction reactions. *Green Chemistry* **2011,** *13* (2), 406-412; (b) Wu, Y. P.; Fang, S.; Jiang, Y.; Holze, R., Effects of doped sulfur on electrochemical performance of carbon anode. *Journal of Power Sources* **2002,** *108* (1–2), 245-249.

141.   (a) Byon, H. R.; Suntivich, J.; Shao-Horn, Y., Graphene-Based Non-Noble-Metal Catalysts for Oxygen Reduction Reaction in Acid. *Chemistry of Materials* **2011,** *23* (15), 3421-3428; (b) Byon, H. R.; Suntivich, J.; Crumlin, E. J.; Shao-Horn, Y., Fe-N-modified multi-walled carbon nanotubes for oxygen reduction reaction in acid. *Physical Chemistry Chemical Physics* **2011,** *13* (48), 21437-21445.

142.   Datsyuk, V.; Kalyva, M.; Papagelis, K.; Parthenios, J.; Tasis, D.; Siokou, A.; Kallitsis, I.; Galiotis, C., Chemical oxidation of multiwalled carbon nanotubes. *Carbon* **2008,** *46* (6), 833-840.

143.   (a) Blizanac, B. B.; Ross, P. N.; Markovic, N. M., Oxygen electroreduction on Ag(1 1 1): The pH effect. *Electrochimica Acta* **2007,** *52* (6), 2264-2271; (b) Antolini, E.; Gonzalez, E. R., Alkaline direct alcohol fuel cells. *Journal of Power Sources* **2010,** *195* (11), 3431-3450; (c) Liang, Y.; Wang, H.; Zhou, J.; Li, Y.; Wang, J.; Regier, T.; Dai, H., Covalent Hybrid of Spinel Manganese–Cobalt Oxide and Graphene as Advanced Oxygen Reduction Electrocatalysts. *Journal of the American Chemical Society* **2012,** *134* (7), 3517-3523.

144.   (a) Zhang, J.; Vukmirovic, M. B.; Xu, Y.; Mavrikakis, M.; Adzic, R. R., Controlling the Catalytic Activity of Platinum-Monolayer Electrocatalysts for Oxygen Reduction with Different Substrates. *Angewandte Chemie International Edition* **2005,** *44* (14), 2132-2135; (b) Steele, B. C. H.; Heinzel, A., Materials for fuel-cell technologies. *Nature* **2001,** *414* (6861), 345-352.

145.   Chen, Z.; Waje, M.; Li, W.; Yan, Y., Supportless Pt and PtPd Nanotubes as Electrocatalysts for Oxygen-Reduction Reactions. *Angewandte Chemie International Edition* **2007,** *46* (22), 4060-4063.

146.   (a) Sheng, Z.-H.; Shao, L.; Chen, J.-J.; Bao, W.-J.; Wang, F.-B.; Xia, X.-H., Catalyst-Free Synthesis of Nitrogen-Doped Graphene via Thermal Annealing Graphite Oxide with Melamine and Its Excellent Electrocatalysis. *ACS Nano* **2011,** *5* (6), 4350-4358; (b) Yang, W.; Fellinger, T.-P.; Antonietti, M., Efficient Metal-Free Oxygen Reduction in Alkaline Medium on High-Surface-Area Mesoporous Nitrogen-Doped Carbons Made from Ionic Liquids and Nucleobases. *Journal of the American Chemical Society* **2010,** *133* (2), 206-209.

147.   (a) Stankovich, S.; Dikin, D. A.; Piner, R. D.; Kohlhaas, K. A.; Kleinhammes, A.; Jia, Y.; Wu, Y.; Nguyen, S. T.; Ruoff, R. S., Synthesis of graphene-based nanosheets via chemical reduction of exfoliated graphite oxide. *Carbon* **2007,** *45* (7), 1558-1565; (b) Stankovich, S.; Dikin, D. A.; Dommett, G. H. B.; Kohlhaas, K. M.; Zimney, E. J.; Stach, E. A.; Piner, R. D.; Nguyen, S. T.; Ruoff, R. S., Graphene-based composite materials. *Nature* **2006,** *442* (7100), 282-286.

148.   Xiong, W.; Du, F.; Liu, Y.; Perez, A.; Supp, M.; Ramakrishnan, T. S.; Dai, L.; Jiang, L., 3-D Carbon Nanotube Structures Used as High Performance Catalyst for Oxygen Reduction Reaction. *Journal of the American Chemical Society* **2010,** *132* (45), 15839-15841.

149.   (a) Xiao, J.; Kuang, Q.; Yang, S.; Xiao, F.; Wang, S.; Guo, L., Surface Structure Dependent Electrocatalytic Activity of Co_3O_4 Anchored on Graphene Sheets toward Oxygen Reduction Reaction. *Sci. Rep.* **2013,** *3*; (b) Kelty, M., straubel, EFFICIENT DUAL SOURCE BATTERY PACK SYSTEM FOR AN ELECTRIC VEHICLE. *US 12/965,000* **2012**.

150.   Kinoshita, K., *Electrochemical Oxygen Technology*. John Wiley & Sons. New York: 1998.

151.   (a) Morcos, I.; Yeager, E., Kinetic studies of the oxygen—peroxide couple on pyrolytic graphite. *Electrochimica Acta* **1970,** *15* (6), 953-975; (b) Qu, D., Investigation of oxygen reduction on activated carbon electrodes in alkaline solution. *Carbon* **2007,** *45* (6), 1296-1301.

152.   (a) Guo, S.; Zhang, S.; Sun, S., Tuning Nanoparticle Catalysis for the Oxygen Reduction Reaction. *Angewandte Chemie International Edition* **2013,** *52* (33), 8526-8544; (b) Debe, M. K., Electrocatalyst approaches and challenges for automotive fuel cells. *Nature* **2012,** *486* (7401), 43-51.

153.   (a) Liang, Y. Y.; Wang, H. L.; Zhou, J. G.; Li, Y. G.; Wang, J.; Regier, T.; Dai, H. J., Covalent Hybrid of Spinel Manganese-Cobalt Oxide and Graphene as Advanced Oxygen Reduction Electrocatalysts. *J. Am. Chem. Soc.* **2012,** *134* (7), 3517-3523; (b) Ramaswamy, N.; Mukerjee, S., Influence of Inner- and Outer-Sphere Electron Transfer Mechanisms during Electrocatalysis of Oxygen Reduction in Alkaline Media. *The Journal of Physical Chemistry C* **2011,** *115* (36), 18015-18026; (c) Cao, R.; Thapa, R.; Kim, H.; Xu, X.; Gyu Kim, M.; Li, Q.; Park, N.; Liu, M.; Cho, J., Promotion of oxygen reduction by a bio-inspired tethered iron phthalocyanine carbon nanotube-based catalyst. *Nat. Commun.* **2013,** *4*.

154.   (a) Haas, O.; Wesemael, J. V., *Encyclopedia of electrochemical power source*. Elsevier: 2009; (b) Büchi, F. N. I., Minoru; Schmidt, Thomas J, *Polymer Electrolyte Fuel Cell Durability*. Springer: 2009.

155.   Maldonado, S.; Morin, S.; Stevenson, K. J., Structure, composition, and chemical reactivity of carbon nanotubes by selective nitrogen doping. *Carbon* **2006,** *44* (8), 1429-1437.

156.   (a) Pels, J. R.; Kapteijn, F.; Moulijn, J. A.; Zhu, Q.; Thomas, K. M., Evolution of nitrogen functionalities in carbonaceous materials during pyrolysis. *Carbon* **1995,** *33* (11), 1641-1653; (b) Matter, P. H.; Zhang, L.; Ozkan, U. S., The role of nanostructure in nitrogen-containing carbon catalysts for the oxygen reduction reaction. *Journal of Catalysis* **2006,** *239* (1), 83-96.

157.   (a) Xu, B.; Hou, S. S.; Cao, G. P.; Wu, F.; Yang, Y. S., Sustainable nitrogen-doped porous carbon with high surface areas prepared from gelatin for supercapacitors. *Journal of Materials Chemistry* **2012,** *22* (36), 19088-19093; (b) Hulicova, D.; Yamashita, J.; Soneda, Y.; Hatori, H.; Kodama, M., Supercapacitors Prepared from Melamine-Based Carbon. *Chem. Mater.* **2005,** *17* (5), 1241-1247.

158.   Lee, J. S.; Park, G. S.; Kim, S. T.; Liu, M. L.; Cho, J., A Highly Efficient Electrocatalyst for the Oxygen Reduction Reaction: N-Doped Ketjenblack Incorporated into Fe/Fe_3C-Functionalized Melamine Foam. *Angew. Chem. Int. Ed.* **2013,** *52* (3), 1026-1030.

159.   (a) Mao, Y.; Duan, H.; Xu, B.; Zhang, L.; Hu, Y. S.; Zhao, C. C.; Wang, Z. X.; Chen, L. Q.; Yang, Y. S., Lithium storage in nitrogen-rich mesoporous carbon materials. *Energy Environ. Sci.* **2012,** *5* (7), 7950-7955; (b) Schnepp, Z.; Zhang, Y.; Hollamby, M. J.; Pauw, B. R.; Tanaka, M.; Matsushita, Y.; Sakka, Y., Doped-carbon electrocatalysts with trimodal porosity from a homogeneous polypeptide gel. *J. Mater. Chem. A* **2013.**

160.   (a) Harris, P. J. F., New Perspectives on the Structure of Graphitic Carbons. *Crit. Rev. Solid State Mater. Sci.* **2005,** *30* (4), 235-253; (b) Lee, J. S.; Park, G. S.; Lee, H. I.; Kim, S. T.; Cao, R. G.; Liu, M. L.; Cho, J., Ketjenblack Carbon Supported Amorphous Manganese Oxides Nanowires as Highly Efficient Electrocatalyst for Oxygen Reduction Reaction in Alkaline Solutions. *Nano Lett.* **2011,** *11* (12), 5362-5366.

161.   Balasubramanian, K.; Burghard, M., Chemically Functionalized Carbon Nanotubes. *Small* **2005,** *1* (2), 180-192.

162.   Eastoe, J., The amino acid composition of fish collagen and gelatin. *Biochemical Journal* **1957,** *65* (2), 363.

163.   (a) Wu, G.; Li, D.; Dai, C.; Wang, D.; Li, N., Well-Dispersed High-Loading Pt Nanoparticles Supported by Shell−Core Nanostructured Carbon for Methanol Electrooxidation. *Langmuir* **2008,** *24* (7), 3566-3575; (b) Li, Z. Q.; Lu, C. J.; Xia, Z. P.; Zhou, Y.; Luo, Z., X-ray diffraction patterns of graphite and turbostratic carbon. *Carbon* **2007,** *45* (8), 1686-1695.

164.   Maldonado, S.; Stevenson, K. J., Influence of Nitrogen Doping on Oxygen Reduction Electrocatalysis at Carbon Nanofiber Electrodes. *The Journal of Physical Chemistry B* **2005,** *109* (10), 4707-4716.

165.   Kundu, S.; Nagaiah, T. C.; Xia, W.; Wang, Y.; Dommele, S. V.; Bitter, J. H.; Santa, M.; Grundmeier, G.; Bron, M.; Schuhmann, W.; Muhler, M., Electrocatalytic Activity and Stability of Nitrogen-Containing Carbon Nanotubes in the Oxygen Reduction Reaction. *The Journal of Physical Chemistry C* **2009,** *113* (32), 14302-14310.

166.   (a) Chen, S.; Bi, J.; Zhao, Y.; Yang, L.; Zhang, C.; Ma, Y.; Wu, Q.; Wang, X.; Hu, Z., Nitrogen-Doped Carbon Nanocages as Efficient Metal-Free Electrocatalysts for Oxygen Reduction Reaction. *Advanced Materials* **2012,** *24* (41), 5593-5597; (b) Jeon, I.-Y.; Choi, H.-J.; Choi, M.; Seo, J.-M.; Jung, S.-M.; Kim, M.-J.; Zhang, S.; Zhang, L.; Xia, Z.; Dai, L.; Park, N.; Baek, J.-B., Facile, scalable synthesis of edge-halogenated graphene nanoplatelets as efficient metal-free eletrocatalysts for oxygen reduction reaction. *Sci. Rep.* **2013,** *3*; (c) Liang, J.; Jiao, Y.; Jaroniec, M.; Qiao, S. Z., Sulfur and Nitrogen Dual-Doped Mesoporous Graphene Electrocatalyst for Oxygen Reduction with Synergistically Enhanced Performance. *Angew. Chem. Int. Ed.* **2012,** *51* (46), 11496-11500; (d) Liang, J.; Zheng, Y.; Chen, J.; Liu, J.; Hulicova-Jurcakova, D.; Jaroniec, M.; Qiao, S. Z., Facile Oxygen Reduction on a Three-Dimensionally Ordered Macroporous Graphitic C3N4/Carbon Composite Electrocatalyst. *Angew. Chem. Int. Ed.* **2012,** *51* (16), 3892-3896; (e) Wang, S.; Yu, D.; Dai, L.,

Polyelectrolyte Functionalized Carbon Nanotubes as Efficient Metal-free Electrocatalysts for Oxygen Reduction. *Journal of the American Chemical Society* **2011,** *133* (14), 5182-5185; (f) Yang, D. S.; Bhattacharjya, D.; Inamdar, S.; Park, J.; Yu, J. S., Phosphorus-doped ordered mesoporous carbons with different lengths as efficient metal-free electrocatalysts for oxygen reduction reaction in alkaline media. *J. Am. Chem. Soc.* **2012,** *134* (39), 16127-30.

167.   Li, Y.; Gong, M.; Liang, Y.; Feng, J.; Kim, J.-E.; Wang, H.; Hong, G.; Zhang, B.; Dai, H., Advanced zinc-air batteries based on high-performance hybrid electrocatalysts. *Nat Commun* **2013,** *4*, 1805.

168.   (a) Jaouen, F.; Proietti, E.; Lefevre, M.; Chenitz, R.; Dodelet, J.-P.; Wu, G.; Chung, H. T.; Johnston, C. M.; Zelenay, P., Recent advances in non-precious metal catalysis for oxygen-reduction reaction in polymer electrolyte fuel cells. *Energy & Environmental Science* **2011,** *4* (1), 114-130; (b) Lefevre, M.; Proietti, E.; Jaouen, F.; Dodelet, J. P., Iron-Based Catalysts with Improved Oxygen Reduction Activity in Polymer Electrolyte Fuel Cells. *Science* **2009,** *324* (5923), 71-74.

169.   Li, W.; Wu, J.; Higgins, D. C.; Choi, J.-Y.; Chen, Z., Determination of Iron Active Sites in Pyrolyzed Iron-Based Catalysts for the Oxygen Reduction Reaction. *ACS Catalysis* **2012,** *2* (12), 2761-2768.

170.   Kramm, U. I.; Herranz, J.; Larouche, N.; Arruda, T. M.; Lefevre, M.; Jaouen, F.; Bogdanoff, P.; Fiechter, S.; Abs-Wurmbach, I.; Mukerjee, S.; Dodelet, J.-P., Structure of the catalytic sites in Fe/N/C-catalysts for O2-reduction in PEM fuel cells. *Physical Chemistry Chemical Physics* **2012,** *14* (33), 11673-11688.

171.   Ward, A. L.; Elbaz, L.; Kerr, J. B.; Arnold, J., Nonprecious Metal Catalysts for Fuel Cell Applications: Electrochemical Dioxygen Activation by a Series of First Row Transition Metal Tris(2-pyridylmethyl)amine Complexes. *Inorganic Chemistry* **2012,** *51* (8), 4694-4706.

172.   Baker, W. A.; Bobonich, H. M., Magnetic Studies of Mixed Ligand Complexes of Iron(II). *Inorganic Chemistry* **1963,** *2* (5), 1071-1072.

173.   Huang, L.; Wang, H.; Chen, J.; Wang, Z.; Sun, J.; Zhao, D.; Yan, Y., Synthesis, morphology control, and properties of porous metal–organic coordination polymers. *Microporous Mesoporous Mater.* **2003,** *58* (2), 105-114.

174.   Burger, K.; Ebel, H.; Madeja, K., The effect of spin states of iron[II] on the XPS of its mixed complexes. *J. Electron Spectrosc. Relat. Phenom.* **1982,** *28* (1), 115-121.

175.   Joubert, L.; Guillemoles, J.-F.; Adamo, C., A theoretical investigation of the dye-redox mediator interaction in dye-sensitized photovoltaic cells. *Chem. Phys. Lett.* **2003,** *371* (3–4), 378-385.

176.   Rao, M. L. B.; Damjanovic, A.; Bockris, J. O. M., OXYGEN ADSORPTION RELATED TO THE UNPAIRED d-ELECTRONS IN TRANSITION METALS. *The Journal of Physical Chemistry* **1963,** *67* (11), 2508-2509.

177.   Kramm, U. I.; Abs-Wurmbach, I.; Herrmann-Geppert, I.; Radnik, J.; Fiechter, S.; Bogdanoff,

P., Influence of the Electron-Density of FeN4-Centers Towards the Catalytic Activity of Pyrolyzed FeTMPPCl-Based ORR-Electrocatalysts. *Journal of The Electrochemical Society* **2011,** *158* (1), B69-B78.

178.   MEET *아연공기전지기술개발현황 및 향후발전 전망 (Zinc air fuel cell for EV)*; 2010.

179.   Logan, B. E.; Hamelers, B.; Rozendal, R.; Schröder, U.; Keller, J.; Freguia, S.; Aelterman, P.; Verstraete, W.; Rabaey, K., Microbial Fuel Cells: Methodology and Technology†. *Environmental Science & Technology* **2006,** *40* (17), 5181-5192.

Acknowledgements